

EMERGENT COLLECTIVE BEHAVIOR IN  
MULTI-AGENT SYSTEMS: AN EVOLUTIONARY  
PERSPECTIVE

DARREN PAIS

A DISSERTATION  
PRESENTED TO THE FACULTY  
OF PRINCETON UNIVERSITY  
IN CANDIDACY FOR THE DEGREE  
OF DOCTOR OF PHILOSOPHY

RECOMMENDED FOR ACCEPTANCE  
BY THE DEPARTMENT OF  
MECHANICAL AND AEROSPACE ENGINEERING  
ADVISER: PROFESSOR NAOMI EHRICH LEONARD

NOVEMBER 2012

© Copyright by Darren Pais, 2012.  
All rights reserved.

# Abstract

The study of collective behavior involves the analysis of interactions among a set of agents that yield collective outcomes at the level of the group. The behavior is said to be emergent when it cannot be understood simply as the sum of its constituent parts. Further, group-level outcomes can in turn influence individual interactions. The complexity of this interplay makes the study of emergence challenging and exciting. This dissertation is focused on the study of emergent collective behavior from the perspective of evolution. Evolution is a simple yet powerful algorithm, which when acting on interacting entities in a dynamic environment, yields an array of fascinating behavior as manifest in the natural world. Natural collectives display a wide variety of cooperative behavior and have evolved to efficiently manage the inherent tradeoff between robust behavior and adaptability to dynamic environments. These properties have motivated the design of bio-inspired algorithms for sensing and decision-making in robotic collectives. In this work, we study the evolutionary mechanisms for co-operation and tradeoff management in biological collectives, with a focus on four related topics: replicator-mutator dynamics, collective migration, collective pursuit and evasion, and decision-making dynamics in swarms.

The *replicator-mutator dynamics* define a canonical model from evolutionary theory and have recently been used to study the evolution of language and the behavioral dynamics of social networks. While the analysis of stable equilibria of these dynamics has been a focus in the literature, we prove that certain conditions suffice for the equations to exhibit stable limit cycles. These cycles correspond to oscillations of grammar dominance in language evolution and to oscillations in behavioral preferences in social networks. For the *collective migration* problem, it is well-established that a small group of leaders can guide a large swarm of followers. It is less clear how presumably self-interested individuals have evolved to take on such divergent roles. We design a network-based evolutionary model to understand the evolution of leadership in migration, with a focus on the role of network topology on the emergent dynamics. *Pursuit and evasive behaviors* are ubiquitous in biology and are key drivers for collective motion. We use computational simulations and analytical calculations to study a co-evolving pursuit and evasive system, and incorporate the evolved strategies in a cyclic pursuit-evasion collective motion model. The ‘stop-signaling’ inhibitory mechanism has been recently shown to be critical to the decentralized *decision-making dynamics* in honeybee swarms. We investigate bifurcations in a model of swarm decision-making as a function of the stop-signal and the values of different alternatives, and present a comprehensive analysis of the dynamics of the model.

## Acknowledgements

First, I would like to acknowledge my advisor Naomi Leonard. Naomi is a brilliant scientist, an immensely creative researcher, and above all, a wonderful and caring person. Naomi's gentle persuasion to always think deeply and clearly about a problem, her discerning taste for exciting research questions, and her extraordinary ability to make connections across diverse areas, have had an immense impact on my development and growth as a graduate student. I am extremely grateful to Naomi for allowing me the freedom to pursue my interests and for helping me build the confidence to tackle challenging new problems. I will fondly remember the countless hours spent discussing ideas in Naomi's office and will always be grateful for her consistent and detailed edits of numerous paper drafts and thesis chapters. Naomi's constant support and encouragement have made for a truly rewarding graduate school experience.

My committee members Phil Holmes and Simon Levin have been important sources of guidance and support over the years. Much of this thesis rests on fundamental tools and ideas that I first encountered in classes that I took with Phil and Simon, early on in graduate school. I am grateful for the interest that they have taken in my research and my career. I am also tremendously grateful for their time and effort spent in reading my thesis and providing meticulous feedback. The process of editing this thesis with help from Naomi, Phil and Simon has been an invaluable learning experience.

I am grateful to my thesis defense examiners Rob Stengel and Howard Stone for taking an interest in my work and for being excellent role models. I appreciate their willingness and enthusiasm to discuss a range of topics including teaching, careers, jobs, and research styles; these discussions have left a lasting impression on me. I immensely enjoyed the opportunity to assist Rob in teaching his 'robotics and intelligent systems' course. Playing regular 'noon hoops' basketball with Howard at Dillon Gym has been a unique privilege; Howard has the same impressive creativity and energy on the basketball court that he does as a professor.

The Mechanical and Aerospace engineering (MAE) department at Princeton is a vibrant and stimulating environment, and has been the perfect place to learn the fundamentals of dynamics and control (D&C), and consider broad applications. The quality of teaching and breath of research in D&C at Princeton is fantastic. I would like to acknowledge the D&C faculty (Naomi, Phil, Rob, Jeremy Kasdin, Mike Littman and Clancy Rowley) and my D&C classmates for helping me build a strong

foundation and for introducing me to their diverse and exciting research interests including planet finding, fluid flow control and neuronal network dynamics.

The work on honeybee swarms in Chapter 7 has come out of a recent collaboration with James Marshall and Patrick Hogan at the University of Sheffield, which began in 2011 at the Mathematical Biosciences Institute in Ohio. Working with James and Patrick has been an extraordinary privilege. I have learnt a tremendous amount from them, not only about the biology of honeybee swarms, but also about successful approaches to interdisciplinary research and collaboration. I am grateful for the many stimulating discussions we have had over the past two years; these discussions have impacted several areas of this thesis. The work in Chapter 5 is inspired in large part by the array of captivating experimental and computational work by Iain Couzin and his collaborators, particularly, Vishu Guttal and Colin Torney. Iain is an extremely gifted speaker and scientist. Interacting with him, Vishu, Colin, and the rest of the Couzin group over the years has been tremendously rewarding.

I would like to acknowledge two former postdoctoral research scholars in our group, Carlos Caicedo-Núñez and Ming Cao. Carlos and I collaborated closely on the work presented in Chapter 4; I appreciate his algebraic tenacity and enthusiasm for new ideas. Ming was a collaborator on my first graduate school research project on tensegrity-based formation control, and was an important mentor during my initial years as a graduate student. I am grateful to both Carlos and Ming for their friendship over the years. I am also grateful for the friendship and support from all the members of the Leonard group, both past and present. Ben Nabet, Dan Swain, Andy Stewart, Kendra Cofield, Stephanie Goldfarb, George Young, Tian Shen and Paul Reverdy have all been good friends and always available to discuss new ideas.

The Princeton campus and the MAE department have been extremely supportive and nurturing environments in which to think, interact and grow. I am grateful for the many close friends that I have made here, beginning with my experience as a first-year resident at the Graduate College. I hesitate to name all these individuals, lest I mistakenly leave someone out. Suffice to say that each of them has impacted me in a unique way and I hope we continue to remain in touch for many years to come. I want to thank Anand Ashok, Katie Fitch, Paul Reverdy, David Turnbull and George Young for helping me proof-read the final draft of this thesis. Of course, any missed typos you may now find are their fault. I am grateful to the MAE graduate administrators Jessica O’Leary and Jill Ray for making the paperwork seamless, and for always having something encouraging to say, even on the toughest days.

My work as a graduate fellow at the McGraw Center for Teaching and Learning has been extremely rewarding. I would like to acknowledge the McGraw center staff (Carol Porter, Nic Voge, Jeff Himpele, Sandra Moskovitz) for their valuable guidance. Much of this thesis was written in the comfort of the beautiful Princeton home of Daisy Fitch and Professor Val Fitch. I thank them for the extraordinary opportunity to spend my final Princeton summer in such a calm and peaceful environment; this thesis would perhaps have taken significantly longer to complete without it.

Finally, I would like to thank my family for their love, support, and encouragement over the years. I thank my sister for always helping me keep things in perspective and for helping me stay balanced. She has been a constant cheerleader of my successes and I value our relationship greatly. I thank my parents for giving us an open-minded multicultural childhood that was fun and dynamic, with never a dull moment. Most importantly, I thank them for helping us prioritize the right things in life and teaching us the immense joy and value of learning. My parents always encouraged us to dream big and I will forever be grateful to them for giving us the resources and ability to freely follow our dreams, wherever that may lead.

My time at Princeton was supported by several generous fellowships, for which I am deeply grateful: the Gordon Y. S. Wu first-year fellowship, the Martin Summerfield memorial graduate fellowship, the Britt and Eli Harari fellowship for an international student, and the Harold W. Dodds honorific fellowship. My research was also supported in part by grants from the Office of Naval Research, the Air Force Office of Scientific Research, the Army Research Office, and the National Science Foundation.

This dissertation is labeled T-3247 in the records of the Department of Mechanical and Aerospace Engineering.

To my parents.

# Contents

Abstract . . . . .	iii
Acknowledgements . . . . .	iv
List of Figures . . . . .	xi
<b>1 Introduction</b>	<b>1</b>
1.1 Overview of Topics . . . . .	4
1.1.1 Replicator-Mutator Dynamics . . . . .	4
1.1.2 Collective Migration . . . . .	5
1.1.3 Pursuit and Evasion . . . . .	7
1.1.4 Swarm Decision-Making . . . . .	7
1.2 Contributions and Thesis Outline . . . . .	8
<b>2 Background</b>	<b>10</b>
2.1 Evolutionary Dynamics . . . . .	10
2.2 Dynamical Systems Tools . . . . .	16
2.3 Graph Theory Tools . . . . .	20
2.4 Stochastic Dynamics . . . . .	22
2.4.1 Random Points on a Simplex . . . . .	25
<b>3 Replicator-Mutator Dynamics in the Plane</b>	<b>26</b>
3.1 Model Description . . . . .	27
3.2 Motivation for Cycles . . . . .	30
3.3 Bifurcations with $N = 2$ Strategies . . . . .	32
3.4 Planar Analysis . . . . .	33
<b>4 Replicator-Mutator Dynamics in Higher Dimensions</b>	<b>41</b>
4.1 Hopf Bifurcation Calculation . . . . .	42
4.2 Criticality of Hopf Bifurcation . . . . .	45
4.3 Illustration of Bifurcations . . . . .	47

4.4	One-Parameter Multi-Cycles . . . . .	49
4.4.1	Case 2 Analysis . . . . .	50
4.5	Extensions and Generalizations . . . . .	54
4.6	Final Remarks . . . . .	58
<b>5</b>	<b>Evolutionary Dynamics of Collective Migration</b>	<b>59</b>
5.1	Model Description . . . . .	61
5.2	Evolutionary Dynamics in the All-to-all Limit . . . . .	66
5.2.1	Adaptive Dynamics Calculations . . . . .	67
5.2.2	Adaptive Dynamics Results . . . . .	68
5.2.3	Evolutionary Simulations . . . . .	70
5.3	Evolutionary Dynamics with Limited Social Interactions . . . . .	72
5.3.1	Fast Timescale Results . . . . .	72
5.3.2	Slow Timescale Evolutionary Dynamics . . . . .	77
5.4	Dynamic Nodes and Bifurcations . . . . .	80
5.5	Final Remarks . . . . .	84
<b>6</b>	<b>Coevolutionary Dynamics of Pursuit and Evasion</b>	<b>87</b>
6.1	Dynamics of Pursuit and Evasion . . . . .	89
6.2	Evolutionary Dynamics . . . . .	93
6.2.1	Monte-Carlo Simulations . . . . .	94
6.2.2	Theoretical Analysis . . . . .	96
6.3	Collective Motion . . . . .	99
6.4	Final Remarks . . . . .	101
<b>7</b>	<b>Decision-Making Dynamics in Honeybee Swarms</b>	<b>103</b>
7.1	Model Description . . . . .	104
7.2	Symmetric Case . . . . .	106
7.3	Asymmetric Case . . . . .	108
7.4	Separation of Timescales . . . . .	112
7.5	Stochastic Dynamics . . . . .	114
7.6	Discussion . . . . .	117
<b>8</b>	<b>Final Remarks</b>	<b>120</b>
8.1	Conclusions . . . . .	120
8.2	Common Themes . . . . .	122
8.3	Looking Ahead . . . . .	123

<b>A Calculation of Lyapunov coefficient</b>	<b>127</b>
<b>B Supporting material for Chapter 3</b>	<b>128</b>
<b>C Supporting material for Chapter 4</b>	<b>130</b>
C.1 Proof of Lemma 4.2 . . . . .	130
C.2 Proof of Lemma 4.3 . . . . .	131
C.3 Proof of Lemma 4.4 . . . . .	133
C.4 Criticality analysis for Corollaries 4.1 and 4.2 . . . . .	135
<b>D Supporting material for Chapter 5</b>	<b>136</b>
<b>E Supporting material for Chapter 6</b>	<b>138</b>
E.1 Proof of Lemma 6.2 . . . . .	138
E.2 Lemma E.1 used in Theorem 6.1 . . . . .	139
<b>F Supporting material for Chapter 7</b>	<b>140</b>
<b>G Edge Detection</b>	<b>146</b>
<b>Bibliography</b>	<b>148</b>

# List of Figures

1.1	Robustness vs. adaptability in collective systems . . . . .	2
2.1	Constant vs. dynamic fitness landscapes ★ . . . . .	12
2.2	Simplex phase space . . . . .	13
2.3	Pairwise invasibility plots . . . . .	15
2.4	Bifurcations in one-dimensional systems . . . . .	17
2.5	Canonical Hopf bifurcation ★ . . . . .	18
2.6	Illustration of cusp catastrophe . . . . .	19
2.7	Illustration of graph adjacency and Laplacian . . . . .	20
2.8	Circulant graphs . . . . .	21
2.9	Spatially embedded graphs . . . . .	22
2.10	Illustration of one-dimensional SDEs . . . . .	23
2.11	Uniformly distributed points on $\Delta_2$ . . . . .	25
3.1	Simulation of RM dynamics with random payoff . . . . .	31
3.2	Simulation of RM dynamics with random payoff and LCs . . . . .	31
3.3	Limit cycle for language dynamics . . . . .	32
3.4	Bifurcations for $N = 2$ ★ . . . . .	33
3.5	One parameter graphs and bifurcations with mutation (Q1) ★ . . . . .	34
3.6	One parameter graphs and bifurcations with mutation (Q2) ★ . . . . .	35
3.7	Phase portraits for all-to-all payoff and $N = 3$ ★ . . . . .	36
3.8	Phase portraits for directed cycle payoff and $N = 3$ ★ . . . . .	37
3.9	$\ell_1(\alpha, \beta)$ in three dimensions for $N = 3$ . . . . .	39
3.10	Limit cycle bifurcations for $N = 3$ ★ . . . . .	39
3.11	Heteroclinic cycle ★ . . . . .	40
4.1	Two-parameter circulant graph . . . . .	42
4.2	Criticality of bifurcation ★ . . . . .	46
4.3	Effect of parameters $\alpha$ and $\beta$ on bifurcations . . . . .	47
4.4	Illustration of an infeasible Hopf bifurcation point . . . . .	48
4.5	One-parameter circulant graphs . . . . .	49

4.6	Multi-cycles for $N = 6$ ★ . . . . .	51
4.7	$N = 3$ limit cycles for non-circulant payoff matrices . . . . .	55
4.8	$N > 3$ limit cycles for non-circulant payoff matrices ★ . . . . .	56
4.9	Limit cycles for the dynamics (3.2) with random payoff graphs ★ . . .	57
5.1	Migratory performance as a function of investment $k_D$ . . . . .	63
5.2	Steady-state migration speed . . . . .	66
5.3	Evolutionary singular strategies $k_*$ . . . . .	69
5.4	Simulations of the evolutionary dynamics in the all-to-all limit ★ . . .	71
5.5	Minimal root sets of social graph . . . . .	74
5.6	Effect of social graph topology on evolutionary outcomes . . . . .	78
5.7	Evolutionary equilibria for lattice and random graphs . . . . .	80
5.8	Bifurcations of the adaptive node dynamics with $N = 2$ nodes ★ . . .	83
5.9	Bifurcations of the adaptive node dynamics with $N = 10$ nodes . . . . .	84
5.10	Nodal dynamics for the undirected star ★ . . . . .	84
5.11	Role of topology in determining locations of leaders ★ . . . . .	85
6.1	Cartoon trajectories of a pursuer and an evader . . . . .	90
6.2	Simulations for the 9 pairs of competing pursuit & evasive strategies .	92
6.3	Monte-Carlo simulations . . . . .	95
6.4	Simulation of smooth dynamics (6.5) . . . . .	99
6.5	Sensing topology for cyclic pursuit and evasion . . . . .	100
6.6	Simulations of pursuit-evasion collective dynamics . . . . .	101
6.7	Pursuit-evasion chains for large $N$ . . . . .	102
7.1	From microscopic to mean-field equations ★ . . . . .	105
7.2	Pitchfork bifurcation for the symmetric case . . . . .	108
7.3	Bifurcation set for the asymmetric case ★ . . . . .	109
7.4	Projected equilibria illustrating bifurcations ★ . . . . .	110
7.5	Full three-parameter bifurcation set . . . . .	111
7.6	Timescale separation in the stop-signalling dynamics ★ . . . . .	114
7.7	Stochastic dynamics comparisons ★ . . . . .	116
7.8	Stochastic dynamics simulations ★ . . . . .	118
8.1	Three instances of hysteresis . . . . .	123
8.2	Exploration, cyclical domination, exploitation . . . . .	125

★ denotes figures in color

# Chapter 1

## Introduction

*Seek simplicity, and distrust it. -Alfred North Whitehead (1861-1947)*

*Emergent collective behavior* involves interactions between individual agents that yield distinct patterns at the level of the group. Emergent systems have group level outcomes that cannot be understood simply as the superposition of their constituent elements, instead emergent group behavior is nonlinearly related to individual interactions. Moreover, just as individual actions affect group outcomes, group outcomes feed back to affect individual actions. This coupling between the microscopic individual level and the macroscopic group level makes the study of emergent behavior vibrant, exciting, and challenging. The past few decades have seen significant research activity in applying computational and analytical tools to studying emergent phenomena in a wide variety of applications. These include ecology [72, 49], cellular biology [127, 21], animal behavior [126], disease dynamics [63, 20], climate [48], economics [131] and more recently, robotic swarms [61, 65] and social networks [146, 4] (the few examples cited here are a small sample from a vast literature).

For problems in biology, *the evolutionary approach* involves studying the fascinating array of observed behavior in natural collectives (flocks, schools, herds, etc.) from the perspective of evolution by natural selection. This approach provides important insights into the mechanisms that drive group behavior in natural collectives. The development of mathematical models to explain evolutionary puzzles such as cooperation and altruism [62, 105, 84] in swarms, flocks, and schools, continues to be an active area of research (see [88, 89, 70] for a recent debate on the topic).

In this thesis, we use a set of relatively simple and tractable evolutionary models to study emergent behavior in selected natural collective systems. We focus our study on four areas described in §1.1, and utilize three related evolutionary models in our analysis: replicator-mutator dynamics for a single population with discrete

strategies, adaptive dynamics for a single population with continuous strategies, and coevolutionary replicator dynamics for a two-population system with discrete strategies. Each of these models is described in detail in §2.1.

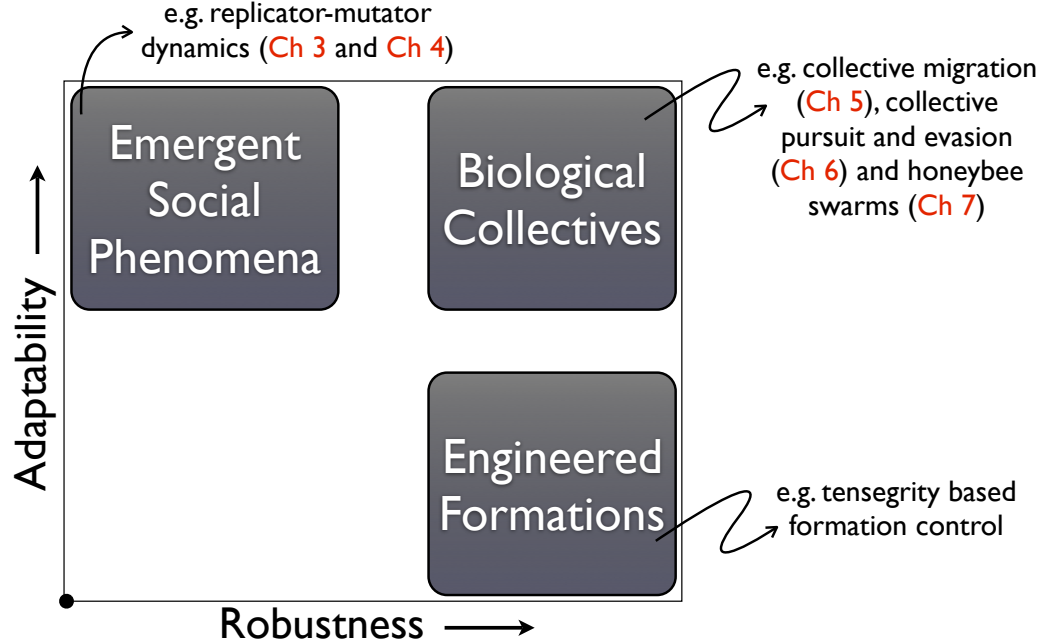


**Figure 1.1:** A classification of collective systems based on robustness and adaptability metrics.

Collective systems can be classified based on a large variety of metrics (system size, heterogeneity, network architecture, dynamics, etc.), but looking broadly, *robustness* and *adaptability* are two key metrics that enable a rough classification as illustrated in Figure 1.1. Robustness refers to the ability of collective systems to reject disturbances and perform specific tasks accurately, predictably, and repeatedly, in stochastic environments. Adaptability refers to the ability of collective systems to continually modify their behavior in reaction to a dynamic environment and to solve a range of problems such as foraging for resources, migrating to new locations, and avoiding threats or prey. Highly adaptive systems have the ability to learn from past experiences and to find innovative solutions to novel problems.

Robustness and adaptability constitute a fundamental tradeoff in engineered collective systems in the sense that systems designed to be significantly robust and predictable for specific tasks (industrial robots for example) are inherently unadaptive, and vice-versa. In Figure 1.1, the three rectangles at the corners of the robustness-adaptability space represent three classes of collective systems and allow us to connect the four focus areas of this thesis:

- Bottom-right; engineered formations: These systems are designed to be highly robust so that they can perform specific tasks reliably (often with provable guarantees on performance). However, they have limited adaptability to problems outside their specific domain of design. Examples include the wide variety of industrial robotic systems and formation control in mobile autonomous robotic collectives. One example of recent work in our group in this area is the use of tensegrity-based control laws (involving simultaneous attraction and repulsion between agents) to stabilize the shapes of formations of autonomous vehicles [78, 94].
- Top-left; emergent social phenomena: These collective systems are highly adaptive in dynamic environments and can display macroscopic behavior that rapidly cascades between extremes. This macroscopic behavior is often unpredictable, and in certain cases can be inherently chaotic, resulting in a limited robustness. Examples include the popular area of social network dynamics, cascades in financial markets, and the dynamics of behavioral preferences and fashion trends. In Chapters 3 and 4 we study a model of behavioral preferences in social networks (known as replicator-mutator dynamics) that fits the paradigm of this quadrant.
- Top-right; biological collectives: One of the main reasons that *bio-inspired* robotic collective behavior has gained tremendous traction over the last two decades is because many biological systems possess the unique ability to act both robustly and adaptively. The seemingly complex emergent collective behavior observed in these biological systems has frequently been shown to be the consequence of simple individual rules at the microscopic level. These rules, and the emergent behavior, have been shaped by evolutionary dynamics on generational timescales. In Chapters 5 and 6 we study two ubiquitous biological collective phenomena, namely, collective migration, and pursuit and evasion, respectively. In Chapter 7 we focus on the decision-making dynamics in swarms of honeybees. A honeybee swarm is a particularly good example of a system in this quadrant, where robust and accurate decision-making in dynamic environments has been shaped by the evolutionary forces of reproduction and colony survival. Individuals in a honeybee swarm can be radically adaptive. For example, scout bees that are involved in locating nesting sites for the swarm are, in fact, forager bees that have switched behavior from seeking bright blossoms to searching for dark nesting crevices [116].

This thesis is the product of interdisciplinary research drawing from ideas in evolutionary biology, animal behavior, engineering and applied mathematics. The background material in Chapter 2 introduces key tools from these areas that are used throughout the thesis. Along with the exciting quest of understanding the complexity of biological collectives, research in our group also strives to draw ideas and principles from biology that can be applied to the design of robotic collectives. From the perspective of Figure 1.1, this effort involves utilizing ideas from the top-right quadrant to push engineered systems (bottom right quadrant) up the adaptability axis, while still managing the adaptability/robustness tradeoff. This is no easy challenge and will remain an area of research emphasis going forward as autonomous collective systems are tasked with solving increasingly complex problems. As a result, together with a focus on understanding collective dynamics in the four areas described below, we also consider how this understanding inspires engineering design in each case.

## 1.1 Overview of Topics

### 1.1.1 Replicator-Mutator Dynamics\*

The replicator-mutator dynamics define a canonical model from evolutionary theory and represent the evolution of a discrete number of strategies in a single large population. The dynamics have received significant attention recently as a model for the evolution of language. They also provide a simple model for the analysis of behavior dominance in social networks where replication is akin to imitation of individuals subscribed to successful behaviors in a population, and mutation is akin to random error in behavior selection. Much of the analysis of the dynamics has focused on stable equilibria and their bifurcations. In this thesis we focus on the existence of structurally stable limit cycles of the dynamics and prove that Hopf bifurcations occur, yielding these cycles. Stable limit cycles correspond to sustained oscillations in strategy dominance across some or all of the population. The form of the dynamics considered, and the interpretation of the oscillations, depends on the applications of interest; the following are three motivating applications.

- a) The replicator-mutator dynamics have been used in the development of a mathematical framework for the evolution of language [85]. For a large population, the strategies represent different grammars in the population and mutations reflect errors in grammar transmission or learning from one generation to the next. A key

---

\*The discussion in this subsection appears verbatim in [93].

result is the bifurcation of the equilibria from a state where several grammars co-exist in a population to a state of high grammatical coherence as mutations in the population decrease (or equivalently, the fidelity of learning increases) [57, 75, 74]. Limit cycles of the replicator-mutator dynamics correspond to oscillations in the dominance of the different grammars in the population. As noted in [76], oscillations appear to be more realistic than stable equilibria for the language dynamics with timescales on the order of several centuries.

- b) The replicator-mutator dynamics were recently proposed [90, 44] as a model for behavior adoption in social networks, with a focus on the emergence of dominance of particular behaviors in these networks. Simulations of the evolutionary social network model show a transition from the dominance of a single strategy (behavior), to the coexistence of several strategies, to the eventual collapse of dominance, as the extent of mutation in the network increases. Limit cycles of the replicator-mutator dynamics correspond to oscillations of behavior preference in this context, for example cycles in trends or fashions.
- c) The replicator-mutator dynamics can also be used to model decision-making dynamics in networked multi-agent systems. It has been shown that simple models with pairwise interactions between agents and noisy imitation of successful strategies reduce (under certain conditions) to the replicator-mutator dynamics [40, 7, 135, 134]. Recent papers have employed the replicator-mutator equations to model wireless multi-agent networks [145, 130]. Hopf bifurcations of replicator-mutator dynamics in this context address the exploration versus exploitation tradeoff: few mutations favor fast convergence to a decision (exploitation) whereas extensive mutations favor exploration of the decision space. In an intermediate range, mutations can lead to limit cycles, which enable dynamic examination of alternative choices.

### 1.1.2 Collective Migration

Collective migration is a natural phenomenon common in a number of species including birds, fish, invertebrates and mammals [119, 42, 22, 6]. Animals migrate by leveraging a variety of environmental cues such as nutrient and thermal gradients, magnetic fields, odor cues, or visual markers [132, 30, 140, 133]. Measuring these stochastic environmental signals is complicated and requires the investment of time and energy, and the development of necessary physiological and sensory machinery.

Animals migrating collectively also have the ability to leverage social information from neighbors in the group [15]. One way of doing so is by imitating invested neighbors (via consensus processes such as attraction and alignment of heading) and thereby effectively achieving good migratory performance, without paying the measurement and processing cost.

Using agent-based models of collective migration, Couzin et al. [14] have shown that a small group of designated leaders is capable of guiding a larger group of naive, socially interacting followers. This situation is similar, for example, to the way in which a small number of informed scout bees directs a large swarm of uninformed conspecifics to a new nest site [116, 120]. The ability of followers in such migratory swarms to leverage the investments made by leaders in the group, and to gain the benefits of successful migration without paying the associated costs, is perplexing from an evolutionary perspective (this question is related to the broader puzzle of the evolution of cooperation).

Our study of the evolutionary dynamics of collective migration is motivated in large part by a recent paper by Guttal and Couzin [33] that addresses this evolutionary question. Simulations in [33] show that the coexistence of leaders and followers in migratory populations is a stable emergent outcome of the evolutionary dynamics for a large region of the parameter space studied. The authors of [33] also examine the role of anthropogenic influences on evolved population migration patterns by studying the impact of increasing habitat fragmentation on the collective dynamics. High levels of habitat fragmentation make it increasingly difficult for individuals to measure external cues; migration is gradually lost because of the higher costs of reaching more distant destinations [120]. Simulations in [33] illustrate a hysteretic effect in restoring lost migration ability in the population - once migration ability is lost for a threshold level of fragmentation, much greater habitat recovery is necessary for the population to recover the ability to migrate.

We are also motivated by the paper by Torney et al. [132] that analytically validates the evolutionary branching simulated in [33] by studying a mean-field model of migration dynamics. The mean-field model in [132] effectively prescribes an all-to-all interconnection between the agents in the migratory system and serves as the starting point for our work, which focuses explicitly on the role of the structure of a limited interaction network on evolved outcomes. Indeed, the structure of the interaction network between agents in a collective has been shown to be critical to the performance of the collective, and to the emergent outcomes observed as a consequence of the local interactions.

### 1.1.3 Pursuit and Evasion<sup>†</sup>

Pursuit and evasion behaviors play a critical role in predator foraging, prey survival, mating and territorial battles in several species. Species such as bats and dragonflies have evolved sophisticated dynamical strategies such as motion camouflage to disguise themselves as stationary during aerial pursuit [77, 27]. Studies on migratory cannibalistic locusts have revealed that pursuit and evasive behavior among conspecifics is integral to the formation of mass-moving migratory bands in dense swarms [35, 5]. Recent experimental work on the dynamics of coordinated predator pursuit and prey evasion among schooling fish has shown that collective behavior, among both predators and prey, plays a vital role in predator hunting and prey evasion under conditions of considerable informational constraints (such as dynamic ocean environments) [37, 45].

The pervasiveness of pursuit and evasion in nature motivates the examination of winning strategies from an evolutionary perspective. Recently, Wei et al. [147] used the evolutionary approach to study pursuit games, with dynamics derived in [50]. The authors of [147, 50] use Monte-Carlo simulations and analytical calculations to study three pursuit strategies competing against a field of deterministic or random nonreactive evasive strategies (an evader with a nonreactive strategy has dynamics that are uncoupled from those of the pursuer). The three chosen pursuit strategies (classical, constant bearing and motion camouflage) are biologically inspired. The authors show convergence of the evolutionary game dynamics between the three strategies to pure motion camouflage and motivate this result by empirical observations of motion camouflage in hoverflies, dragonflies and bats [27]. We build on the work in [147] by studying the coevolution of the three strategies of pursuit from [147] playing against three distinct evasive strategies, two of which are *reactive* strategies (an evader with a reactive strategy has dynamics that are coupled to those of the pursuer).

### 1.1.4 Swarm Decision-Making

Honeybee colonies reproduce by casting out swarms, each of which comprises a queen accompanied by several thousand worker bees. A small fraction of the worker bees are known as scout bees and perform the task of locating suitable nest sites for the swarm by engaging in a decentralized *democratic* [116] decision-making process of choosing among several competing options. This process involves the famous waggle dance [144] in which scout bees advertise the location and quality of a suitable nest site by

---

<sup>†</sup>The discussion in this subsection is adapted from [96].

performing a distinctive dance on the surface of the swarm. The book by Seeley [116] provides an engaging description of the waggle dance, as well as a detailed discussion of the organization and behavior of honeybee swarms.

In a recent paper, Seeley et al. [118] have shown that scouts send inhibitory stop-signals to other scouts advertising alternative nest sites, thereby causing these scouts to cease dancing. This cross-inhibitory process has been shown to be critical to the ability of swarms to make decisions effectively, particularly when choosing between competing options of near-equal value. In this thesis we study bifurcations in a model of honeybee swarm decision-making and illustrate the critical role played by stop-signal inhibition in enabling swarms to manage the speed-accuracy tradeoff inherent to most decision-making problems. We show that an intermediate evolved level of stop-signaling is necessary for swarms to effectively make decisions when presented with both equal and unequal alternatives. Our analysis also shows that cross-inhibition is a potentially valuable mechanism for enabling effective collective decision-making in decentralized artificial swarms.

## 1.2 Contributions and Thesis Outline

The chapters of this thesis are organized according to the four topics described in §1.1. *Chapter 2* comprises background material and establishes the mathematical notation that will be used throughout the thesis. Background material is presented in four main areas: Evolutionary Dynamics, Dynamical Systems, Graph Theory and Stochastic Processes.

*Chapters 3 and 4* focus on limit cycles and Hopf bifurcations of the replicator-mutator dynamics. The analysis in Chapter 3 is restricted to  $N = 3$  strategies and the corresponding planar phase space. The restriction to  $N = 3$  is convenient for visualization and allows us to motivate the general results for  $N \geq 3$  strategies to follow in Chapter 4. In Chapter 4 we prove conditions for the existence of stable limit cycles arising from multiple distinct Hopf bifurcations of the dynamics in the case of circulant fitness matrices. In the noncirculant case we illustrate how stable limit cycles of the dynamics are coupled to embedded directed cycles in the payoff graph. We study special conditions where multiple cycles in the payoff graph yield multiple stable limit cycle attractors. The stability of the limit cycles is determined by an analytical calculation of the first Lyapunov coefficient of the dynamics.

In *Chapter 5* we study the role of the social interconnection network on the evolutionary dynamics of collective migration. We design a networked migration model

and study evolution and adaptation as a function of network topology. Our model has two timescales: the fast timescale corresponds to fitness/utility calculations and the slow timescale corresponds to the evolution/adaptation of the network. We present a comprehensive analysis of the all-to-all limit of the model and prove conditions for population branching into leaders and followers. For networks with limited connectivity, we derive analytical tools for computing fitness on the fast timescale and show a minimum connectivity threshold necessary for branching. We also study a simple model of selfish local adaptation of nodes on a graph, and illustrate bifurcations in the dynamics as a function of increasing cost. We show the prominent role played by network topology in determining the location of leaders in the adaptive network.

*Chapter 6* focuses on the coevolutionary dynamics of pursuit and evasion. We consider an evolutionary game between three strategies of pursuit (classical, constant bearing, motion camouflage) and three strategies of evasion (classical, random, optical-flow based). Pursuer and evader agents are modeled as self-propelled steered particles with constant speed and strategy-dependent heading control. We use Monte-Carlo simulations and theoretical analysis to show convergence of the evolutionary dynamics to a pure strategy Nash equilibrium of classical pursuit versus classical evasion. We extend our work to consider a novel pursuit and evasion based collective motion scheme, motivated by collective pursuit and evasion in bands of migrating cannibalistic locusts.

In *Chapter 7* we study the collective decision-making dynamics of honeybee swarms. The cross-inhibitory stop-signalling mechanism has been shown to be critical to the decision-making dynamics in swarms of house-hunting honeybees. We study a model of stop-signal based collective decision-making and present a comprehensive picture of the dynamics and bifurcations of this model. We prove a separation of timescales in the decision-making process and show how swarms must evolve to an intermediate level of stop-signalling to address a fundamental speed-accuracy tradeoff. We also present several stochastic simulations to help elucidate the decision-making process.

*Chapter 8* presents our conclusions and topics for future work. We discuss how some of the analysis and conclusions of this thesis inspire algorithms for control and decision-making in decentralized collective artificial systems.

# Chapter 2

## Background

In this chapter we describe some of the main mathematical tools that will be used in the rest of the thesis and we establish notation. Each of the areas discussed in the sections to follow is a significant domain of research by itself. Consequently, this chapter is not intended to be a comprehensive presentation of these areas, but rather an introduction to selected tools from these areas that will be useful going forward. The cited references provide more detail.

In §2.1, we discuss models of evolutionary dynamics and make connections with game theory, genetic algorithms, and optimization. §2.2 focuses on bifurcations in continuous dynamical systems, including the Hopf bifurcation theorem, which features prominently in Chapters 3 and 4. §2.3 introduces some notation and results from graph theory and §2.4 introduces some basic results from stochastic dynamics; these are employed in Chapters 5 and 7.

*Basic Notation:* Matrices are denoted in capital letters and vectors are denoted in boldface lowercase letters.  $m_{ij}$  denotes the  $(i, j)$  element of matrix  $M$  ( $M = [m_{ij}] \in \mathbb{R}^{M \times N}$ ) and  $x_i$  denotes the  $i^{\text{th}}$  element of vector  $\mathbf{x}$  ( $\mathbf{x} = [x_1 \ \dots \ x_N]^T \in \mathbb{R}^N$ ).  $\mathbf{1}$  and  $\mathbf{0}$  denote the vectors of ones and zeros respectively.  $D = [d_{ij}] = \text{diag}(\mathbf{x})$  denotes a diagonal matrix with elements of vector  $\mathbf{x}$  on the main diagonal, i.e.  $d_{ii} = x_i$  and  $d_{ij} = 0$  for all  $i \neq j$ . The  $N \times N$  identity matrix is given by  $\mathbb{I}_N = \text{diag}(\mathbf{1}_N)$ .

### 2.1 Evolutionary Dynamics

Evolutionary dynamics [142, 87, 41, 141] are, broadly speaking, an effort to cast the basic tenets of Darwinian natural selection (replication, competition, strategy dependent fitness, mutation) in a mathematical framework that can be simulated,

interpreted, and often rigorously analyzed. Our understanding of the evolutionary process has its roots in Darwin's three simple postulates [142, 16]:

1. Like tends to beget like, and there is heritable variation in traits associated with each type of organism. (replication and mutation)
2. Among organisms there is a struggle for existence. (competition)
3. Heritable traits influence the struggle for existence. (strategy dependent fitness)

These postulates inherently define a game-theoretic interaction between individuals in the population as a function of their strategies (expressed as phenotypes or traits), and their interactions with the environment and other individuals. These strategies and interactions map to payoffs, which in turn translate to reproductive fitness. The game theoretic mechanism implies that evolutionary solutions are not necessarily optimal in terms of maximizing the fitness of the population as a whole.

Nonetheless, the ability of evolutionary dynamics to shape natural systems towards a fascinating array of effective solutions has inspired powerful tools for optimization in engineering design, e.g. genetic algorithms [73]. In genetic optimization algorithms, agents imitate the evolutionary process to search for local optima on a *constant* landscape as shown in Figure 2.1. This is in contrast with biological (game-theoretic) evolutionary dynamics where the strategies interact and influence the landscape on which they are evolving (see Figure 2.1). In this thesis, we focus on studying the outcomes of models of game-theoretic evolutionary dynamics, while also making connections with how these solutions inspire the design of engineered collective systems.

The replicator dynamics [129] are the simplest model of evolutionary dynamics for a large population comprised of  $N$  sub-populations, each subscribed to a different competing strategy. These differential equations model the game theoretic interactions among the sub-populations and determine how each sub-population changes in size as a consequence of these interactions. Let  $x_i$  ( $i = 1, \dots, N$ ) denote the fraction of individuals in the population subscribed to strategy  $i$  ( $\sum_{i=1}^N x_i = 1$ ). The replicator dynamics are given by

$$\dot{x}_i = x_i(f_i(\mathbf{x}) - \phi); \quad \phi = \mathbf{f}^T \mathbf{x}, \quad (2.1)$$

where  $f_i(\mathbf{x})$  denotes the fitness function of individuals with strategy  $i$  and  $\phi$  is the population average fitness. The average fitness  $\phi$  is obtained by summing over the individual fitness terms  $f_i(\mathbf{x})$  weighted by their appropriate fractions  $x_i$ . For pairwise

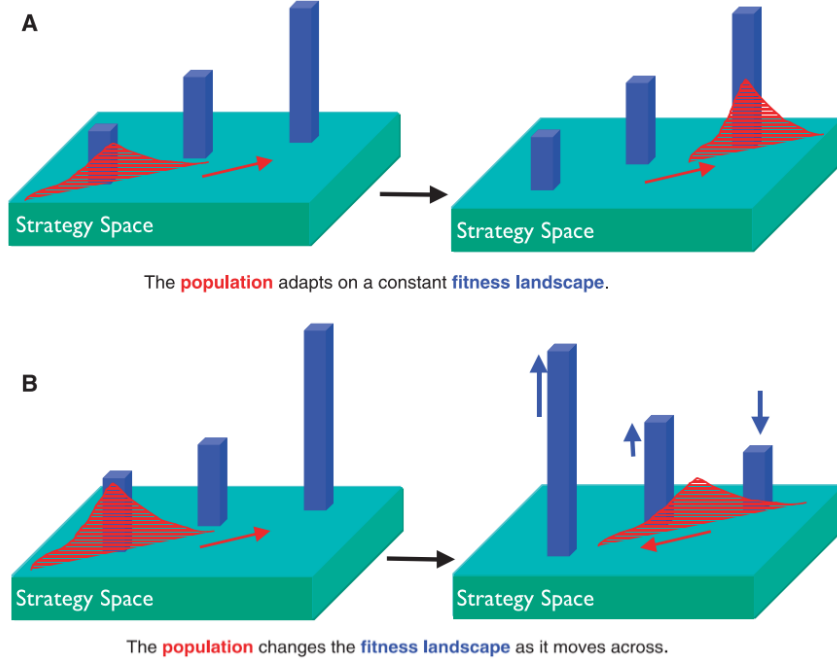


**Figure 2.1:** (A) Optimization picture: evolutionary optimization dynamics on a constant fitness landscape; population evolves on the landscape towards the fitness peak. (B) Game-theoretic picture: evolutionary dynamics on an adaptive landscape; the population co-evolves with the dynamic landscape. (adapted from Fig. 1 in [87])

encounters in a large population, the fitness functions are linear [87, 135] and  $\mathbf{f} = A\mathbf{x}$ , where  $A \in \mathbb{R}^{N \times N}$  is known as the payoff matrix.

John Maynard Smith's pioneering work [122] made formal connections between classical game theory and evolutionary dynamics. Particularly important was Maynard Smith's definition of evolutionarily stable strategies (ESSes), which are equilibria of an evolutionary dynamical system that are uninvadable by other competing strategies in the environment, and hence stable in an evolutionary sense. From a game theoretic perspective, ESSes are a subset of the Nash equilibria of a game: they satisfy both the Nash best reply condition and evolutionary uninvadability. Lyapunov stable equilibria of the replicator dynamics (2.1) are Nash equilibria of the corresponding game [148]. Further, all ESSes of the replicator dynamics are asymptotically stable [148].

Although the replicator dynamics have proved to be a powerful tool in analyzing a variety of classical games from an evolutionary perspective, they do not model mutation, a key ingredient of selection theory. Mutation can be included by adding the possibility that individuals spontaneously change from one strategy to another.

This yields the replicator-mutator dynamics [9, 92] given by

$$\dot{x}_i = \sum_{j=1}^N x_j f_j(\mathbf{x}) q_{ji} - x_i \phi; \quad \phi = \mathbf{f}^T \mathbf{x}, \quad (2.2)$$

where  $q_{ij}$  denotes the probability of mutation from strategy  $i$  to strategy  $j$  ( $\sum_{j=1}^N q_{ij} = 1$ ). The replicator-mutator dynamics have played a prominent role in evolutionary theory and contain as limiting cases many other important equations in biology [55]; these include models of language evolution [85], autocatalytic reaction networks [124], and population genetics [36]. The dynamics have also recently been employed to model social and multi-agent network interactions [90]. The replicator-mutator equations have been shown in [92] to be equivalent to the generalized Price equation from evolutionary genetics [105, 106]. The standard replicator dynamics (2.1) can be obtained from the replicator-mutator dynamics (2.2) in the limit of zero mutation ( $q_{ii} = 1$  for all  $i$  and  $q_{ij} = 0$  for all  $i \neq j$ ).

Biological evolutionary models typically consider small mutation probabilities while larger mutation probabilities are more common in models of language dynamics and social interactions. Both sets of dynamics (2.1) and (2.2) evolve on the  $(N - 1)$ -dimensional simplex phase space (see Figure 2.2) defined as

$$\Delta_{N-1} = \{\mathbf{x} \in \mathbb{R}^N \mid x_i \geq 0, \mathbf{x}^T \mathbf{1} = 1\}.$$

In chapters 3 and 4 we focus on stable limit cycle attractors for the replicator-mutator dynamics (2.2).

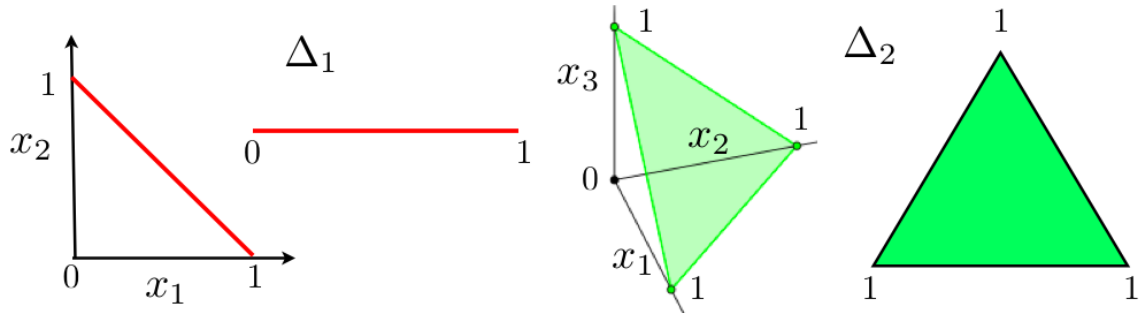


**Figure 2.2:** Illustration of the simplices  $\Delta_1$  and  $\Delta_2$ .

The replicator and replicator-mutator equations model the evolutionary dynamics for a discrete number of strategies. However, certain problems require the consideration of a continuous strategy space, and can be studied using tools from adaptive

dynamics [25, 26, 18]. Adaptive dynamics are particularly well-suited for studying the evolution of a one-dimensional trait in a population undergoing small mutations in strategy. Consider a continuous strategy space parameterized by  $k \in [a, b] \subset \mathbb{R}$ . The fitness of a resident population with strategy  $k_R$  is given by  $F_R(k_R)$ . The adaptive dynamics approach considers the consequences of a small group of mutants with strategy  $k_M$  invading the resident population. Let  $F_M(k_R, k_M)$  denote the fitness of the mutants in the environment of the residents. The relative fitness of the mutants with respect to the residents is known as the differential fitness and is given by

$$S(k_R, k_M) = F_M(k_R, k_M) - F_R(k_R). \quad (2.3)$$

The two-parameter function  $S$  allows us to predict which mutant strategies can invade a particular resident population. For example, for a given resident strategy  $k_R$ , the values of  $k_M$  that result in  $S > 0$  correspond to the mutant strategies that when rare, can invade the established resident population. Further, a study of the selection landscape  $S$  can help us predict when we expect to see an evolutionarily stable [122] monomorphic population (all individuals having the same strategy) and when we expect to see opportunities for branching (speciation into sets of individuals having different strategies) in evolutionary simulations.

The evolutionary dynamics of the resident strategy  $k_R$  are given by

$$\frac{dk_R}{dt} = \alpha \left. \frac{\partial S}{\partial k_M} \right|_{k_M=k_R} =: \alpha g(k_R), \quad (2.4)$$

where  $g(k_R)$  is known as the selection gradient and  $\alpha > 0$  is related to the extent of mutation in the population. As the strategy  $k_R$  of the population evolves according to (2.4), the small mutations  $k_M$  about the resident strategy  $k_R$  also evolve accordingly. The sign of the selection gradient  $g(k_R)$  is indicative of the direction in which the strategy of the population will evolve. In particular, the strategy of the population will increase for  $g(k_R) > 0$  and decrease for  $g(k_R) < 0$ . Evolutionary singular strategies  $k_*$  correspond to a vanishing selection gradient  $g(k_*) = 0$ . Singular strategies are evolutionary attractors for the population (also known as Convergent Stable Strategies (CSS)) if they satisfy the condition

$$\left. \frac{\partial g}{\partial k_R} \right|_{k_R=k_*} < 0. \quad (2.5)$$

CSS stable attractive strategies  $k_*$  can be either monomorphic evolutionary stable strategies for the population, or can be branching opportunities where the population speciates. The condition for a CSS singular strategy to be a branching point for the population is given by

$$\frac{\partial^2 S}{\partial k_M^2} \Big|_{k_M=k_R=k_*} > 0. \quad (2.6)$$

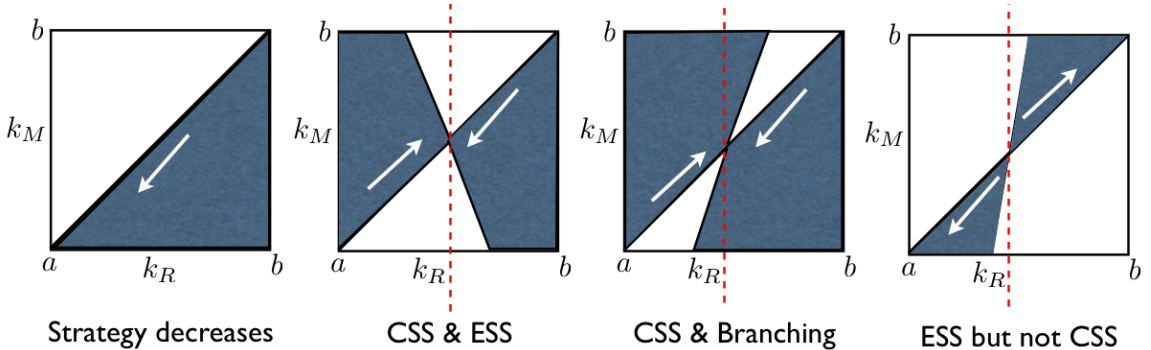


**Figure 2.3:** Pairwise invasibility plots. Dark regions correspond to differential fitness (2.3)  $S > 0$  and white regions to  $S < 0$ . The resident population on the main diagonal moves in the direction of the white arrows shown, corresponding to the dynamics (2.4). The red vertical lines mark singular strategies. Singular strategies with arrows pointing towards them are convergence stable (CSS). Singular strategies with vertical lines passing through regions that are exclusively white are evolutionarily stable (ESS).

Figure 2.3 shown pairwise invasibility plots (PIP) [25] corresponding to the CSS and branching cases described above. PIPs provide a geometric method for analyzing evolutionary dynamics. The population strategy at any instant is distributed about a point on the main diagonal of each plot, with resident strategy  $k_R$  and small mutations  $k_M$  about the resident strategy. The population distribution moves in the direction of the arrows shown on the plot, eventually arriving at a CSS attractor, or at the boundaries of the strategy space. At the CSS attractor, the population can remain monomorphic when attractor is at a fitness maximum, or can branch when the attractor is at a local fitness minimum. We employ PIPs to study collective migration in Chapter 5.

The replicator (2.1), replicator-mutator (2.2), and adaptive dynamics (2.3), (2.5) model the evolution of strategies in a single large population. However certain co-evolutionary processes, such as interactions between predators and prey for example, involve the coupled evolutionary dynamics between two distinct populations. The single-population models described here can be extended to study such coevolution-

ary processes; we will consider an extension of the replicator dynamics to model the evolutionary dynamics of pursuit and evasion in Chapter 6.

## 2.2 Dynamical Systems Tools

A dynamical system is a mathematical model describing the time evolution of a set of variables which collectively define the state of the system at any given point in time. There is a rich set of tools in the dynamical system literature (for example see [32, 59, 125]) for computing and understanding the solutions to these systems, including the study of bifurcations. A bifurcation is a qualitative change in the solutions of a dynamical system as a result of the smooth change in a system parameter (known as the bifurcation parameter). Bifurcations that are detected by studying small neighborhoods of equilibria and limit cycles of dynamical systems are known as *local* bifurcations. In Chapters 3, 4, 5 and 7, we study local bifurcations of specific continuous-time dynamical systems, and in this section we introduce the kinds of bifurcations that appear in these chapters.

Consider the continuous-time dynamical system with state  $\mathbf{x} \in \mathbb{R}^N$  and bifurcation parameter  $\mu \in \mathbb{R}$  given by

$$\dot{\mathbf{x}} = \mathbf{f}(\mathbf{x}, \mu), \quad (2.7)$$

with the vector field  $\mathbf{f} : \mathbb{R}^N \times \mathbb{R} \mapsto \mathbb{R}^N$ . The range of behavior for one-dimensional systems ( $x \in \mathbb{R}$ ) is limited; solutions either approach stable equilibria or diverge to infinity. Nonetheless, the analysis of certain bifurcations in higher dimensional systems can be reduced to studying one-dimensional normal forms (nonlinear analog of matrix diagonalization or matrix Jordan normal form [32, 59]) by using the center manifold theorem (see [32] for details). The four main bifurcations for one-dimensional systems are given below, and illustrated in Figure 2.4.

- (a) Saddle-Node: Normal form  $\dot{x} = \mu + x^2$ . Equilibria exist for  $\mu < 0$ . As  $\mu \rightarrow 0^-$  an unstable saddle and a stable sink collide and disappear.
- (b) Transcritical: Normal form  $\dot{x} = \mu x - x^2$ . A stable branch and an unstable branch of equilibria exist for all  $\mu \neq 0$ . The branches exchange stability at  $\mu = 0$ .
- (c) Supercritical Pitchfork: Normal form  $\dot{x} = \mu x - x^3$ . The  $x = 0$  equilibrium is stable for  $\mu < 0$  and unstable for  $\mu > 0$ . There are two additional stable equilibria for  $\mu > 0$ , which appear at the pitchfork bifurcation point  $\mu = 0$ .

- (d) Subcritical Pitchfork: Normal form  $\dot{x} = \mu x + x^3$ . The  $x = 0$  equilibrium is stable for  $\mu < 0$  and unstable for  $\mu > 0$ . There are two additional unstable equilibria for  $\mu < 0$ .

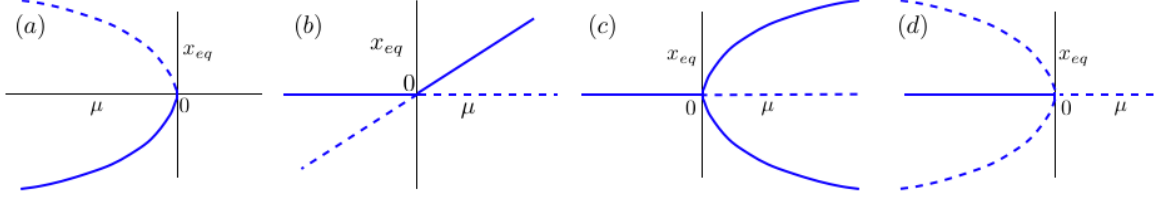


**Figure 2.4:** Illustration of the four canonical bifurcations in one-dimensional systems. Solid curves are stable equilibria and dashed curves are unstable. (a) Saddle-Node (b) Transcritical (c) Supercritical pitchfork (d) Subcritical pitchfork.

In addition to stable and unstable equilibria,  $N(\geq 2)$ -dimensional systems ( $\mathbf{x} \in \mathbb{R}^N$ ) can also have periodic orbits, limit cycles, homo/hetero-clinic connections and chaotic attractors (chaotic attractors may exist only for  $N \geq 3$ , see the Poincaré-Bendixson theorem in [32] and Peixoto's theorem in [32, 100]). Bendixson's criterion provides sufficient conditions for the nonexistence of periodic orbits for planar systems ( $\mathbf{x} \in \mathbb{R}^2$ ) [32].

**Theorem 2.1.** (Bendixson's Criterion) An autonomous planar vector field (2.7) defined on a simply connected region  $D \subset \mathbb{R}^2$  has no periodic orbits lying entirely in  $D$  if  $\frac{\partial f_1}{\partial x_1} + \frac{\partial f_2}{\partial x_2}$  is not identically zero and does not change sign in  $D$ .

One-parameter bifurcations in dynamical systems with a one- or two-dimensional state space can be conveniently plotted in two and three dimensions respectively. Constructing bifurcation plots is more challenging for higher dimensional ( $N \geq 3$ ) systems, for which we can either plot projections in two or three dimensions (as in Chapters 4 and 5), or construct reduced dimensional approximations of the dynamics (as in Chapter 7).

For high dimensional systems, our focus in Chapter 4 will be on the existence of stable limit cycles, arising out of Hopf bifurcations of the dynamics. The normal form of the Hopf bifurcation is given by

$$\begin{aligned}\dot{x}_1 &= \mu x_1 - x_2 + \sigma x_1(x_1^2 + x_2^2) \\ \dot{x}_2 &= x_1 + \mu x_2 + \sigma x_2(x_1^2 + x_2^2),\end{aligned}\tag{2.8}$$

where  $\sigma = \pm 1$  ( $\sigma = \text{sign}(\ell_1(0))$  from Theorem 2.2 below). The Hopf bifurcation point is  $\mu = 0$ . The origin is asymptotically stable for  $\mu < 0$  and unstable for  $\mu > 0$ . The

bifurcation is supercritical for  $\sigma = -1$  and subcritical for  $\sigma = +1$ . The supercritical bifurcation results in stable limit cycles of radius  $\sqrt{\mu}$  for  $\mu > 0$  as shown in Figure 2.5. For general  $N \geq 3$  dimensional systems, the Hopf bifurcation theorem [32, 59]

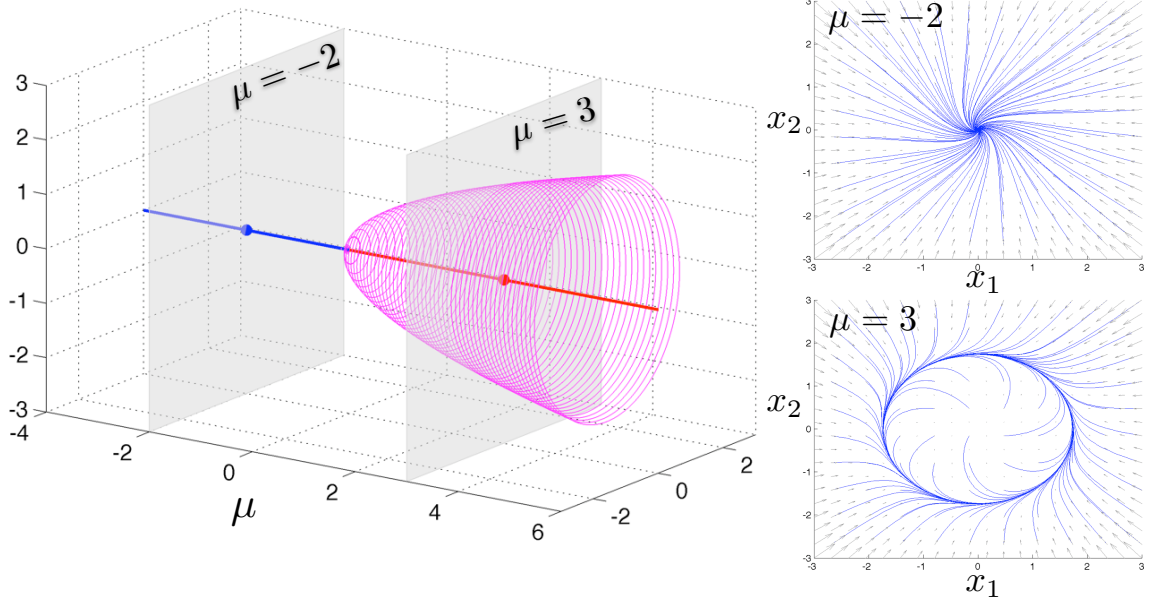


**Figure 2.5:** Bifurcation plot (left) for the supercritical Hopf bifurcation normal form (2.8). Blue curves are stable equilibria, red curves are unstable equilibria and magenta curves are stable limit cycles. The two right plots are phase portraits for  $\mu = -2$  and  $\mu = 3$ , corresponding to the grey slices on the bifurcation plot.

provides sufficient conditions for the existence of stable limit cycles arising out of supercritical Hopf bifurcations.

**Theorem 2.2.** (Hopf bifurcation) Suppose that the system  $\dot{\mathbf{x}} = \mathbf{f}(\mathbf{x}, \mu)$ ,  $\mathbf{x} \in \mathbb{R}^N$ ,  $\mu \in \mathbb{R}$ , has an equilibrium  $(\mathbf{x}_0, \mu_0)$  and the following properties are satisfied:

- (H1) The Jacobian  $D_{\mathbf{x}}\mathbf{f}|_{(\mathbf{x}_0, \mu_0)}$  has a simple pair of pure imaginary eigenvalues  $\lambda(\mu_0)$  and  $\overline{\lambda(\mu_0)}$  and no other eigenvalues with zero real parts,
- (H2)  $\frac{d}{d\mu}(Re \lambda(\mu))|_{(\mu=\mu_0)} \neq 0$ .

Then the dynamics undergo a Hopf bifurcation at  $(\mathbf{x}_0, \mu_0)$  resulting in a one-parameter family of periodic solutions. The system is locally topologically equivalent to the normal form (2.8) near the origin. The stability of the periodic solutions is given by the sign of the first Lyapunov coefficient of the dynamics  $\sigma = \text{sign}(\ell_1|_{(\mathbf{x}_0, \mu_0)})$ . If  $\ell_1 < 0$  then these solutions are stable limit cycles and the Hopf bifurcation is supercritical, while if  $\ell_1 > 0$  the periodic solutions are repelling.

A key challenge is determining the right sets of coordinate transformations to convert the center manifold dynamics to the normal form (2.8); details of the calculation of the Lyapunov coefficient  $\ell_1$  are provided in Appendix A.

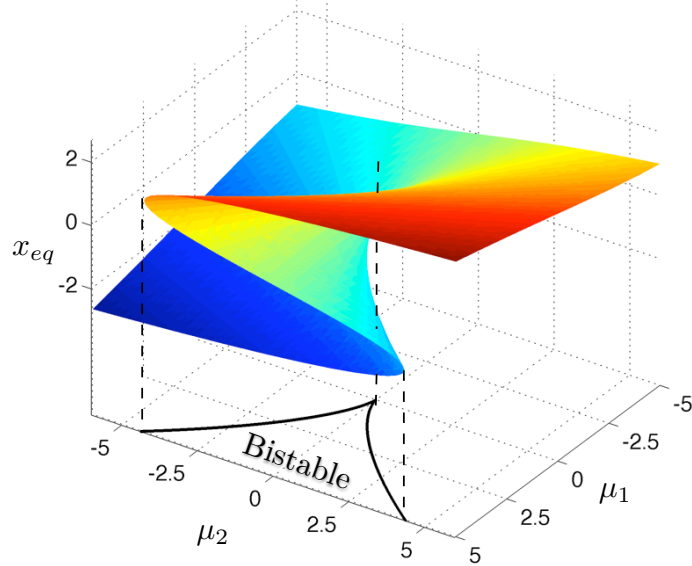


**Figure 2.6:** Cusp catastrophe bifurcation plot. The surface corresponds to the equilibria of the cusp catastrophe normal form (2.9) plotted as a function of the bifurcation parameters  $\mu_1$  and  $\mu_2$ . The planar projection on the  $\mu_1 - \mu_2$  surface shows the bifurcation set of the system, including the region with bistability. Outside this region, the system has one stable equilibrium.

Our discussion on bifurcations so far has focused on bifurcations as a single parameter  $\mu$  is varied. There exist several classes of multi-parameter bifurcations, one of which is the two-parameter *cusp catastrophe* [102], the normal form of which is given by

$$\dot{x} = x^3 - \mu_1 x - \mu_2. \quad (2.9)$$

Figure 2.6 shows the equilibria and bifurcation set of this system as a function of bifurcation parameters  $\mu_1$  and  $\mu_2$ . Saddle node bifurcations occur along the bifurcation set defined by  $\mu_2 = \frac{-2}{3\sqrt{3}}\mu_1^{3/2}$  except at the point  $\mu_1 = \mu_2 = 0$ , which is a pitchfork bifurcation point (pitchfork bifurcation moving along the line  $\mu_2 = 0$ ). This results in a region of bistability (two stable equilibria), as shown in the plot. We will encounter systems with a cusp catastrophe in Chapter 3 (Figure 3.4) and in Chapter 7 (Figure 7.3).

## 2.3 Graph Theory Tools

Graphs are a convenient tool for representing interactions between agents in a multi-agent network. For a graph with  $N$  nodes, the structure of the graph is encoded in an  $N \times N$  non-negative adjacency matrix  $A = [a_{ij}]$ . Each  $a_{ij} > 0$  ( $i \neq j$ ) is the weight of a directed edge from node  $i$  to node  $j$ . Each  $a_{ii} > 0$  corresponds to the weight of a self cycle at node  $i$ . An edge exists from node  $i$  to node  $j$  if and only if  $a_{ij} > 0$ . Let  $\mathcal{N}_i$  denote the set of *neighbors* of node  $i$ , i.e.,  $j \in \mathcal{N}_i$  if and only if  $a_{ij} > 0$ . For unweighted graphs,  $a_{ij} \in \{0, 1\}$ . A graph is said to be undirected if its adjacency matrix is symmetric, i.e.,  $a_{ij} = a_{ji}$  for all  $i, j$ . For a graph with adjacency matrix  $A$ , the Laplacian matrix of the graph is given by  $L = \text{diag}(A\mathbf{1}) - A$ . Let  $\mathcal{G}(L)$  denote the directed graph with Laplacian matrix given by  $L$ . Figure 2.7 illustrates the adjacency and Laplacian matrices for a particular graph.

Graph	$A$	$L = \text{diag}(A\mathbf{1}) - A$
	$A = \begin{bmatrix} 0 & 1 & 0 & 0 & 0 & 0 \\ 0 & 0 & \frac{1}{2} & \frac{1}{2} & 0 & 0 \\ 0 & 0 & 0 & 0 & 0 & 0 \\ 0 & 0 & \frac{1}{2} & 0 & 0 & \frac{1}{2} \\ 0 & \frac{1}{3} & 0 & \frac{1}{3} & 0 & \frac{1}{3} \\ 0 & 0 & \frac{1}{2} & \frac{1}{2} & 0 & 0 \end{bmatrix}$	$L = \text{diag}(A\mathbf{1}) - A = \begin{bmatrix} 1 & -1 & 0 & 0 & 0 & 0 \\ 0 & 1 & -\frac{1}{2} & -\frac{1}{2} & 0 & 0 \\ 0 & 0 & 0 & 0 & 0 & 0 \\ 0 & 0 & -\frac{1}{2} & 1 & 0 & -\frac{1}{2} \\ 0 & -\frac{1}{3} & 0 & -\frac{1}{3} & 1 & -\frac{1}{3} \\ 0 & 0 & -\frac{1}{2} & -\frac{1}{2} & 0 & 1 \end{bmatrix}$

**Figure 2.7:** Adjacency and Laplacian matrices for a specific directed graph with  $N = 6$  nodes. Graph edge weights are chosen such that the Laplacian matrix is normalized to zeros and ones on the main diagonal.

In biological systems, individual agents such as birds in a flock, or fish in a school, are represented as nodes on a graph and interactions between agents are represented as directed edges with a prescribed (possibly state dependent) weight. For example, an edge from node  $i$  to node  $j$  with weight  $a_{ij}$  could represent that agent  $i$  senses agent  $j$  with strength  $a_{ij}$ . Similarly, in robotic networks, nodes can represent individual robots with edges corresponding to communication or sensing links between them.

The Laplacian matrix features prominently in the multi-agent systems literature to model the continuous-time consensus or agreement process [111, 91, 47]. Consider a state vector  $\mathbf{x} \in \mathbb{R}^N$  with dynamics given by

$$\dot{\mathbf{x}} = -L\mathbf{x}. \quad (2.10)$$

Here  $x_i$  corresponds to the state of each node of the network and the dynamics (2.10) correspond to agents on the graph updating their state to reach agreement with the mean of their neighbors (as defined at the beginning of this section). The dynamics (2.10) converge to the agreement subspace  $\alpha\mathbf{1}$  for some scalar  $\alpha$  if and only if the directed graph corresponding to  $L(\mathcal{G}(L))$  is connected. Connectivity of  $\mathcal{G}(L)$  requires that there exists at least one node, labeled the root, such that a directed path exists from every other node of the network to the root [111, 64, 110]. For example, the graph in Figure 2.7 is connected with root node 3. In Chapter 5 we discuss graph connectivity and consensus in more detail in the context of collective migration.

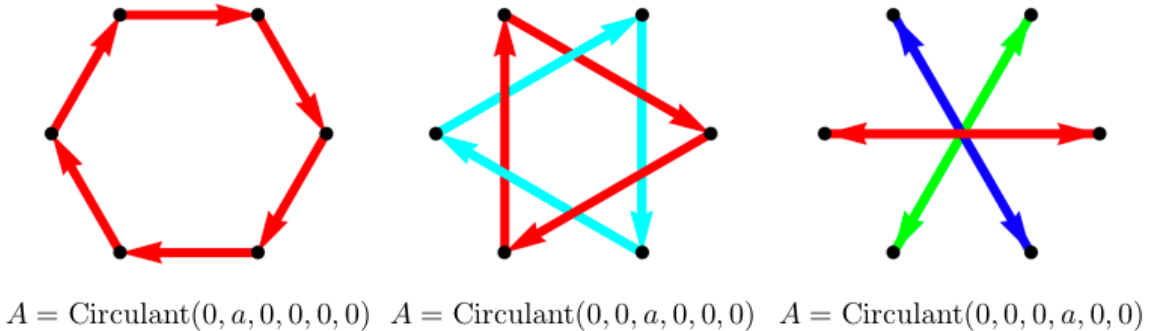


**Figure 2.8:** Illustration of circulant graphs for  $N = 6$  nodes where each node has one outgoing edge.

In Chapters 3 and 4 we focus on a specific class of graph topologies with circulant adjacency matrices. A circulant matrix is fully specified by its first row; the subsequent rows are cyclic permutations of the first row to the right with offset given by the row index. Let circulant matrix  $C$  be given by

$$C = \text{Circulant}(c_1, c_2, \dots, c_N) = \begin{bmatrix} c_1 & c_2 & \cdots & \cdots & c_N \\ c_N & c_1 & c_2 & \ddots & \vdots \\ \vdots & \ddots & \ddots & \ddots & \vdots \\ \vdots & \cdots & c_N & c_1 & c_2 \\ c_2 & \cdots & \cdots & c_N & c_1 \end{bmatrix}. \quad (2.11)$$

In Figure 2.8 we illustrate three circulant graph topologies. The symmetry of circulant graphs, and corresponding well-known properties such as an analytical characterization of eigenvalues and eigenvector of circulant adjacency and Laplacian matrices, make these topologies particularly well-suited for analysis [43].

Graphs can also be constructed by considering the spatial embedding of nodes and using spatial metrics to define the existence and weights of edges. This is particularly

useful when considering models of collective motion where agents interact with others within a specific distance from them (distance metric) [14, 15], or with a specific number of nearest neighbors (topological metric) [3, 10]. Graphs with the distance metric are undirected by definition if the specific distance is the same for every agent; see Figure 2.9 for an illustration.

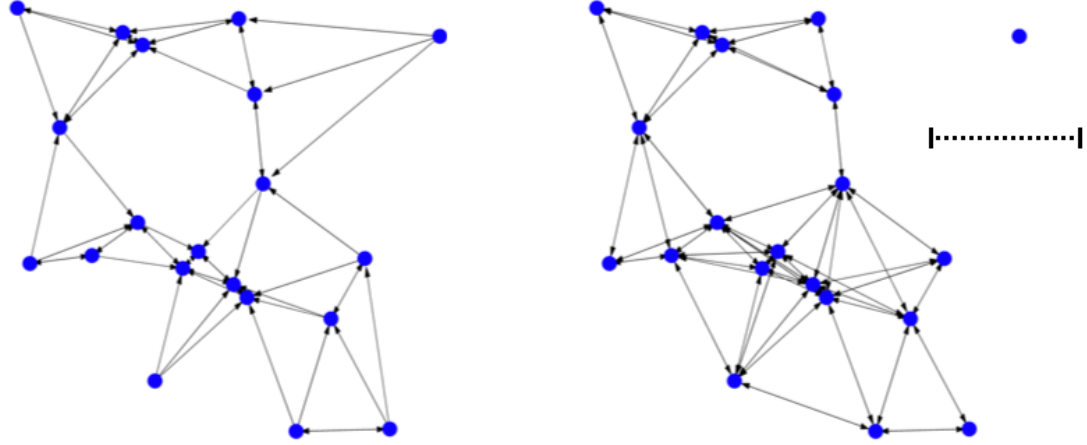


**Figure 2.9:** Spatially embedded graphs with  $N = 20$  nodes. The blue circles indicate node positions, both graphs have an identical set of nodes. For the graph on the left, each node is connected to its three nearest neighbors. For the graph on the right, each node is connected to all nodes within the distance indicated by the dashed line segment.

## 2.4 Stochastic Dynamics

It is often the case that in modeling physical systems one chooses to ignore or neglect the role of noise and disturbances that drive these systems, either by a rigorous calculation, or informally. Indeed a large part of the field of control theory is devoted to designing controllers for systems that minimize the impact of external noise and disturbances, thereby enabling such systems to track and converge efficiently. Nonetheless, the lack of predictability is inherent to a large variety of natural phenomena. In this section, we will be concerned with noisy (stochastic) systems that have *limited* predictability: the mean motion of these stochastic systems is often easy to determine, but the fluctuations about this mean motion are not predictable. As we will see in Chapters 5 and 7, quantifying the magnitude of these fluctuations is important for understanding the dynamics of specific collective systems.

The simplest one-dimensional stochastic system can be represented using an Ito stochastic differential equation (SDE) [24]

$$dx = \alpha(x, t)dt + \beta(x, t)dW. \quad (2.12)$$

Here  $x$  denotes the stochastic state variable,  $\alpha(x, t)$  and  $\beta(x, t)$  are the drift and noise intensity functions respectively, and  $dW$  is the standard Wiener increment. The Wiener process  $dx = dW \iff x(t) = W(t)$  has mean  $x(0)$  and variance that grows linearly with time. There is a one-to-one correspondence between the SDE representation of the stochastic process (2.12) and the Fokker-Planck (FP) representation of the evolution of the probability density of the state  $x$  with time. Specifically, let  $p(x, t)$  represent the probability density function of the state  $x$  at time  $t$  with initial condition  $x(t=0) = x_0$ . Then  $p(x, t)$  evolves according to

$$\frac{\partial p}{\partial t} = -\frac{\partial}{\partial x} [\alpha(x, t)p(x, t)] + \frac{1}{2}\frac{\partial^2}{\partial x^2} [\beta(x, t)^2 p(x, t)], \quad (2.13)$$

with initial distribution  $p(x, 0) = \delta(x - x_0)$ . There is a complete equivalence between the SDE (2.12) and the FP equation (2.13) with drift coefficient  $\alpha(x, t)$  and diffusion coefficient  $\beta(x, t)^2$  [24].

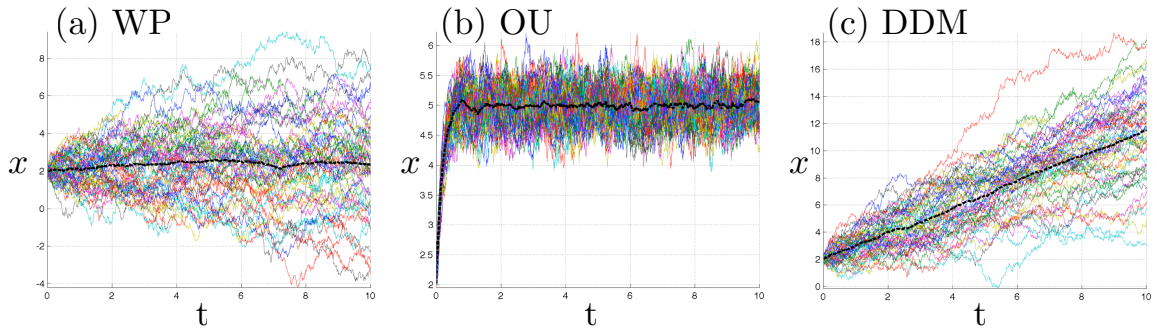


**Figure 2.10:** Simulations of the stochastic dynamics (2.12)  $dx = (a + bx)dt + \sigma dW$  with initial condition  $x_0 = 2$ ; each figure shows 50 sample trajectories with the ensemble mean plotted in the darker dashed curve. (a) Wiener Process (WP) with parameters  $a = b = 0$ ,  $\sigma = 1$ . (b) Ornstein Uhlenbeck process (OU) with parameters  $a = -5$ ,  $b = 25$  and  $\sigma = 1$ . (c) Drift Diffusion process (DDM) with parameters  $a = 0$ ,  $b = 1$ ,  $\sigma = 1$ . Note that only the stable OU process (b) has finite steady-state variance. We use the first order Euler-Mayurama method for all simulations of SDEs [39].

Let  $\mathcal{N}(\mu, \sigma^2)$  denote a Gaussian distribution with mean  $\mu$  and variance  $\sigma^2$ . If  $\alpha = 0$  and  $\beta = \sigma$ , the system (2.12) reduces to the standard Wiener process ( $x(t) = \sigma W(t)$  or equivalently  $p(x, t) = \mathcal{N}(x_0, \sigma^2 t)$ ) illustrated in Figure 2.10(a). For a linear drift term

$\alpha(x, t) = ax + b$  and constant noise term  $\beta(x, t) = \sigma$  the equation (2.12) corresponds to the one-dimensional Ornstein-Uhlenbeck (OU) process. For  $a < 0$  the OU process is stable with a stationary steady state solution with mean  $E[x]_{ss} = -b/a$  and variance  $\sigma_{ss}^2 = \sigma^2/(2a)$ . Equivalently  $\lim_{t \rightarrow \infty} p(x, t) = \mathcal{N}(\frac{-b}{a}, \frac{\sigma^2}{2a})$ . The stable OU is illustrated in Figure 2.10(b). The SDE with  $\alpha = b$  and  $\beta = \sigma$  is the continuum limit of the random walk model and is also known as the drift diffusion model (DDM), widely studied as a model for optimal decision making in neural systems [8]. This model does not converge to a steady state solution, but rather has solution mean and variance that grow linearly with time, i.e.,  $p(x, t) = \mathcal{N}(x_0 + bt, \sigma^2 t)$ . The DDM is illustrated in Figure 2.10(c).

For a multi-dimensional stochastic state vector  $\mathbf{x} \in \mathbb{R}^N$ , the multivariate stochastic dynamics are given by

$$d\mathbf{x} = \boldsymbol{\alpha}(\mathbf{x}, t)dt + \boldsymbol{\beta}(\mathbf{x}, t)d\mathbf{W}, \quad (2.14)$$

where  $\boldsymbol{\alpha} : \mathbb{R}^N \times \mathbb{R} \mapsto \mathbb{R}^N$ ,  $\boldsymbol{\beta} : \mathbb{R}^N \times \mathbb{R} \mapsto \mathbb{R}^N$ , and  $d\mathbf{W} \in \mathbb{R}^N$  is the multi-dimensional Wiener increment. Similar to (2.13), the multivariate FP equation equivalent to (2.14) is given by

$$\frac{\partial p}{\partial t} = - \sum_i \frac{\partial}{\partial x_i} [\alpha_i(\mathbf{x}, t)p(\mathbf{x}, t)] + \frac{1}{2} \sum_i \sum_j \frac{\partial^2}{\partial x_i \partial x_j} \left\{ [\boldsymbol{\beta}(\mathbf{x}, t)\boldsymbol{\beta}(\mathbf{x}, t)^T]_{ij} p(\mathbf{x}, t) \right\}, \quad (2.15)$$

where  $p(\mathbf{x}, t)$  is the multivariate probability density function for the state  $\mathbf{x}(t)$  with initial condition  $\mathbf{x}(t=0) = \mathbf{x}_0$ .

Let  $\mathcal{N}(\boldsymbol{\mu}, \Sigma)$  denote the multivariate Gaussian distribution with mean  $\boldsymbol{\mu}$  and covariance matrix  $\Sigma$  (symmetric, positive semi-definite). The multivariate Wiener process is given by  $\boldsymbol{\alpha} = \mathbf{0}$  and  $\boldsymbol{\beta} = B$  where  $B$  is a constant matrix; this process has solution  $p(\mathbf{x}, t) = \mathcal{N}(\mathbf{x}_0, BB^T)$ .  $\boldsymbol{\alpha} = A\mathbf{x} + \mathbf{b}$  and  $\boldsymbol{\beta} = B$  results in the multivariate OU process

$$d\mathbf{x} = (A\mathbf{x} + \mathbf{b})dt + Bd\mathbf{W}, \quad (2.16)$$

where  $A \in \mathbb{R}^{N \times N}$  and  $B \in \mathbb{R}^{N \times N}$  are constant square matrices and  $\mathbf{b} \in \mathbb{R}^N$  is a constant vector. If  $A$  is Hurwitz (all eigenvalues in the open left half of the complex plane), then the process (2.16) has a steady-state mean given by  $E[\mathbf{x}]_{ss} = -A^{-1}\mathbf{b}$  and state state covariance matrix  $\Sigma_{ss}$  given by the solution to the system of linear equations (Lyapunov equation) [24]

$$A\Sigma_{ss} + \Sigma_{ss}A^T = -BB^T. \quad (2.17)$$

We employ the system of equations (2.17) to study the evolutionary dynamics of a networked migration model in Chapter 5.

Setting  $A = -L$ ,  $\mathbf{b} = b\mathbf{1}$  and  $B = \sigma\mathbb{I}$  in (2.16) results in a coupled version of the DDM studied recently in [104]. Here  $L$  is the positive semi-definite Laplacian matrix from (2.10) that encodes the networked coupling between different drift-diffusing decision-making units.

### 2.4.1 Random Points on a Simplex

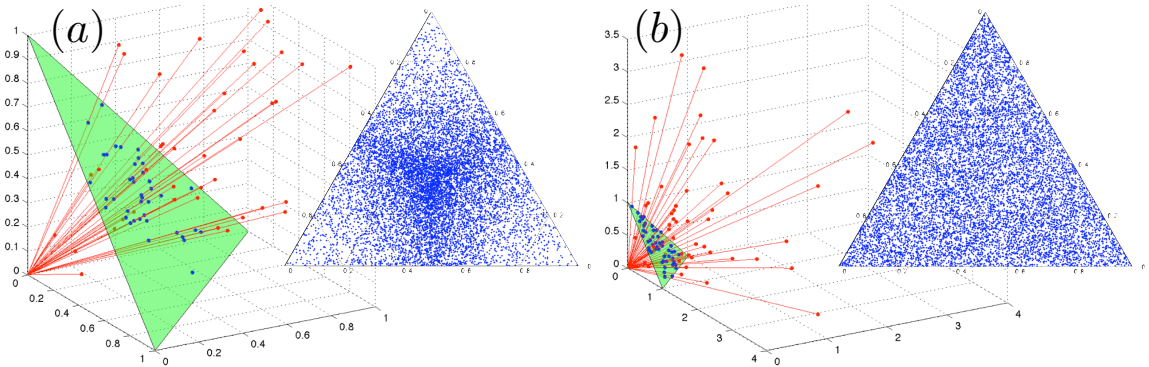


**Figure 2.11:** Random distributions of points on  $\Delta_2$ . The red points in  $\mathbb{R}^3$  are drawn randomly from a uniform distribution in (a) and an exponential distribution in (b). The intersection of the line joining each red point and the origin, with the simplex  $\Delta_2$ , is marked in blue (this is the geometric illustration of the division by sum normalization).

For several of the simulations in the chapters to follow, we pick initial conditions that are uniformly randomly distributed on the simplex  $\Delta_{N-1}$ . A seemingly reasonable method to do this would be to choose  $N$  independent uniformly randomly distributed values on the interval  $[0, 1]$  and divide each by the total sum of the values to get a simplex vector. This method, however, results in points that are clustered in the middle of the simplex as illustrated in Figure 2.11. The correct method to do this is to draw  $N$  values independently from an *exponential* distribution and then normalize. The resultant vectors are then uniformly distributed on the simplex, as illustrated geometrically in Figure 2.11. We refer the reader to the Dirichlet distribution described in [58] for more details.

# Chapter 3

## Replicator-Mutator Dynamics in the Plane

As discussed in Chapters 1 and 2, the replicator-mutator dynamics define a canonical model from evolutionary theory and have been recently applied to model the evolution of language and the decision-making dynamics of social networks. In this chapter, we study a form of the replicator-mutator dynamics and prove necessary and sufficient conditions for the existence of stable limit cycles for  $N = 3$  competing strategies; we generalize these results to  $N \geq 3$  strategies in Chapter 4. Stable limit cycles correspond to sustained oscillations in strategy dominance across some or all of the population. The form of the dynamics considered, and the interpretation of the oscillations, depends on the applications of interest; three motivating applications are discussed in §1.1. The results presented in this chapter have been published in [97].

The analysis of the replicator-mutator dynamics in the literature has focused primarily on stable limiting equilibrium behavior where the fitness terms are assumed to have a lot of symmetry (e.g. [75, 85, 90]). However, the recent  $N = 2$  analysis in [56] (discussed in §3.3) shows that the symmetric case is structurally unstable and that breaking symmetry in fitness yields qualitatively different bifurcations of the dynamics. Further, in [76] the authors illustrate that the replicator-mutator dynamics exhibit limit cycles and chaos for specific model parameter values. In this chapter, we show that the limiting behaviors of the replicator-mutator dynamics are tied to the structure of the fitness model, and we prove how breaking symmetry yields some of the richer outcomes simulated in [76]. It is known that the replicator dynamics for  $N \geq 4$  can generate limit cycles and chaos for particular choices of fitness [76, 124, 86]. Here we investigate the role that both fitness and mutation play in generating limit cycles for the replicator-mutator dynamics.

With mutation strength as the bifurcation parameter, we prove that Hopf bifurcations can occur for the replicator-mutator dynamics with  $N = 3$  and characterize the existence of stable limit cycles using an analytical derivation of the Hopf bifurcation points and the corresponding first Lyapunov coefficients [32, 59]. It is important to emphasize that the limit cycles discussed in this chapter are fundamentally different from the *rock-paper-scissors* game dynamics cycles of the replicator equations (e.g. [121, 53, 41]). This is because the limit cycles of the replicator-mutator dynamics here are driven in part by mutation, and exist as a consequence of bifurcations that occur as mutation strength changes. Indeed, in the absence of mutation, the corresponding replicator game dynamics would yield stable equilibria at the simplex boundaries for the models studied here.

### 3.1 Model Description\*

Consider a large population of agents and  $N$  distinct strategies  $S_i$ ,  $i = 1, 2, \dots, N$ . Let  $x_i \in [0, 1]$  be the fraction of individuals in the population with strategy  $S_i$  such that  $\sum_{i=1}^N x_i = 1$ . Let the population distribution vector  $\mathbf{x} = [x_1, \dots, x_N]^T$ . The fitness  $f_i$  of agents with strategy  $S_i$  is given by

$$f_i = \sum_{k=1}^N b_{ik} x_k.$$

Let  $\mathbf{f} = [f_1, \dots, f_N]^T$ . Then  $\mathbf{f} = B\mathbf{x}$ , where  $B = [b_{ij}] \in \mathbb{R}^{N \times N}$ , and the average population fitness is  $\phi = \mathbf{f}^T \mathbf{x} = \mathbf{x}^T B \mathbf{x}$ .  $B$  is known as the payoff matrix where  $b_{ij} \geq 0$  represents the payoff to an agent with strategy  $S_i$  on interacting with an agent with strategy  $S_j$ .

We assume that payoffs are all non-negative and that agents get a maximal payoff (normalized to 1) on interacting with others subscribed to the same strategy. Hence  $B$  satisfies

$$b_{ii} = 1 \text{ and } b_{ij} \in [0, 1] \text{ for } i \neq j. \quad (3.1)$$

As noted in [90], the payoff matrix  $B$  can be interpreted from a graph theoretic perspective as the adjacency matrix of a directed graph. The nodes of the graph correspond to the strategies  $S_i$ . The diagonal elements of  $B$  ( $b_{ii} = 1$ ) correspond to self-cycles at each node. Each of the non-zero off-diagonal elements  $b_{ij}$  corresponds to

---

\*This section is presented verbatim as in [93].

the weight of a directed edge from node  $S_i$  to node  $S_j$ . Symmetric payoff matrices  $B$  correspond to undirected graphs. This graph theoretic viewpoint is important in our work, particularly as a tool to visualize the structure of the payoff matrix. Consider the following condition:

**Condition 3.1.** *Every row and column of  $B$  has at least one non-zero off diagonal element.*

From the graph theoretic perspective, Condition 1 requires that every node of the graph has at least one outgoing and one incoming link; this ensures that there are no isolated disconnected nodes of the payoff graph. We will restrict to examining graphs that satisfy Condition 1.

Next we define  $q_{ij}$  to be the probability that agents with strategy  $S_i$  mutate (spontaneously change) to strategy  $S_j$ . Note that since  $\sum_j q_{ij} = 1$ , the mutation matrix  $Q = [q_{ij}]$  is row stochastic. The elements of the mutation matrix  $Q$  are defined in terms of a mutation parameter  $\mu \in [0, 1]$ . The mutation parameter represents the probability of error in replication. For example,  $\mu = 0$  denotes perfect replication and no mutation whereas  $\mu = 1$  denotes pure mutation.

In this chapter, we use two specific models for the mutation matrix  $Q$ . The first model defines the mutation probabilities  $q_{ij}$  as a function of the payoffs  $b_{ij}$  and the mutation strength  $\mu$  as follows:

$$q_{ii} = (1 - \mu), \quad q_{ij} = \frac{\mu b_{ij}}{\sum_{i \neq j} b_{ij}} \text{ for } i \neq j. \quad (\text{Q1})$$

The form of  $q_{ij}$  in (Q1) is motivated by the graph theoretic perspective on the replicator-mutator dynamics and is a generalization of the structured mutational models in [60, 56]. Intuitively, this model implies that spontaneous mutation to alternative strategies is weighted in favor of strategies that yield higher payoff. The mutation models in [90, 60, 75, 85] are special cases of (Q1) in which the payoff matrix  $B$  is symmetric. We call (Q1) the *dependent* mutation model since (Q1) is dependent on  $B$ .

The second mutation model we consider corresponds to a uniform random probability of mutating to alternative strategies as follows:

$$q_{ii} = (1 - \mu), \quad q_{ij} = \frac{\mu}{N - 1} \text{ for } i \neq j. \quad (\text{Q2})$$

We call (Q2) the *independent* mutation model since (Q2) is independent of  $B$ .

There are several alternative possibilities for the mutation matrix  $Q$ . Our choice of (Q1) and (Q2) enables a comparison between independent and dependent mutation models, and represents two generic models that are popular in the literature and meaningful in the context of our motivating applications.

The strategies  $S_i$ , payoffs  $b_{ij}$  and mutation probabilities  $q_{ij}$  can be interpreted in each of our motivating contexts from §1.1:

- a) For the evolution of language, each  $S_i$  is a specific grammar in the population and  $b_{ij}$  is the probability that a sentence spoken at random by individuals with grammar  $S_j$  can be parsed by individuals with grammar  $S_i$ . Higher values of the diagonal terms  $q_{ii} = 1 - \mu$  of the mutation matrix  $Q$  correspond to more effective language transmission or learning, and the off-diagonal terms  $q_{ij}$  correspond to mutation probabilities to alternative grammars.
- b) In social networks, each  $S_i$  represents a particular behavior in a population and  $b_{ij}$  represents the degree to which agents with behavior  $S_i$  are attracted to behavior  $S_j$ . Higher values of the mutation probabilities  $q_{ij}$  correspond to a greater tendency for individuals to explore and adopt alternative behaviors in the population.
- c) In multi-agent decision-making, each  $S_i$  represents an alternative choice for the group and the  $b_{ij}$  represent the perceived relative advantage of choice  $S_j$  for agents currently subscribed to choice  $S_i$ . The mutation terms  $q_{ij}$  model errors in the decision-making process, or agent random exploratory behavior.

The replicator-mutator dynamics describe the dynamics of the population distribution  $\mathbf{x}$  as a result of replication driven by fitness  $\mathbf{f}$  and mutation driven by  $Q$ :

$$\dot{x}_i = \sum_{j=1}^N x_j f_j(\mathbf{x}) q_{ji} - x_i \phi =: g_i(\mathbf{x}); \quad \phi = \mathbf{f}^T \mathbf{x}. \quad (3.2)$$

The replicator-mutator dynamics (3.2) can be derived as the limit of a simple stochastic error-prone imitation process, where agents imitate successful strategies proportional to relative payoffs ( $f_i/\phi$ ) and mutate to alternative strategies with probabilities  $q_{ij}$ ; see [40, 7, 135] for details. As illustrated in [135, 7], there exist several possible microscopic imitation mechanisms that yield alternatives to the replicator-mutator dynamics in the limit. For this chapter, we focus on the replicator-mutator dynamics as these are popular in the literature and hence allow for comparisons with past work [75, 90, 60, 76].

The dynamics (3.2) evolve on the  $(N - 1)$ -dimensional simplex phase space as follows. Define the  $n$ -simplex as

$$\Delta_n = \left\{ \mathbf{x} \in \mathbb{R}^{n+1} \mid x_i \geq 0, \mathbf{x}^T \mathbf{1} = 1 \right\},$$

where  $\mathbf{1}$  is a column vector of ones of appropriate dimension. Let  $\mathbf{g}(\mathbf{x}) : \mathbb{R}^N \rightarrow \mathbb{R}^N$  be  $\mathbf{g}(\mathbf{x}) = [g_1(\mathbf{x}), \dots, g_N(\mathbf{x})]^T$  where  $g_i(\mathbf{x})$  is defined in (3.2). One can compute directly from (3.2) that  $\mathbf{x}^T \mathbf{1} = 1 \implies \mathbf{1}^T \mathbf{g}(\mathbf{x}) = \mathbf{0}$ . Hence  $\mathbf{x}^T \mathbf{1} = 1$  is an invariant hyperplane for the dynamics. Further, the non-negative orthant of  $\mathbb{R}^N$  is a trapping region for the dynamics; this follows from the fact that  $\dot{x}_i|_{x_i=0} \geq 0$ . The intersection of the invariant hyperplane and the non-negative orthant of  $\mathbb{R}^N$  is the simplex  $\Delta_{N-1}$ . Hence  $\Delta_{N-1}$  is a trapping region for the replicator-mutator dynamics (3.2) (see Figure 2.2 for an illustration of  $\Delta_1$  and  $\Delta_2$ ).

Given the restriction to the simplex  $\Delta_{N-1}$ , the  $N$ -dimensional dynamics (3.2) can be reduced to an  $(N - 1)$ -dimensional system of equations:

$$\begin{aligned} \dot{x}_i &= h_i(\tilde{\mathbf{x}}), \quad i \in \{1, 2, \dots, N - 1\}, \\ h_i(\tilde{\mathbf{x}}) &:= g_i \left( x_1, x_2, \dots, x_{N-1}, 1 - \sum_{j=1}^{N-1} x_j \right), \end{aligned} \tag{3.3}$$

where  $\tilde{\mathbf{x}} = [x_1, \dots, x_{N-1}]^T$  and  $\mathbf{h} : \mathbb{R}^{N-1} \rightarrow \mathbb{R}^{N-1}$ .

For  $\mu = 0$ , the replicator-mutator dynamics reduce to the replicator dynamics (2.1) with payoff matrix  $B$  (3.1). Since  $B$  is diagonally dominant, the corresponding replicator dynamics are fairly constrained [74]. In particular, the vertices of the simplex (pure strategies  $x_i = 1, x_{j \neq i} = 0$ ) are asymptotically stable, and are also the only evolutionarily stable states.

## 3.2 Motivation for Cycles<sup>†</sup>

Our motivation to prove the existence of limit cycles in replicator-mutator dynamics comes in part from simulations of the dynamics (3.2) for random payoff matrices  $B$  ( $b_{ij}$  chosen from the uniform distribution on the interval  $[0, 1]$  for  $i \neq j$ ), which frequently exhibit oscillations. Figure 3.1 shows one simulation of the dynamics that is typical for mutation matrix (Q1) or (Q2). The dynamics in this simulation illustrate the transition from dominance of a single strategy (Figure 3.1(a)), to the coexistence

---

<sup>†</sup>This section is presented verbatim as in [93], except for the last paragraph and Figure 3.3.

of several strategies (Figure 3.1(b)), to eventually the collapse of dominance (Figure 3.1(c)), as the extent of mutation (parameterized by  $\mu$ ) increases. The study of this shift in dominance, as a consequence of bifurcations in the dynamics, has received significant attention in the literature (e.g. [75, 85, 57, 60]).

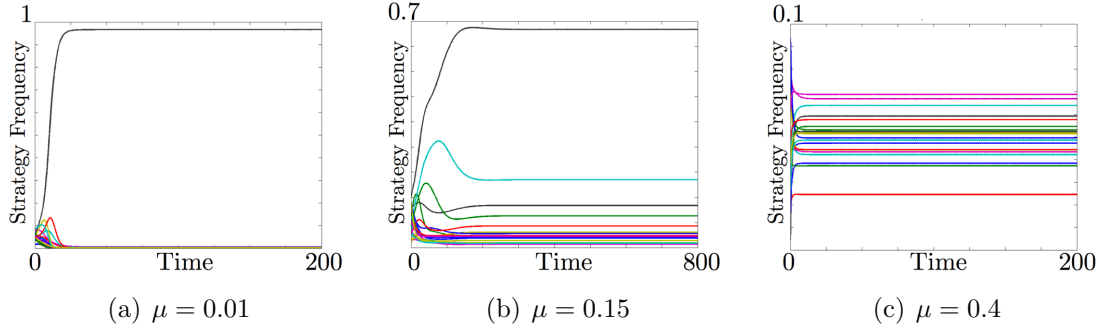


**Figure 3.1:** A first typical simulation of the dynamics (3.2) for  $N = 20$  nodes and  $b_{ij} \in [0, 1]$  chosen randomly from the uniform distribution. The dynamics transition from (a) a highly coherent state for small  $\mu$ , to (b) coexistence for intermediate  $\mu$ , and eventually to (c) a mixed collapse of dominance for large  $\mu$ .

Figure 3.2 shows another simulation of the replicator-mutator dynamics that is also typical for mutation matrix (Q1) or (Q2). The dynamics in this simulation also transition from dominance of a single strategy (Figure 3.2(a)) to collapse of dominance (Figure 3.2(c)). However, unlike the first simulation, the dynamics exhibit sustained oscillations in strategy dominance at intermediate values of mutation strength  $\mu$  (Figure 3.2(b)).

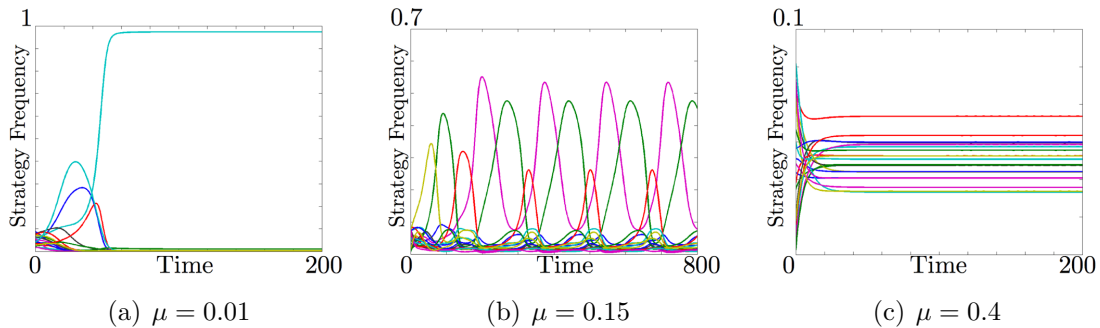


**Figure 3.2:** A second typical simulation of the dynamics (3.2) for  $N = 20$  nodes and  $b_{ij} \in [0, 1]$  chosen randomly from the uniform distribution. The dynamics transition from (a) a highly coherent state for small  $\mu$ , to (b) oscillating dominance for intermediate  $\mu$ , and eventually to (c) a mixed collapse of dominance for large  $\mu$ .

We are also motivated in part by simulations of the replicator-mutator dynamics in [76] that illustrate stable limit cycles for specific asymmetric payoff matrices (Figure

3.3). The authors in [76] study language dynamics and are particularly motivated by the observation that oscillations appear more realistic than stable equilibria for the language dynamics with timescales on the order of several centuries.

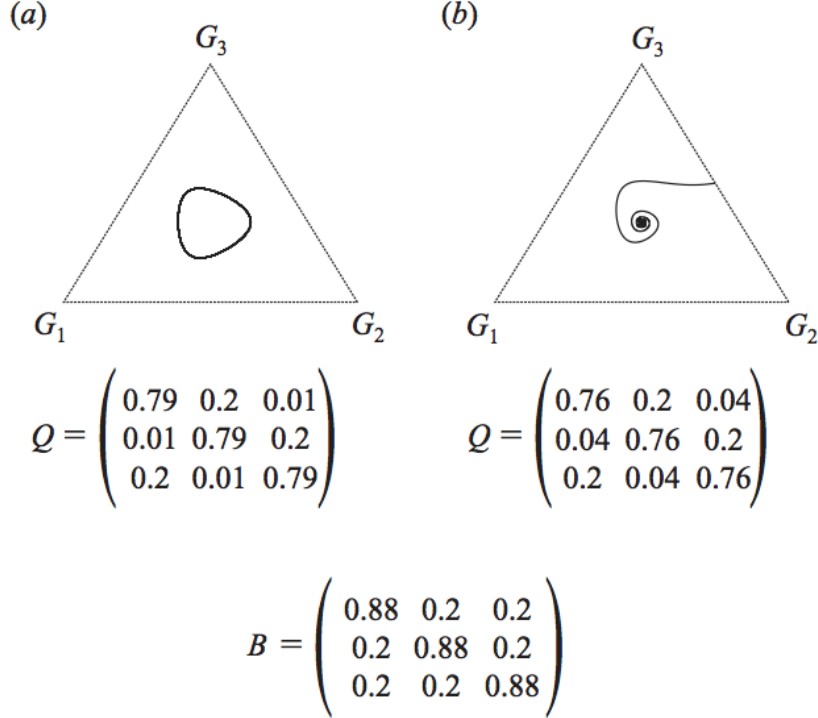


**Figure 3.3:** Illustration of a limit cycle (left simplex) for the dynamics (3.2) with payoff and mutation matrix as shown (from Figure 1 in [76]).

### 3.3 Bifurcations with $N = 2$ Strategies<sup>‡</sup>

Before we move on to study the  $N = 3$  (planar) case, we summarize the results from [56] for dynamics (3.2) with  $N = 2$  strategies. To simplify notation, define  $b_{12} := b_1$  and  $b_{21} := b_2$ . With this notation and following the reduction (3.3), we have the one-dimensional system

$$\begin{aligned} \dot{x}_1 &= h_1(x_1) = x_1 f_1 q_{11} + x_2 f_2 q_{21} - x_1^2 f_1 - x_1 x_2 f_2 \\ &= x_1 [b_1 + x_1(1 - b_1)] (1 - \mu - x_1) \\ &\quad + (1 - x_1) [1 + x_1(b_2 - 1)] (\mu - x_1). \end{aligned} \tag{3.4}$$

---

<sup>‡</sup>This section is presented verbatim as in [97].

Figure 3.4 shows the equilibria of the dynamics (3.4), and their stability, as a function of the bifurcation parameter  $\mu$ . The bifurcation plot shows a transition from bistability to a mixed equilibrium via a pitchfork bifurcation in the case  $b_1 = b_2$ . The pitchfork bifurcation is structurally unstable; for  $b_1 \neq b_2$  a saddle-node bifurcation occurs at a critical value  $\mu_c$  as shown in Figure 3.4. Three branches of equilibria exist. One of the branches remains stable for all  $\mu$  and approaches  $x_1 = 0.5$  as  $\mu$  approaches 1. The other two branches exist for  $\mu < \mu_c$  and collide in a saddle-node bifurcation at  $\mu_c$ . Note that  $b_1 \neq b_2$  corresponds to a directed payoff graph between the two nodes.

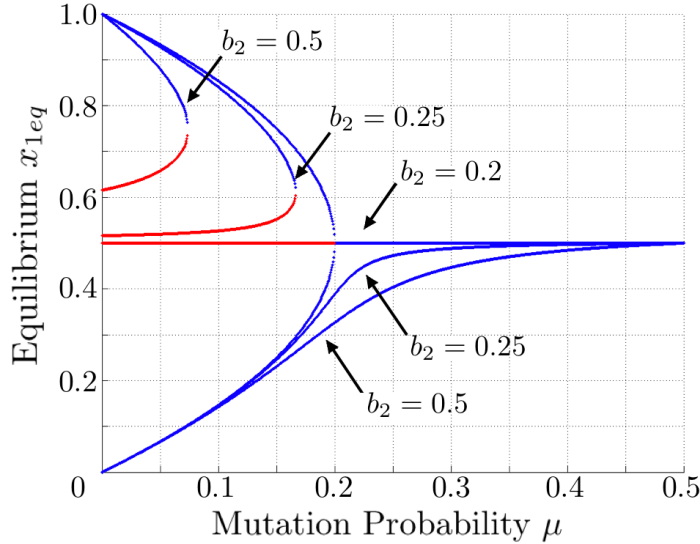


**Figure 3.4:** Three bifurcation plots for  $N = 2$  nodes with parameters  $b_1 = 0.2$  and  $b_2 = 0.2, 0.25$  and  $0.5$ . Blue curves are the stable equilibria and the red curves are the unstable equilibria. Similar to Figure 14 of [56].

A key observation from Figure 3.4 is that directed payoff graphs yield qualitatively different bifurcations when compared to undirected (symmetric) payoffs; this feature persists in higher dimensions. The equilibria and bifurcations plotted in Figure 3.4 correspond to vertical slices through a cusp catastrophe, the normal form of which is given in §2.2 and plotted in Figure 2.6.

### 3.4 Planar Analysis<sup>§</sup>

To build intuition for our general results in Chapter 4, we focus here on the bifurcations of the dynamics (3.2) as a function of the bifurcation parameter  $\mu$  for  $N = 3$

---

<sup>§</sup>This section is presented verbatim as in [93] except for the discussion of the topology cases, which is taken from [97], and Figures 3.7 and 3.9, which are new.

strategies. Because the simplex is two-dimensional for  $N = 3$  (3.3), it is easier than in higher dimensions to prove necessary and sufficient conditions for limit cycles and to visualize codimension-one bifurcations in three dimensions. We will show a transition from multiple stable dominant equilibria to a unique stable mixed equilibrium for increasing  $\mu$ , and prove conditions for stable limit cycles to exist over an intermediate range of  $\mu$ .

Consider the dynamics (3.2) with  $N = 3$  and with the payoff parameters  $b_{ij}$  in (3.1) set to be either 0 or equal to a constant value  $b \in (0, 1)$ . There are five non-isomorphic graph topologies with three nodes that satisfy the connectivity specified by Condition 1 and have edges of identical weight  $b$ ; these are shown in Figure 3.5. Figure 3.5 also shows the analytically computed<sup>¶</sup> bifurcation plots for each of the topologies as a function of the mutation strength  $\mu$  for mutation matrix (Q1) and payoff matrix (3.1). The corresponding plots for mutation matrix (Q2) are shown in Figure 3.6.

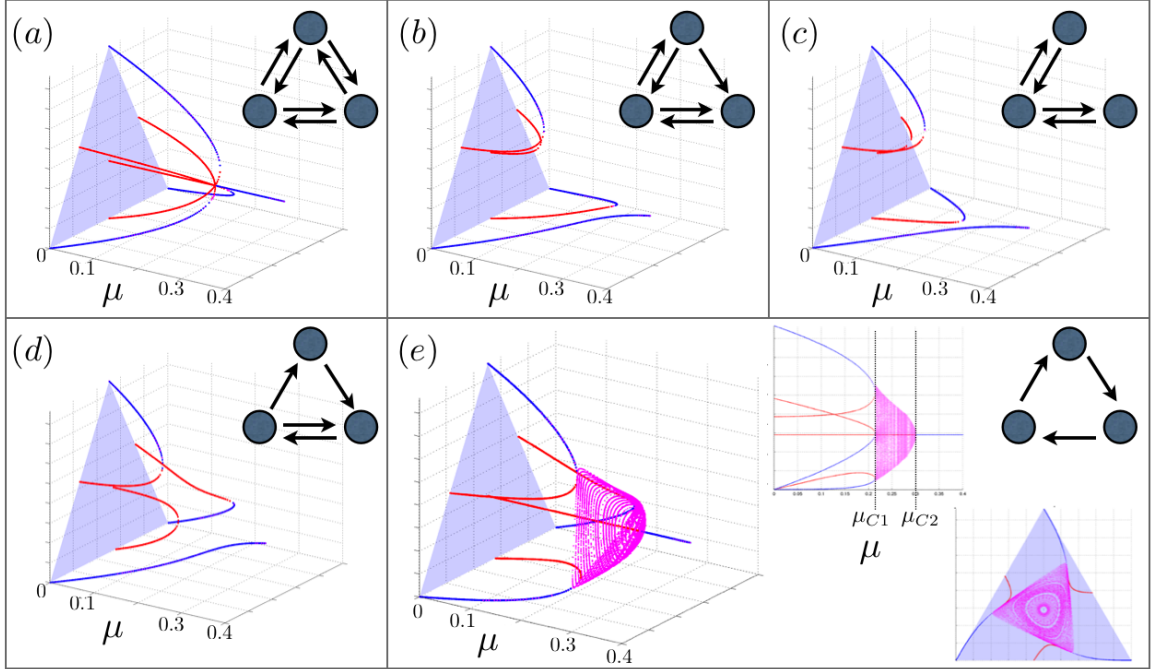


**Figure 3.5:** Bifurcation plots for the  $N = 3$  case of dynamics (3.2), constant edge weights  $b = 0.2$  and mutation matrix (Q1). The  $x$ -axis in each plot is the mutation strength  $\mu$ , blue and red curves are stable and unstable equilibria, respectively, and the magenta curves are stable limit cycles. The three-node graphs in each subplot have adjacency matrix  $B$  with self-cycles (not shown) at each node. Panels (a) and (e) with circulant payoff matrices each have an unstable central equilibrium  $x_1 = x_2 = x_3 = \frac{1}{3}$  which stabilizes for large enough  $\mu$  (see Lemma 4.1).

<sup>¶</sup>Equilibria and nullclines are solved using the MATLAB symbolic toolbox.

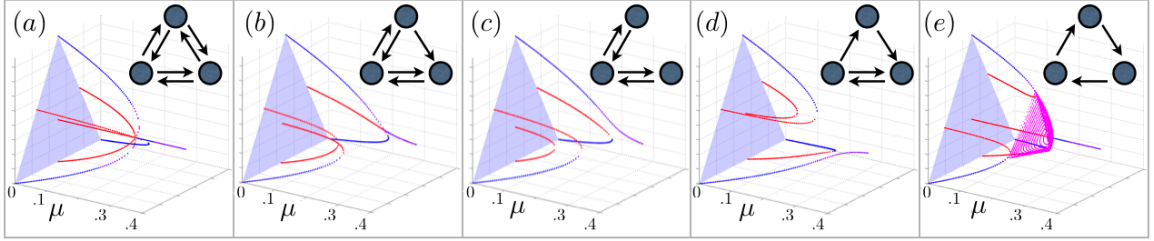


**Figure 3.6:** Bifurcation plots for the  $N = 3$  case of dynamics (3.2), constant edge weights  $b = 0.2$  and mutation matrix (Q2). The  $x$ -axis in each plot is the mutation strength  $\mu$ , blue and red curves are stable and unstable equilibria, respectively, and the magenta curves are stable limit cycles. The three-node graphs in each subplot have adjacency matrix  $B$  with self-cycles (not shown) at each node.

Note that for  $\mu = 0$  the only stable equilibria for the replicator-mutator dynamics with payoffs (3.1) are the three pure strategy dominant equilibria at the corners of the triangle simplex. In all the subplots in Figures 3.5 and 3.6, bifurcations yield a unique mixed strategy interior equilibrium for increasing  $\mu$ . The transition from the dominant equilibria to the mixed equilibrium for increasing  $\mu$  depends strongly on the topology of the payoff graph  $B$  under consideration; there are three distinct cases:

1. All-to-all Interconnection: The replicator-mutator dynamics with all-to-all interconnection and identical weights is studied in detail in [75]. For  $N = 3$  the payoff and mutation matrices are

$$B = \begin{bmatrix} 1 & b & b \\ b & 1 & b \\ b & b & 1 \end{bmatrix} \text{ and } Q1 = Q2 = \begin{bmatrix} 1 - \mu & \frac{\mu}{2} & \frac{\mu}{2} \\ \frac{\mu}{2} & 1 - \mu & \frac{\mu}{2} \\ \frac{\mu}{2} & \frac{\mu}{2} & 1 - \mu \end{bmatrix}.$$

The bifurcation plot Figure 3.5(a) (or identically 3.6(a)) has two bifurcation points

$$\begin{aligned} \mu_{CA1} &= \frac{2(1-b)}{3(2+b)} \text{ and} \\ \mu_{CA2} &= \frac{6+2b}{1-b} - \sqrt{\left(\frac{6+2b}{1-b}\right)^2 - 4}. \end{aligned} \tag{3.5}$$

At  $\mu = \mu_{CA1}$  the equilibrium  $\mathbf{x}_{mix,3} = \frac{1}{3}\mathbf{1}_3$  changes stability via an  $S_3$ -symmetric transcritical bifurcation [75]. At  $\mu = \mu_{CA2}$  six equilibria disappear via three symmetric saddle-node bifurcations. Thus for  $\mu > \mu_{CA2}$  the only remaining equilibrium is the stable  $\mathbf{x}_{mix,3}$ . Figure 3.7 shows phase portraits of the dynamics with the all-to-all payoff topology, for various choices of  $\mu$ .

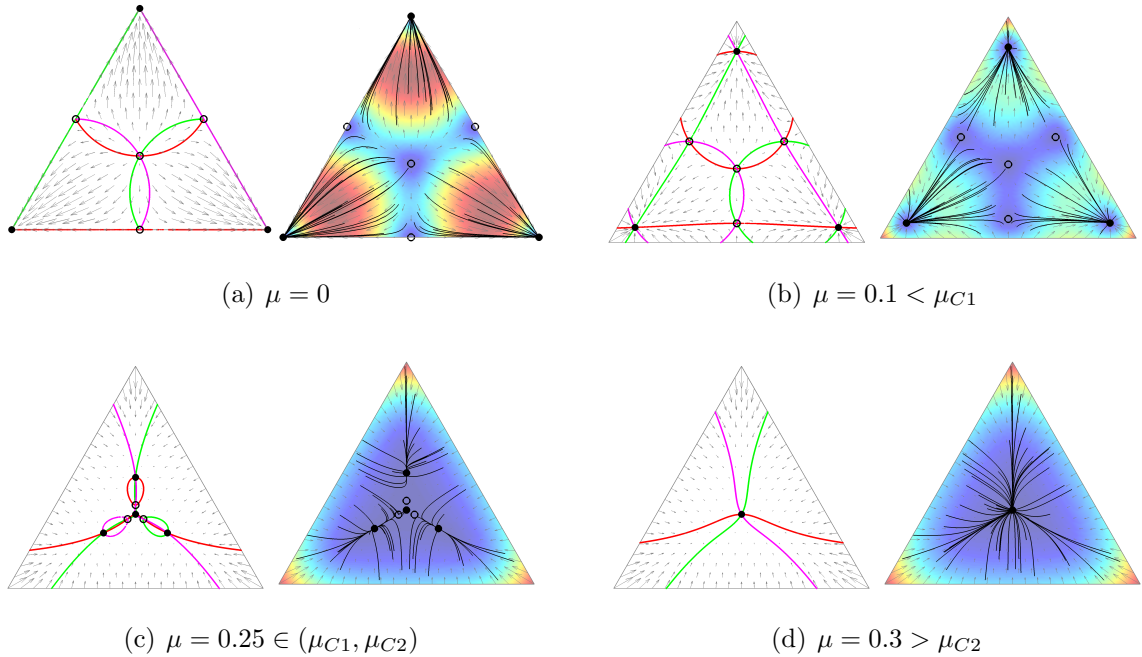


**Figure 3.7:** Phase portraits for dynamics (3.2) and with all-to-all payoff as in Figure 3.5(a) or Figure 3.6(a). The figure on the left of each of the four sub-figures shows nullclines (red  $\dot{x}_1 = 0$ , green  $\dot{x}_2 = 0$  and magenta  $\dot{x}_3 = 0$ ), vector field (grey arrows) and fixed points (filled circles are stable, unfilled circles are unstable). The figure on the right of each of the four sub-figures shows sample trajectories for randomly chosen initial conditions. The color scale indicates the magnitude of the flow (vector field) with hot colors corresponding to fast flow.  $b = 0.2$  for this set of plots which gives  $\mu_{CA1} = 0.2424$  and  $\mu_{CA2} = 0.2540$  from (3.5).

2. Limited Interconnections: The bifurcation plots for graphs in Figures 3.5(b)-(d) and Figures 3.6(b)-(d) each have a stable branch of equilibria for all  $\mu$ . They also have two other stable and four unstable equilibria at  $\mu = 0$  which disappear in saddle-node bifurcations as  $\mu$  increases. Perturbations of the structurally unstable symmetric all-to-all case yield bifurcations that are qualitatively similar to the limited interconnection cases, much like the  $N = 2$  bifurcations in Figure 3.4.
3. Directed Cycle Interconnection: The bifurcation plots in Figures 3.5(e) and 3.6(e) correspond to a directed cycle interconnection between nodes with payoff and mutation matrices

$$B = \begin{bmatrix} 1 & b & 0 \\ 0 & 1 & b \\ b & 0 & 1 \end{bmatrix}, Q1 = \begin{bmatrix} 1 - \mu & \mu & 0 \\ 0 & 1 - \mu & \mu \\ \mu & 0 & 1 - \mu \end{bmatrix} \text{ and } Q2 = \begin{bmatrix} 1 - \mu & \frac{\mu}{2} & \frac{\mu}{2} \\ \frac{\mu}{2} & 1 - \mu & \frac{\mu}{2} \\ \frac{\mu}{2} & \frac{\mu}{2} & 1 - \mu \end{bmatrix}.$$

The equilibrium  $\mathbf{x}_{mix,3}$  exists for all values of  $\mu \in [0, 1]$ . Three symmetric saddle-node bifurcations occur at  $\mu = \mu_{C1}$  as shown in Figure 3.5(e); because of symmetry, the unstable manifold of each saddle-node lies in the stable manifold of the next, forming a degenerate heteroclinic cycle with three non-hyperbolic saddle-nodes. This gives rise to stable limit cycles as  $\mu$  increases further. A Hopf bifurcation at  $\mu = \mu_{C2}$  where  $\mathbf{x}_{mix,3}$  changes stability from an unstable to a stable focus and is surrounded by stable limit cycles for  $\mu < \mu_{C2}$ . Figure 3.8 shows phase portraits of the dynamics with the directed cycle payoff, for various choices of  $\mu$ .

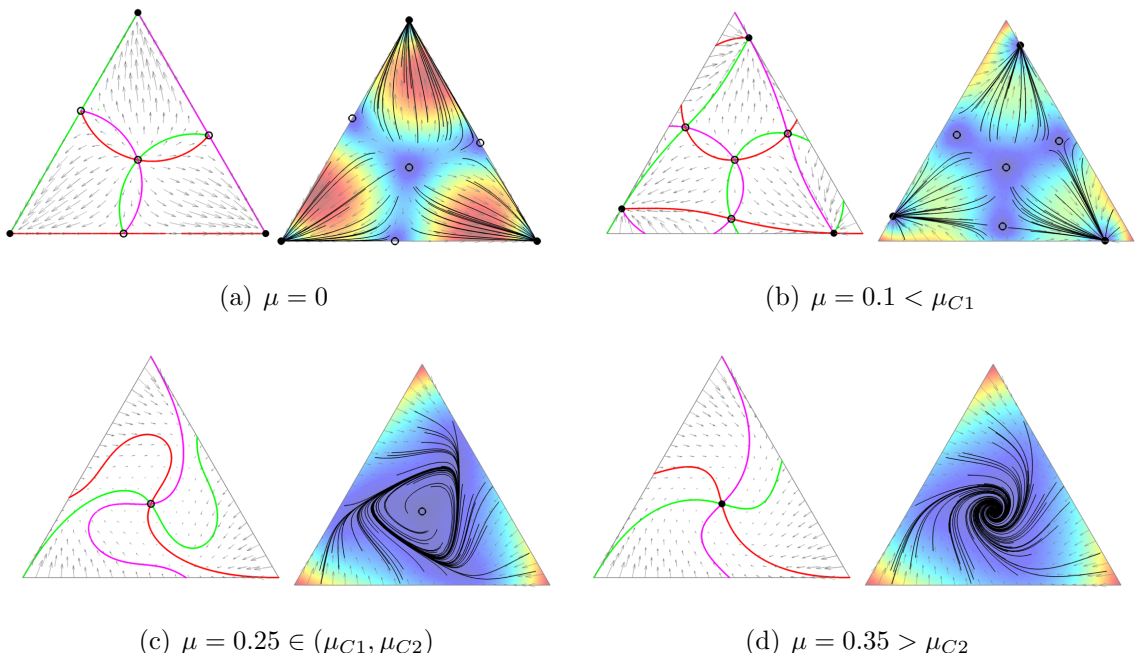


**Figure 3.8:** Phase portraits for dynamics (3.2) and with directed cycle topology as in Figure 3.5(e) and mutation matrix (Q1). The figure on the left of each of the four sub-figures shows nullclines (red  $\dot{x}_1 = 0$ , green  $\dot{x}_2 = 0$  and magenta  $\dot{x}_3 = 0$ ), vector field (grey arrows) and equilibria (filled circles are stable, unfilled circles are unstable). The figure on the right of each of the four sub-figures shows sample trajectories for randomly chosen initial conditions. The color scale indicates the magnitude of the flow (vector field) with hot colors corresponding to fast flow.  $b = 0.2$  for this set of plots which gives  $\mu_{C1} = 0.2136$  and  $\mu_{C2} = 0.3$ .

Stable limit cycles of the dynamics exist in a wide region of parameter space for circulant payoff matrices  $B$ , for which the directed cycle topology in Case 3 above is a special case. Here we state necessary and sufficient conditions for the existence of

stable limit cycles for (3.2) with circulant payoff matrix given by

$$B := B_{C,3} = \text{Circulant}(1, \alpha, \beta) = \begin{bmatrix} 1 & \alpha & \beta \\ \beta & 1 & \alpha \\ \alpha & \beta & 1 \end{bmatrix}, \{\alpha, \beta\} \in [0, 1) \text{ and } \alpha + \beta > 0.$$

Our choice of circulant payoff matrix  $B_{C,3}$  is in part for analytical tractability; we discuss limit cycles for non-circulant payoffs in Chapter 4. Lemma 3.1 provides necessary conditions for the existence of limit cycles for (3.2) with  $N = 3$  and payoff matrix  $B_{C,3}$ . Corollary 3.1 provides sufficient conditions for Hopf bifurcations and stable limit cycles and is a special case of the more general result in Theorem 4.1 to follow in Chapter 4.

**Lemma 3.1.** *The dynamics (3.2) with payoff matrix  $B_{C,3}$  have no closed orbits in the simplex  $\Delta_2$  for*

$$\mu > \frac{(2 - \alpha - \beta)(\alpha + \beta)}{6(\alpha + \beta + \alpha\beta)} =: \mu_{01} \text{ for mutation (Q1), and}$$

$$\mu > \frac{2(2 - \alpha - \beta)}{3(4 + \alpha + \beta)} =: \mu_{02} \text{ for mutation (Q2).}$$

*Proof.* The simplex  $\Delta_2$  (a simply connected subset of  $\mathbb{R}^2$ ) is a trapping region for the dynamics (3.2) (see §3.1). The divergence of the vector field on  $\Delta_2$  is negative semi-definite for  $\mu > \mu_{0i}$ ,  $i \in \{1, 2\}$  (see Lemmas B.1 and B.2 in Appendix B). Therefore Bendixson's Criterion (Theorem 2.1) implies that no closed orbits can lie in  $\Delta_2$  for  $\mu > \mu_{0i}$ .  $\square$

**Corollary 3.1.** *Equilibrium  $x_{mix,3}$  of the dynamics (3.2) with  $N = 3$  strategies, payoff matrix  $B_{C,3}$ , mutation matrix  $(Qi)$  ( $i = 1, 2$ ) and bifurcation parameter  $\mu$ , undergoes a supercritical Hopf bifurcation at  $\mu = \mu_{0i}$  leading to stable limit cycles for  $\mu < \mu_{0i}$  if  $\alpha \neq \beta$  and additionally if  $2\alpha + 2\beta + 5\alpha\beta + \alpha^2 + \beta^2 \neq 2$  for mutation matrix (Q1).*

*Proof.* The proof relies on satisfying the conditions of the Hopf Bifurcation Theorem 2.2. This is shown for  $N \geq 3$  in Theorem 4.1. For  $N = 3$ , the first Lyapunov coefficient is given by  $\ell_1(\alpha, \beta) = \frac{3(\alpha+\beta-2)}{\omega_{0i}}$ , where,

$$\omega_{0i} = |\tilde{\omega}_i|, \quad \tilde{\omega}_i = \begin{cases} \frac{(\alpha-\beta)(\alpha^2+\beta^2+2\alpha+2\beta+5\alpha\beta-2)}{6\sqrt{3}(\alpha+\beta+\alpha\beta)} & i = 1 \\ \frac{(\alpha-\beta)(1+\alpha+\beta)}{\sqrt{3}(4+\alpha+\beta)} & i = 2. \end{cases}$$

This follows from the calculation of  $\ell_1$  in Lemma 4.4. Supercriticality follows from  $\omega_{0i} \neq 0 \implies \ell_1 < 0$ . See Figure 3.9 for a plot of  $\ell_1(\alpha, \beta)$ .  $\square$

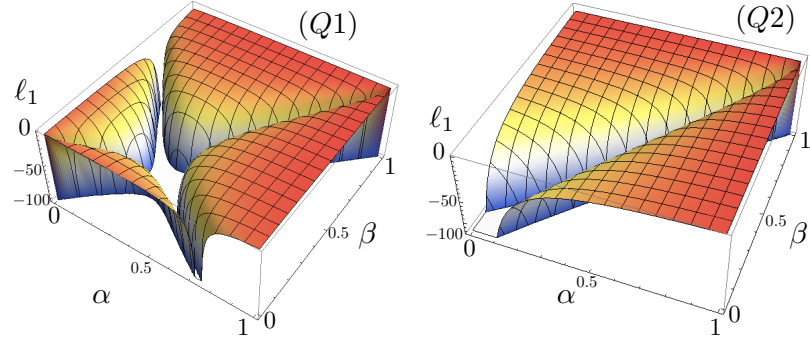


**Figure 3.9:** Plot of  $\ell_1(\alpha, \beta)$  from Corollary 3.1.

Figures 3.5(e) and 3.6(e) show limit cycles for the specific case of  $B_{C,3}$  with  $\alpha = b$  and  $\beta = 0$ . Figure 3.10 shows three more limit cycle bifurcation plots for non-zero  $\alpha$  and  $\beta$  and mutation matrix (Q1). Interestingly, for the parameter values selected in Figure 3.10(b) stable limit cycles coexist with multiple stable equilibria. This coexistence of stable equilibria and stable limit cycles implies that different initial conditions can yield qualitatively distinct limiting behavior even with fixed parameters for the dynamics (i.e., without bifurcations).

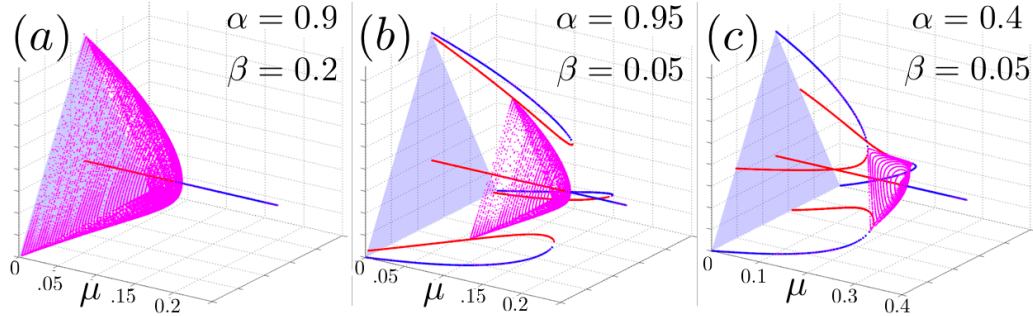


**Figure 3.10:** Bifurcation plots for the dynamics (3.2), payoff matrix  $B_{C,3}$  and parameters  $\alpha$  and  $\beta$  as shown. The existence of Hopf bifurcations and stable limit cycles for the set of parameter choices follows from Corollary 3.1. Note the coexistence of stable equilibria with stable limit cycles in panel (b).

While the focus of this chapter and the one to follow is on (local) Hopf bifurcations of the dynamics, we note that the dynamics also have global bifurcations. For example, for  $\mu$  increasing from zero in the bifurcation plot in Figure 3.10(b), a heteroclinic cycle containing three *hyperbolic* saddle points exists at  $\mu = 0.1$ . A heteroclinic

bifurcation yields stable limit cycles as  $\mu$  increases further. Phase portraits illustrating the heteroclinic cycle and one of the stable limit cycles are shown in Figure 3.11. In contrast, for the bifurcation plot in Figure 3.5(e), the directed cycle at  $\mu = \mu_{C1}$  occurs because the unstable manifold of each of the *non-hyperbolic* saddle-nodes lies in the stable manifold of the next.

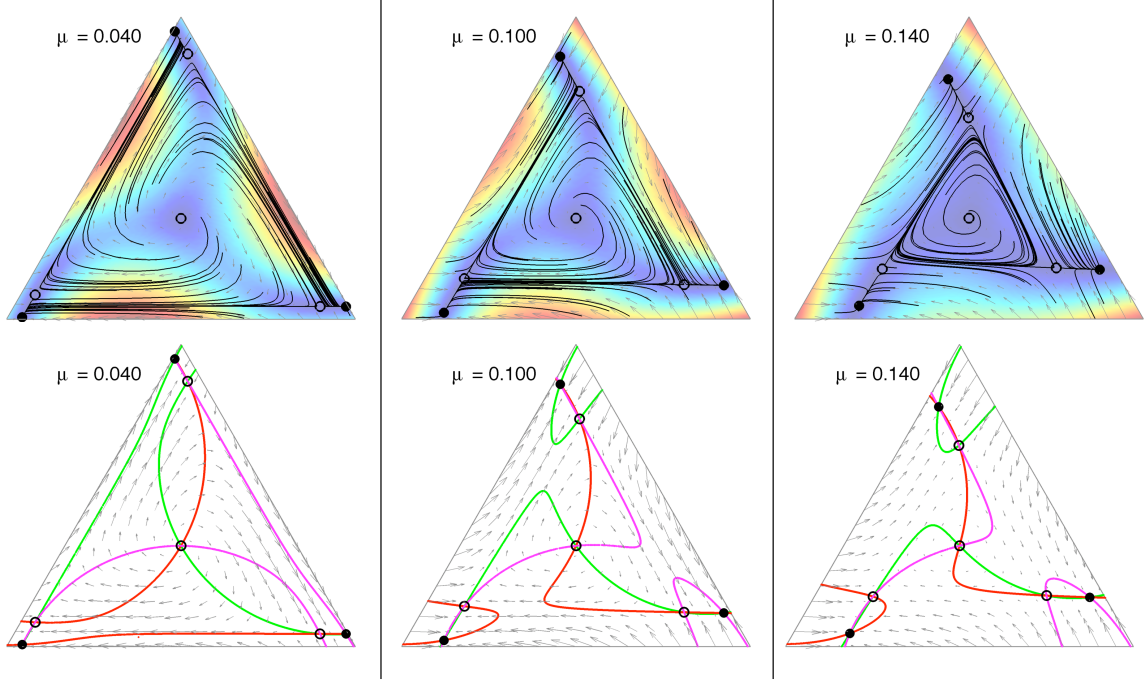


**Figure 3.11:** Phase portraits for dynamics (3.2) and parameters  $\alpha = 0.95$  and  $\beta = 0.05$  as in Figure 3.10(b) and mutation matrix (Q1). The top row of plots shows sample trajectories for randomly chosen initial conditions. The color scale indicates the magnitude of the flow (vector field) with hot colors corresponding to fast flow. The bottom row of plots shows nullclines (red  $\dot{x}_1 = 0$ , green  $\dot{x}_2 = 0$  and magenta  $\dot{x}_3 = 0$ ), vector field (grey arrows) and equilibria (filled circles are stable, unfilled circles are unstable). For  $\mu = 0.1$  (center pair), a heteroclinic connection exists between the three hyperbolic saddles. For  $\mu = 0.14 \in (0.1, 0.19)$  (right pair), stable limit cycles coexist with three stable sinks.

In the next chapter we will consider bifurcations of the replicator-mutator dynamics in the general  $N \geq 3$  case and prove conditions for the existence of stable limit cycles. We will also consider perturbations of the circulant fitness cases studied in this chapter, along with more general payoff graph topologies.

# Chapter 4

## Replicator-Mutator Dynamics in Higher Dimensions <sup>\*</sup>

In Chapter 3 we looked at Hopf bifurcations for the replicator-mutator dynamics (3.2) with  $N = 3$  strategies and circulant payoff matrix  $B_{C,3}$ . While the focus on three strategies was convenient for visualization, the simulations in Figure 3.2 indicate that the dynamics have stable limit cycles in higher dimensions as well ( $N \geq 4$ ). In this chapter, we show that this is indeed the case by proving two main results. Theorem 4.1 shows that the dynamics undergo multiple Hopf bifurcations at distinct bifurcation points for  $N \geq 3$ , and Lemma 4.4 provides analytical conditions for the stability of the limit cycles arising from these Hopf bifurcations.

We focus on the dynamics with circulant payoff matrix  $B_{C,N} \in \mathbb{R}^{N \times N}$ ,  $N \geq 3$  given by

$$B_{C,N} := \text{Circulant}(1, \alpha, 0, \dots, 0, \beta), \{\alpha, \beta\} \in [0, 1) \text{ and } \alpha + \beta > 0, \quad (4.1)$$

and mutation matrices (Q1) and (Q2). The directed graph corresponding to the payoff matrix  $B_{C,N}$  is illustrated in Figure 4.1.

We have chosen to study the circulant two-parameter payoff structure  $B_{C,N}$  both for purposes of tractability and to gain important insights regarding Hopf bifurcations of the dynamics in  $N$  dimensions. In particular, we show the existence of multiple Hopf bifurcations as several distinct pairs of eigenvalues cross the imaginary axis with increasing mutation parameter  $\mu$  in §4.1. Further, the criticality of the bifurcations, and correspondingly the existence of stable limit cycles, depends on the choice of parameters  $\alpha$  and  $\beta$ , unlike the  $N = 3$  case where all existing bifurcations are super-

---

<sup>\*</sup>Sections 4.1–4.5 are presented verbatim as in [93].

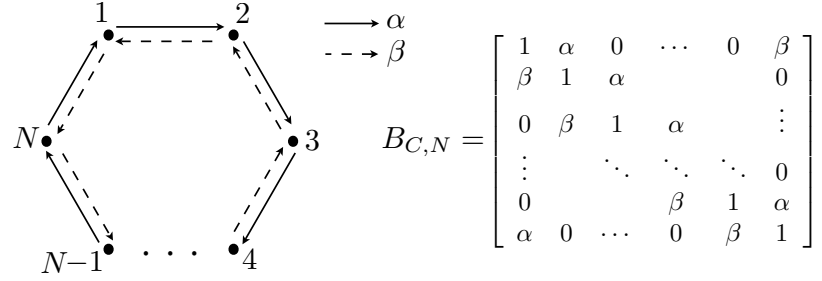


**Figure 4.1:** Graph topology corresponding to the payoff matrix  $B_{C,N}$  from (4.1).

critical; this is shown in §4.2. The illustrations in §4.2 and §4.3 show that the choice of the mutation matrix (Q1) or (Q2) plays an important role in determining the existence and criticality of the Hopf bifurcations. In §4.4 we extend the results from the previous sections to study multi-cycle dynamics for one-paramter graphs and show the existence of multiple stable limit cycle attractors. §4.5 focuses on generalizations to non-circulant and random payoff graphs and shows the tight connection between the existence of embedded cycles in these graphs and corresponding limit cycles of the dynamics.

## 4.1 Hopf Bifurcation Calculation

For payoff matrix  $B_{C,N}$ , the equilibrium  $\mathbf{x}_{mix,N} = \frac{1}{N}\mathbf{1}_N = \left[\frac{1}{N} \ \dots \ \frac{1}{N}\right]^T \in \mathbb{R}^N$  undergoes Hopf bifurcations. Lemma 4.1 shows that  $\mathbf{x}_{mix,N}$  is always an equilibrium of (3.2) for circulant  $B$ .

**Lemma 4.1.** *If the payoff matrix  $B$  is circulant, then  $\mathbf{x}_{mix,N}$  is an equilibrium of the replicator-mutator dynamics (3.2) with mutation matrix (Q1) or (Q2).*

*Proof.* Suppose  $B$  is circulant. Then  $\mathbf{1}$  is an eigenvector of  $B$  with eigenvalue  $r_B = \sum_{j=1}^N b_{1j}$ , i.e.,  $B\mathbf{1} = r_B\mathbf{1}$ . Matrix  $Q$  is also circulant by construction from (Q1) and (Q2). This means that  $\sum_{j=1}^N q_{ji} = \sum_{j=1}^N q_{ij} = 1$ . Let  $\mathbf{x} = \mathbf{x}_{mix,N}$ . Then  $\mathbf{f} = B\mathbf{x}_{mix,N} = \frac{1}{N}B\mathbf{1} = \frac{r_B}{N}\mathbf{1}$ . From (3.2),

$$\dot{x}_i \Big|_{\mathbf{x}_{mix,N}} = \frac{1}{N} \sum_{j=1}^N f_j \left( q_{ji} - \frac{1}{N} \right) = \frac{r_B}{N^2} \sum_{j=1}^N q_{ji} - \frac{r_B}{N^2} = 0,$$

and  $\mathbf{x}_{mix,N}$  is an equilibrium.  $\square$

To proceed with the analysis, we start by calculating  $D_{\mathbf{x}}\mathbf{g}|_{\mathbf{x}_{mix,N}}$ , the Jacobian matrix of the dynamics evaluated at the equilibrium point  $\mathbf{x}_{mix,N}$ . We then prove conditions for the existence of  $\lfloor \frac{N-1}{2} \rfloor$  pairs of complex conjugate eigenvalues of the Jacobian. We prove that each of these pairs of complex eigenvalues has distinct real part and hence each pair crosses the imaginary axis at different values of the bifurcation parameter  $\mu$ . We show that each such crossing satisfies the conditions of the Hopf Bifurcation Theorem 2.2.

The  $(i, j)$  entry of the Jacobian  $D_{\mathbf{x}}\mathbf{g}|_{\mathbf{x}_{mix,N}}$ , denoted  $[D_{\mathbf{x}}\mathbf{g}|_{\mathbf{x}_{mix,N}}]_{ij}$ , is given by

$$\frac{1}{N} \left[ (2 + \alpha + \beta) q_{ji} + \alpha q_{j-1,i} + \beta q_{j+1,i} - \left( \frac{2}{N} + \delta_{ij} \right) (1 + \alpha + \beta) \right], \quad (4.2)$$

where  $\delta_{ij}$  is the Kronecker delta and the indices  $i, j$  are denoted modulo  $N$ , i.e.  $1 \equiv N + 1, 0 \equiv N$ , etc. For circulant fitness  $B$ , the Jacobian  $D_{\mathbf{x}}\mathbf{g}|_{\mathbf{x}_{mix,N}}$  is also circulant.

Let  $\omega_N = \cos\left(\frac{2\pi}{N}\right) + \mathbf{i} \sin\left(\frac{2\pi}{N}\right)$  be a complex, primitive  $N^{\text{th}}$  root of unity. Let  $\omega_{N,k} = \omega_N^k = \cos\left(\frac{2\pi}{N}k\right) + \mathbf{i} \sin\left(\frac{2\pi}{N}k\right)$  for any integer  $k$ . For a circulant matrix  $M = [m_{ij}] \in \mathbb{R}^{N \times N}$ , let

$$\lambda_k(M) = \sum_{j=1}^N m_{1j} \omega_{N,k}^{j-1}. \quad (4.3)$$

Then, the  $N$  eigenvalues of  $M$  are  $\{\lambda_k(M), \lambda_{k+1}(M), \dots, \lambda_{N+k-1}(M)\}$  for any  $k$  [43]. Lemma 4.2 provides necessary and sufficient conditions for the existence of complex eigenvalues for the Jacobian  $D_{\mathbf{x}}\mathbf{g}|_{\mathbf{x}_{mix,N}}$ .

**Lemma 4.2.** *The Jacobian  $D_{\mathbf{x}}\mathbf{g}|_{\mathbf{x}_{mix,N}}$  has  $\lfloor \frac{N-1}{2} \rfloor$  pairs of complex conjugate eigenvalues if and only if  $\alpha \neq \beta$  and*

$$\mu \neq \frac{\alpha + \beta}{2(1 + \alpha + \beta)} \text{ for mutation (Q1), or, } \mu \neq \frac{N-1}{N} \text{ for mutation (Q2).}$$

*Proof.* The proof relies on the cyclic properties of complex roots of unity. Details are in Appendix C.1.  $\square$

Note that if the conditions in Lemma 4.2 are not satisfied (either for the mutation (Q1) or for the mutation (Q2)), then the eigenvalues of the Jacobian are strictly real. When the conditions are satisfied,  $\omega_{N,k}$  is complex if and only if  $\lambda_k(D_{\mathbf{x}}\mathbf{g}|_{\mathbf{x}_{mix,N}})$  is complex. There are  $\lfloor \frac{N-1}{2} \rfloor$  complex conjugate pairs among the  $\omega_{N,k}$  for  $k = 1, \dots, N$ . For  $N = 3$ , the one complex pair is associated with the unique Hopf bifurcation point as seen in Figures 3.5(e), 3.6(e) and 3.10.

To prove the existence of Hopf bifurcations we need to show that conditions (H1) and (H2) of Theorem 2.2 are satisfied. We begin by calculating critical values of the bifurcation parameter  $\mu$  corresponding to pairs of eigenvalues crossing the imaginary axis. Since mutation matrices (Q1) and (Q2) have entries that are linear in  $\mu$ , the entries of the Jacobian  $D_{\mathbf{x}}\mathbf{g}|_{\mathbf{x}_{mix,N}}$  are also all linear in  $\mu$ . In order to simplify the notation, we set

$$\left[ D_{\mathbf{x}}\mathbf{g}|_{\mathbf{x}_{mix,N}} \right]_{1j} = \gamma_j + \mu\eta_j, \quad j = 1, \dots, N, \quad (4.4)$$

where both  $\gamma_j$  and  $\eta_j$  are independent of  $\mu$ . Using this notation, we compute the bifurcation points for the dynamics in Lemma 4.3.

**Lemma 4.3.** *The pair of complex conjugate eigenvalues  $\lambda_r, \lambda_{N-r}$  of the Jacobian  $D_{\mathbf{x}}\mathbf{g}|_{\mathbf{x}_{mix,N}}$ , for each  $r = 1, \dots, \lfloor \frac{N-1}{2} \rfloor$ , is purely imaginary if and only if*

$$\mu = - \left[ \sum_{j=1}^N \gamma_j \cos \left( \frac{2\pi}{N}(j-1)r \right) \right] \left[ \sum_{j=1}^N \eta_j \cos \left( \frac{2\pi}{N}(j-1)r \right) \right]^{-1} =: \mu_{0,r}, \quad (4.5)$$

and  $\mu_{0,r}$  satisfies the conditions of Lemma 4.2. Further, the bifurcation points  $\mu_{0,r}$  are distinct, i.e.  $\mu_{0,k} \neq \mu_{0,l}$  when  $k \neq l$ .

*Proof.* The proof is in Appendix C.2. □

From Lemma 4.3, a unique pair of eigenvalues of  $D_{\mathbf{x}}\mathbf{g}|_{(\mathbf{x}_{mix,N}, \mu_{0,r})}$  is purely imaginary at each  $\mu_{0,r}$ ; this implies condition (H1). Lemma 4.3 also implies that  $\frac{d}{d\mu} \operatorname{Re}(\lambda_r) = \sum_{j=1}^N \eta_j \cos \left( \frac{2\pi}{N}(j-1)r \right) \neq 0$ , which is condition (H2). We can now collect these results and state our main theorem.

**Theorem 4.1.** *The equilibrium point  $\mathbf{x}_{mix,N}$  with payoff matrix  $B_{C,N}$  undergoes  $\lfloor \frac{N-1}{2} \rfloor$  Hopf bifurcations, with the  $r^{th}$  ( $r = 1, \dots, \lfloor \frac{N-1}{2} \rfloor$ ) such bifurcation located at*

$$\mu_{0,r} = - \left[ \sum_{j=1}^N \gamma_j \cos \left( \frac{2\pi}{N}(j-1)r \right) \right] \left[ \sum_{j=1}^N \eta_j \cos \left( \frac{2\pi}{N}(j-1)r \right) \right]^{-1}$$

when  $\alpha \neq \beta$  and

$$\mu_{0,r} \neq \frac{\alpha + \beta}{2(1 + \alpha + \beta)} \text{ for mutation (Q1), or, } \mu_{0,r} \neq \frac{N-1}{N} \text{ for mutation (Q2).}$$

**Remark 4.1.** *Equation (4.5) gives an analytic expression for  $\mu_{0,r}$  corresponding to a unique pair of purely imaginary eigenvalues of the Jacobian. However, not all values*

of  $\mu_{0,r}$  are feasible. That is, there might be pairs  $(\alpha, \beta) \in [0, 1] \times [0, 1]$  that yield bifurcation points  $\mu_{0,r}$  outside the feasible parameter range  $0 \leq \mu_{0,r} \leq 1$  of our model. This is illustrated in §4.3.

## 4.2 Criticality of Hopf Bifurcation

In Theorem 4.1 we proved conditions for the existence of Hopf bifurcations for the replicator-mutator dynamics with payoff  $B_{C,N}$ . In this section we study the criticality of the bifurcations (and correspondingly the existence of stable limit cycles for the dynamics) by computing an analytical expression for the first Lyapunov coefficient  $\ell_1|_{(\mathbf{x}_{mix,N}, \mu_{0,r})}$  in Lemma 4.4.

**Lemma 4.4.** *Let  $A_0 = D_{\mathbf{x}}\mathbf{g}|_{(\mathbf{x}_{mix,N}, \mu_{0,r})}$ . Then  $A_0$  has a pair of purely imaginary eigenvalues  $\lambda_r(A_0) = \mathbf{i}\hat{\omega}$  and  $\lambda_{N-r}(A_0) = -\mathbf{i}\hat{\omega}$ , where  $\hat{\omega} \in \mathbb{R}$  is calculated from (4.3). Define  $t = r \operatorname{sign}(\hat{\omega})$  and  $\omega_0 = |\hat{\omega}|$ . The first Lyapunov coefficient of the dynamics (3.2) with payoff  $B_{C,N}$  evaluated at the fixed point  $\mathbf{x}_{mix,N}$  and bifurcation point  $\mu_{0,r}$  is given by*

$$\begin{aligned} \ell_1|_{(\mathbf{x}_{mix,N}, \mu_{0,r})} &= \frac{1}{2\omega_0} \operatorname{Re}(T_1 + T_2), \text{ where,} \\ T_1 &= -2N [2 + (\alpha + \beta)(\omega_N^t + \omega_N^{-t})] \quad \text{and} \\ T_2 &= \frac{2\lambda_t(Q^T) \lambda_{2t}(Q^T)}{2 \mathbf{i} \omega_0 - \lambda_{2t}(A_0)} (1 + \alpha\omega_N^t + \beta\omega_N^{-t}) [2 + (1 + \omega_N^{3t}) (\beta\omega_N^{-2t} + \alpha\omega_N^{-t})]. \end{aligned}$$

$A_0$  is the Jacobian  $D_{\mathbf{x}}\mathbf{g}|_{(\mathbf{x}_{mix,N}, \mu_{0,r})}$  with purely imaginary eigenvalue  $\lambda_r(A_0) = \mathbf{i}\hat{\omega}$  calculated from (4.3).

*Proof.* The function  $\lambda_k(M)$  is defined for a general integer  $k$  and square matrix  $M$  in Equation (4.3). We exploit the circulant structure of the dynamics to obtain this analytical result. The details of the calculation are in Appendix C.3.  $\square$

Lemma 4.4 allows us to study the criticality of the Hopf bifurcations at each of the bifurcation points  $\mu_{0,r}$  as a function of the parameters  $(\alpha, \beta) \in [0, 1] \times [0, 1]$ . In Figure 4.2 we plot regions of positive and negative  $\ell_1$  as a function of  $\alpha$  and  $\beta$ . For each of the subplots in Figure 4.2, black denotes negative  $\ell_1$  (supercritical Hopf bifurcation, stable limit cycles) and white denotes positive  $\ell_1$  (subcritical Hopf bifurcation, repelling periodic solutions). Gray denotes the unfeasibility region for  $\mu_{0,r}$  (either  $\mu_{0,r} < 0$  or  $\mu_{0,r} > 1$ , see Remark 4.1). The red curves correspond to critical points  $\mu_{0,r}$  that do not satisfy the conditions of Lemma 4.2.

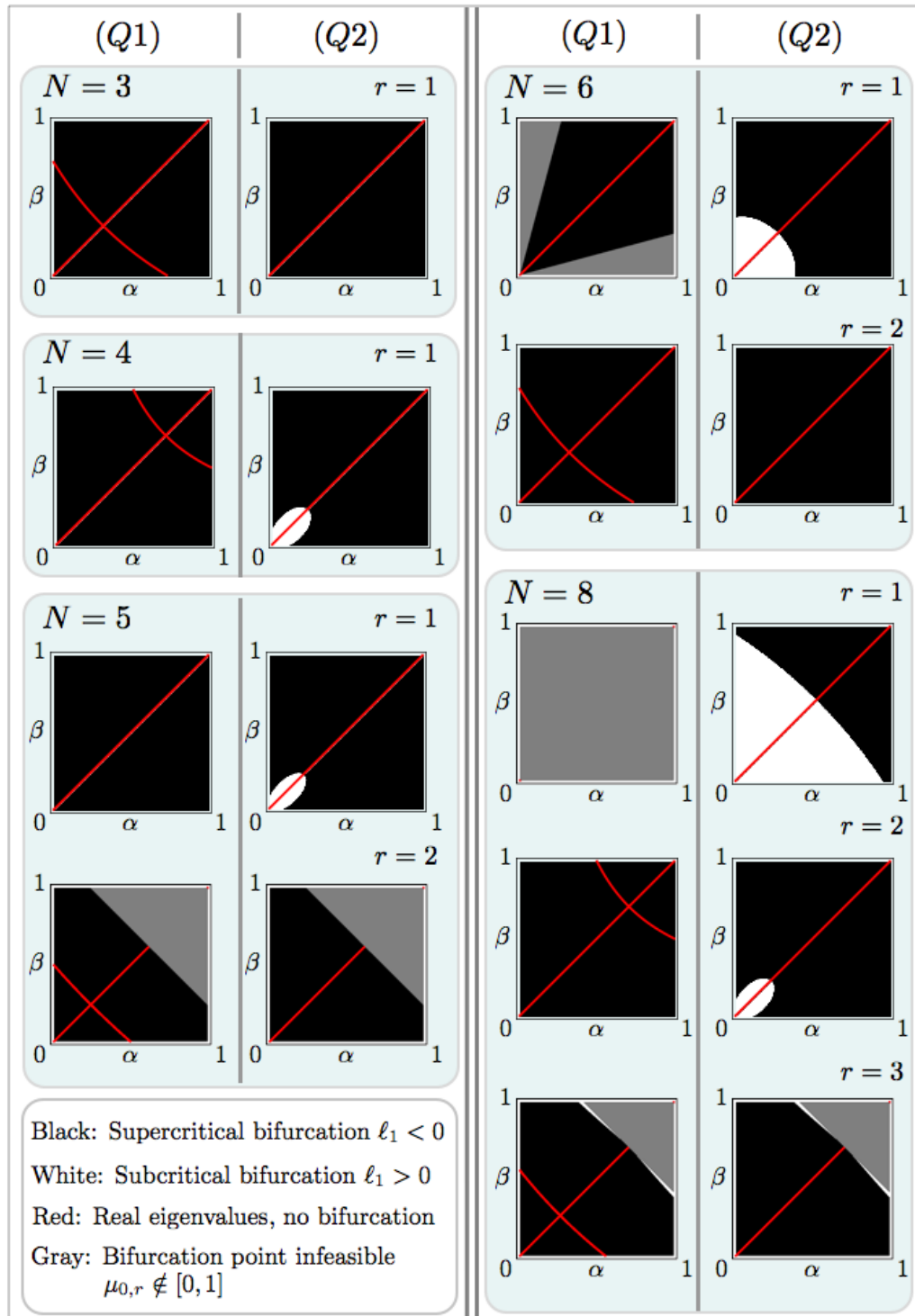


**Figure 4.2:** Criticality of the Hopf bifurcations as a function of parameters  $\alpha$  and  $\beta$  for  $N = 3, 4, 5, 6$  and  $8$ .

Figure 4.2 illustrates the effect of the number of strategies  $N$  and payoff parameters  $\alpha$  and  $\beta$  on the existence and criticality of Hopf bifurcations for the dynamics. Several different cases exist. For example, there are cases corresponding to a supercritical bifurcation throughout  $(\alpha, \beta) \in [0, 1] \times [0, 1]$  (as when  $N = 3$ ), and cases for which the bifurcation is subcritical on a subset of the parameter space (as when  $N = 4$  and with mutation matrix (Q2)). The regions corresponding to infeasible critical points ( $\mu_{0,r}$  outside the range  $[0, 1]$ ) can be connected as when  $N = 8$ ,  $r = 3$ , or disconnected, as when  $N = 6$ ,  $r = 1$  and with mutation matrix (Q1). Some cases are illustrated in §4.3.

### 4.3 Illustration of Bifurcations

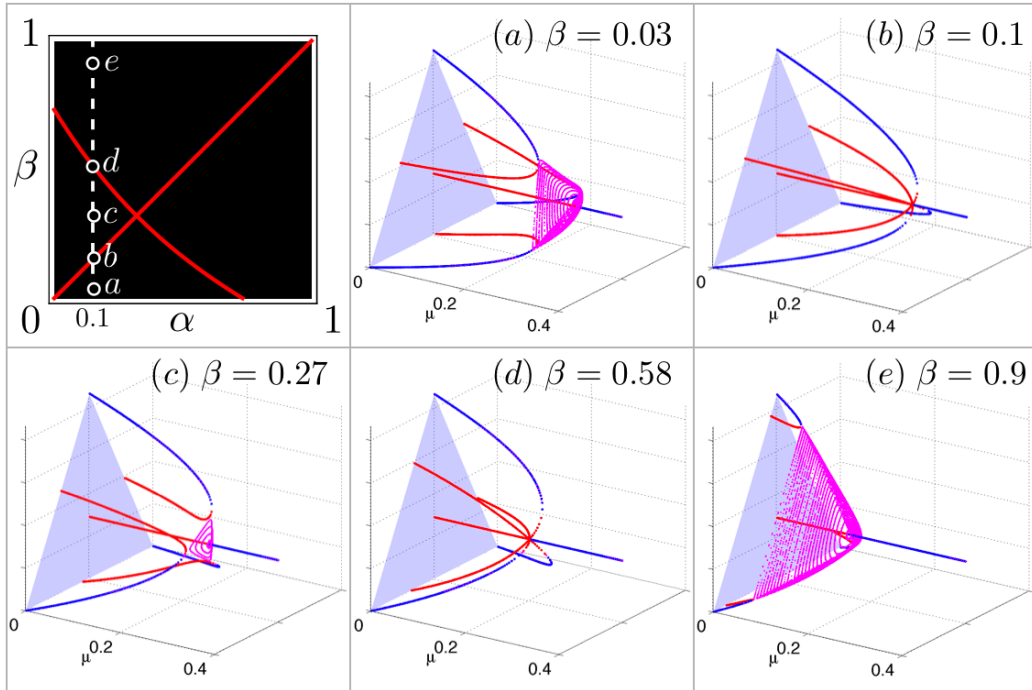


**Figure 4.3:** Effect of parameters  $\alpha$  and  $\beta$  on bifurcations. Subplots labeled (a)–(e) are bifurcation plots for the dynamics with  $N = 3$  strategies, mutation matrix (Q1),  $\alpha = 0.1$  and  $\beta$  as shown. The top left subplot shows the criticality and existence of the Hopf bifurcations (taken from Figure 4.2:  $N = 3$ , (Q1)) with parameters corresponding to subplots (a)–(e) marked. Subplot (b) corresponds to the all-to-all payoff matrix; the corresponding bifurcations are discussed in Section 3.4 with bifurcation points given by (3.5).

The existence and criticality of Hopf bifurcations computed in Lemma 4.3 and Theorem 4.1 vary as a function of parameters  $\alpha$  and  $\beta$  in ways that may not be

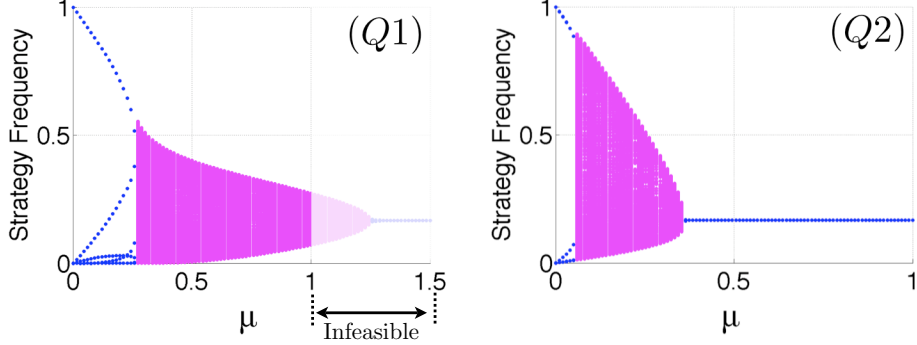


**Figure 4.4:** Bifurcation plots for the dynamics with  $N = 6$  strategies, parameters  $\alpha = 0.8$ ,  $\beta = 0.05$ , and mutation matrix as indicated on each subplot. In the case of the left subplot with mutation matrix (Q1), the Hopf bifurcation point  $\mu_{0,1} = 1.24$  lies outside the feasible range  $\mu \in [0, 1]$ .

immediately obvious. In this section, we explore the parameter dependence of the Hopf bifurcations using a set of selected simulations to help illustrate this variation.

Figure 4.3 shows bifurcation plots for the dynamics with  $N = 3$  and mutation matrix (Q1). Parameter  $\alpha$  is set to 0.1 and  $\beta$  is varied between 0 and 1. Looking at the corresponding criticality plot in Figure 4.3 (reproduced from Figure 4.2), we expect that the bifurcation is supercritical for all  $\beta$  except at two points labeled (b) and (d). These are precisely the points that violate the conditions of Lemma 4.2 and Theorem 4.1. i.e., at (b),  $\alpha = \beta = 0.1$  and at (d),  $\mu_{0,1} = \frac{\alpha+\beta}{2(1+\alpha+\beta)}$  for  $\alpha = 0.1$  and  $\beta = 0.58$ . As a result, the bifurcation plots show the existence of stable limit cycles for all values of  $\beta$  along the line  $\alpha = 0.1$ , except at the points (b) and (d). In Figure 4.3 stable limit cycles are apparent in Figures 4.3(a), 4.3(c) and 4.3(e), but not in 4.3(b) and 4.3(d). The payoff topology corresponding to the parameters in 4.3(b) is fully symmetric, with a bifurcation plot analogous to Figure 3.5(a).

Figure 4.4 shows the bifurcation plots for the dynamics with  $N = 6$ ,  $\alpha = 0.8$ ,  $\beta = 0.05$ , and mutation matrices (Q1) and (Q2). The corresponding criticality plots in Figure 4.2 show that the supercritical Hopf bifurcation point  $\mu_{0,1}$  lies outside the feasible range  $\mu \in [0, 1]$  for (Q1) and inside the feasible range for (Q2), for the chosen parameters. This is illustrated in Figure 4.4; the left plot shows a Hopf bifurcation at  $\mu = 1.249$  while the right plot shows a Hopf bifurcation at  $\mu = 0.363$ . The left plot in Figure 4.4 also illustrates that infeasible supercritical bifurcation points can yield stable limit cycles within the range of feasible  $\mu$ .

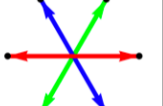
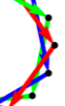
## 4.4 One-Parameter Multi-Cycles

In §4.1 and §4.2 we focused on a particular two-parameter circulant payoff structure given by (4.1) and illustrated in Figure 4.1. In this section we leverage the results from the previous sections to study the dynamics corresponding to a class of circulant payoff structures with each node having a single outgoing edge. For simplicity of presentation, we consider only mutation matrix (Q1) in this section. We show that for a particular set of topologies in this class, the dynamics exhibit multiple simultaneous Hopf bifurcations about distinct fixed points. The analysis in this section points to the fact that the dynamics with payoff graphs having multiple embedded cycles can have multiple distinct stable limit cycle attractors; we explore these multi-cycle dynamics more generally in §4.5.

Consider the dynamics (3.2) where the payoff matrix  $B$  is given by

$$B := B_{N,k} = \text{Circulant}(1, a_1, \dots, a_{N-1}), \text{ with } a_k = \alpha \text{ and } a_s = 0 \text{ for } s \neq k. \quad (4.6)$$

Let  $\gcd(a, b)$  denote the greatest common divisor of  $a$  and  $b$ . Two graphs with payoff

	Case 1 $d = 1$	Case 2	Case 3 $d = N/2$
$N = 5$	 $k = 1, 2, 3, 4$		
$N = 6$	 $k = 1, 5$	 $d = 2; k = 2, 4$	 $k = 3$
$N = 15$	 $k = 1, 2, 4, 7, 8, 11, 13, 14$	 $d = 3$	 $d = 5$

**Figure 4.5:** Graph topologies corresponding to circulant payoff matrix  $B_{N,k}$  from (4.6) for  $N = 5, 6, 15$ . Three cases are shown, Case 1 corresponds to simple cycles, Case 2 to multiple cycles, and Case 3 to connected pairs of vertices (only exists for  $N$  even). Note that multiple values of  $k$  can yield the same graph topology modulo a vertex relabeling; non-isomorphic topologies have distinct  $d$ .

matrices  $B_{N,k_1}$  and  $B_{N,k_2}$  are isomorphic if and only if  $\gcd(N, k_1) = \gcd(N, k_2)$ . Hence, among the payoff matrices  $B_{N,k}$ , the set of matrices  $B_{N,d}$  where  $d$  belongs to the set of proper divisors of  $N$ , corresponds to a set of non-isomorphic graph topologies. We split the set of graph topologies with payoff  $B_{N,d}$  ( $d$  a proper divisor of  $N$ ) into three distinct cases as described below:

- (1)  $d = 1$ , the graph is a directed cycle containing all vertices
- (2)  $1 < d < N/2$ , the graph consists of  $d$  disjoint cycles, each of length  $N/d$
- (3)  $d = N/2$ , the graph consists of  $N/2$  disjoint pairs of connected vertices. This case exists only for  $N$  even.

Figure 4.5 illustrates the three cases of graph topologies for  $N = 5$ ,  $6$ , and  $15$ .

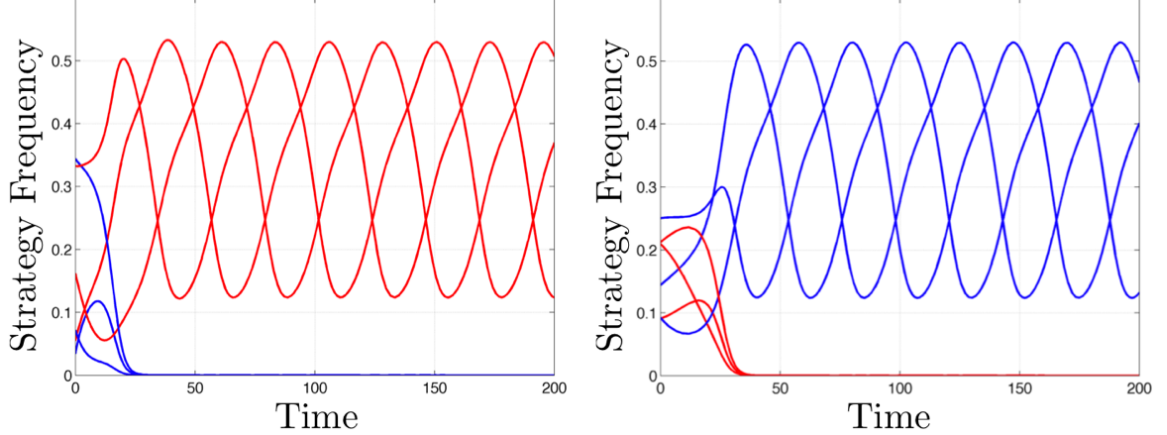
In addition to  $\mathbf{x}_{\text{mix},N}$ , the dynamics with payoff matrix  $B_{N,d}$  and mutation matrix (Q1) have  $d$  equilibria denoted  $\mathbf{x}_{j,d,N}$  and given by

$$\mathbf{x}_{j,d,N} = \left[ \begin{array}{c|c} \mathbf{0}_{j-1}^T & \frac{d}{N} \\ \hline & \mathbf{0}_{d-j}^T \end{array} \middle| \cdots \middle| \begin{array}{c|c} \mathbf{0}_{j-1}^T & \frac{d}{N} \\ \hline & \mathbf{0}_{d-j}^T \end{array} \right]^T \in \mathbb{R}^N, j = 1, \dots, d. \quad (4.7)$$

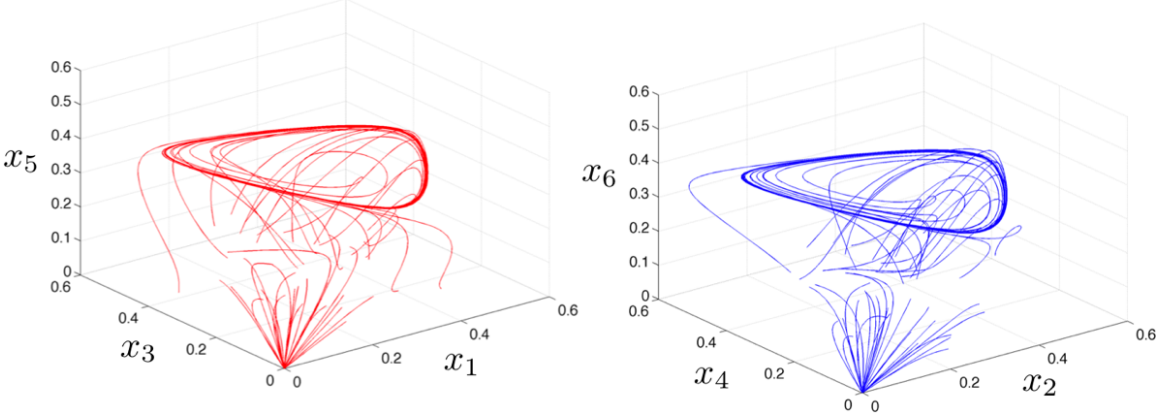
In Case 1,  $d = 1$ , and correspondingly  $j = 1$ , and  $\mathbf{x}_{1,1,N} = \mathbf{x}_{\text{mix},N}$ . For a given  $N$  and  $d \neq 1$ , the  $d$  equilibria  $\mathbf{x}_{j,d,N}$  are cyclically and symmetrically spaced around  $\mathbf{x}_{\text{mix},N}$ . Case 1 is studied in detail in §4.1 and obtained by setting  $\beta = 0$  (a simple one-parameter cycle). For the topology with pairs of connected nodes in Case 3, the Jacobian of (3.2) evaluated at the equilibrium  $\mathbf{x}_{\text{mix},N}$ , or also at any of the equilibria  $\mathbf{x}_{j,N/2,N}$ , is real and symmetric and therefore has only real eigenvalues. Thus the system cannot have Hopf bifurcations for these equilibria in this case. We henceforth focus on Case 2 and study the dynamics with payoff topologies comprising multiple cycles.

#### 4.4.1 Case 2 Analysis

We begin the analysis of the dynamics with multi-cycle graph topologies by first looking at the case  $N = 6$ ,  $d = 2$  (payoff  $B_{6,2}$ ), before generalizing to higher dimensions. The two disjoint cycles in the graph corresponding to  $B_{6,2}$  suggest that the behavior of the system might be similar to that observed for the  $N = 3$  cycles in Chapter 3. Indeed, simulations of the dynamics shown in Figure 4.6 suggest the existence of two stable limit cycle attractors, each dominated exclusively by three strategies, corresponding to the connected nodes of the graph. Further, simulations of the phase



(a) Trajectories of the dynamics (3.2) for  $N = 6$ ,  $d = 2$ , and  $B = B_{6,2}$  = Circulant  $(1, 0, \alpha, 0, 0, 0)$ , and for two different random initial conditions. Red corresponds to components  $x_1, x_3, x_5$  while blue corresponds to components  $x_2, x_4, x_6$ .



(b) Phase portrait for dynamics with payoff  $B_{6,2}$  and 50 different initial conditions showing two stable limit cycle attractors.

**Figure 4.6:** Simulation of the dynamics (3.2) for  $N = 6$ , payoff  $B_{6,2}$  and  $\mu = 0.25$ . Panel (a) shows two typical trajectories for the system while panel (b) illustrates the limit cycle attractors in a decoupled phase space. The red trajectories correspond to the components  $x_1, x_3$  and  $x_5$ , while the blue trajectories correspond to  $x_2, x_4$  and  $x_6$ .

space for 50 different randomly selected initial conditions, as in Figure 4.6(b), indicate that the two limit cycles are the only stable attractors for the dynamics for an appropriate range of bifurcation parameter  $\mu$ .

The linearization of the system at equilibrium  $\mathbf{x}_{mix,6}$  violates condition (H1) of Theorem 2.2 (i.e., complex eigenvalues of the Jacobian have algebraic multiplicity greater than one). However the dynamics with payoff  $B_{6,2}$  have two other equilibria

(as in (4.7)) given by

$$\begin{aligned}\mathbf{x}_{1,2,6} &= \left[ \begin{array}{cccccc} 1/3 & 0 & 1/3 & 0 & 1/3 & 0 \end{array} \right]^T, \\ \mathbf{x}_{2,2,6} &= \left[ \begin{array}{cccccc} 0 & 1/3 & 0 & 1/3 & 0 & 1/3 \end{array} \right]^T.\end{aligned}$$

The simulations in Figure 4.6 suggest that the dynamics undergo Hopf bifurcations at each of these equilibria. In Corollary 4.1, which follows from Corollary 3.1, we prove that this is indeed the case by showing that  $\mathbf{x}_{1,2,6}$  and  $\mathbf{x}_{2,2,6}$  undergo two simultaneous Hopf bifurcations at the critical point  $\mu = \frac{2-\alpha}{6}$ .

**Corollary 4.1.** *The system (3.2) with payoff matrix  $B_{6,2}$  and mutation matrix (Q1) has equilibria  $\mathbf{x}_{1,2,6}$  and  $\mathbf{x}_{2,2,6}$  that undergo supercritical Hopf bifurcations at the critical point  $\mu = \frac{2-\alpha}{6}$  with  $\alpha \neq \sqrt{3} - 1$ .*

*Proof.* Here we analyze the equilibrium  $\mathbf{x}_{1,2,6}$ . The analysis for  $\mathbf{x}_{2,2,6}$  is similar. The Jacobian  $D_{\mathbf{x}}\mathbf{g}|_{\mathbf{x}_{1,2,6}}$  is given by

$$D_{\mathbf{x}}\mathbf{g}|_{\mathbf{x}_{1,2,6}} = \begin{bmatrix} \frac{1-2\alpha-6\mu}{9} & 0 & \frac{-2+\alpha-3\alpha\mu}{9} & 0 & \frac{3\alpha\mu+6\mu-2-2\alpha}{9} & 0 \\ 0 & \frac{-\alpha-1}{3} & 0 & 0 & 0 & 0 \\ \frac{3\alpha\mu+6\mu-2-2\alpha}{9} & 0 & \frac{1-2\alpha-6\mu}{9} & 0 & \frac{-2+\alpha-3\alpha\mu}{9} & 0 \\ 0 & 0 & 0 & \frac{-\alpha-1}{3} & 0 & 0 \\ \frac{-2+\alpha-3\alpha\mu}{9} & 0 & \frac{3\alpha\mu+6\mu-2-2\alpha}{9} & 0 & \frac{1-2\alpha-6\mu}{9} & 0 \\ 0 & 0 & 0 & 0 & 0 & \frac{-\alpha-1}{3} \end{bmatrix}.$$

Permuting rows and columns (i.e. reindexing the nodes), this matrix can be rewritten as the block matrix  $M_{6,2}$  given by

$$M_{6,2} = \left[ \begin{array}{ccc|c} \frac{1-2\alpha-6\mu}{9} & \frac{-2+\alpha-3\alpha\mu}{9} & \frac{3\alpha\mu+6\mu-2-2\alpha}{9} & 0_{3 \times 3} \\ \frac{3\alpha\mu+6\mu-2-2\alpha}{9} & \frac{1-2\alpha-6\mu}{9} & \frac{-2+\alpha-3\alpha\mu}{9} & \\ \frac{-2+\alpha-3\alpha\mu}{9} & \frac{3\alpha\mu+6\mu-2-2\alpha}{9} & \frac{1-2\alpha-6\mu}{9} & \\ \hline & 0_{3 \times 3} & & -\frac{1+\alpha}{3} I_{3 \times 3} \end{array} \right], \quad (4.8)$$

which has the same eigenvalues as  $D_{\mathbf{x}}\mathbf{g}|_{\mathbf{x}_{1,2,6}}$ . The upper diagonal block of  $M_{6,2}$  is the same as the Jacobian of the system (3.2) for  $N = 3$ , payoff  $B_{C,3}$  with  $\beta = 0$ , mutation (Q1) and evaluated at equilibrium  $\left[ \begin{array}{ccc} 1/3 & 1/3 & 1/3 \end{array} \right]^T$ . The lower diagonal block is a Hurwitz matrix. Also the two blocks are decoupled, hence the eigenvalues of  $M_{6,2}$  are given by the union of the sets of eigenvalues of each block. A pair of the

eigenvalues crosses the imaginary axis resulting in a Hopf bifurcation for precisely the conditions given in Corollary 3.1 with  $\beta = 0$  and mutation matrix (Q1) (i.e., a critical point  $\mu = \frac{2-\alpha}{6}$  and complex eigenvalue condition  $\alpha \neq \sqrt{3} - 1$ ). In Appendix C.4, we leverage the reindexing and decoupling (as in  $M_{6,2}$ ) to compute the first Lyapunov coefficient for the dynamics and show that the Hopf bifurcations in this case are supercritical.  $\square$

Following the intuition developed from the analysis of the two-cycle dynamics for  $N = 6$  above, and the illustrations in Figure 4.6, we now extend the analysis to general  $N$ . Just as in the  $N = 6$  case, a decoupling in the Jacobian allows us to prove the existence of multiple Hopf bifurcations about the  $d$  fixed points  $\mathbf{x}_{j,d,N}$ . The  $(m, n)$  entry for the Jacobian of the system (3.2) with payoff  $B_{N,d}$  and mutation matrix (Q1) is given by

$$\begin{aligned} [D_{\mathbf{x}} \mathbf{g}]_{mn} &= (2x_n + \alpha x_{n+d}) q_{nm} + \alpha x_{n-d} q_{n-d,m} - x_m [2x_n + \alpha (x_{n-d} + x_{n+d})] \\ &\quad - \left( \sum_{k=1}^N x_k^2 + \alpha \sum_{k=1}^N x_k x_{k+d} \right) \delta_{mn}. \end{aligned} \quad (4.9)$$

Evaluating the Jacobian from (4.9) at the equilibrium  $\mathbf{x}_{j,d,N}$ , and rearranging its rows and columns analogous to (4.8), we obtain the matrix

$$M_{N,d} = \left[ \begin{array}{c|c} A_{N_1 \times N_1} & 0_{N_2 \times N_1} \\ \hline 0_{N_1 \times N_2} & -\frac{1+\alpha}{N_1} I_{N_2 \times N_2} \end{array} \right], \text{ where } N_1 = \frac{N}{d}, N_2 = N - N_1,$$

and  $A$  is the Jacobian of the system (3.2) with payoff  $B_{N_1,1}$  (simple cycle), mutation (Q1) and evaluated at equilibrium  $\mathbf{x}_{1,1,N_1} = \frac{1}{N_1} \mathbf{1}_{N_1} = \mathbf{x}_{mix,N_1}$ .

$M_{N,d}$  has a block diagonal structure with  $N - N_1$  eigenvalues equal to  $-\frac{1+\alpha}{N_1}$ . Its remaining  $N_1$  eigenvalues are given by the eigenvalues of the circulant matrix  $A$ . The Jacobian (4.9) evaluated at each of the  $d$  equilibria  $\mathbf{x}_{j,d,N}$  is similar to  $M_{N,d}$ , hence making the Hopf bifurcation analysis of all of these equilibria equivalent. The matrix  $A$  is precisely the Jacobian studied in §4.1 for the case  $N = N_1$  and  $\beta = 0$ ; hence the existence of Hopf bifurcations follows from Theorem 4.1. The criticality of each of these  $d$  simultaneous Hopf bifurcations of equilibria  $\mathbf{x}_{j,d,N}$  is analogous to the criticality calculations in §4.2 and is computed in Appendix C.4. Corollary 4.2 below summarizes the bifurcation result described above and is the multi-cycle extension to Theorem 4.1. To simplify notation, analogous to (4.4) we set  $[A]_{1n} = \gamma_n + \mu \eta_n$ .

**Corollary 4.2.** *The system (3.2) with payoff matrix  $B_{N,d}$  (with  $N \geq 6$ ,  $d = 1, \dots, N/2$ ,  $d$  a proper divisor of  $N$ ) and mutation matrix (Q1) has  $d$  equilibria  $\mathbf{x}_{j,d,N}$  ( $j = 1, \dots, d$ ) that concurrently undergo  $\lfloor \frac{N-d}{2d} \rfloor$  Hopf bifurcations, with the  $r^{th}$  of such bifurcations located at*

$$\mu_{0,r} = - \left[ \sum_{n=1}^{N/d} \gamma_n \cos \left( \frac{2\pi}{N} (n-1)rd \right) \right] \left[ \sum_{n=1}^{N/d} \eta_n \cos \left( \frac{2\pi}{N} (n-1)rd \right) \right]^{-1}$$

for  $r = 1, \dots, \lfloor \frac{N-d}{2d} \rfloor$ , if  $\alpha > 0$  and  $\mu_{0,r} \neq \frac{\alpha}{2(1+\alpha)}$ .

In this section we have shown the coexistence of multiple stable limit cycles for the dynamics, when the underlying circulant payoff graph topologies have multiple distinct cycles. In the following section we investigate the connections between cycles in the payoff graph topology and limit cycles in the dynamics for more general payoff structures.

## 4.5 Extensions and Generalizations

Studying the fully general model (3.2), even with  $N = 3$  strategies, is highly complex. This complexity motivated our restriction to circulant payoff matrices of the form  $B_{C,N}$  (4.1) and  $B_{N,d}$  (4.6) for the analysis in §4.1 and §4.4. These results might lead one to conclude that the circulant structure of payoff matrix  $B$  is a *necessary* condition for Hopf bifurcations of the dynamics. In this section we illustrate that this is not the case. We show examples of limit cycles for selected noncirculant payoff matrices, first for  $N = 3$  strategies, and then for  $N \geq 4$ . The simulations in this section illustrate a tight connection between the topology of the payoff graphs and the existence of stable limit cycles for the dynamics. In particular, embedded cycles in the payoff graph appear to be necessary for (and often lead to) the existence of limit cycles, and amplitude and frequency of limit cycles appear to be related to symmetries in the graph.

Consider  $3 \times 3$  payoff matrices  $B$  satisfying (3.1) and Condition 3.1 that have directed links of two kinds: strong links with weights  $b$  and weak links with weights  $\epsilon b$  where  $b \in (0, 1)$  and  $0 < \epsilon \ll 1$ . There are 73 corresponding non-isomorphic graph topologies in the set [97]. Figure 4.7 shows stable limit cycles for four topologies in this set corresponding to noncirculant payoff matrices. Each of these topologies has an embedded directed cycle.

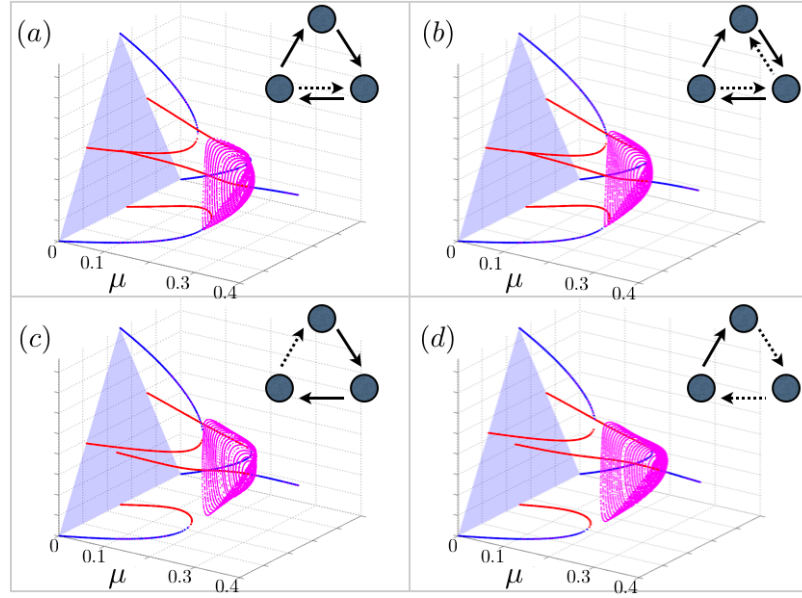


**Figure 4.7:** Limit cycles for noncirculant payoff matrices  $B$ ,  $N = 3$ , and mutation matrix (Q1). The solid arrows in the graphs are strong links with weight  $b$  and the dashed arrows are weak links with weight  $\epsilon b$ . Parameters for all plots are  $b = 0.2$  and  $\epsilon = 0.1$ .

We next look at selected noncirculant payoff topologies with  $N \geq 4$  nodes in Figure 4.8. The bifurcation plots (middle panel in Figure 4.8) are obtained by simulating the dynamics for a range of different values of mutation parameter  $\mu$  and random initial conditions. Stable equilibria are marked blue and limit cycles are marked magenta. Also shown in the right panel of the figure are limit cycle trajectories of the dynamics for specific chosen values of  $\mu$  in the magenta range. The colors of the nodes in the topologies (left panel) match the colors of the corresponding trajectories.

Several interesting features can be observed in the plots in Figure 4.8. In topology (a), the connection between the amplitude of oscillation of a given strategy in the trajectory plot and the location of the corresponding node on the graph is apparent. In particular, the cyan node, which is part of two directed cycles, has a significantly higher oscillation amplitude than the green node, which is part of only one directed cycle. The symmetry of topology (b) about the red node leads to the existence of two stable limit cycle attractors, much like the illustrations in §4.4. On the other hand, topology (c) has two embedded cycles but only one limit cycle attractor for both (Q1) and (Q2) mutation matrices.

In Figure 4.9, we go a little further and consider random payoff graph topologies having strong links with weight  $b$  and weak links with weight  $\epsilon b$ , much like in Figure 4.7. We simulate the dynamics for a set of different random graphs and a range of

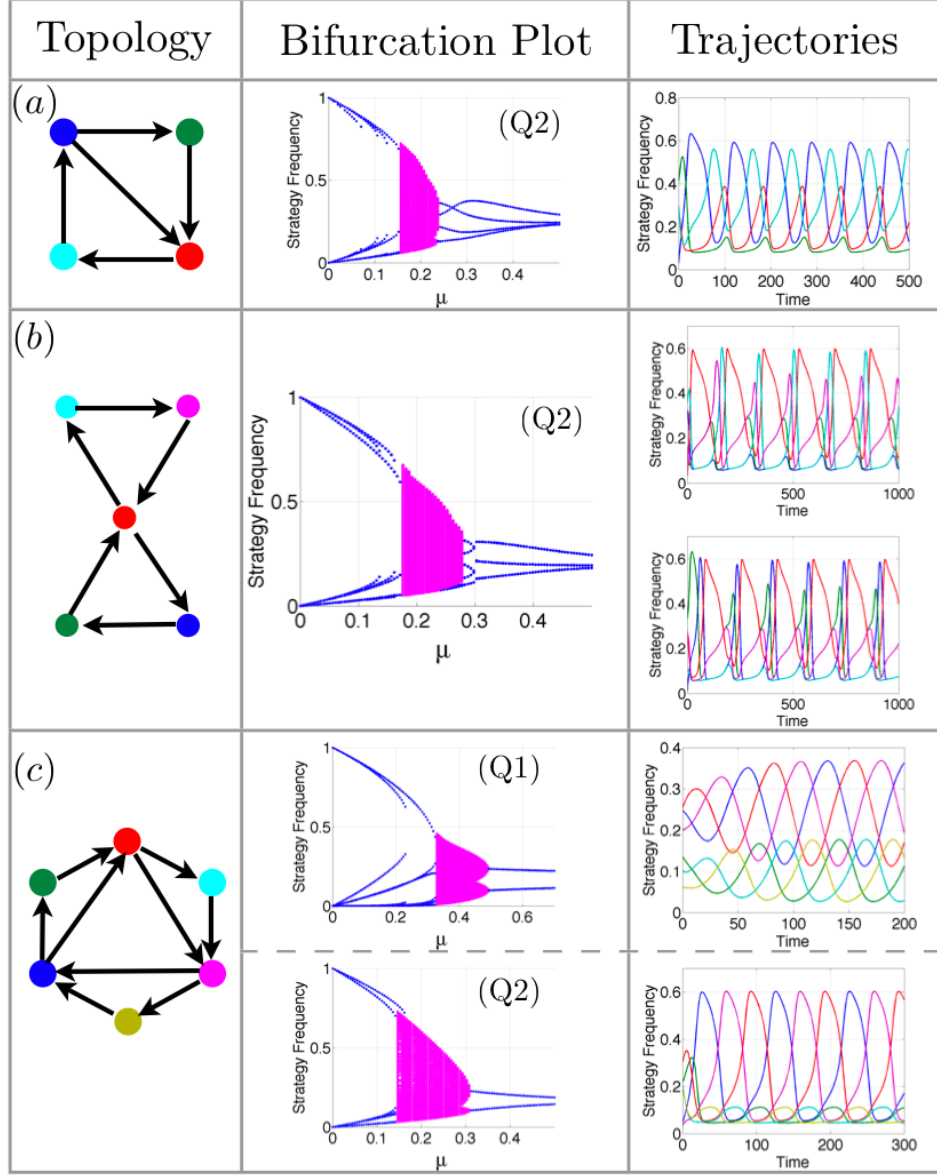


**Figure 4.8:** Limit cycles for the dynamics (3.2) with noncirculant payoff graph topology. The left panel shows the payoff graph; all edges have equal weight  $b = 0.7$ . The center panel shows the bifurcation plot for each topology and mutation matrix (Q1) or (Q2) as indicated. The bifurcation plot is obtained by simulating the dynamics for 120 values of the mutation parameter  $\mu$  in the range shown on the x-axis of each plot. For each  $\mu$ , the dynamics are simulated for 12 randomly chosen initial conditions and the limiting set (stable equilibria or limit cycles) is obtained. Stable equilibria are plotted in blue and limit cycles are plotted in magenta. The right panel shows trajectory plots of the dynamics for a value of  $\mu$  chosen in the magenta (limit cycle) range of the bifurcation plot ( $\mu = 0.2$  in (a), (b) and (c) (Q2);  $\mu = 0.4$  in (c) (Q1)). The colors of each trajectory match the colors of the nodes on the corresponding payoff graph. For topology (b), the two trajectory plots correspond to different initial conditions.

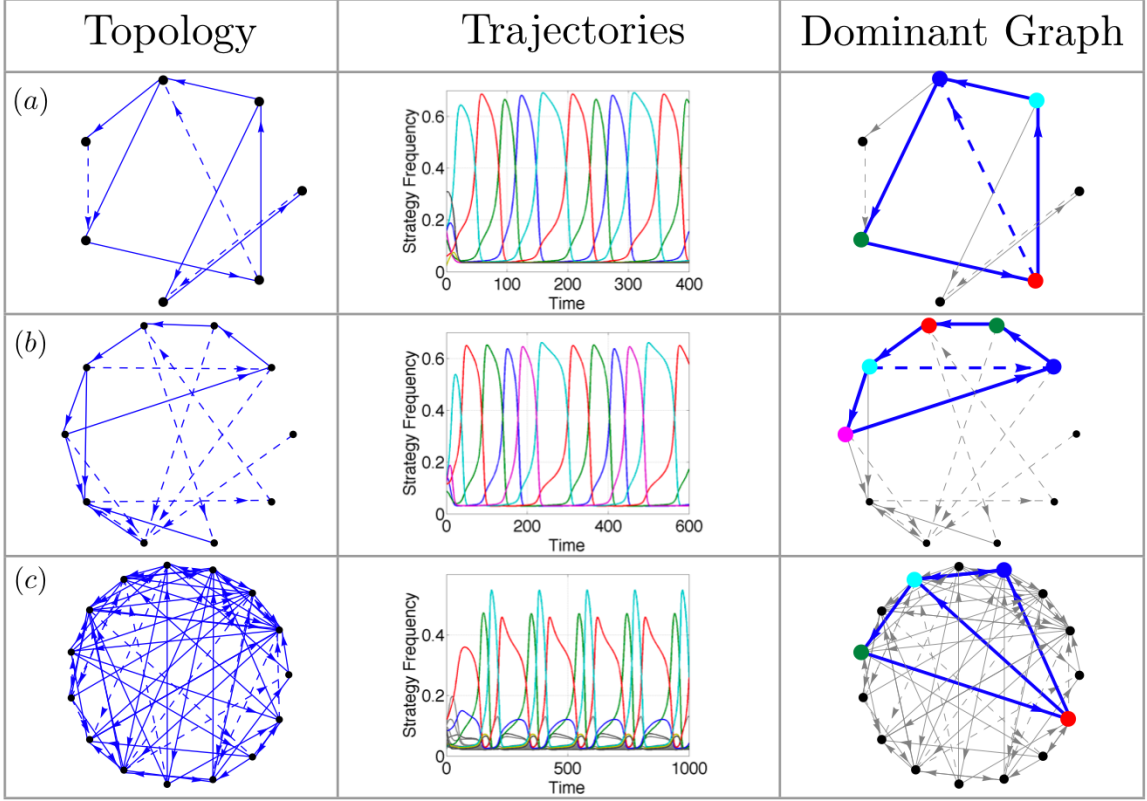


**Figure 4.9:** Limit cycles for the dynamics (3.2) with random payoff graphs. The left panel shows the payoff graph with two types of edges: strong edges (solid lines) with a weight of  $b$  and weak edges (dashed lines) with a weight of  $\epsilon b$ ; here  $b = 0.7$  and  $\epsilon = 0.1$ . The center panel shows the resulting trajectories with mutation (Q2) and suitable  $\mu$  (0.2 in (a), 0.25 in (b) and 0.27 in (c)). The right panel highlights the interconnection between nodes corresponding to the dominant components of the limit cycle trajectories. The color of each of the nodes on the payoff graph matches the color of the corresponding trajectory in the center panel. In each case, it is observed that there is a directed cycle between the dominant component nodes.

values for the mutation parameter  $\mu$ , and focus specifically on graphs and parameters that induce a limit cycle oscillation for the dynamics. We show three such examples in Figure 4.9. For each set of simulated limit cycle trajectories, the dominant components are obtained; dominant components are defined as those having a relatively high oscillation amplitude, or correspondingly a trajectory with standard deviation above a set threshold. The main observation we make here is that the existence of limit cycles for the dynamics is tied to the existence of a directed cycle between nodes of the payoff graph. In all our simulations of random graphs, for both mutation matrices (Q1) and (Q2), we consistently find that the dominant components of stable limit cycles correspond to the existence of at least one directed cycle between the

corresponding nodes of the payoff graph, as illustrated in the right panel of Figure 4.9.

The purpose of the simulations in this section is to illustrate that one can break symmetry in the payoff graph significantly (as compared to the modest symmetry breaking that yields the circulant structures analyzed in this chapter) and still obtain stable limit cycles for the dynamics, even in the case of random graph topologies, as long as the topologies have at least one embedded cycle. In addition to limit cycles, the dynamics can also have chaotic attractors as found in [74, 76]. We have not seen chaotic attractors for the payoff topologies and mutation matrices (Q1) and (Q2) studied in this chapter; we conjecture that alternative mutation models such as the one used in [76] will exhibit chaotic dynamics.

## 4.6 Final Remarks

Much of the existing analysis of the replicator-mutator dynamics has been focused on stable equilibria. The analysis in the literature has also primarily considered payoff and mutation matrices that are symmetric, which correspond to undirected payoff graph topologies. Recent work [60] on a graph theoretic model of language dynamics has shown that the graph connectivity plays a critical role in determining the location of bifurcation points in the dynamics, but the restriction to undirected graphs confines the range of limiting behavior to stable equilibria. In [76], it is shown that considering asymmetric payoff and mutation matrices (corresponding to directed graphs) can yield limit cycle behavior and even chaos for replicator-mutator dynamics.

Here we have proved conditions guaranteeing stable limit cycles in the replicator-mutator dynamics. These arise as a consequence of Hopf bifurcations for  $N \geq 3$  strategies and for circulant payoff matrices. From a graph perspective, we showed how breaking symmetry by considering directed graphs allows for oscillatory limiting behavior. We emphasize that the limit cycles are not restricted to circulant payoffs, but can exist for noncirculant payoffs as shown in §4.5. The simulations in §4.5 illustrate the connection between embedded directed cycles in the payoff graph and the existence of stable limit cycles for the dynamics. A Hopf bifurcation analysis of these more general cases is an intended future direction. We will also explore the effects of the structure of the mutation matrix, beyond (Q1) and (Q2) considered here, as a step towards understanding the transition to chaos illustrated in [76]. Further directions of future research, including applications to the design of decision-making protocols in multi-agent robotic systems, are discussed in Chapter 8.

# Chapter 5

## Evolutionary Dynamics of Collective Migration

Collective migration is a ubiquitous natural phenomenon common in a number of species including birds, fish, invertebrates and mammals [119, 42, 22, 6]. The migratory process is often an adaptive response to conditions such as competition for resources in a dynamic environment, seasonal variability, and selection of new habitats for breeding, for example [132, 119]. Animals perform such migratory tasks by leveraging a variety of environmental cues such as nutrient and thermal gradients, magnetic fields, odor cues, or visual markers [132, 30, 140, 133]. Measuring these stochastic environmental signals is complicated and requires the investment of time and energy, as well as the development of necessary physiological and sensory machinery such as vision in insects and vertebrates [42] and chemical signaling in bacteria [136]. Along with environmental cues, animals migrating collectively also have the ability to leverage social information from neighbors in the group [15]. One way of doing so is by imitating invested neighbors (via consensus processes such as attraction and alignment of heading) and thereby effectively achieving good migratory performance, without paying the measurement and processing cost. The interplay between costly information acquisition from the environment and relatively less expensive social information from the group raises two pertinent questions regarding leadership and social interactions in migratory populations.

The first question relates to the migratory performance of large groups in the presence of a limited number of leaders, i.e., can a subset of informed leaders effectively lead a large group? The authors in [14] address this question using individual-based simulations (involving attraction, repulsion and alignment between individuals) and demonstrate that in a group of socially interacting individuals, a small fraction of

informed leaders can effectively determine the direction of travel of a large group of uninformed followers. Further, they show that for a fixed fraction of leaders, the accuracy of group direction improves with increasing group size.

The second question relates to the evolution of leadership in collective migration, i.e., under what conditions is the coexistence of invested leaders and social followers stable in an evolutionarily sense? This question is especially pertinent when the cost of investing in signal acquisition is sufficiently high; followers can leverage the investments made by leaders via social interactions, without paying the investment costs. In a recent paper [33] (also see related commentary [120]), the authors address this question using an individual-based model (similar to [14]) and evolutionary simulations, and show that under certain conditions, the specialization of groups into coexisting leaders and followers (also known as branching or speciation) is a stable evolutionary outcome.

Individual-based bio-inspired models such as those used in [14, 33] provide important insights about the relevant biological processes being modeled, but are challenging to analyze. In particular, it can be difficult to ascertain what aspects of the low-level interactions (social network topology, cost functions, movement dynamics, etc.) are most critical to the observed high-level behavior of interest (evolution of leadership for example). This analysis can be done more effectively by constructing appropriate simpler (lower-dimensional) models that capture the relevant high-level behavior, while also being tractable for analysis. In [132], the authors construct one such lower-dimensional mean-field approximation to the evolutionary model studied in [33], and using tools from evolutionary adaptive dynamics [25, 26] prove conditions for the branching of a migrating population into leader and follower groups.

While simpler models have the advantage of analytical tractability, this comes at the cost of abstracting some potentially important features of the corresponding detailed model. In the case of the migration model in [132], the mean-field approach effectively prescribes an all-to-all social interaction topology between the individuals in order to reduce dimensionality; this ignores the potentially important role of limited social interactions. Indeed, it has been shown [98, 151, 3, 10] that network topology plays a critical role in determining outcomes in biological as well as robotic collectives.

In this chapter, we design a model to study the evolution of collective migration that is explicitly dependent on the social interaction graph topology. We present a comprehensive analysis of the all-to-all limit of the model, recovering the speciation results of the mean-field analysis in [132], and demonstrating the hysteretic effect associated with recovering lost migration ability described in [33, 34]. We then go

on to study the effect of topology on the evolutionary model, and show a minimum social connectivity threshold necessary for the evolution of leadership in migration.

Our evolutionary model has two timescales. The fast timescale corresponds to the stochastic migration dynamics and individual fitness computations as a consequence of migratory performance. The slow timescale corresponds to the evolutionary dynamics of the population and changes in population strategy distribution as a consequence of replication and mutation. A key advantage of our model is that it allows for analytically computing fitness on the fast timescale by solving a set of coupled linear equations. For the detailed model in [33], the fitness computation requires extensive Monte-Carlo simulations using agent-based models. On the other hand, the detailed model has the advantage of incorporating a time-varying social interconnection topology between individuals, which eventually results in *fission-fusion* spatial dynamics (where groups constantly merge and split) described in [33]; the model studied in this chapter assumes a time-invariant social interaction graph for fitness computation. In ongoing work on generalizing the model presented here to time-varying graphs, we intend to investigate the observed fission-fusion result of the detailed model.

There is significant recent interest in understanding the mechanisms of interaction, signal processing and information transfer in evolved natural collectives in order to design better algorithms for collective motion and decision-making in robotic groups [128, 98, 66, 142]. Robotic collectives often have resource constraints (analogous to the measurement and processing cost for migration tracking), operate in dynamic and stochastic environments, and interact with neighbors on some networked graph topology. In Section 5.4, we consider the migration model from this multi-agent robotic perspective and study a simple model of adaptive dynamic nodes on a network. We illustrate the critical role that the structure of the interaction graph plays in determining the location of leaders (highly invested nodes) in the adaptive network and in bifurcations in the nodal dynamics as a function of increasing cost.

The outline of this chapter is as follows. In Section 5.1 we present our graph-dependent evolutionary migration model and study its all-to-all limit in Section 5.2. We study evolutionary dynamics with limited interconnection in Section 5.3 and focus on adaptive dynamic nodes in small networks in Section 5.4.

## 5.1 Model Description

Our model is derived from the mean-field migration model in [132] with two key modifications; we explicitly account for a limited social interaction graph topology

in the dynamics and we introduce a slightly modified social noise model to allow for analytical fitness computations as a function of graph topology and individual investments, as described below.

Consider a set of  $N$  agents indexed by  $i \in \{1, \dots, N\}$  that each intend to control their direction of migration represented by a stochastic scalar variable  $x_i \in \mathbb{R}$ , thereby tracking some desired ‘true’ direction  $\mu \in \mathbb{R}$  with high fidelity. Accurate tracking of the desired direction  $\mu$  over time may correspond to benefits such as improvement in environmental conditions for foraging, predator evasion, early access to breeding grounds, etc. Following [132], the stochastic dynamics of each agent are given by

$$dx_i = k_i dx_{Di} + (1 - k_i) dx_{Si}, \quad (5.1)$$

where  $dx_{Di}$  and  $dx_{Si}$  are the driven tracking and social consensus stochastic processes respectively.  $k_i \in [0, 1]$  is an adaptive parameter that tunes the level of investment made by agent  $i$  in the driven and social processes.  $k_i = 1$ , for example, corresponds to an individual  $i$  fully invested in the tracking process and ignoring social information from neighbors, while  $k_i = 0$  corresponds to the individual exclusively leveraging social information without tracking the environmental signal. The  $k_i$ ’s are the adaptive evolutionary parameters in the simulations and analysis in the sections to follow.

The driven process  $dx_{Di}$  is modeled as an Ornstein-Uhlenbeck stochastic process [137, 24] of the form

$$dx_{Di} = -k_{Di}(x_i - \mu)dt + \sigma_D dW_{Di}. \quad (5.2)$$

Here, the parameter  $k_{Di} \geq 0$  corresponds to the gain associated with tracking,  $\sigma_D^2 > 0$  is the noise intensity associated with measuring the environmental signal  $\mu$ , and  $dW_{Di}$  represents the standard Wiener increment. For  $k_{Di} > 0$ , the process (5.2) has a steady-state mean and variance given by

$$E[x_i] = \mu, \quad E[(x_i - \mu)^2] = \frac{\sigma_D^2}{2k_{Di}}. \quad (5.3)$$

Higher values of tracking gain  $k_{Di}$  result in lower steady-state variance in migration direction  $x_i$ , which corresponds to improved tracking. Figure 5.1 shows the spatial dynamics of migrating agents with driven process (5.2) and varying levels of investment  $k_{Di}$ , illustrating the effect of increasing investment on improved tracking performance.

We use basic tools from graph theory [111, 91, 47] (see also §2.3) to model the social consensus process. Individuals are modeled as nodes on a directed social inter-

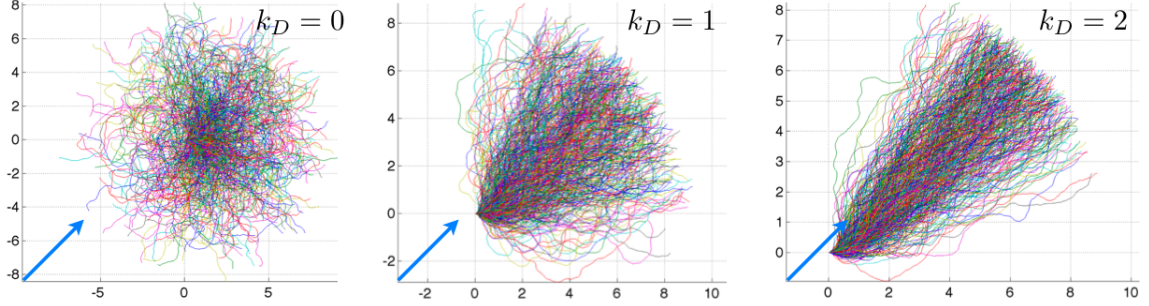


**Figure 5.1:** Migratory performance as a function of investment  $k_D$ . Agents are modeled as steered particles with constant speed, headings  $x_i$  given by (5.2), and starting at the origin with random orientations. Each plot shows 500 trajectories with agents each having the same value of investment  $k_{Di} = k_D$  as indicated and noise parameter  $\sigma_D = 1$ . The blue arrow shows the desired direction of migration  $\mu$ . Increasing investment  $k_D$  results in improved tracking performance as agent trajectories track the blue arrow  $\mu$  more effectively.

connection graph with adjacency matrix  $A = [a_{ij}] \in \mathbb{R}^{N \times N}$ . A directed edge in the graph from individual  $i$  to individual  $j$  is read as ‘ $i$  can sense  $j$ ’. Let  $\mathcal{N}_i$  denote the set of neighbors of individual  $i$  (i.e., the set of agents that individual  $i$  can sense), and  $\|\mathcal{N}_i\|$  denote the cardinality of this set (number of neighbors). For the social model in this work, we assume that agents weight their neighbors equally by distributing a total weight normalized to 1. This corresponds to the adjacency matrix

$$a_{ij} = \begin{cases} 0 & \text{if } i = j \\ \|\mathcal{N}_i\|^+ & \text{if } i \neq j, \end{cases} \quad (5.4)$$

where  $\|\mathcal{N}_i\|^+$  is the pseudoinverse of  $\|\mathcal{N}_i\|$  ( $\|\mathcal{N}_i\|^+ = 0$  when  $\|\mathcal{N}_i\| = 0$ ,  $\|\mathcal{N}_i\|^+ = 1/\|\mathcal{N}_i\|$  otherwise). The Laplacian matrix of the graph corresponding to the adjacency matrix  $A$  is given by  $L = \text{diag}(A\mathbf{1}) - A$ , where  $\mathbf{1}$  is a vector of ones of appropriate dimension. In subsequent sections we use the terms individual or node/agent, and population or network, interchangeably.

The social consensus process  $dx_{Si}$  is dependent on the social interaction graph Laplacian  $L$ , the gain associated with the social process  $k_{Si} \geq 0$ , and the noise associated with measuring the social signal  $\sigma_{Si} > 0$  as follows:

$$dx_{Si} = -k_{Si}L_i\mathbf{x}dt + \sigma_{Si}dW_{Si}. \quad (5.5)$$

In the social process (5.5),  $dW_{Si}$  is the standard Wiener increment, and  $L_i$  denotes the  $i^{\text{th}}$  row of the Laplacian matrix  $L$ . Let  $\mathbf{x}$  be the vector of individual directions  $x_i$ . Then  $L_i \mathbf{x} = \|\mathcal{N}_i\|^+ \sum_{j \in \mathcal{N}_i} (x_i - x_j)$ .

Following the setup in [132], we make a simplification to reduce the parameter space to one dimension by assuming that the gains are proportional to the relative investments in each process, i.e.,  $k_{Di} = k_i$  and  $k_{Si} = 1 - k_i$ . Substituting this simplification in (5.2), (5.5) and (5.1) we have

$$\begin{aligned} dx_i &= k_i dx_{Di} + (1 - k_i) dx_{Si} \\ &= -k_i^2(x_i - \mu)dt - (1 - k_i)^2 L_i \mathbf{x} dt + \sqrt{k_i^2 \sigma_D^2 + (1 - k_i)^2 \sigma_{Si}^2} dW_i. \end{aligned} \quad (5.6)$$

In order to simplify the notation we make a coordinate transformation and define the normalized direction  $\tilde{x}_i$  as

$$\tilde{x}_i = \frac{x_i - \mu}{\sigma_D}, \text{ and correspondingly } \tilde{\mathbf{x}} = \frac{\mathbf{x} - \mu \mathbf{1}}{\sigma_D}. \quad (5.7)$$

Substituting the transformation (5.7) in (5.6) and observing that  $L_i \mathbf{1} = 0$  we have the normalized dynamics

$$d\tilde{x}_i = -k_i^2 \tilde{x}_i dt - (1 - k_i)^2 L_i \tilde{\mathbf{x}} dt + \sqrt{k_i^2 + (1 - k_i)^2 \frac{\sigma_{Si}^2}{\sigma_D^2}} dW_i. \quad (5.8)$$

The social noise term  $\sigma_{Si}$  reflects the difficulty that agents have in extracting social information gained from interactions with neighbors. In [132], it is assumed that this difficulty (magnitude of  $\sigma_{Si}$ ) decreases as the ordering or coherence of the population increases. Here we take a slightly different local (and graph dependent) approach and relate the social noise term for an individual agent to the average investment of the neighbors of that agent (i.e. average magnitude of parameter  $k_j, j \in \mathcal{N}_i$ ). Specifically, agents that interact socially with neighbors having a high level of investment, have a correspondingly lower social noise term, and are hence better able to extract social information from their neighbors. The specific relationship can take many forms, but for simplicity we use a linear relationship between the ratio  $\sigma_{Si}^2/\sigma_D^2$  and the average neighborhood investment,

$$\frac{\sigma_{Si}^2}{\sigma_D^2} = \beta^2(1 - k_{nbhd,i}), \quad (5.9)$$

where  $k_{nbhd,i}$  is the average value of the investment made by the neighbors of agent  $i$  and  $\beta^2$  is a social noise scaling parameter. In vector form,  $\mathbf{k}_{nbhd} = A\mathbf{k}$ .

The stochastic system (5.8) can be written compactly in matrix form as

$$d\tilde{\mathbf{x}} = -(K_1 + K_2 L)\tilde{\mathbf{x}} dt + S d\mathbf{W}, \quad (5.10)$$

where the diagonal matrices  $K_1$ ,  $K_2$  and  $S$  are given by  $K_1 = \text{diag}(k_i^2)$ ,  $K_2 = \text{diag}((1 - k_i)^2)$  and  $S = \text{diag}\left(\sqrt{k_i^2 + \beta^2(1 - k_i^2)(1 - k_{\text{nbhd},i})}\right)$ .

As discussed in [33, 132], the long-term migratory performance of an individual with dynamics (5.8) can be computed by projecting the steady-state distribution of directions  $x_i$  in the desired direction of migration  $\mu$ . This quantity is given by  $\exp\left(\frac{-\sigma_{ss,i}^2}{2}\right)$ , where  $\sigma_{ss,i}^2$  is the steady-state variance of  $x_i$ , and corresponds to the expected migration speed of an individual  $i$  in the desired direction  $\mu$ . The fitness or utility of an agent as a function of the steady state migratory performance and the level of investment  $k_i$  is defined in [33, 132] as

$$F_i = \exp\left(\frac{-\sigma_{ss,i}^2}{2}\right) \exp(-ck_i^2), \quad (5.11)$$

where the second term of the fitness function models the cost associated with investment in tracking with a scaling cost parameter  $c > 0$ . The choice of cost function (5.11) is not unique; the multiplicative exponential form is chosen for analytical tractability. Simulations in [132, 33] show that reasonable variations of fitness function yield qualitatively comparable results. The saturating form of the performance function  $\exp\left(\frac{-\sigma_{ss,i}^2}{2}\right)$  as a function of investment can be interpreted as modeling the diminishing returns of increasing investment. Further, the quadratic form of the cost  $ck_i^2$  implies that higher investments in the driven process are increasingly costly. In the absence of any social interactions, the optimal strategy for solitary migrating individuals can be found by maximizing (5.11) with respect to  $k_{Di}$  resulting in

$$k_{D,opt} = \sqrt[3]{\frac{\sigma_D^2}{8c}}. \quad (5.12)$$

While disconnected individuals adopt the optimal strategy from (5.12), the presence of social interactions between individuals dramatically alters this picture; along with having the ability to invest in measuring the environmental signal, migrating individuals can leverage relatively less expensive social information available from neighbors by effectively imitating or flocking with their neighbors. We explore this dynamic in the sections to follow.

## 5.2 Evolutionary Dynamics in the All-to-all Limit

As a first step in analyzing the social migration model (5.10), we consider the limit of all-to-all interconnection ( $a_{ij} = \frac{1}{N-1}$  for all  $i \neq j$  in (5.4)) in a large population (labeled the *resident* population with subscript  $R$ ), with all individuals having a common level of investment  $k_R > 0$ . This limit corresponds to the mean-field dynamics analyzed in [132]. By the law of large numbers, the average direction of population migration in the limit of large  $N$  is the same as the desired migration direction  $\mu$  after the decay of transients (i.e., in steady-state,  $\lim_{N \rightarrow \infty} L\mathbf{x} = \mathbf{x} - \mu\mathbf{1}$ ). Substituting  $L\tilde{\mathbf{x}} = \tilde{\mathbf{x}}$  in (5.10), the dynamics of an individual in the population are given by

$$d\tilde{x}_R = -[k_R^2 + (1 - k_R)^2] \tilde{x}_R dt + \sqrt{k_R^2 + \beta^2(1 - k_R)^3} dW. \quad (5.13)$$

The corresponding steady-state variance of an individual's direction is given by

$$\sigma_{ss,R}^2 = \frac{k_R^2 + \beta^2(1 - k_R)^3}{2[k_R^2 + (1 - k_R)^2]}, \quad (5.14)$$

with steady-state migration speed (performance) given by  $\exp(-\sigma_{ss,R}^2/2)$ . In Figure 5.2 we plot this steady-state migration speed as a function of investment  $k_R$  for varying social noise term  $\beta$ . As defined in Equation (5.9), the parameter  $\beta$  reflects

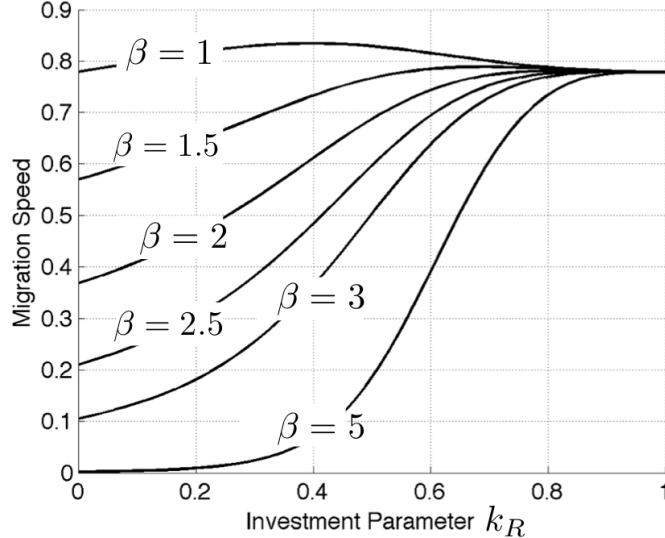


**Figure 5.2:** Steady-state migration speed as a function of resident population investment parameter  $k_R$  and noise parameter  $\beta$  for a large population with all-to-all interconnection and common investment  $k_R$ .

the strength of the noise from social interactions relative to the noise associated with the tracking process. In Figure 5.2 we see that the migration performance saturates at high levels of investment  $k_R$ , and remains low over greater  $k_R$  ranges, for large  $\beta$ . We use  $\beta > 2$  in this work to model noisier social interactions relative to tracking (consistent with [132]); this provides an incentive for individuals to invest in the tracking process.

Now consider the evolution of strategies for such an all-to-all connected population. A key part of any evolutionary algorithm is the computation of fitness of individuals in the population as a function of strategy distribution, model parameters, environmental conditions, and other such features. In certain cases (such as the all-to-all limit here), fitness can be analytically computed, which allows for an explicit calculation of the outcomes of the evolutionary process using tools from adaptive dynamics [25, 26, 18]. Adaptive dynamics are well-suited for studying the evolution of a continuous one-dimensional trait in a population undergoing small mutations (see §2.1 for a detailed discussion).

### 5.2.1 Adaptive Dynamics Calculations

Using (5.14) and (5.11), the fitness of an individual in the resident population with dynamics (5.13) is given by

$$F_R(k_R) = \exp\left(-\frac{k_R^2 + \beta^2(1 - k_R)^3}{4(2k_R^2 - 2k_R + 1)} - ck_R^2\right). \quad (5.15)$$

Consider a small population of mutants with strategy  $k_M$  interacting with each other and with all the residents. The mutants (owing to their small numbers) will experience the same social noise as the residents so that they have dynamics given by

$$d\tilde{x}_M = -[k_M^2 + (1 - k_M)^2] \tilde{x}_M dt + \sqrt{k_M^2 + \beta^2(1 - k_R)(1 - k_M)^2} dW. \quad (5.16)$$

Correspondingly, the fitness of individuals in the mutant population is given by

$$F_M(k_R, k_M) = \exp\left(-\frac{k_M^2 + \beta^2(1 - k_R)(1 - k_M)^2}{4(2k_M^2 - 2k_M + 1)} - ck_M^2\right). \quad (5.17)$$

The relative fitness of the mutant strategy in the environment of the resident is known as the differential fitness and is given by (2.3),

$$S(k_R, k_M) = F_M(k_R, k_M) - F_R(k_R). \quad (5.18)$$

The two-dimensional function  $S$  allows us to predict which mutant strategies can invade a particular resident population. For example, for a given resident strategy  $k_R$ , the values of  $k_M$  that result in  $S > 0$  correspond to the mutant strategies that when rare can invade the established resident population. Further, a study of the selection landscape  $S$  can help us predict when we can expect to see an evolutionarily stable monomorphic population (all individuals having the same strategy) and when we can expect to see opportunities for branching in evolutionary simulations (resulting in leader ( $k_i \approx 1$ ) and follower ( $k_i \approx 0$ ) populations) as we vary the cost  $c$  associated with strategy investment.

The evolutionary dynamics of the resident strategy  $k_R$  are given by (2.4), where  $g(k_R)$  is the selection gradient (note that the timescale  $t$  associated with (2.4) corresponds to slow evolutionary time and is different from the fast timescale associated with the stochastic migrations dynamics (5.10) and (5.13)). For the differential fitness  $S$  defined in (5.18), (5.15) and (5.17), singular strategies  $k_*$  (defined as  $g(k_*) = 0$ ) are given by the solutions to the polynomial equation (details in Appendix D)

$$k_* [\beta^2(1 - k_*) - 1] (k_* - 1) + 4ck_*(2k_*^2 - 2k_* + 1)^2 = 0. \quad (5.19)$$

A singular strategy  $k_*$  is known as a Convergent Stable Strategy (CSS) if it is locally asymptotically stable for the dynamics (2.4), which is equivalent to satisfying the condition (2.5). As discussed in §2.1, a CSS strategy  $k_*$  can be either locally evolutionary stable (local ESS) for the population, or can be a branching opportunity where the population speciates. For  $S$  defined in (5.18), the branching condition (2.6) evaluates to (details in Appendix D)

$$0 < k_* < \frac{5 - \sqrt{7}}{6} \approx 0.3923. \quad (5.20)$$

The branching condition in (5.20) is exactly the same as that obtained in [132] (Equation (18)). Parameters  $\beta$  and  $c$  that yield CSS singular strategies  $k_* \in \left(0, \frac{5-\sqrt{7}}{6}\right)$  result in speciated populations via evolutionary branching.

### 5.2.2 Adaptive Dynamics Results

The bifurcation diagram in Figure 5.3 summarizes the singular strategy condition (5.19), CSS condition (2.5) and branching condition (5.20) to obtain four distinct sets of evolutionary outcomes (in ranges A, B, C and D) for our model for increasing cost parameter  $c$  (calculations in Appendix D):

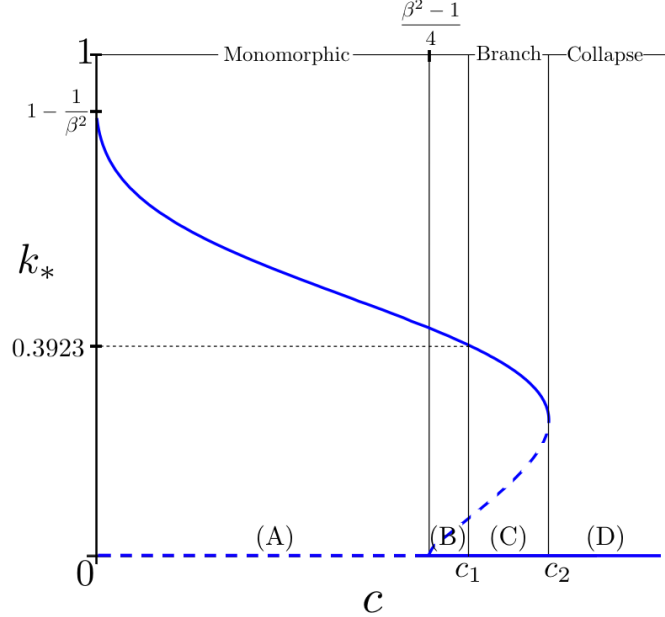


**Figure 5.3:** Evolutionary singular strategies  $k_*$  as a function of cost parameter  $c$ . The two sets of singular strategies defined by (5.19) are plotted in blue. One set corresponds to  $k_* = 0$  and the other corresponds to the curve given by the equation  $c = \frac{(1-k_*)(\beta^2(1-k_*)-1)}{4(2k_*^2-2k_*+1)^2}$ . Solid curves are CSS strategies, and dashed curves are unstable singular strategies. The regions marked (A)-(D) correspond to the descriptions in the text. Analytical derivations for the cost parameters  $\frac{\beta^2-1}{4}$ ,  $c_1$  and  $c_2$  that divide the regions are given in Appendix D.

- (A) Monomorphic: For  $0 < c < \frac{\beta^2-1}{4}$  there exists only one CSS strategy. This strategy is also evolutionarily stable (evolutionary stability since  $k_* > \frac{5-\sqrt{7}}{6}$ ), resulting in a monomorphic population with strategy  $k_*$ . The  $k_* = 0$  singular strategy is not convergent stable.
- (B) Two local CSS's that are each evolutionarily stable: For  $\frac{\beta^2-1}{4} < c < c_1$  there exist two convergent stable strategies, one of which is the fully social strategy  $k_* = 0$ . Both singular strategies are locally evolutionarily stable.  $c_1$  is defined implicitly as the solution to the equation  $g(\frac{5-\sqrt{7}}{6}) \Big|_{c=c_1} = 0$ .
- (C) Branching: For  $c_1 < c < c_2$  the convergent stable interior ( $k_* \in (0, 1)$ ) singular strategy satisfies the branching condition (5.20) resulting in the speciation of the population.
- (D) Collapse of Migration:  $c > c_2$  represents the high cost scenario in which the only singular strategy that exists is the convergent stable fully social strategy  $k_* = 0$  and the population does not develop any migration ability.

These four cases constitute a comprehensive picture of the evolutionary dynamics of the migration model (5.10) in the all-to-all limit, and encompass key features of the branching calculations in [132] and evolutionary simulations in [33]. The existence of two locally evolutionary stable attractors in case (B) above implies that the evolutionary dynamics can potentially yield speciated outcomes in the population without evolutionary branching (case (C)). We illustrate this using simulations in §5.2.3.

A hysteretic effect associated with restoring population migration ability once destroyed is apparent in Figure 5.3. In particular, once migration ability in the population is lost for high cost parameter  $c > c_2$ , the cost parameter needs to be reduced below the level  $\frac{\beta^2 - 1}{4}$  ( $c_1 < c_2$ ) for migration ability to be regained. This compares to the simulations in [33, 34] where agent-based models are used to study the effect of habitat fragmentation on the evolution of migration. In these simulations, the authors study the impacts of progressively more fragmented habitats on migratory outcomes, and show that once migration ability is lost for a threshold level of fragmentation, much greater habitat recovery is necessary to restore lost migration ability (a hysteretic effect). Higher levels of habitat fragmentation are comparable to higher cost parameter  $c$ .

### 5.2.3 Evolutionary Simulations\*

In Figure 5.4 we show the pairwise invasibility plots (PIPs) [25, 26, 18] (see Figure 2.3 in §2.1 for a description) of the differential fitness  $S(k_R, k_M)$  for increasing cost  $c$  to illustrate the four sets of outcomes described above. These plots show the sign of  $S$  as a function of the resident and mutant population strategies. Dark regions correspond to differential fitness  $S > 0$  and allow mutant invasions; white regions correspond to  $S < 0$  and prohibit mutant invasions. Comparing the PIPs from Figure 5.4 to the canonical classes of PIPs in Figure 2.3, we see conditions for an initially monomorphic population for low values of cost parameter  $c$ , a branching speciated solution for intermediate values of  $c$ , and for high values of  $c$  we see conditions that prevent individuals from developing any significant investment, i.e., the population is unable to develop any significant migration ability.

We confirm our predictions from the adaptive dynamics analysis by running evolutionary simulations in the case of a monomorphic initial condition and also a uniformly randomly distributed initial condition as shown in Figure 5.4 (bottom two rows). These simulations comprise the roulette-wheel selection and small mutation

---

\*Results from this subsection were presented at the SIAM Conference on Applications of Dynamical Systems, Snowbird, UT, 2011.

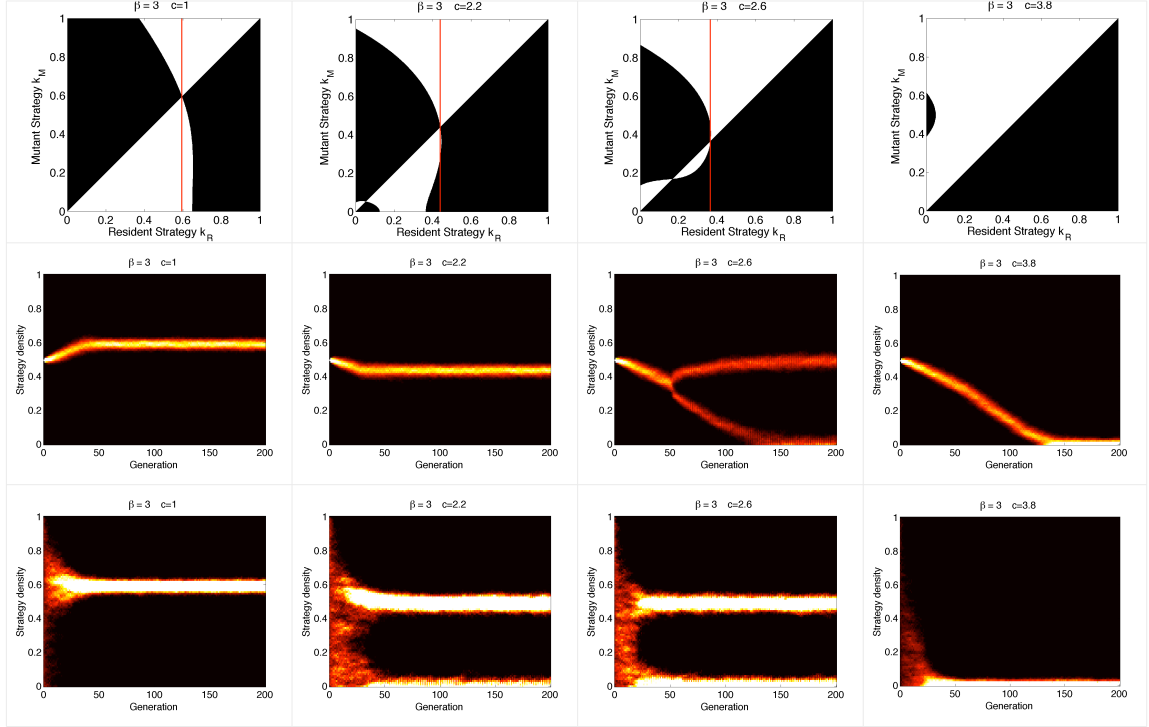


**Figure 5.4:** Evolutionary dynamics for the migration model with all-to-all interconnection, noise parameter  $\beta = 3$ , and with increasing cost parameter  $c$  as indicated in each column. The top row shows the pairwise invasibility plots. Black regions correspond to differential fitness  $S(k_R, k_M) > 0$  (mutants can invade) and white regions to  $S < 0$ . The red vertical lines pass through convergent stable interior strategies  $k_R = k_*$ . The middle row of plots are evolutionary simulations starting with a monomorphic population with strategy  $k = 0.5$ ; hot colors correspond to high population density. The bottom row of plots are also evolutionary simulations, but having an initial population with a uniformly randomly distributed strategy  $k \in [0, 1]$ . We use  $N = 2000$  individuals for these simulations; corresponding to  $\beta = 3$ , boundary cost parameters from Figure 5.3 are  $c_1 = 2.48$  and  $c_2 = 2.77$ .

operations on each generation of a population of  $N = 2000$  individuals with all-to-all social graph, dynamics (5.10), and fitness (5.11).

The columns in Figure 5.4 from left to right correspond to the cases (A)-(D) respectively. In case (A), both initial conditions result in a monomorphic evolutionary outcome. In case (B), the polymorphic solution for the evolutionary simulation with random initial conditions (Column 2, last Row) is a consequence of the stability of the  $k_* = 0$  singular strategy, and not as a consequence of branching, as in case (C). Case (D) corresponds to the collapse of migration with all individuals having an insignificant level of investment.

The analysis in this section shows the range of evolutionary outcomes for the migration model with all-to-all social interconnection. We are particularly motivated by conditions that result in the speciation or branching of the population into invested leaders and social followers. In the following section we study the role that limited social interconnection topology plays in the emergence of this evolutionary branching.

### 5.3 Evolutionary Dynamics with Limited Social Interactions<sup>†</sup>

In this section we study the role that graph topology plays in the evolutionary dynamics of the migration model (5.10). While the all-to-all topology assumption of §5.2 allows for a detailed analysis of the evolutionary dynamics in a large population, it is unrealistic for most biological and decentralized artificial systems. In §5.3.1, we relax the all-to-all assumption and study the migration model (5.10) with limited interconnection. We prove two main results. Theorem 5.1 provides necessary and sufficient conditions for a population with limited interconnections to develop the ability to migrate. Theorem 5.2 presents an analytical technique for computing migratory performance (solution to fast timescale dynamics) as a function of interconnection topology and individual node investments.

In §5.3.2 we utilize the analytical fast timescale calculation from Theorem 5.2 to simulate evolutionary dynamics for three classes of limited interconnection topologies: undirected ring lattices, undirected random graphs, and directed random graphs. In each case, the simulations show a minimum connectivity threshold necessary for speciated evolutionary outcomes in the population.

#### 5.3.1 Fast Timescale Results

As we will see in Theorem 5.2, the steady-state probability distribution of the state  $\tilde{\mathbf{x}}$  for the migration dynamics (5.10) exists if and only if the zero equilibrium of the noise-free form of the dynamics (5.10) are asymptotically stable. The noise-free form of the dynamics (5.10) are given by

$$\dot{\tilde{\mathbf{x}}} = M\tilde{\mathbf{x}}, \text{ where } M = -(K_1 + K_2L). \quad (5.21)$$

---

<sup>†</sup>Results from this section were presented at the SIAM Conference on Applications of Dynamical Systems, Snowbird, UT, 2011.

Intuitively, the asymptotic stability of the zero equilibrium of the noise-free dynamics (5.21) corresponds to the population developing the ability to collectively migrate since  $\tilde{\mathbf{x}} \rightarrow \mathbf{0} \implies \mathbf{x} \rightarrow \mu\mathbf{1}$ . The lack of asymptotic stability for (5.21) implies that there exist individuals in the population that do not have an ability to migrate because their direction states  $x_i$  diverge away from the desired direction  $\mu$ , and correspondingly, the steady-state variance of  $x_i$  given by  $\sigma_{ss,i}^2$  does not exist. The linear dynamics (5.21) are asymptotically stable if and only if matrix  $M$  is Hurwitz [113], i.e., all eigenvalues of  $M$  have real part strictly less than 0. Lemmas 5.1 and 5.2 provide necessary and sufficient conditions, respectively, for matrix  $M$  to be Hurwitz.

**Lemma 5.1.** *If matrix  $M$  is Hurwitz, then there exists some node  $i$  such that  $k_i > 0$ .*

*Proof.* If the condition is not satisfied, i.e.,  $k_i = 0$  for all  $i \in \{1, \dots, N\}$ , then  $M = -L$ . The Laplacian matrix  $L$  has a zero eigenvalue associated with the eigenvector  $\mathbf{1}$  and hence  $M$  is not Hurwitz.  $\square$

**Lemma 5.2.** *If  $k_i > 0$  for all  $i \in \{1, \dots, N\}$ , then  $M$  is Hurwitz.*

*Proof.* This can be checked by a straightforward application of the Gershgorin circle theorem [43]. The Laplacian matrix  $L$  is given by  $L = [l_{ij}]$ . The eigenvalues of  $M$  lie in the union of  $N$  disks, each centered about  $-k_i^2 - (1 - k_i)^2 l_{ii}$  with radius  $(1 - k_i)^2 l_{ii}$ . If  $k_i > 0$  for all  $i$ , then the disks all lie strictly in the left half complex plane.  $\square$

Lemmas 5.1 and 5.2 are extreme cases of investment that can be interpreted in the context of migration as follows. Lemma 5.1 says that regardless of social interconnection topology, the population does not develop migration ability unless *at least* one individual is invested in acquiring the external signal  $\mu$ . Lemma 5.2 says that if *all* individuals in the population are invested, then the population develops the ability to migrate in the direction  $\mu$ , for any social graph. In Theorem 5.1 we derive necessary and sufficient conditions for the population to develop migration ability (matrix  $M$  Hurwitz) that depend explicitly on the topology of the social interconnection graph. The proof of Theorem 5.1 requires the following lemma from [110] (see also [111, 64]).

**Lemma 5.3.** *For a general Laplacian matrix  $\tilde{L} = [\tilde{l}_{ij}] \in \mathbb{R}^{N \times N}$  given by  $\tilde{l}_{ij} \leq 0$  for  $i \neq j$  and  $\sum_{j=1}^N \tilde{l}_{ij} = 0$  for all  $i \in \{1, \dots, N\}$ , the following conditions are equivalent:*

- (i)  $\tilde{L}$  has a simple zero eigenvalue and all of the other eigenvalues have positive real parts.

- (ii) The directed graph  $\mathcal{G}(\tilde{L})$  of  $\tilde{L}$  (graph with adjacency matrix  $\tilde{A} = [\tilde{a}_{ij}]$ ,  $\tilde{a}_{ii} = 0$  for all  $i$  and  $\tilde{a}_{ij} = -\tilde{l}_{ij}$  for all  $i \neq j$ ) has a directed spanning tree (see Definition 5.1 below).
- (iii) For  $\mathbf{z} \in \mathbb{R}^N$ , the dynamics  $\dot{\mathbf{z}} = -\tilde{L}\mathbf{z}$  converge asymptotically to  $\alpha\mathbf{1}$  for some scalar  $\alpha$ .

*Proof.* See Lemma 3.1 in [110], Theorem 2 in [111], and Lemma 2 in [64].  $\square$

**Definition 5.1.** *Spanning Tree:* A directed graph has a directed spanning tree (condition (ii) in Lemma 5.3) if there exists at least one node  $k$  on the graph such that a directed path exists from every other node on the graph to node  $k$ . Node  $k$  is known as a root node of the graph.

For undirected connected graphs, every node is a root node. For general (connected or disconnected) directed graphs, one can define a root set that is accessible from every other node in the network, i.e. there is a directed path from every node to at least one node in the root set. Let  $\mathcal{R}(\tilde{L})$  denote a minimal root set (set with smallest cardinality) of the graph with Laplacian  $\tilde{L}$  (denoted  $\mathcal{G}(\tilde{L})$ ). Note that for a given graph, the set  $\mathcal{R}(\tilde{L})$  is not necessarily unique. For example, for an undirected connected graph,  $\mathcal{R}(\tilde{L}) = \{i\}$  for any node  $i$  (see Figure 5.5(a) for an illustration).

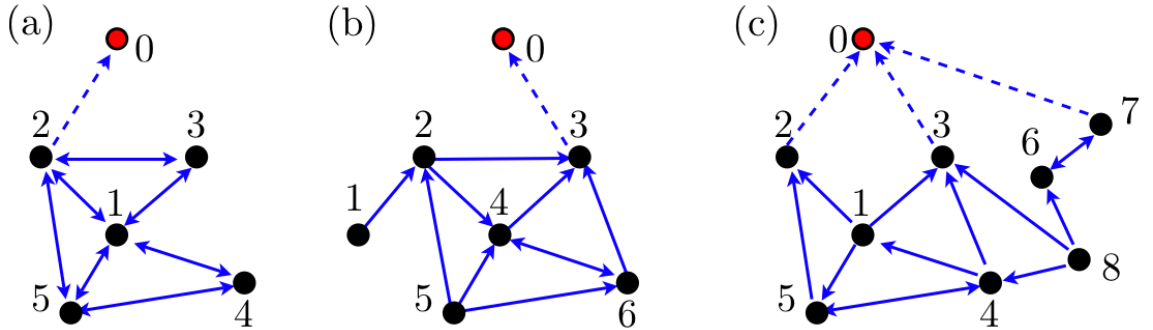


**Figure 5.5:** Illustrations of the root set  $\mathcal{R}(L)$  and the conditions of Theorem 5.1. In each graph, the set of nodes labeled  $1, \dots, N$  and solid arrows correspond to the social graph  $\mathcal{G}(L)$ . The complete set of nodes labeled  $0, 1, \dots, N$  and all the arrows correspond to the augmented graph  $\mathcal{G}(\hat{L})$ . Node 0 represents the external signal. All three graphs shown have a spanning tree rooted at node 0, and hence satisfy the conditions of Theorem 5.1. (a) Social graph is undirected and connected, hence  $\mathcal{R}(L) = \{1\}, \{2\}, \{3\}, \{4\}$ , or  $\{5\}$ . (b) Directed social graph with  $\mathcal{R}(L) = \{3\}$ . (c) Directed social graph with  $\mathcal{R}(L) = \{2, 3, 6\}$  or  $\{2, 3, 7\}$ .

**Theorem 5.1.** *Matrix  $M$  from (5.21) is Hurwitz if and only if there exists a minimal root set  $\mathcal{R}(L)$  such that  $k_j > 0$  for all nodes  $j \in \mathcal{R}(L)$ , where  $L$  is the Laplacian matrix of the social graph with adjacency matrix (5.4).*

*Proof.* Define the normalized external signal state ( $x_i = \mu$  in (5.7))  $\tilde{x}_0 = 0$  and the augmented state vector  $\mathbf{z} = [\tilde{x}_0 \ \tilde{\mathbf{x}}]^T$ . Consider the dynamics

$$\dot{\mathbf{z}} = \begin{bmatrix} \dot{\tilde{x}}_0 \\ \dot{\tilde{\mathbf{x}}} \end{bmatrix} = - \left[ \begin{array}{c|c} 0 & 0_{N \times 1} \\ \hline -K_1 \mathbf{1} & -M \end{array} \right] \begin{bmatrix} \tilde{x}_0 \\ \tilde{\mathbf{x}} \end{bmatrix} = -\hat{L}\mathbf{z}. \quad (5.22)$$

Then  $\hat{L}$  satisfies the properties of general Laplacian matrices given in Lemma 5.3. The graph corresponding to Laplacian  $\hat{L}$  is the same as the graph corresponding to Laplacian  $K_2 L$  with an additional node (labeled 0, with state  $\tilde{x}_0$ ) having incoming links with weights  $k_j^2$  from all nodes  $j = 1, \dots, N$  (see Figure 5.5 for an illustration, links to node 0 are shown as dashed arrows).

Since node 0 of  $\mathcal{G}(\hat{L})$  has no outgoing links, from Definition 5.1 we have the following condition,

$$\mathcal{G}(\hat{L}) \text{ has a spanning tree} \iff \mathcal{R}(\hat{L}) = \{0\}. \quad (5.23)$$

We claim the following

$$\mathcal{G}(\hat{L}) \text{ has a spanning tree} \implies \exists \mathcal{R}(L) \text{ s.t. } k_j > 0 \text{ for all } j \in \mathcal{R}(L). \quad (5.24)$$

We prove the statement above by contradiction. Assume that  $\mathcal{G}(\hat{L})$  has a spanning tree and for each root set  $\mathcal{R}(L)$ , there exists a node  $j$  such that  $k_j = 0$ . Since  $\mathcal{G}(\hat{L})$  has a spanning tree,  $\mathcal{R}(\hat{L}) = \{0\}$ , which means that there is a directed path from every node to node 0. Now consider any root set  $\mathcal{R}(L)$ . Since  $k_j = 0$ , node  $j$  in  $\mathcal{R}(L)$  can only reach node 0 by a path to a node  $m \notin \mathcal{R}(L)$ , for which  $k_m > 0$ . However, if such a path exists, then the set  $\mathcal{R}(L)$  where node  $j$  is replaced with node  $m$  is another root set. By assumption we must have  $k_m = 0$ . Thus there exists no directed path from node  $j$  to node 0. Hence  $\mathcal{G}(\hat{L})$  does not have a spanning tree and we have proved the claim.

Consider any root set  $\mathcal{R}(L)$  and assume that  $k_j > 0$  for all  $j \in \mathcal{R}(L)$ . Then all nodes  $j \in \mathcal{R}(L)$  are connected to node 0 of  $\mathcal{G}(\hat{L})$ . For all nodes  $m \notin \mathcal{R}(L)$ , either  $k_m > 0$  and  $m$  has a direct link to node 0, or  $k_m = 0$  in which case  $m$  has a link to at least one other node on a directed path to the root node 0, via an element of  $\mathcal{R}(L)$ .

Hence

$$\exists \mathcal{R}(L) \text{ s.t. } k_j > 0 \text{ for all } j \in \mathcal{R}(L) \implies \mathcal{G}(\hat{L}) \text{ has a spanning tree .} \quad (5.25)$$

Combining (5.23), (5.24) and (5.25), we have the condition,

$$\begin{aligned} \exists \mathcal{R}(L) \text{ s.t. } k_j > 0 \forall j \in \mathcal{R}(L) &\iff \mathcal{G}(\hat{L}) \text{ has a spanning tree} \\ &\iff \mathcal{R}(\hat{L}) = \{0\} . \end{aligned} \quad (5.26)$$

From Lemma 5.3,  $\mathcal{G}(\hat{L})$  has a spanning tree if and only if the dynamics (5.22) converge asymptotically to  $\alpha \mathbf{1}$  for some scalar  $\alpha$ . However in (5.22), the state  $\tilde{x}_0 = 0$  is invariant and hence  $\alpha = 0$ . The linear dynamics (5.21) converge asymptotically to 0 if and only if matrix  $M$  is Hurwitz [113]. This gives the condition

$$\mathcal{G}(\hat{L}) \text{ has a spanning tree} \iff M \text{ is Hurwitz.} \quad (5.27)$$

Combining (5.26) and (5.27) we have the desired result.  $\square$

Sets of root nodes  $\mathcal{R}(L)$  are illustrated for a set of simple social graphs in Figure 5.5. The directed connected graph in Figure 5.5(b) has a single root node, whereas the graph in Figure 5.5(c) has two possible minimal sets of root nodes.

We now return to the noisy migration model given by the system of stochastic equations (5.10). In order to compute the fitness of an individual in a migratory collective using (5.11), a computation of the steady-state variance of the individuals dynamics  $\sigma_{ss,i}^2$  is necessary. This quantity in turn depends on the level of investment of the individuals in the network (represented by the vector  $\mathbf{k}$ ) and the underlying topology of the social interconnection graph  $\mathcal{G}(L)$ , and can be computed by solving the matrix Lyapunov equation, as shown in Theorem 5.2 (see also [151, 103] for related results on the consensus and drift-diffusion models respectively).

**Theorem 5.2.** *For the stochastic dynamics (5.10) with social graph  $\mathcal{G}(L)$ , suppose there exists an  $\mathcal{R}(L)$  such that  $k_j > 0$  for all  $j \in \mathcal{R}(L)$ . Then the system of stochastic differential equations (5.10) has steady-state mean  $\lim_{t \rightarrow \infty} E[\tilde{\mathbf{x}}(t)] = \mathbf{0}$  and steady-state covariance matrix  $\Sigma = \lim_{t \rightarrow \infty} E[\tilde{\mathbf{x}}(t)^T \tilde{\mathbf{x}}(t)]$  given by the solution to the Lyapunov equation  $(K_1 + K_2 L)\Sigma + \Sigma(K_1 + K_2 L)^T = SS^T$ .*

*Proof.* The system (5.10) is a multivariate Ornstein-Uhlenbeck process with mean given by [24]

$$E[\tilde{\mathbf{x}}(t)] = \exp(Mt) E[\tilde{\mathbf{x}}(0)] .$$

By Theorem 5.1,  $M$  is Hurwitz and hence  $\lim_{t \rightarrow \infty} E[\tilde{\mathbf{x}}(t)] = \mathbf{0}$ .

The covariance matrix of  $\tilde{\mathbf{x}}$  is given by

$$\begin{aligned} & E[(\tilde{\mathbf{x}}(t) - E[\tilde{\mathbf{x}}(t)])(\tilde{\mathbf{x}}(t) - E[\tilde{\mathbf{x}}(t)])^T] \\ &= \exp(Mt)E[\tilde{\mathbf{x}}(0)\tilde{\mathbf{x}}^T(0)]\exp(Mt) + \int_0^t \exp(M(t-s))SS^T\exp(M(t-s))ds. \end{aligned}$$

Since  $M$  is Hurwitz, the steady-state covariance matrix is given by

$$\Sigma = \lim_{t \rightarrow \infty} E[\tilde{\mathbf{x}}(t)^T \tilde{\mathbf{x}}(t)] = \lim_{t \rightarrow \infty} \int_0^t \exp(M(t-s))SS^T\exp(M(t-s))ds,$$

which as is shown in [24] is the solution to the Lyapunov equation

$$M\Sigma + \Sigma M^T + SS^T = 0. \quad (5.28)$$

□

### 5.3.2 Slow Timescale Evolutionary Dynamics

The Lyapunov equation (5.28) in Theorem 5.2 allows us to compute the migratory performance (and correspondingly fitness (5.11)) of individuals since the diagonal terms of the steady-state covariance matrix  $\Sigma$  are the individual steady-state variances  $\sigma_{ss,i}^2$ . In this section, we use evolutionary simulations based on fast timescale fitness calculations from (5.28) to study the role that graph connectivity plays in the evolution of branching.

We focus on three classes of social graph topologies of which one is ordered (ring lattice) and two are random (undirected and directed). In each class, a single parameter controls the level of connectivity of the graph. The three classes of graphs used are listed below:

- Undirected Ring Lattice: A graph with  $N$  nodes, each connected to  $K$  nearest neighbors,  $K/2$  on each side, for  $K$  even. An undirected edge exists between nodes  $i$  and  $j$  if and only if  $0 < \min\{|i - j|, N - |i - j|\} \leq K/2$ . The graph is connected for  $K \geq 2$ .
- Random Undirected (Erdős-Rényi) [19, 82]: Undirected graph with  $N$  nodes. Every edge in the graph exists randomly with a uniform probability  $p$ . The

expected number of neighbors of a node is  $E[K] = Np$  for large  $N$ . The graph is almost surely connected if  $p > \ln(N)/N$  or equivalently  $E[K] > \ln(N)$ .

- Random Directed [83, 2]: Directed graph with  $N$  nodes. Each node has a probability  $p$  of having a directed link to every other node in the network. The expected number of neighbors of a node is  $E[K] = Np$  for large  $N$ .

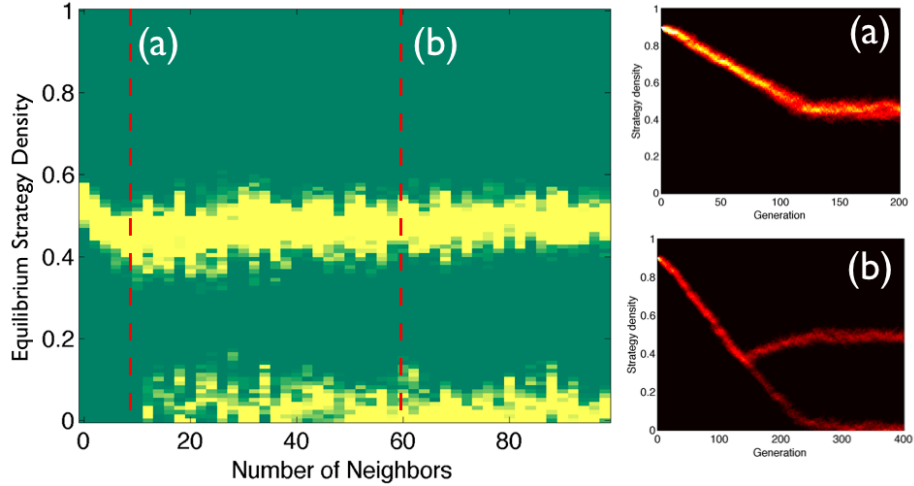


**Figure 5.6:** Effect of social graph topology on the evolutionary outcomes of the migration model. The left plot shows the equilibrium strategy distribution as a function of number of nearest neighbors for the ring lattice graph model with  $N = 400$  nodes and parameters  $\beta = 3$  and  $c = 2.6$ ; bright colors correspond to higher population density. The two plots on the right labeled (a) and (b) are evolutionary simulations, the steady state conditions in these plots correspond to the red dashed slices in the left plot. Notice that the speciated two-strategy equilibrium exists only once the graph connectivity exceeds a threshold number of neighbors ( $\approx 18$  for parameters chosen here).

For each class of topologies, the parameters  $K$  and  $p$  allow us to explore a range of connectivities; for  $K = p = 0$ , the social graphs are fully disconnected and individuals must resort to solitary migration with a monomorphic optimal strategy (5.12). For  $K \rightarrow N - 1$  (for the ring lattice) and  $p \rightarrow 1$  (for the random graphs), the social graph is fully connected, resulting in the leader-follower speciated evolutionary equilibrium for certain parameter choices as discussed in Section 5.2. Between these two connectivity extremes, intuition suggests that an intermediate level of limited connectivity can provide adequate information flow in the network for followers to leverage the investments made by leaders, thereby resulting in a speciated population. In Figures 5.6 and 5.7 we confirm this intuition by showing that the transition from a monomor-

phic, to a branched evolutionary solution as a function of topology (parameterized by  $K$  and  $p$ ), occurs at an intermediate threshold level of connectivity.

For the simulation in Figure 5.6 we use the ring lattice topology for the social graph with  $N = 400$  individuals and choose a set of parameters for which the all-to-all social graph is known to have a two-strategy solution,  $\beta = 3$  and  $c = 2.6$  (see Figure 5.4, column 3). For a range of values of the number of neighbors  $K = 2, 4, \dots, 100$ , we compute the fitness of individuals using (5.28) and (5.11) and evolve the strategies of the populations to an evolutionary steady state. This steady-state strategy distribution is plotted as a function of number of neighbors  $K$  in the figure. We see that there exists an intermediate threshold for social connectivity (given by  $K \approx 18$ ) that allows for adequate information flow in the network to result in evolutionary branching. In particular, social graphs that are much sparser (fewer edges) than the all-to-all case analyzed in Section 5.2 can yield speciated evolutionary outcomes.

In Figure 5.7 we present simulations similar to those described for Figure 5.6 above, for all three classes of social graph topologies (ring lattice, undirected random, directed random) and for  $N = 200, 400, 600$ . In each case, we see a threshold connectivity for evolutionary branching that is higher than the minimum thresholds for the social graph to be connected. We also see that the number of individuals in the population  $N$  does not have a significant affect on this threshold in the range considered. Further, the location of the threshold is dependent on the class of graph being considered; the two classes of random graphs have lower thresholds than the ordered ring lattice.

The simulations in this section illustrate the significant effect of limited social graph connectivity on the evolution of branching in migration. In particular, we show that social connectivity above threshold levels can yield speciated outcomes in the evolutionary dynamics. The thresholds depend on the classes of social graph topology being considered. Determining the analytical minimum connectivity threshold as function of parameters  $\beta$ ,  $c$  and class of graph, is a topic of ongoing work. We also intend to look at other classes of graph topologies such as spatially embedded graphs with a topological metric on connectivity (such as in [3]), and classes of small-world graphs parameterized by a single rewiring parameter [146, 82] (the ring lattice and undirected random graphs considered here are two extreme limits of the Watts-Strogatz small world model).

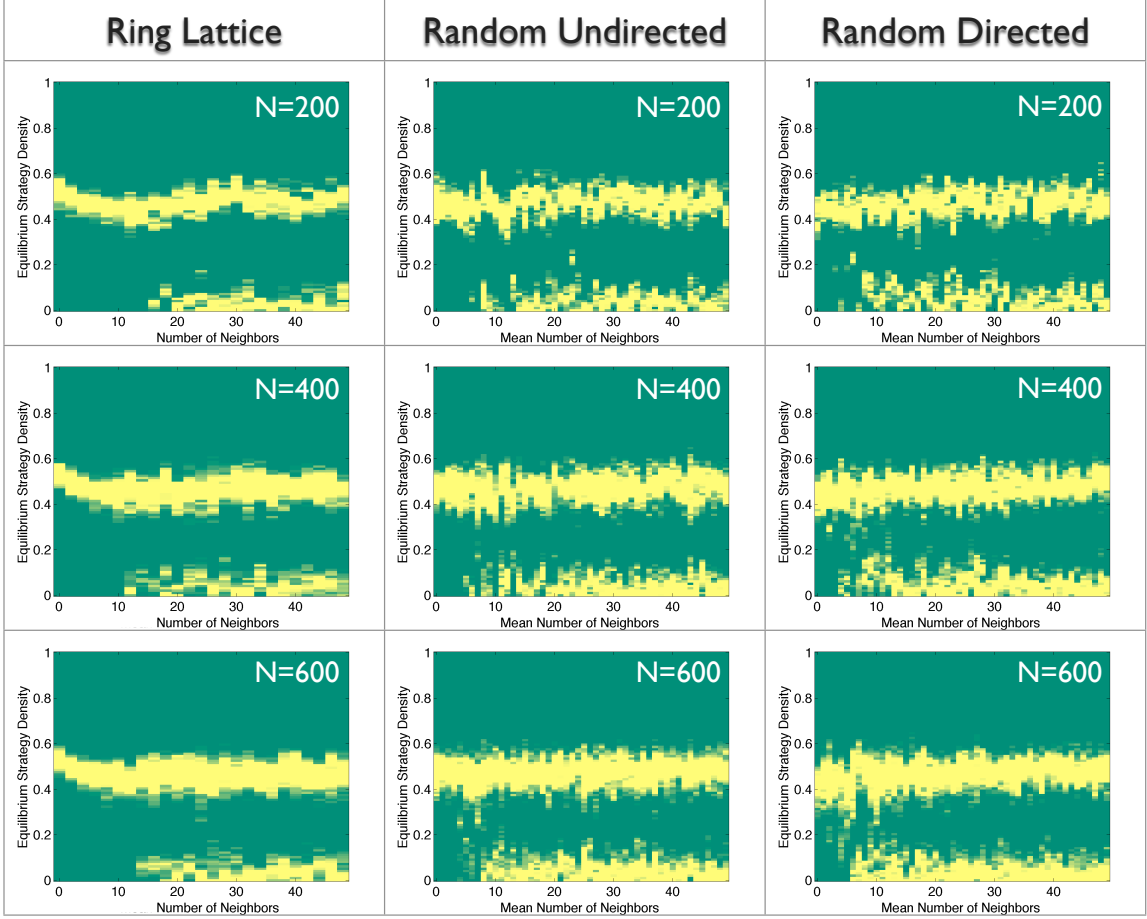


**Figure 5.7:** Evolutionary equilibria as a function of social graph topology for ring lattice, random undirected and random directed graph models with parameters  $\beta = 3$  and  $c = 2.6$ ; number of nodes  $N$  are shown on each plot. The minimum number of neighbors (or mean number for the random graphs) is independent of the number of nodes  $N$  in these plots,  $\approx 18$  for the ring lattice,  $\approx 9$  for the random undirected graphs and  $\approx 8$  for the random directed graphs.

## 5.4 Dynamic Nodes and Bifurcations

Our analysis of the collective migration model (5.10) thus far has focused on the evolutionary perspective, typically considering the dynamics of networks with large numbers of nodes. In this section we shift focus and consider the model from an adaptive perspective on much smaller dynamic networks. This analysis is motivated in part by questions about leadership, task assignment and robust adaptive behavior in multi-agent robotic systems [128, 98, 107]. We consider a simple model of greedy local optimization by nodes on a graph, which yields individual adaptation of investments  $k_i$ . For this model we show bifurcations as a function of cost that yield leader-follower

emergent behavior as equilibria of the adaptive process. We also illustrate the critical role played by graph topology in determining the *location* of leaders in the network of adaptive nodes using several examples.

Consider a system of interconnected agents with fast-timescale tracking dynamics given by (5.10). Further, suppose that each agent seeks to maximize its local utility function by adapting its investment parameter  $k_i$ . We assume that the utility function for each agent  $U_i$  is given by the fitness function (5.11),

$$U_i = \exp\left(\frac{-\sigma_{ss,i}^2}{2}\right) \exp(-ck_i^2). \quad (5.29)$$

In this setting, the utility function for a focal agent  $i$  depends on the agent's investment  $k_i$ , as well as the investments of other nodes in the network; we assume that the agent can measure its own utility, but not the investments of other nodes. Given the measured local utility  $U_i$ , agents modify their investments  $k_i$  on a slow timescale by climbing the gradient of their local utility to reach its local maximum,

$$\frac{dk_i}{dt} = \frac{\partial U_i}{\partial k_i}. \quad (5.30)$$

Our goal is to study the outcomes of this simple adaptive process by computing equilibria of the dynamics defined by (5.30), (5.29) and (5.10), and studying their bifurcations. Let  $\tilde{U}_i = \ln U_i$  and consider the non-homogeneous time scaling  $\tau = \int_0^t U_i(\sigma) d\sigma$ . Then the dynamics (5.30) transform to

$$\dot{k}_i = \frac{dk_i}{d\tau} = \frac{\partial \tilde{U}_i}{\partial k_i} = \frac{\partial}{\partial k_i} \left( \frac{-\sigma_{ss,i}^2}{2} - ck_i^2 \right), \quad i = \{1, \dots, N\}. \quad (5.31)$$

The dynamics (5.31) are identical to (5.30), modulo the time-scaling, and are notationally simpler. In particular, the equilibria of (5.31) are identical to those of (5.30). We focus on these dynamics for the remainder of the section.

We first look at the simplest case of the dynamics with  $N = 2$  nodes, with an all-to-all graph. The steady-state covariance matrix  $\Sigma$  (from (5.28)) in this case can be computed analytically [24] as

$$\Sigma = \frac{(\text{Det } M)SS^T + [-M + (\text{Tr } M)]SS^T[-M + (\text{Tr } M)]^T}{-2(\text{Det } M)(\text{Tr } M)}, \quad (5.32)$$

where matrices  $M$  and  $S$  are defined in (5.10) and (5.21). For each pair  $\{i, j\} = \{1, 2\}, \{2, 1\}$ , the diagonal elements of  $\Sigma$  from (5.32) are given by

$$\sigma_{ss,i}^2 = \frac{f_{ij}(k_i - 1)^4 + f_{ji}(2(k_j - 1)k_j + 1)^2 + f_{ji}((k_j(3k_j - 2) + 1)k_i^2 - 2k_j^2k_i + k_j^2)}{4((k_i - 1)k_i + (k_j - 1)k_j + 1)((k_j(3k_j - 2) + 1)k_i^2 - 2k_j^2k_i + k_j^2)}, \quad (5.33)$$

where  $f_{ij} = (k_j^2 - \beta^2(k_i - 1)(k_j - 1)^2)$ .

Substituting (5.33) in (5.31), we compute the equilibria  $\mathbf{k}_{eq}$  of the dynamics (5.31) and (5.10) and their stability as a function of increasing cost parameter  $c$ . Analytical expressions of the equilibria are complicated, but the equilibria are illustrated for  $\beta = 3$  in Figure 5.8. For low cost, both individuals make a significant equal investment corresponding to the symmetric equilibrium  $k_{eq,1} = k_{eq,2} \gg 0$ . As cost increases, the level of this equilibrium investment decreases and eventually a pair of stable leader-follower equilibria appear via two saddle-node bifurcations. As the cost increases further, the symmetric stable equilibrium loses stability in a subcritical pitchfork bifurcation, leaving the leader-follower pair of stable equilibria and an unstable symmetric saddle equilibrium.

For larger all-to-all networks with the dynamics (5.31) and (5.10), bifurcations in cost  $c$  yield generalizations of the leader-follower equilibria for the  $N = 2$  case: the fraction of nodes in the leader populations decreases with increasing cost parameter  $c$  as a consequence of several bifurcations in the dynamics. This is illustrated for  $N = 10$  nodes in Figure 5.9.

The topology of the social graph and the cost parameter  $c$  together play an important role in determining the location of leader and follower nodes on the graph at equilibrium. This is illustrated for an undirected star graph in Figure 5.10. At low values of cost  $c$ , the fringe nodes of the star invest strongly in the external signal and the central node leverages these neighbors as a follower with small investment. At intermediate cost  $c$  all individuals make similar investments, while at high cost  $c$  the central node adapts to become the leader with all the fringe nodes leveraging this investment as followers.

We show equilibrium outcomes for three more graph topologies in Figure 5.11. For the undirected ring lattice, alternate nodes adapt to become leaders and followers, while for more complicated nearest-neighbor type topologies, the precise connection between topology and location of leaders is more challenging to interpret. This interpretation requires the development of a graph- and investment-dependent metric to

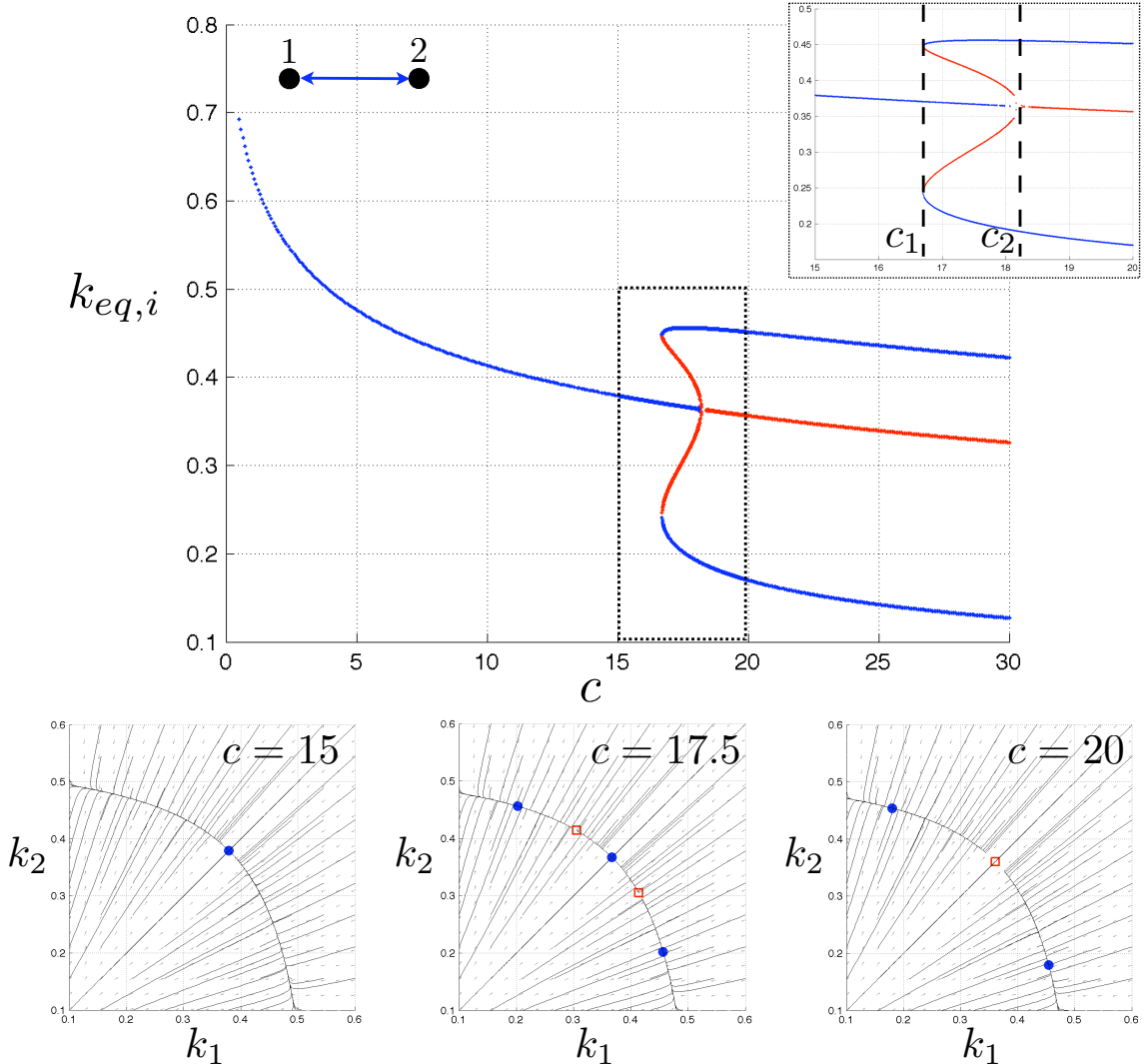


**Figure 5.8:** Bifurcations for the adaptive node dynamics (5.30) with  $N = 2$  nodes, an all-to-all social graph, and noise parameter  $\beta = 3$ . The top plot shows the two components of  $\mathbf{k}_{eq}$  (equilibria of the dynamics (5.30) and (5.10)) as a function of the cost parameter  $c$ . Stable sinks are marked blue and unstable saddles are marked red. The inset shows a zoomed in view of the region with  $15 \leq c \leq 20$  marked in the dotted square. The dashed lines in the inset  $c_1 \approx 16.7$  and  $c_2 \approx 18.2$  denote the saddle-node and pitchfork bifurcation points respectively. The row of bottom plots are phase portraits for the dynamics with parameter  $c$  as indicated; the circles are stable sinks and the squares are saddles. These plots remains qualitatively the same for different values of  $\beta > 2$ ; the bifurcation points  $c_1$  and  $c_2$  move further to the right for higher  $\beta$ .

rank nodes for their leadership potential, perhaps analogous to the *information centrality* metric used for drift-diffusion stochastic networks in [104], a topic of ongoing work.

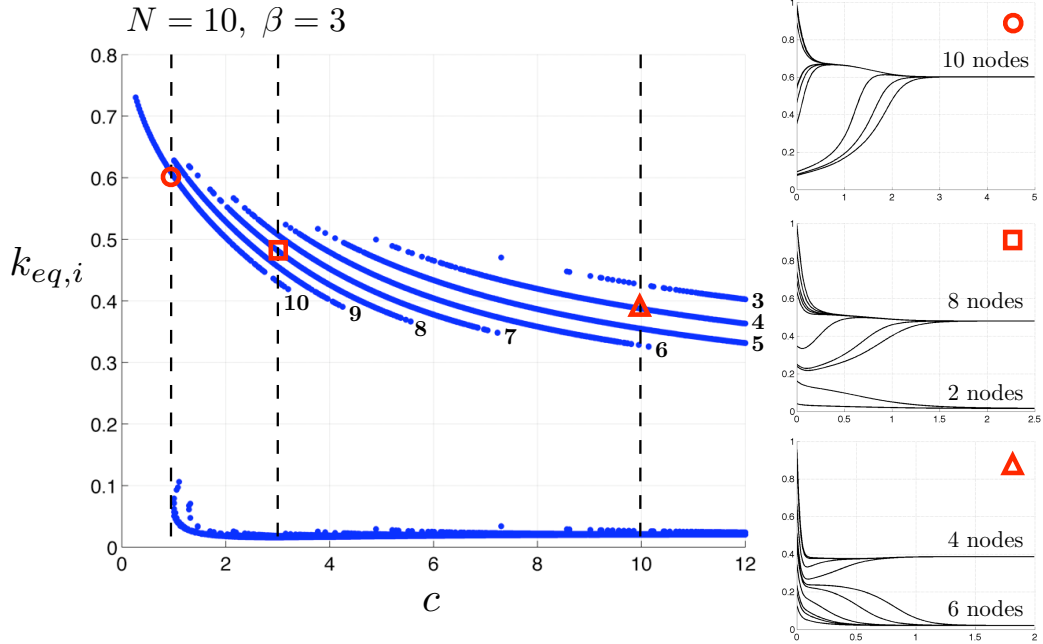


**Figure 5.9:** Bifurcations for the adaptive node dynamics (5.30) and (5.10) with  $N = 10$  nodes, an all-to-all social graph, and noise parameter  $\beta = 3$ . The left plot shows stable equilibria of the dynamics as a function of  $c$ ; trajectories for the points marked with the circle ( $c = 1$ ), square ( $c = 3$ ) and triangle ( $c = 10$ ) are shown on the right. The labels on the left plot indicate the number of leaders in each branch of stable solutions. Notice that bifurcations yield fewer leaders for increasing cost.

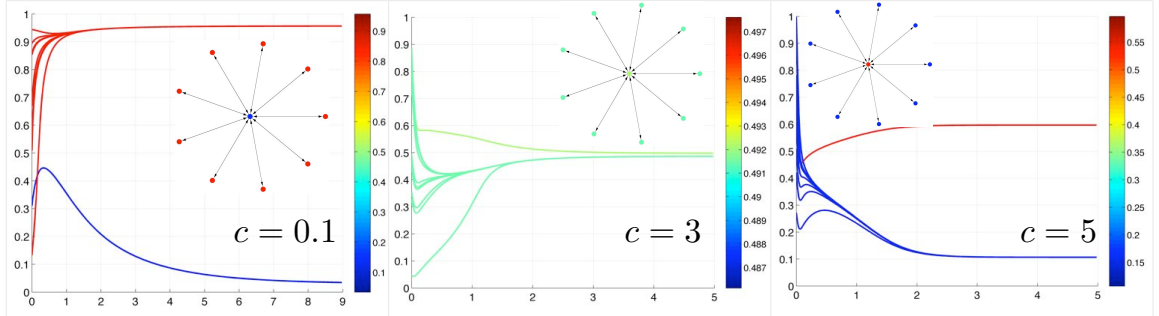


**Figure 5.10:** Role of topology and cost parameter for the adaptive node dynamics on the undirected star graph. Parameter  $c$  is indicated on each plot. The  $x$ -axis of each plot is time and the  $y$ -axis is strategy  $k_i$ . The color-scale corresponds to the magnitude of equilibrium investment  $k_{eq,i}$ .

## 5.5 Final Remarks

The study of leadership has received significant attention in both biology and multi-agent robotics. One focus in biology has been on determining conditions for the

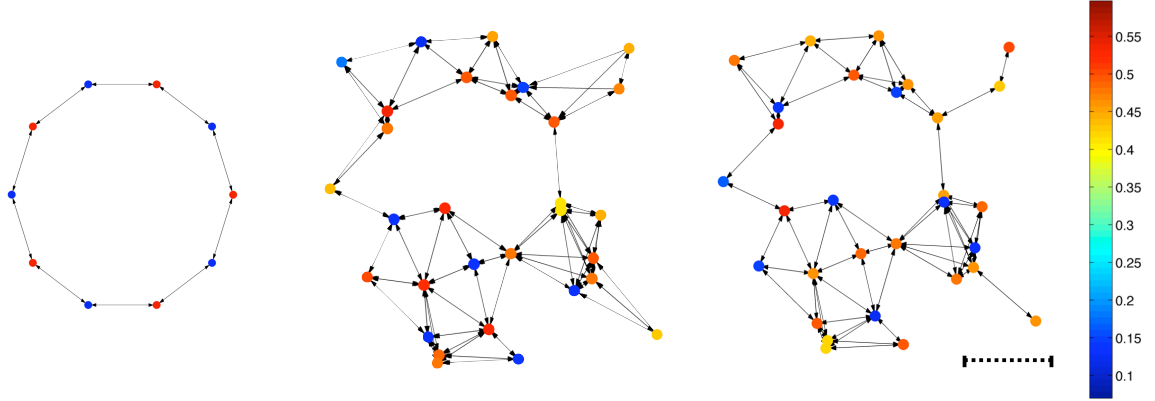


**Figure 5.11:** *Role of topology in determining locations of leaders on the social graph.* Parameters for all three plots are  $\beta = 3$  and  $c = 4$ . The colors of nodes on each plot correspond to equilibrium investments  $k_i$  for the dynamics (5.30) and (5.10) with magnitudes indicated in the color-bar. The left graph is an undirected star with  $N = 10$  nodes. The two right plots show a random spatial embedding of nodes with two different interconnection models. In the middle plot, each node is connected to its three nearest neighbors (topological metric) and in the right-most plot, each node is connected to all neighbors within a fixed radius given by the dashed line drawn (distance metric).

stable evolution of leadership behavior in collective systems, since followers in such systems have good performance at a lower cost. In networked robotic systems, the *leader-follower* paradigm has been studied in a variety of contexts as a tool to design control protocols that achieve desired performance. In this work we focus on the role that the social graph connectivity plays in a networked model of collective migration. We use tools from adaptive dynamics to study the all-to-all limit of the evolutionary model and derive bounds for branching of the population into leader and follower groups. For limited connectivity, we prove necessary and sufficient conditions for convergence of the noise-free migration model, and show that fitness of individuals in the stochastic model can be derived analytically using the Lyapunov equation. For random networks and lattices, we show a minimum connectivity bound that yields evolutionary branching in the population. In the final section, we study smaller networks inspired by collective robotic systems, and show that the network topology plays a critical role in determining the location of leaders in the adaptive system.

Our goal here was not to design the best system for a given task, as is often the case in the leader-follower work, but rather to understand the role of networked topology in the emergence of leadership. One interesting avenue for future work is to understand where the top-down engineering design approach meets the bottom-up adaptive approach taken in this chapter. This understanding will aid in the design of

collective systems that are near optimal, and also robust to failures such as lost nodes or links. For the evolutionary model, further work involves analytically deriving the minimal connectivity threshold for branching, and generalizing to study arbitrary social graphs, beyond the lattice and random networks studied here.

# Chapter 6

## Coevolutionary Dynamics of Pursuit and Evasion

Pursuit and evasion behaviors are widely observed in nature and play a critical role in predator foraging, prey survival, mating, and territorial battles in several species. Species such as bats and dragonflies have evolved sophisticated dynamical strategies such as motion camouflage to disguise themselves as stationary during aerial pursuit [77, 27]. Studies on migratory cannibalistic locusts have revealed that pursuit and evasive behavior among conspecifics is integral to the formation of mass-moving migratory bands in dense swarms [35, 5]. Recent experimental work on the dynamics of coordinated predator pursuit and prey evasion among schooling fish has shown that collective behavior, among both predators and prey, plays a vital role in predator hunting and prey evasion under conditions of considerable informational constraints (such as dynamic ocean environments) [37, 45].

Pursuit-evasion contests have been studied extensively from a game-theoretic perspective as differential games [46]. Unlike classical (matrix-based) games, the dynamics of players in differential games are modeled using differential equations, with payoffs corresponding to particular states of the system, or to system trajectories. In engineering, pursuit and evasion games have received much attention, particularly in the context of missile guidance and avoidance [101, 51] and aircraft pursuit and evasion [108, 81]. The book by Nahin [80] provides a review of the topic along with relevant historical background.

The pervasiveness of pursuit and evasion in nature motivates the examination of winning strategies from an evolutionary perspective. Here one can think of a strategy as a control law that a particular pursuer (evader) employs to capture (escape). Correlates of evolutionary fitness, such as time-to-capture, provide natural metrics that

connect the dynamics of individual pursuer-evader pairs to evolutionary dynamics of populations comprising individuals playing different strategies. ESSes of the pursuit-evasion game point to strategies or behaviors one would expect to observe in nature. Recently, Wei et al. [147] used the evolutionary approach to study pursuit games with dynamics derived in [50]. The authors of [147, 50] use Monte-Carlo simulations and analytical calculations to study three pursuit strategies competing against a field of deterministic or random nonreactive evasive strategies (an evader with a nonreactive strategy has dynamics that are uncoupled from those of the pursuer). The three chosen pursuit strategies (classical, constant bearing and motion camouflage) are biologically inspired. The authors show convergence of the evolutionary game dynamics between the three strategies to pure motion camouflage and motivate this result by empirical observations of motion camouflage in hoverflies, dragonflies and bats [27].

In this chapter, we build on the work in [147] by studying the *coevolution* of the three strategies of pursuit from [147] playing against three distinct evasive strategies, two of which are *reactive* strategies (an evader with a reactive strategy has dynamics that are coupled to those of the pursuer). In contrast to the analysis in Chapters 3, 4 and 5, which involve the evolutionary dynamics of a *single* population, the analysis in this chapter involves the interaction between *two distinct* populations (pursuers and evaders). This will require us to look at an extension of the standard replicator equations to a double simplex phase space.

We use Monte-Carlo simulations and theoretical analysis to show convergence to an equilibrium of classical pursuit versus classical evasion. We point out that extending the ‘games against nature’ approach [147] (evolution of pursuers with respect to nonreactive evaders) to competitions between two sets of strategies does not result in a motion camouflage as the winning pursuit strategy, as in [147]. Indeed, the environment of evasive strategies that a pursuer population encounters is critical to determining the winning pursuit strategy. It is anticipated that analysis of strategy spaces different again from those studied in the present chapter will yield other interesting evolutionary outcomes.

We explore the winning strategies (classical pursuit and classical evasion) in a collective motion model with agents pursuing and evading designated neighbors on a cyclical interaction topology. This exploration is motivated by collective motion in cannibalistic locusts [5] and has strong parallels to prior work in cyclic pursuit [23, 67, 69, 68]. Simulation results suggest a rich set of solutions for this collective motion model.

The outline of this chapter is as follows. §6.1 describes the planar dynamics for pursuit and evasive agents and the different pursuit and evasion strategies under consideration. In §6.2 we study the coevolutionary dynamics of the two populations, and in §6.3 we focus on the collective motion model with the winning strategies.

**NOTATION:** For notational convenience, the Euclidean plane  $\mathbb{R}^2$  is identified with the complex plane  $\mathbb{C}$ . Thus  $(x, y) \in \mathbb{R}^2 \equiv x + iy \in \mathbb{C}$ . For two complex numbers  $c_1, c_2 \in \mathbb{C}$ , the complex inner product is defined as  $\langle c_1, c_2 \rangle := \text{Re}(c_1 c_2^*)$ , the real part of  $c_1 c_2^*$ , where  $c_2^*$  is the complex conjugate of  $c_2$ .  $|c_1|$  is the complex modulus of  $c_1$ .  $M^\#$  denotes the element-wise inverse of matrix  $M = [m_{ij}]$ , i.e.  $m_{ij}^\# = 1/m_{ij}$ .

## 6.1 Dynamics of Pursuit and Evasion\*

We study a two-agent planar pursuit and evasion problem where each agent is modeled as a self-propelled steered particle with constant speed and with angular velocity determined by the interaction between the particles. We consider three pursuit behaviors: *classical*, *constant bearing* and *motion camouflage*, and three evasive behaviors: *classical*, *random motion*, and *optical-flow based* [123]. The choice of the three pursuit behaviors is motivated by work in [147] and [50], where it is proved that if the speed of the pursuer is greater than that of the evader, the pursuer captures the evader in finite time. Here ‘capture’ means that the Euclidean distance between the pursuer and evader reaches a designated minimum.

Consider a pursuer and an evader moving on the complex plane with positions  $r_P = x_P + iy_P \in \mathbb{C}$  and  $r_E = x_E + iy_E \in \mathbb{C}$ , and headings  $\theta_P \in \mathbb{S}^1$  and  $\theta_E \in \mathbb{S}^1$ , respectively. The dynamics of the two-agent system are given by

$$\begin{aligned}\dot{r}_P &= e^{i\theta_P}, & \dot{\theta}_P &= u_P \\ \dot{r}_E &= \nu e^{i\theta_E}, & \dot{\theta}_E &= u_E.\end{aligned}\tag{6.1}$$

Here, the speed of the pursuer is normalized to be 1 and the evader has a constant positive speed  $\nu < 1$ . We define the *baseline vector* [147]  $r$  as the relative position of pursuer with respect to evader, i.e.,

$$r = r_P - r_E.$$

---

\*Sections 6.1 – 6.3 are presented verbatim as in [96] with some minor modifications.

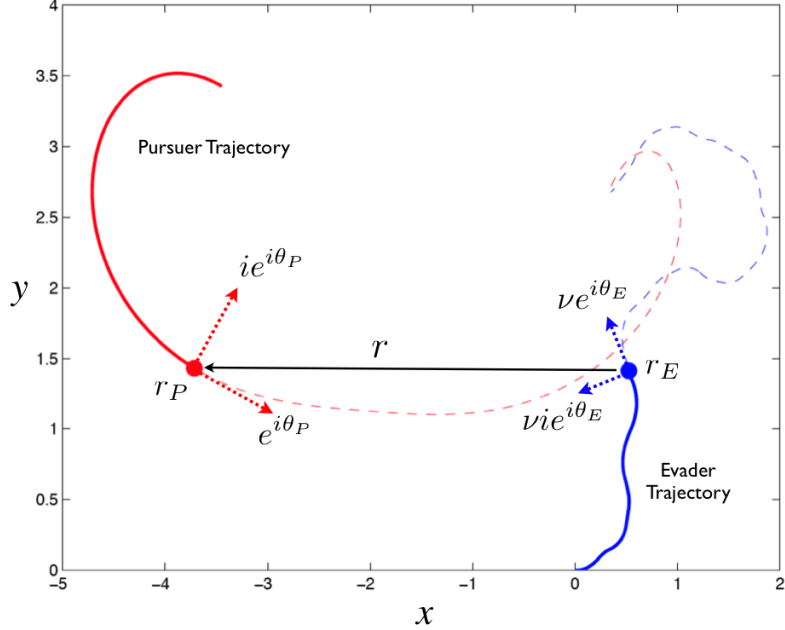


**Figure 6.1:** Cartoon trajectories of a pursuer and an evader. Pursuer position  $r_P$  and evader position  $r_E$  at time  $t_0$  are shown as circles. The corresponding velocities  $e^{i\theta_P}$  and  $\nu e^{i\theta_E}$  (and the vectors  $i e^{i\theta_P}$  and  $\nu i e^{i\theta_E}$  normal to these) are shown as dotted arrows. Also shown is the baseline vector  $r$ . Solid trajectories correspond to  $t < t_0$  and dashed trajectories to  $t > t_0$ .

Figure 6.1 shows the positions and velocity vectors for each particle, and the baseline vector. Note that  $\dot{r} = e^{i\theta_P} - \nu e^{i\theta_E}$ . We define the three *pursuit control laws* following [147] (with some change of notation):

- Classical pursuit<sup>†</sup>:

$$u_P = -\eta \left\langle \frac{r}{|r|}, i e^{i\theta_P} \right\rangle, \quad (\text{P1})$$

where  $\eta$  is a constant gain.

- Constant bearing pursuit<sup>†</sup>:

$$u_P = -\eta \left\langle \frac{r}{|r|}, i e^{i\phi} e^{i\theta_P} \right\rangle, \quad (\text{P2})$$

where  $\phi \in (-\pi/2, \pi/2)$  is a chosen constant bearing angle.

---

<sup>†</sup>Pursuer strategies (P1) and (P2) are modified slightly for clarity from those used previously in [96]. We have dropped the second terms in each control law; these terms were only relevant in the fast initial transient dynamics and do not affect the results described here.

- Motion camouflage pursuit:

$$u_P = -\mu \left\langle \frac{r}{|r|}, i\dot{r} \right\rangle, \quad (\text{P3})$$

where  $\mu$  is a constant gain.

We define the three *evasion control laws* as follows:

- Classical evasion:

$$u_E = -\eta \left\langle \frac{r}{|r|}, ie^{i\theta_E} \right\rangle, \quad (\text{E1})$$

where  $\eta$  is a constant gain.

- Random motion evasion:

Piecewise linear paths with turns every  $\alpha$  time units, and turning rate  $u_E$  selected uniformly randomly from  $[-\kappa, \kappa]$  at every turn. (E2)

- Optical-flow based evasion:

$$u_E = -\eta \tan^{-1}(\dot{\theta}), \quad (\text{E3})$$

where  $\theta$  is the complex argument of  $r$  and  $\dot{\theta} = -\frac{1}{|r|^2} \langle r, i\dot{r} \rangle$ .

Intuitively, classical pursuit (evasion) involves the pursuer (evader) aligning its velocity vector with the baseline. In constant bearing pursuit, the pursuer maintains a constant bearing angle  $\phi$  between its velocity vector and the baseline, whereas in motion camouflage, the pursuer contracts the magnitude of the baseline, while leaving the argument of the baseline unchanged. In [147, 50], the authors use elegant geometric ideas to show that the pursuit control laws (P1)-(P3) provably correspond to the desired pursuit strategies described above. This is done by defining pursuit manifolds for each strategy ('states of the interacting system that satisfy particular relative position and velocity criteria') and proving convergence to these manifolds for sufficiently high gains  $\eta$  and  $\mu$ . In optical-flow based evasion, the evader reacts to the changes in the argument of the baseline vector; these changes are intended to mimic optical flow generated by the pursuer on the retina of the evader [123]. Figure 6.2 shows a simulation of the three pursuit and three evasion strategies pitted against one another. Note that the baseline vectors remain roughly parallel in each case of motion camouflage pursuit (bottom row of panels in Figure 6.2). The evader

trajectory in optical-flow based evasion is a straight line when competing against a motion camouflage pursuit strategy.

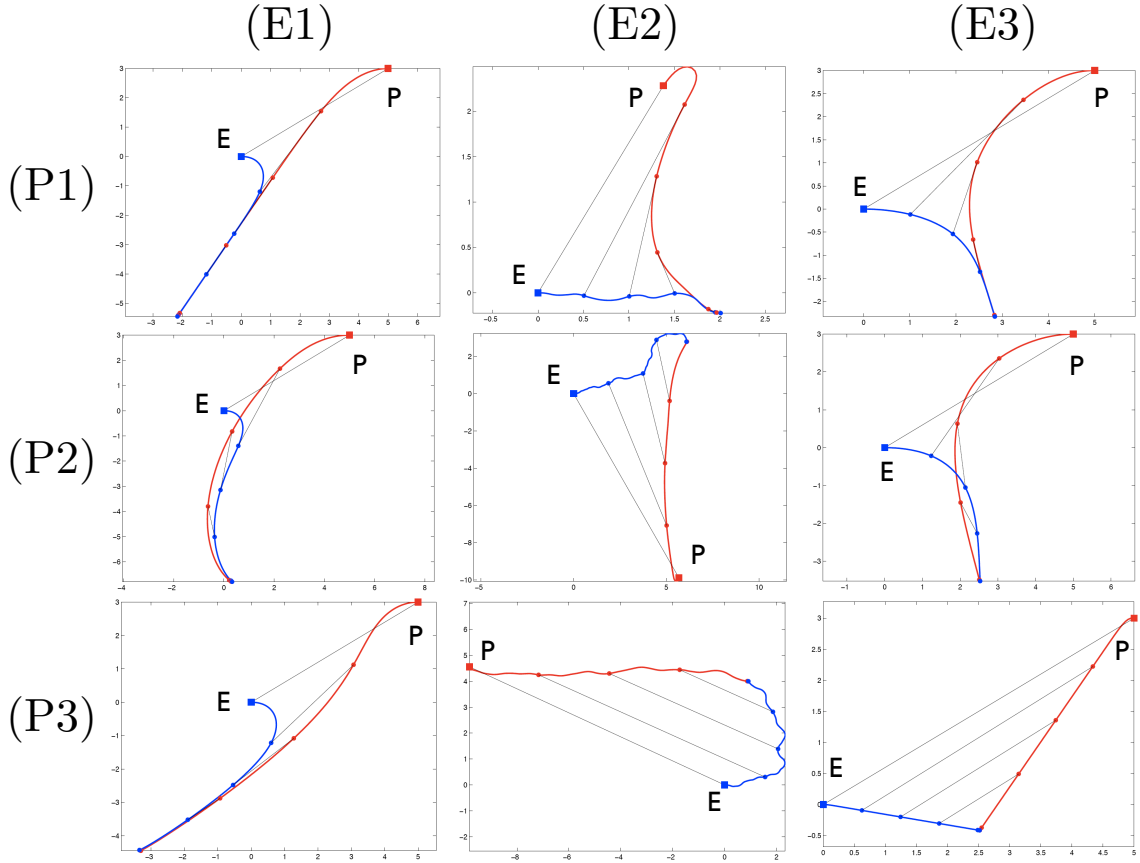


**Figure 6.2:** Simulated trajectories of each of the nine pairs of competing pursuit and evasion strategies. The rows correspond to pursuit control laws (P1), (P2) and (P3) respectively and the columns correspond to evasive control laws (E1), (E2) and (E3) respectively. For example, the plot in the middle corresponds to constant bearing pursuit versus random motion evasion. The starting positions are indicated with ‘P’ and ‘E’. In all plots the evader (E) starts at the origin with  $\theta_E(0) = 0$ . The pursuers (P) in columns 1 and 3 start at  $r_P(0) = 5 + 3i$  with a heading  $\theta_P(0) = \pi$ . In the second column the pursuers start at random positions and with random headings. The straight lines in each plot are snapshots of the baseline vector at specific points in time.

For all control laws  $u_P$  and  $u_E$  defined above, Lemma 6.1 ensures that capture is always possible in finite time.

**Lemma 6.1.** Consider dynamics (6.1) and control laws (P1)-(P3) and (E1)-(E3). For every capture radius  $\epsilon > 0$  and every initial condition  $r_P(0)$ ,  $r_E(0)$  such that  $|r(0)| = |r_P(0) - r_E(0)| > \epsilon$ , there exists a finite capture time  $T$  such that  $|r(T)| = \epsilon$ .

*Proof.* Refer to [147, 50] for proof. Note that the evasive controls (E1)-(E3) satisfy the continuity and boundedness assumptions of Proposition 3.3 in [147].  $\square$

The central question we ask in this chapter is which strategies win out in a co-evolutionary contest between the three proposed pursuit strategies and the three proposed evasive strategies? In [147] the authors studied the evolutionary dynamics of the three pursuit strategies (P1)-(P3) playing against an environment of nonreactive deterministic or random evasive strategies such as (E2). In the following section we consider an evolutionary scenario in which the pursuit strategies coevolve with *reactive* evasive strategies (E1) and (E3) as well.

## 6.2 Evolutionary Dynamics

To model the evolutionary dynamics of pursuer-evader interactions, fitnesses are determined by the cumulative effect of several one-on-one contests between pursuers and evaders such that a long time-to-capture for a particular contest corresponds to a high evader fitness and a low pursuer fitness. Consider a pursuer population represented by the population vector  $\mathbf{p} = \begin{bmatrix} p_1 & p_2 & p_3 \end{bmatrix}^T$ . Here  $p_i, i \in \{1, 2, 3\}$ , corresponds to the fraction of individuals in the population playing strategy (Pi). Hence the vector  $\mathbf{p}$  is restricted to the simplex  $\Delta_2$ . Similarly, the evader population is represented by the population vector  $\mathbf{q} = \begin{bmatrix} q_1 & q_2 & q_3 \end{bmatrix}^T$  which is also restricted to  $\Delta_2$ . The fitness vectors for the pursuer and evader populations are denoted by  $\mathbf{f}_P \in \mathbb{R}_+^3$  and  $\mathbf{f}_E \in \mathbb{R}_+^3$  respectively, where  $f_{Pi}$  is the fitness of pursuit strategy (Pi) and  $f_{Ej}$  is the fitness of evasive strategy (Ej). Define population mean fitness by  $\widehat{f}_P = \mathbf{p}^T \mathbf{f}_P$  and  $\widehat{f}_E = \mathbf{q}^T \mathbf{f}_E$ .

We can now write down a discrete update equation for each population that depends on the relative fitnesses of the different strategies in that population. For transition from generation  $g$  to generation  $g+1$ , we have for  $i = 1, 2, 3$  and  $j = 1, 2, 3$ :

$$\begin{aligned} p_i(g+1) &= p_i(g) \frac{f_{Pi}}{\widehat{f}_P} \\ q_j(g+1) &= q_j(g) \frac{f_{Ej}}{\widehat{f}_E}. \end{aligned} \tag{6.2}$$

One can verify that the equations (6.2) ensure that each population vector remains in the simplex  $\Delta_2$ . Intuitively, strategies with fitness greater than the population mean fitness are favored. Given an expression for the fitness vectors, we can study the outcomes of the dynamics (6.2). As in [147] we use time-to-capture as a measure

of fitness. The fitness of the set of pursuer strategies  $\mathbf{f}_P$  depends on the distribution of evaders in the population  $\mathbf{q}$  and  $\mathbf{f}_E$  depends on the distribution of pursuers in the population  $\mathbf{p}$ . This implies that the equations (6.2) are coupled. We simulate the evolutionary dynamics (6.2) using Monte-Carlo calculations that determine fitnesses. We then perform a theoretical analysis.

### 6.2.1 Monte-Carlo Simulations

We follow the setup in [147] for our Monte-Carlo experiments. The important step is the construction of the capture time matrix  $T \in \mathbb{R}^{3 \times 3}$  such that  $t_{ij} > 0$  represents the time-to-capture for pursuit strategy ( $P_i$ ) competing against evasive strategy ( $E_j$ ). Lemma 6.1 gives us that all elements of  $T$  are positive and finite. To construct  $T$ , we perform nine simulations, one for each element of  $T$ , such that each simulation has a pursuer and an evader starting from the same initial conditions. In each simulation the evader starts at the origin with a heading of zero. The pursuer's initial position is chosen from a uniform distribution on the square  $[-10, 10] \times [-10, 10]$ , and its initial heading from a uniform distribution on  $\mathbb{S}^1$ . The other parameters are the same for each simulation:  $\eta = \mu = 10$ ,  $\nu = .6$ ,  $\epsilon = 0.05$ ,  $\phi = 0.3$ ,  $\alpha = 0.2$ , and  $\kappa = 2$ . The results presented here remain qualitatively consistent for reasonable variations of these parameters. A detailed study of the effect of each parameter on capture times is a direction of future work.

For each generation, we compute ten time matrices  $T^k = [t_{ij}^k]$ ,  $k \in \{1, \dots, 10\}$ , such that each matrix corresponds to a different choice of pursuer initial conditions and evader random trajectory for column 2 (note that  $T^k$  denotes the  $k^{th}$  time matrix, not to be confused with matrix multiplication). The average matrix  $\bar{T} = [\bar{t}_{ij}]$  is defined by  $\bar{t}_{ij} = \frac{1}{10} \sum_{k=1}^{10} t_{ij}^k$ . Let  $\bar{T}(g)$  denote the average time matrix computed at generation  $g$ . For matrices  $\bar{M}(g) = \bar{T}^\#(g)$  and  $\bar{N}(g) = \bar{T}^T(g)$ , the fitness vectors are defined by

$$\begin{aligned}\mathbf{f}_P(g) &= \bar{M}(g)\mathbf{q}(g) \\ \mathbf{f}_E(g) &= \bar{N}(g)\mathbf{p}(g).\end{aligned}\tag{6.3}$$

The inverse and direct relationships between the time matrix and fitness for pursuers and evaders, respectively, ensure that high capture times have asymmetric fitness consequences for pursuers and evaders. Fitnesses (6.3) also encode the frequency dependence and coupling of the evolutionary dynamics (6.2) since the fitness of a

pursuer (evader) strategy depends on the population distribution of evader (pursuer) strategies. Another way of interpreting equations (6.3) is from the perspective of a focal pursuer (evader) employing a specific strategy in a given generation. The expected fitness of this individual depends on expected interactions with each evasive (pursuit) strategy, which in turn depends on the population distribution of evaders (pursuers).

Equations (6.2) and (6.3) give us the necessary tools to simulate the pursuit-evasion dynamics defined on the direct product of two simplexes. This is done for a set of 50 randomly chosen pairs of initial distributions  $\mathbf{p}(0)$  and  $\mathbf{q}(0)$ . Each set of initial conditions is propagated using equations (6.2) and (6.3) for 100 generations with new fitness matrices  $\bar{\mathbf{M}}(g)$  and  $\bar{\mathbf{N}}(g)$  calculated at each generation. The results of the simulation are plotted in Figure 6.3. Note that the trajectories eventually converge to the point corresponding to pure classical pursuit and pure classical evasion, i.e.  $\mathbf{p}_{eq} = \mathbf{q}_{eq} = \begin{bmatrix} 1 & 0 & 0 \end{bmatrix}^T$ . Further, the Monte-Carlo simulations point to a structure in the matrix  $\bar{\mathbf{T}}$  (and correspondingly in  $\bar{\mathbf{M}} = \bar{\mathbf{T}}^\#$  and  $\bar{\mathbf{N}} = \bar{\mathbf{T}}^T$ ) which we state below in Conjecture 6.1 without proof.

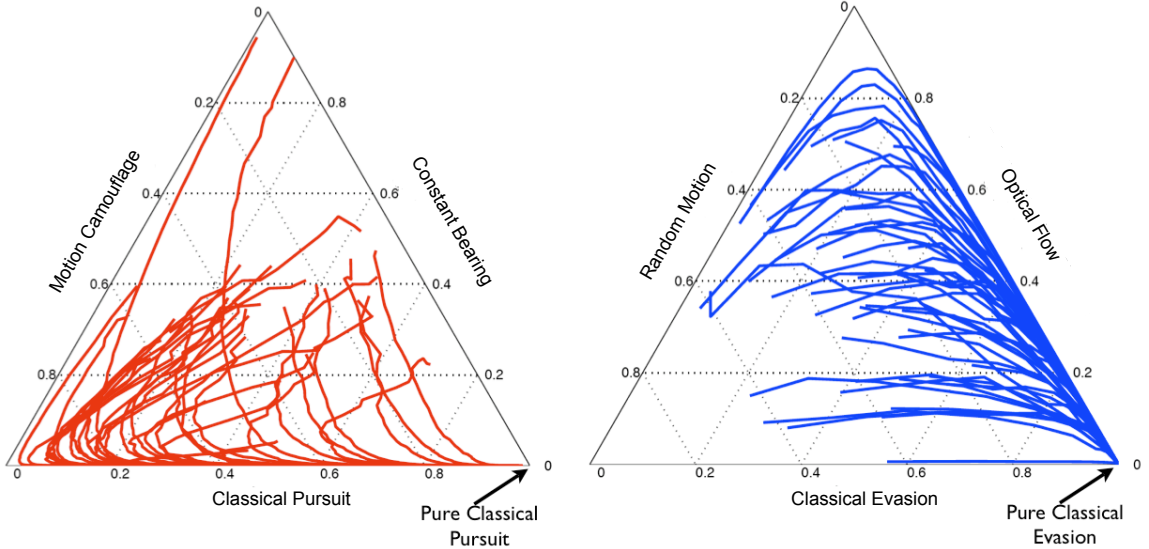


**Figure 6.3:** Monte-Carlo simulation of equations (6.2) and (6.3). The simplex on the left corresponds to pursuit strategies and the simplex on the right to evasive strategies. The curves on each simplex evolve in pairs  $(\mathbf{p}, \mathbf{q}) \in \Delta_2 \times \Delta_2$ ; there are 50 pairs in all corresponding to 50 different initial conditions  $(\mathbf{p}(0), \mathbf{q}(0))$ . Each pair of trajectories comprises 100 generations (iterations of equation (6.2)) and hence  $100 \times 10 = 1000$  evaluations of matrix  $\mathbf{T}$ . The trajectories all eventually converge to pure classical pursuit (left figure) and pure classical evasion (right figure), indicating that classical pursuit and classical evasion is the evolutionarily stable equilibrium of the dynamics.

**Conjecture 6.1.** *The first column of matrix  $\bar{T}$  is dominant, i.e.  $\overline{t_{i1}} > \overline{t_{i2}}$  and  $\overline{t_{i1}} > \overline{t_{i3}}$  for all  $i$ . Further, in the first column  $\overline{t_{11}} < \overline{t_{21}}$  and  $\overline{t_{11}} < \overline{t_{31}}$ .*

The claim in Conjecture 6.1 is made as a consequence of Monte-Carlo computations of matrix  $\bar{T}$  and consistent observations of the proposed matrix structure. A rigorous proof of Conjecture 6.1 requires careful analytical computations of capture times for the different strategies, a topic for future work. The structure of Conjecture 6.1 provides a useful tool for analyzing the evolutionary dynamics on the direct product of two simplexes and for proving convergence properties. We investigate this in the following subsection.

### 6.2.2 Theoretical Analysis

For some small time step  $\Delta t > 0$ , we can rewrite the equations (6.2) as follows:

$$\begin{aligned} \frac{1}{\Delta t} (p_i(g+1) - p_i(g)) &= p_i(g) \frac{f_{Pi} - \widehat{f}_P}{\Delta t \widehat{f}_P} \\ \frac{1}{\Delta t} (q_j(g+1) - q_j(g)) &= q_j(g) \frac{f_{Ej} - \widehat{f}_E}{\Delta t \widehat{f}_E}. \end{aligned}$$

In the limit  $\Delta t \rightarrow 0$  and with a change of timescale, we arrive at the set of differential equations

$$\begin{aligned} \dot{p}_i &= \frac{p_i}{\widehat{f}_P} \left( f_{Pi} - \widehat{f}_P \right) \\ \dot{q}_j &= \frac{q_j}{\widehat{f}_E} \left( f_{Ej} - \widehat{f}_E \right). \end{aligned} \tag{6.4}$$

Consider a constant matrix  $T$  that obeys the structure of Conjecture 6.1. Further let  $M = T^\#$  and  $N = T^T$ . Defining fitness vectors  $\mathbf{f}_P = M\mathbf{q}$  and  $\mathbf{f}_E = N\mathbf{p}$  analogous to equation (6.3), and substituting into (6.4) we get

$$\begin{aligned} \dot{p}_i &= \frac{p_i}{\mathbf{p}^T M \mathbf{q}} ((M\mathbf{q})_i - \mathbf{p}^T M \mathbf{q}) \\ \dot{q}_j &= \frac{q_j}{\mathbf{q}^T N \mathbf{p}} ((N\mathbf{p})_j - \mathbf{q}^T N \mathbf{p}). \end{aligned} \tag{6.5}$$

Equations (6.5) are a form of the replicator dynamics (see Chapter 2) for two interacting populations with fitnesses defined by linear functions of the population distributions. Critical to arriving at equations (6.5) is the assumption that  $T$  is constant and thus  $M$  and  $N$  are constant, which is justified by a ‘law of large numbers’ argument

[147]. Further, the assumption makes the analysis of equations (6.5) tractable, and hence allows us to formally investigate the convergence shown in the Monte-Carlo experiments.

The system of equations (6.5) is a four-dimensional system evolving on  $\Delta_2 \times \Delta_2$ . There are several possible solutions of the dynamics on these simplexes. For instance, all vertex pairs (pairs of pure strategies) are fixed points. Further, a strategy that is initially absent does not emerge, i.e.,  $p_i(0) = 0 \implies p_i(t) = 0, \forall t$ , and the same holds for  $q_j$  (replicator dynamics are said to be *non-innovative* as they lack mutation). In order to investigate the coupled replicator dynamical system (6.5), we first study the simpler single population replicator dynamics given by

$$\dot{q}_i = \frac{q_i}{\mathbf{q}^T \mathbf{f}} (f_i - \mathbf{q}^T \mathbf{f}), \text{ for } i = 1, 2, 3. \quad (6.6)$$

The fitness functions for the system of equations (6.6) are assumed to satisfy the following properties:

- *Property 1:*  $f_i \equiv f_i(t)$ ,  $i = 1, 2, 3$ , are each distinct functions of time, i.e.,  $f_i \neq f_j$  pointwise. If this were not the case then populations  $i$  and  $j$  would be indistinguishable from the perspective of evolutionary dynamics.
- *Property 2:* The functions  $f_i(t)$  are each globally Lipschitz, bounded and positive for all  $t \geq 0$ .
- *Property 3:* The functions  $f_i(t)$  have a single dominant fitness; without loss of generality,  $f_3(t) > f_2(t)$  and  $f_3(t) > f_1(t)$  for all  $t \geq 0$ .

**Lemma 6.2.** *Assume initial conditions are restricted to the domain  $D = \{\mathbf{q} \in \Delta^2 | q_3 > 0\}$ . The dynamics (6.6), satisfying Properties 1-3, have a unique asymptotically stable equilibrium point  $\mathbf{q}_{eq} = \begin{bmatrix} 0 & 0 & 1 \end{bmatrix}^T$  attracting all initial conditions in  $D$ .*

*Proof.* The proof is in Appendix E.1. □

The case of Lemma 6.2 with each  $f_i$  constant is considered in [147]. We now return to the coupled set of equations (6.5) and state the main theorem of this section. Here we employ the dominant structure of matrix  $T$ , assuming that Conjecture 6.1 holds, to prove convergence.

**Theorem 6.1.** *Assume initial conditions are restricted to the domain  $D_2 = \{(\mathbf{p}, \mathbf{q}) \in \Delta_2 \times \Delta_2 | p_1 > 0, q_1 > 0\}$ . Let matrix  $T$  satisfy Conjecture 6.1 with  $M = T^\#$*

and  $N = T^T$ . Then, the coupled replicator dynamics (6.5) have a unique asymptotically stable equilibrium point  $\mathbf{p}_{eq} = \mathbf{q}_{eq} = \begin{bmatrix} 1 & 0 & 0 \end{bmatrix}^T$  attracting all initial conditions in  $D_2$ .

*Proof.* The invariance of the domain  $D_2$  with respect to the dynamics (6.5) follows from the invariance of the domain  $D$  in the proof of Lemma 6.2. The column dominant structure of matrix  $T$  implies that the first element of the fitness vector  $\mathbf{f}_E = N\mathbf{p} = T^T\mathbf{p}$  is dominant. That is, regardless of the population distribution  $\mathbf{p}$  at any time instant,  $f_{E1} > f_{E2}$  and  $f_{E1} > f_{E3}$ . Hence we can use Lemma 6.2 to conclude that regardless of the evolution of the population vector  $\mathbf{p}$ , the population vector  $\mathbf{q}$  will asymptotically converge to  $\mathbf{q}_{eq} = \begin{bmatrix} 1 & 0 & 0 \end{bmatrix}^T$ .

Asymptotic stability implies that for every  $\epsilon > 0$  there exists a time  $t_1 \geq 0$  such that  $t > t_1 \implies \|\mathbf{q} - \mathbf{q}_{eq}\| < \epsilon$ . From the calculations in Lemma E.1 in Appendix E,  $\|\mathbf{q} - \mathbf{q}_{eq}\| < \epsilon \implies f_{P1} > f_{P2}$  and  $f_{P1} > f_{P3}$  for

$$\epsilon = \min \left\{ \frac{2(m_{11} - m_{21})}{(m_{11} - m_{21}) + \|M\|_1}, \frac{2(m_{11} - m_{31})}{(m_{11} - m_{31}) + \|M\|_1} \right\}.$$

Hence we can apply Lemma 6.2 again to the dynamics of  $\mathbf{p}$  to conclude that after time  $t_1$ , the population vector  $\mathbf{p}$  will also asymptotically converge to  $\mathbf{p}_{eq} = \begin{bmatrix} 1 & 0 & 0 \end{bmatrix}^T$ .  $\square$

In Figure 6.4 we simulate the dynamics in equations (6.5), for a particular calculation of matrix  $T$ , showing smooth convergence to the unique stable equilibrium. This can be compared to the Monte-Carlo simulations of Figure 6.3. From a game-theoretic perspective, the stable equilibrium point corresponds to the single unique pure Nash equilibrium of the bi-matrix game, for payoff matrices  $M$  and  $N$ .

In this section we have performed a computational and theoretical analysis of the evolutionary dynamics corresponding to the competition between a population of pursuers and a population of evaders, each having three strategies. We have shown convergence to a unique stable pure-strategy equilibrium corresponding to classical pursuit and classical evasion. This differs from the solution in [147], where the authors study the three pursuit strategies as a ‘game against nature’, each competing independently against nonreactive evasive strategies. There the evolutionary dynamics converge to the motion camouflage pursuit strategy. The competition of pursuers with a reactive set of evaders introduces a rich set of possibilities for evolutionary outcomes. Indeed, by comparison to the results of [147], we see that making available alternative evader strategies affects the evolved strategies for both pursuers and

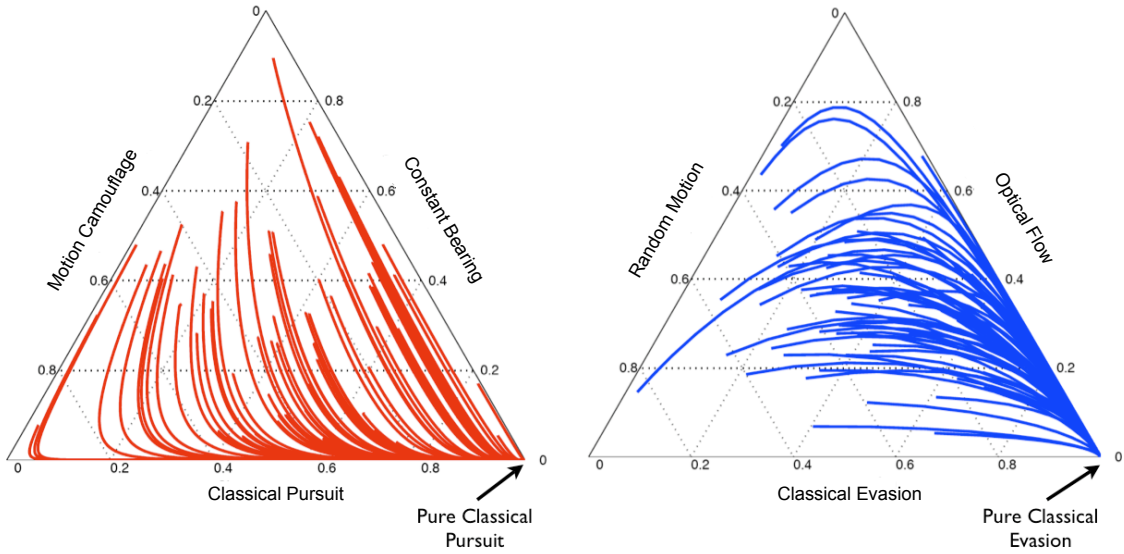


**Figure 6.4:** Simulation of smooth dynamics (6.5). The capture time matrix  $T$  is chosen to be the mean of 50 Monte-Carlo computations of capture time matrices  $T^k$ ;  $M = T^\#$  and  $N = T^T$ . The plot on the left shows the population vector  $\mathbf{p}$  and the one on the right shows  $\mathbf{q}$ . 50 pairs of trajectories are plotted with initial conditions chosen from a uniform random distribution on the space of two simplexes  $\Delta_2 \times \Delta_2$ . Comparisons to the Monte-Carlo simulations in Figure 3 show strong similarities.

evaders. We note that one need not restrict to the three chosen pursuit or evasive strategies; other choices of strategies may be appropriate depending on the context.

We now shift focus to employing pursuit and evasive behaviors for collective motion. In the following section we examine classical pursuit and classical evasion as this pair constitutes the evolutionary equilibrium of our strategy space.

### 6.3 Collective Motion

The multi-agent dynamics described in this section are motivated in part by the intriguing dynamics of social forging in groups of cannibalistic migratory locusts [5, 112]: individuals pursue other conspecifics in front of them and evade individuals approaching from behind. Inspired by these dynamics of cannibalistic locusts, and also by prior work on cyclic pursuit [67, 69, 68], we study the collective dynamics of steered particles with each exhibiting classical pursuit and evasive behaviors simultaneously.

Consider a system of  $N$  agents indexed by  $j = 1, \dots, N$ , each having position  $r_j = x_j + iy_j$  and heading  $\theta_j$ . The agents are steered particles with constant speed  $v > 0$  and steering control  $u_j$ . Similar to equations (6.1), the kinematics of the agents

are given by

$$\dot{r}_j = v e^{i\theta_j}, \quad \dot{\theta}_j = u_j. \quad (6.7)$$

For each agent we define baseline vectors  $b_{j+} = r_{j+1} - r_j$  and  $b_{j-} = r_{j-1} - r_j$ . Note that  $j + 1$  and  $j - 1$  are defined mod  $N$ ; i.e.,  $b_{N+} = r_1 - r_N$  and  $b_{1-} = r_N - r_1$ . The control law  $u_j$  is given by

$$u_j = u_{jP} + u_{jE} = K \left\langle i e^{i\theta_j}, \frac{b_{j+}}{\|b_{j+}\|} \right\rangle - \beta K \left\langle i e^{i\theta_j}, \frac{b_{j-}}{\|b_{j-}\|} \right\rangle, \quad (6.8)$$

for scalar gain  $K > 0$  and scaling parameter  $\beta > 0$ . The first term in the control law (6.8) is a classical pursuit term, with agent  $j$  pursuing agent  $j + 1$  by attempting to align its heading with the baseline between  $j$  and  $j + 1$  (i.e.,  $b_{j+}$ ). The second term is an evasive term with agent  $j$  evading agent  $j - 1$  by attempting to align its heading anti-parallel to the baseline between  $j$  and  $j - 1$ . The dynamics correspond to a cyclical interaction (sensing) topology between agents as illustrated in Figure 6.5.

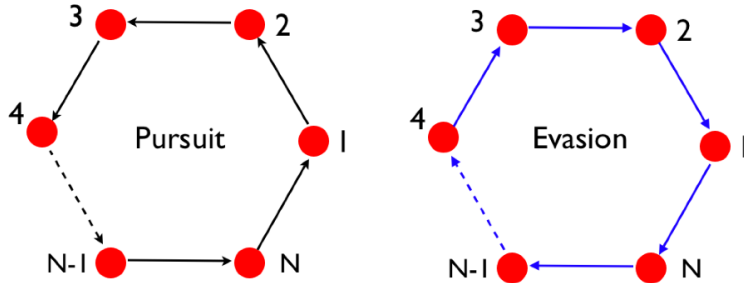


**Figure 6.5:** Sensing topology for cyclic pursuit and evasion. An arrow from agent  $j$  to agent  $k$  should be read as ‘ $j$  senses  $k$ ’. Agents pursue the agent immediately ahead and evade the agent immediately behind.

Simulations of the collective dynamics show several interesting outcomes:

- For  $\beta < 1$ , stable circular motions exist with agents traveling equally spaced around a circle of radius  $\frac{v}{K(1-\beta)\sin(\pi/N)}$ . This is illustrated for a formation of  $N = 8$  agents in Figure 6.6(a).
- At  $\beta = 1$  we observe a bifurcation. Specifically, the steady circular motions disappear and the agents diverge into an incoherent state for  $\beta > 1$  as shown in Figure 6.6(b).
- For  $\beta < 1$ , the circular motions are not the only stable steady motions. We also observe convergence to regular figure eight weaving patterns as illustrated

in Figure 6.6(c); the initial conditions in Figure 6.6(c) are the only change from the simulation in Figure 6.6(a). Observation of such weaving patterns was also reported for pure cyclic pursuit [67].

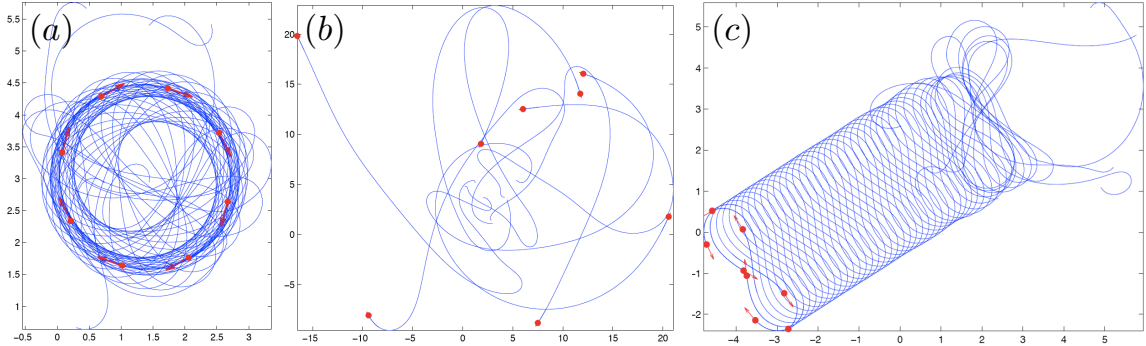


**Figure 6.6:** (a) Convergence to a circle for a group of  $N = 8$  agents with  $\beta < 1$ . Parameters are  $K = 5$ ,  $v = 1$  and  $\beta = 0.5$ . (b) Divergence into an incoherent state for  $\beta \geq 1$ , i.e., evasion is stronger than pursuit. Parameters are  $K = 5$ ,  $v = 1$  and  $\beta = 1.2$ . (c) Weaving figure eight solution for  $N = 8$  agents and  $\beta < 1$ . Parameters are  $K = 5$ ,  $v = 1$  and  $\beta = 0.5$ .

These results suggest that for stable circular motions to emerge from cyclic pursuit and evasion, the pursuit action must be stronger than the evasive action. This is consistent with [112] in which stable vortices for pursuit agents are observed. The authors [112] note that ‘pursuit facilitates the formation of clusters’ (cohesion) whereas ‘escape (evasion) leads to a homogenization of density’ (dispersion).

In the case of a large number of agents following the pursuit-evasion dynamics (6.7), (6.8), the agents settle quickly into a cyclical chain-like formation. The chain starts off with an arbitrary shape (dependent on initial conditions) and continually deforms (changes shape) on a slow time scale as illustrated in Figure 6.7. Simulations run for extended time do not show convergence of the formation to a regular motion; instead they show the continued slow deformation of the chain. An analysis of the chain-like formations as shown in Figure 6.7, perhaps using continuum methods and knot theory, is another topic of future work.

## 6.4 Final Remarks

In this chapter we have considered an evolutionary game of three strategies of pursuit against three strategies of evasion, two of which are reactive. Monte-Carlo simulations

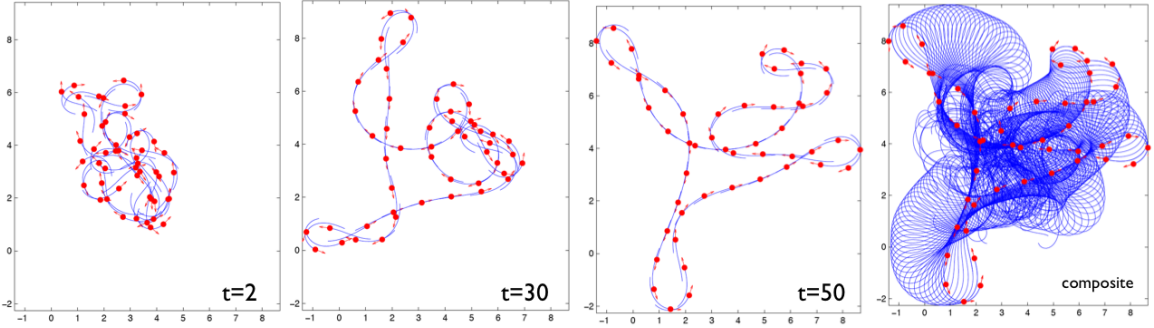


**Figure 6.7:** Chains for large  $N$ , here  $N = 50$ . The plots from left to right show snapshots at indicated times. The plot on the right is a composite showing trajectories of all agents over time. Parameters are  $K = 5$ ,  $v = 1$  and  $\beta = 0.5$ .

of the evolutionary dynamics, involving fitness computations for the interactions between the different pursuer and evader pairs, show convergence to a stable equilibrium of classical pursuit and classical evasion. Using the structure of the fitness matrices observed in these simulations, we analytically prove the convergence of replicator dynamics to the same classical pursuit and classical evasion equilibrium as in our Monte-Carlo simulations. This effort builds on prior work [147] where it was shown that replicator dynamics converge to motion camouflage pursuit when competing against nonreactive evasion strategies. Our result provides an interesting contrast to the earlier result [147] and further illustrates that the consequences of evolutionary dynamics depend significantly on the space of strategies considered.

Motivated by the outcome of the evolutionary game, and by the behavior of cannibalistic locusts, we have investigated a novel control scheme involving agents performing simultaneous pursuit and evasion on cyclical interaction topologies. In the case that the pursuit gain is larger than the evasion gain, simulations indicate local convergence to circular motion formations of specified radius, as well as local convergence to more complex weaving patterns. Exploring the use of different pursuit and evasive behaviors and their corresponding collective outcomes is a topic of future work.

# Chapter 7

## Decision-Making Dynamics in Honeybee Swarms

A honeybee colony\* is a fascinating natural example of an emergent system where an aggregation of thousands of individuals functions together as a composite integrated unit. Other examples include the gigantic colonies of leafcutter ants [149], army ants [13], or fungus growing termites [1, 116]. The colony functions as a truly decentralized system where local interactions among the bees yield group-level structure and function, critical to survival. A typical bee colony is composed mostly of (predominantly) sterile female worker bees, all of whom are daughters of the one fertile queen bee that lives in their midst [116]. A small set of male drone bees in the colony performs the fundamental reproductive task of mating with young queen bees from other nearby colonies. The worker bees perform most of the colony survival tasks including foraging, rearing the queen for reproduction, hive construction, and scouting for new potential nest sites during swarming. The scout bees in the swarm are among the most experienced, and correspondingly oldest, forager workers [28]. The focus of this chapter is on the decision-making dynamics of nest site selection among these scout bees during the colony swarming process. The book by Seeley [116] is an excellent reference for an in-depth look at all of the other captivating elements of honeybee colonies, in addition to the swarm decision-making discussed here.

Honeybee colonies reproduce by casting swarms, each of which comprises a queen accompanied by several thousand worker bees. A small fraction of the worker bees are known as scout bees and perform the task of locating suitable nest sites for the

---

\*While we use the term honeybee quite generally, the experimental evidence for the features of honeybees and swarms described in this chapter comes from *Apis mellifera*, the most commonly domesticated species [116].

swarm by engaging in a *democratic* [116] decision-making process of choosing among several competing options. This process involves the famous waggle dance [144] in which scouts advertise the location and quality of suitable nest sites by performing a distinctive dance on the surface of the swarm (the waggle dance is also used in foraging to signal flower locations). The collective nest site selection process among the scouts is known to have several of the typical elements of decentralized decision-making systems: *commitment* of individuals to options after sampling, *recruitment* of uncommitted individuals by those already subscribed to an option, and *decay* of preference affiliation over time (akin to the ‘leaking’ in leaky-accumulator models of neuronal decision-making [8]). Seeley et al. in a recent paper [118] have shown that scouts also send inhibitory *stop signals* to other scouts advertising alternative nest sites, thereby causing these scouts to cease dancing. This cross-inhibitory process has been shown to be critical to the ability of swarms to make decisions effectively, particularly when choosing between competing options of near-equal value.

In this chapter we study bifurcations in an analytical model of honeybee swarm decision-making from [118] and illustrate the critical role played by stop-signal inhibition in enabling swarms to manage the speed-accuracy tradeoff in the decision-making problem. The model from [118] is described in §7.1. §7.2 summarizes the analysis of the symmetric case of options with equal value from [118] and illustrates a pitchfork bifurcation in the dynamics. In §7.3 we present a general description of the bifurcations of the model for the asymmetric case of options with unequal value, and illustrate how the pitchfork bifurcation in the symmetric case is one slice through a more general cusp catastrophe bifurcation set corresponding to the dynamics. In §7.4 we show that the model has two timescales and derive an analytical expression for the slow manifold of the dynamics. We study a stochastic version of the model in §7.5 and summarize our findings in §7.6.

## 7.1 Model Description

We study a mean-field model of the swarm decision-making dynamics derived in [118]. We restrict to looking at the decision-making process of choosing between two options  $A$  and  $B$  for analytical tractability. Also, while scouts might advertise several options (on the order of 10 [116]) early on in the selection activity, only two or three options usually remain in the more advanced stages. The model has states  $y_A$ ,  $y_B$  and  $y_U$  corresponding to the fraction of scouts subscribed to (i.e., dancing for) option  $A$ , the fraction subscribed to option  $B$ , and the fraction uncommitted ( $U$ ) to either option,

respectively. The vector  $\mathbf{y} = [y_A \ y_B \ y_U]^T$  is a simplex vector satisfying  $y_i \geq 0$  for all  $i \in \{A, B, U\}$  and  $y_A + y_B + y_U = 1$ . The dynamics have four main processes:

- Commitment: Uncommitted scout bees commit to an option upon independently encountering one in the scouting process at rate  $\gamma_i$  for option  $i \in \{A, B\}$ .
- Recruitment: Scout bees committed to a particular option recruit uncommitted scouts to subscribe to that option (using the waggle dance) at rate  $\rho_i$  for option  $i \in \{A, B\}$ .
- Decay: The number of waggle dance circuits declines over time due to the fading interest of a committed scout at rate  $\alpha_i$  for option  $i \in \{A, B\}$ . Decay has been shown to be essential to consensus forming in the decision-making dynamics [115].
- Stop-signal: By the cross-inhibitory mechanism, scouts subscribed to a particular option inhibit those subscribed to alternative options at rate  $\sigma_i$  for option  $i \in \{A, B\}$ . The stop-signal is known to reduce waggle dancing and is typically delivered as a vibrational signal by the sender butting her head against the dancer [118].

$$\begin{array}{lll}
\text{COMMITMENT} & U \xrightarrow{\gamma_A} A & U \xrightarrow{\gamma_B} B \\
\text{RECRUITMENT} & A + U \xrightarrow{\rho_A} 2A & B + U \xrightarrow{\rho_B} 2B \\
\text{DECAY} & A \xrightarrow{\alpha_A} U & B \xrightarrow{\alpha_B} U \\
\text{STOP-SIGNAL} & A + B \xrightarrow{\sigma_A} A + U & B + A \xrightarrow{\sigma_B} B + U \\
\dot{y}_A = & \boxed{\gamma_A y_U} + \boxed{\rho_A y_A y_U} - \boxed{\alpha_A y_A} - \boxed{\sigma_B y_A y_B} \\
\dot{y}_B = & \boxed{\gamma_B y_U} + \boxed{\rho_B y_B y_U} - \boxed{\alpha_B y_B} - \boxed{\sigma_A y_B y_A}
\end{array}$$

**Figure 7.1:** Connections between the microscopic (top) and macroscopic (bottom) descriptions of the swarm decision-making dynamics. The set of four categories on the top show the four processes that are part of the decision-making dynamics (commitment, recruitment, decay, stop-signal), and the microscopic rate equations corresponding to each (for example  $U \xrightarrow{\gamma_A} A$  denotes the transition from  $U$  to  $A$  at rate  $\gamma_A$ ). The bottom pair of macroscopic mean-field equations (7.1) is color-coded to match each of the four processes.

The microscopic rate equations for the four processes described above are shown in Figure 7.1 (top). The corresponding mean-field equations are given by

$$\begin{aligned}\frac{dy_A}{dt} &= \gamma_A y_U + \rho_A y_A y_U - \alpha_A y_A - \sigma_B y_A y_B \\ \frac{dy_B}{dt} &= \gamma_B y_U + \rho_B y_B y_U - \alpha_B y_B - \sigma_A y_B y_A.\end{aligned}\tag{7.1}$$

These equations have been derived rigorously in [118] as a system-size expansion [139, 24] of the microscopic master equations [24]. Note that  $\dot{y}_U = -\dot{y}_A - \dot{y}_B$ .

The nest sites of swarms are typically tree cavities that provide good protection from predators and from harsh environmental conditions. Scout bees evaluate potential nest sites on a variety of metrics including cavity volume, cavity entrance size, height of the entrance from the ground, and the presence of earlier combs [143]. Further, various studies [31, 29, 116] have shown that scout bees have an innate scale of absolute nest site goodness or value that encapsulates these metrics. We use  $v_i > 0$  to denote this absolute value of nest site  $i \in \{A, B\}$ . Following the parameterization used previously in [118], we assume that all of the rates  $\gamma_i$ ,  $\rho_i$ , and  $\alpha_i$  may depend on the value  $v_i$  of the potential nest site with which they are associated. We set the commitment and recruitment rates  $\gamma_i = v_i$  and  $\rho_i = v_i$ , and the decay rates  $\alpha_i = \frac{1}{v_i}$ . The parameterization in [118] also assumes that the stop-signal rate  $\sigma_i$  is independent of site choice and hence  $\sigma_A = \sigma_B = \sigma$ . Substituting for these rates in (7.1) we obtain a pair of quadratic differential equations in three parameters  $v_A$ ,  $v_B$ , and  $\sigma$ :

$$\begin{aligned}\frac{dy_A}{dt} &= -\frac{1}{v_A} y_A + v_A y_U (1 + y_A) - \sigma y_A y_B \\ \frac{dy_B}{dt} &= -\frac{1}{v_B} y_B + v_B y_U (1 + y_B) - \sigma y_A y_B.\end{aligned}\tag{7.2}$$

Our analysis of bifurcations and timescale separation in the sections to follow focuses on this pair of coupled equations.

## 7.2 Symmetric Case

The symmetric case of equal options  $v_A = v_B = v$  was studied in [118]; we summarize the results here. Substituting  $v_A = v_B = v$  in (7.2), the symmetric dynamics are

given by

$$\begin{aligned}\frac{dy_A}{dt} &= \frac{-y_A}{v} + vy_U(1 + y_A) - \sigma y_A y_B \\ \frac{dy_B}{dt} &= \frac{-y_B}{v} + vy_U(1 + y_B) - \sigma y_A y_B.\end{aligned}\tag{7.3}$$

The dynamics (7.3) have three sets of equilibria (the fourth equilibrium set is always outside the simplex  $\Delta_2$ ) denoted  $(y_{Aeq}, y_{Beq})$  and given by

$$\begin{aligned}p_1 &= \left( \frac{2v^2}{1 + v^2 + \sqrt{1 + 2v^2 + 9v^4 + 4v^3\sigma}}, \frac{2v^2}{1 + v^2 + \sqrt{1 + 2v^2 + 9v^4 + 4v^3\sigma}} \right) \\ p_2 &= \left( \frac{1}{2} - \frac{1}{2v^2} + \frac{1}{2v^2} \sqrt{(v^2 - 1)^2 - \frac{4v^3}{\sigma}}, \frac{1}{2} - \frac{1}{2v^2} - \frac{1}{2v^2} \sqrt{(v^2 - 1)^2 - \frac{4v^3}{\sigma}} \right) \\ p_3 &= \left( \frac{1}{2} - \frac{1}{2v^2} - \frac{1}{2v^2} \sqrt{(v^2 - 1)^2 - \frac{4v^3}{\sigma}}, \frac{1}{2} - \frac{1}{2v^2} + \frac{1}{2v^2} \sqrt{(v^2 - 1)^2 - \frac{4v^3}{\sigma}} \right).\end{aligned}\tag{7.4}$$

These equilibria correspond to a pitchfork bifurcation in the dynamics with a bifurcation set (parameterized by  $v$ ):

$$\sigma^* = \frac{4v^3}{(v^2 - 1)^2}.\tag{7.5}$$

For  $\sigma < \sigma^*$ , the equilibria  $p_2$  and  $p_3$  from (7.4) are imaginary and  $p_1$  is stable. A pitchfork bifurcation occurs at  $\sigma = \sigma^*$  resulting in two stable equilibria  $p_2$  and  $p_3$  and one unstable equilibrium  $p_1$  for  $\sigma > \sigma^*$ , as illustrated in Figure 7.2 (see also Case 1 in Figure 7.4).

The pitchfork bifurcation describes an important feature of the stop-signal based cross-inhibition on the decision dynamics. For values of stop-signal below the threshold  $\sigma^*$ , the only stable equilibrium of the dynamics is the symmetric ( $y_A = y_B$ ) equilibrium resulting in a deadlock in the decision-making process with equal fractions of the population subscribed to each option. This situation is suboptimal from a speed-accuracy perspective since the time spent in deadlock between equal options does not yield any greater accuracy in decision-making. Ideally, we would like for the system to be able to spontaneously ‘flip a coin’ between the equal alternatives in order to make a fast decision. This is exactly what is enabled by the cross-inhibitory mechanism. Post bifurcation ( $\sigma > \sigma^*$ ), the two stable equilibria correspond to a choice of one of the two alternatives, and the system dynamics are attracted to one or the other based on initial conditions, thereby breaking deadlock (see inset phase portraits in Figure 7.3).

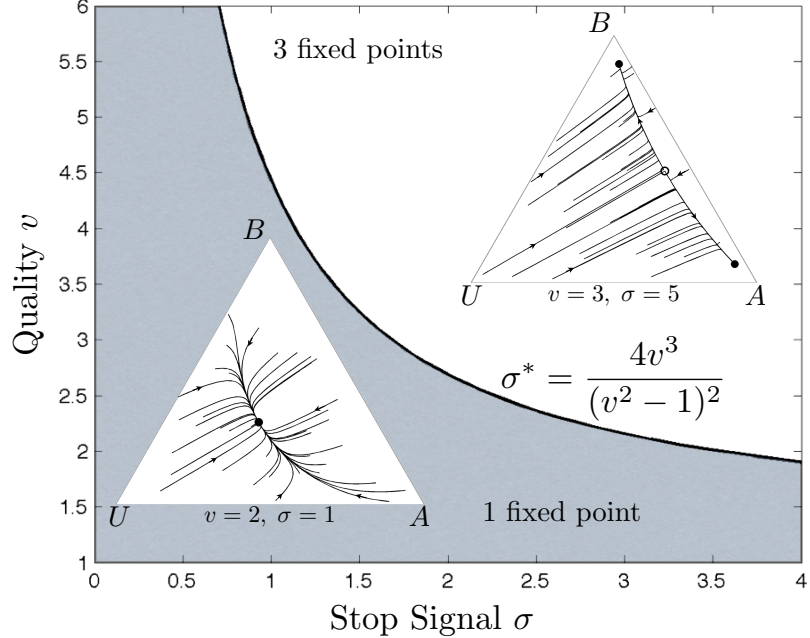


**Figure 7.2:** Pitchfork bifurcation set for the stop-signalling dynamics with equal alternatives (7.3). The dark region below the curve  $\sigma^* = \frac{4v^3}{(v^2-1)^2}$  has a single stable equilibrium; the light region above the curve has three equilibria, two of which are stable. The pitchfork bifurcation for adequately high stop-signal  $\sigma$  breaks the deadlock in decision-making between equal alternatives. Insets show typical phase portraits in each region.

### 7.3 Asymmetric Case

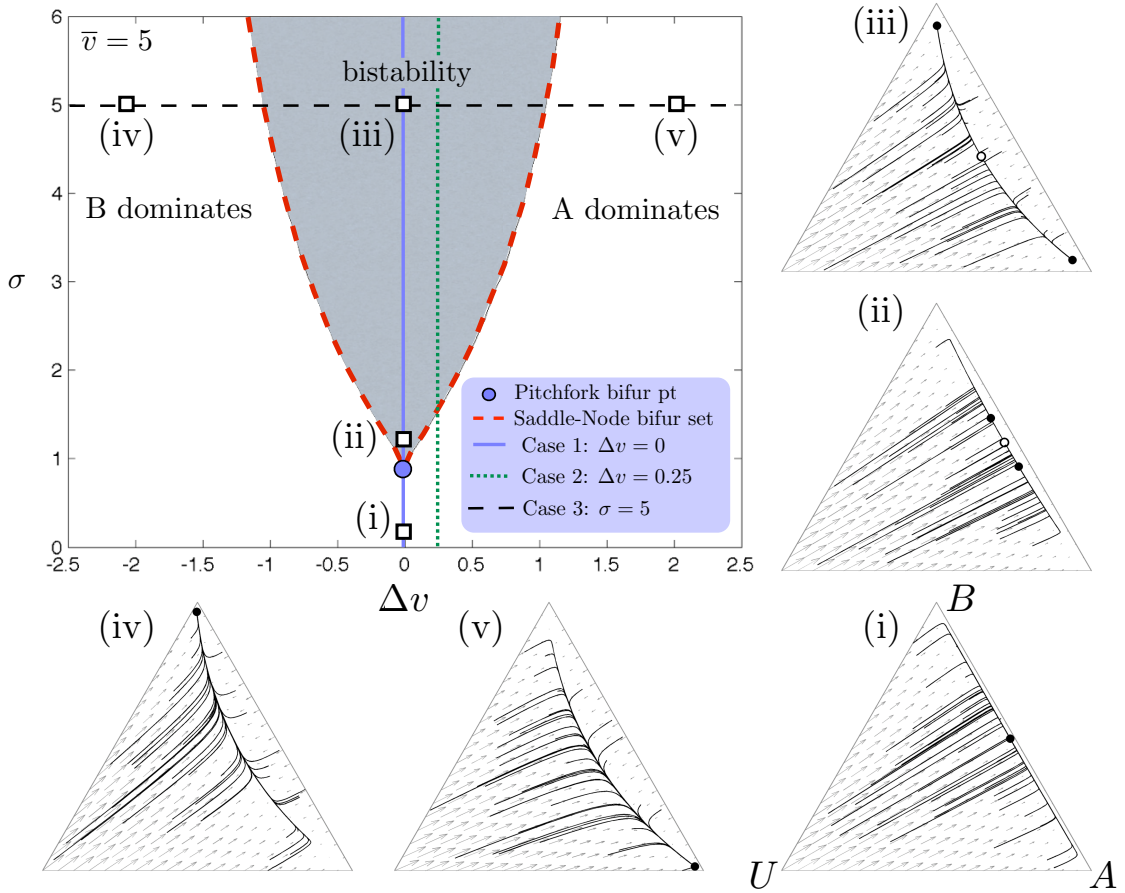
Looking back at the bifurcations for the  $N = 2$  case of the replicator-mutator dynamics shown in Figure 3.4, we see that as symmetry is broken, the (structurally unstable) pitchfork bifurcation disintegrates into a saddle-node bifurcation and a stable branch of equilibria. These bifurcation plots correspond to slices through the cusp catastrophe, plotted in Figure 2.6. In a qualitatively similar sense, the symmetric pitchfork bifurcation for the stop-signaling dynamics from §7.2 disintegrates into saddle nodes for  $v_A \neq v_B$ , with a corresponding cusp catastrophe bifurcation set. Before we plot this bifurcation set, the following change of variables helps simplify notation: let mean quality  $\bar{v} = \frac{v_A + v_B}{2}$  and quality difference  $\Delta v = v_A - v_B$ . Then

$$v_A = \bar{v} + \frac{\Delta v}{2} \text{ and } v_B = \bar{v} - \frac{\Delta v}{2}. \quad (7.6)$$

Substituting (7.6) in (7.2) gives

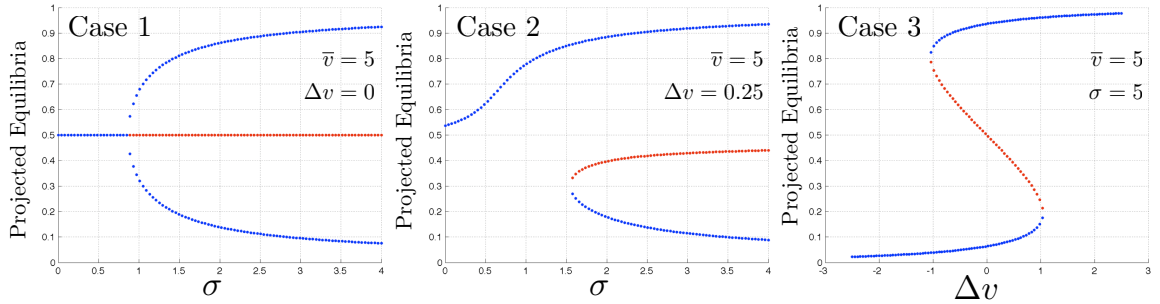
$$\begin{aligned}\frac{dy_A}{dt} &= \frac{-2y_A}{2\bar{v} + \Delta v} + \left(\bar{v} + \frac{\Delta v}{2}\right)y_U(1 + y_A) - \sigma y_A y_B \\ \frac{dy_B}{dt} &= \frac{-2y_B}{2\bar{v} - \Delta v} + \left(\bar{v} - \frac{\Delta v}{2}\right)y_U(1 + y_B) - \sigma y_A y_B.\end{aligned}\quad (7.7)$$

The bifurcation set for the dynamics (7.7) is plotted for a chosen value of  $\bar{v}$  in Figure



**Figure 7.3:** Bifurcation diagram for the stop-signaling dynamics (7.7). The dashed red curves are the saddle-node bifurcation set for  $\Delta v \neq 0$ , the blue circle is the pitchfork bifurcation point for  $\Delta v = 0$ . The horizontal and vertical lines mark three bifurcation cases as indicated in the legend (see also Figure 7.4). Case 1 corresponds to a pitchfork bifurcation, Case 2 corresponds to a saddle-node bifurcation, and Case 3 corresponds to hysteresis (these can be seen clearly in Figure 7.4). The phase portraits marked (i)-(v) correspond to the squares marked on the  $\Delta v - \sigma$  space. The bifurcation set is qualitatively identical to that of the cusp catastrophe shown in Figure 2.6. This plot corresponds to  $\bar{v} = 5$ ; plots for other values of  $\bar{v}$  are qualitatively similar as shown in Figure 7.5.

7.3<sup>†</sup>. The corresponding sets for other values of  $\bar{v}$  are qualitatively identical (see also Figure 7.5). The set divides the equilibria of the dynamics into three regions: *bistability* with two stable equilibria close to the  $A$  and  $B$  corners of the simplex and an unstable central equilibrium; *A dominates* with a single equilibrium such that  $y_{Aeq} > y_{Beq}$ ; *B dominates* with a single equilibrium such that  $y_{Beq} > y_{Aeq}$ . Figure 7.3 also shows typical phase portraits of the dynamics at various points in the  $\Delta v - \sigma$  parameter space, illustrating the pitchfork and saddle-node bifurcations.



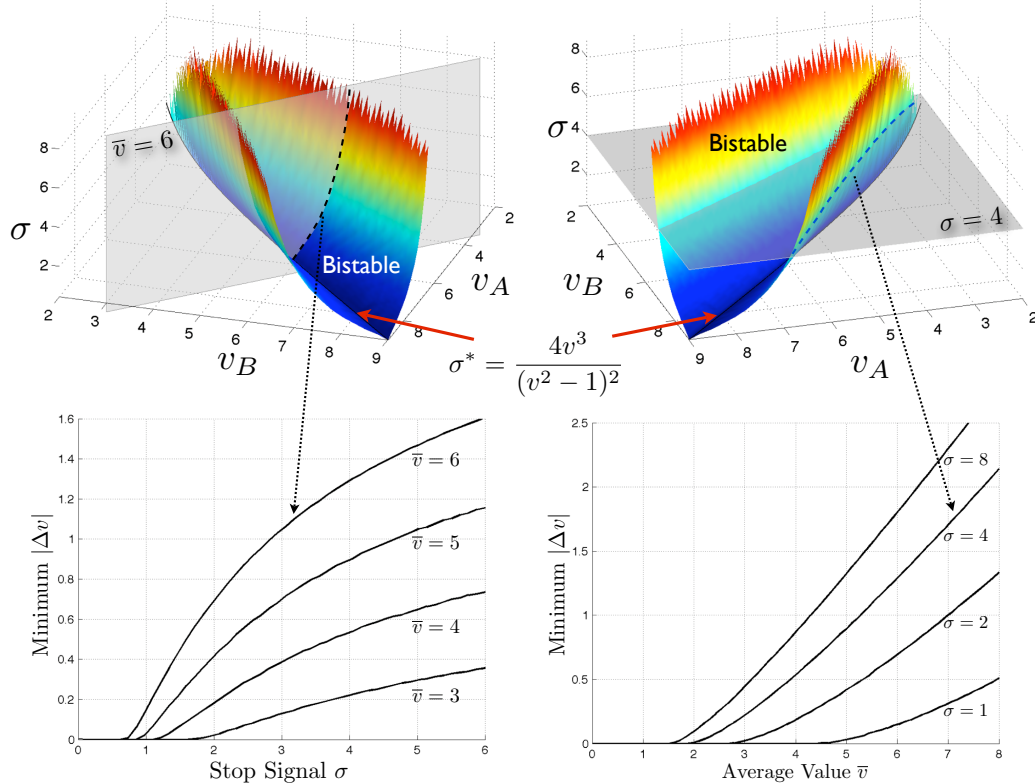
**Figure 7.4:** Bifurcations of the three cases from Figure 7.3. The vertical axis on each plot is given by  $\frac{1}{2} + \frac{y_{Aeq} - y_{Beq}}{2}$ , and corresponds to equilibria of the dynamics projected orthogonally onto the  $y_U = 0$  boundary of the simplex. Blue curves correspond to stable sinks and red curves to unstable saddles.

Figure 7.4 shows bifurcation plots of the dynamics corresponding to the three cases (slices of the cusp catastrophe bifurcation set) from Figure 7.3. The two-dimensional equilibria of the dynamics denoted  $(y_{Aeq}, y_{Beq})$  are plotted in one dimension (vertical axis ‘Projected Equilibria’) in Figure 7.4 by projecting each equilibrium orthogonally onto the  $y_U = 0$  boundary of the simplex. This projection is given by  $\frac{1}{2} + \frac{y_{Aeq} - y_{Beq}}{2}$ . Figure 7.4 clearly shows the pitchfork bifurcation (Case 1), saddle-node bifurcation (Case 2), and hysteresis (Case 3) of the cusp catastrophe.

The full bifurcation set of the dynamics (7.2) in three parameters  $v_A$ ,  $v_B$  and  $\sigma$  is plotted in Figure 7.5. The bifurcation set in Figure 7.3 is a slice through this three-parameter set corresponding to  $\bar{v} = \frac{v_A + v_B}{2} = \text{constant}$  (i.e., orthogonal to  $\Delta v = 0$ ). The bottom two plots in Figure 7.5 are level curves of the three parameter bifurcation set corresponding to the  $\sigma - \Delta v$  (bottom left) and  $\bar{v} - \Delta v$  (bottom right) planes. The vertical axis in the level curve plots titled  $|\Delta v|$  corresponds to the minimum

<sup>†</sup>Analytical expressions for the equilibria of the dynamics in the asymmetric case are cumbersome to write down, but solvable using symbolic manipulation software. The bifurcation set is computed using analytical calculations of the equilibria of the dynamics and an iterative algorithm to determine the boundary of the set. This algorithm is described in Appendix G.

absolute difference in alternatives necessary for a unique equilibrium ( $A$  dominates or  $B$  dominates). Hence the region of parameter space below each level curve has bistability, and the region above has a unique stable equilibrium close to the correct alternative (the one with higher value).



**Figure 7.5:** Bifurcation set for the dynamics (7.2) in three parameters  $v_A$ ,  $v_B$  and  $\sigma$ . The top panels show two views of the three-dimensional bifurcation set. A vertical cut through this set orthogonal to the line  $v_A = v_B \iff \Delta v = 0$  gives the two-dimensional set shown in Figure 7.3. Hot colors correspond to higher values of  $\sigma$ . The bottom left plot shows level curves corresponding to a series of vertical slices of the the three-dimensional set orthogonal to  $\Delta v = 0$ . The bottom right plot shows level curves corresponding to a series of horizontal slices of the three-dimensional set parallel to the  $v_A - v_B$  plane.

There are four key decision-making features that are apparent in the bifurcation plots in Figures 7.3-7.5. *First*, while bistability is favorable for ‘fast’ decision-making when alternatives have near-equal value (plot (iii) in Figure 7.3), it is not favorable when alternatives are adequately different ( $|\Delta v|$  adequately large) since the ‘distracting’ attractor close to the incorrect low value alternative can lead to errors in decision-making (large  $\sigma$  Case 2 in Figure 7.4).

*Second*, for a given mean value  $\bar{v}$ , the minimum  $|\Delta v|$  necessary to precipitate a bifurcation in the dynamics resulting in a single attractor increases, with increasing stop-signal  $\sigma$  (Figure 7.5 bottom left); i.e. high-values of stop-signal make the collective decision dynamics less *sensitive* to differences between options. Another way of interpreting this is that for a high value of stop-signal, a high magnitude of difference in options is necessary (low sensitivity) to prevent the swarm from picking the incorrect low-value alternative by falling into the distracting attractor.

*Third*, for a given value of stop-signal  $\sigma$ , the minimum  $|\Delta v|$  for a single attractor grows asymptotically linearly with increasing  $\bar{v}$  (Figure 7.5 bottom right). This is similar to Weber's law of just-noticeable differences [17] from psychology which states that 'minimum difference in stimulus intensity required to discriminate between sources varies linearly with average intensity' [95].

*Fourth*, the level of stop-signal  $\sigma$  introduces a tradeoff in the collective dynamics between speed and sensitivity. High values of stop-signal enable fast dynamics when alternatives are of nearly equal value, but make the collective insensitive to differences between alternatives. Lower values of stop-signal promote sensitivity, at the cost of potentially expensive deadlock when alternatives are nearly equal. This tradeoff can potentially lead to intermediate evolved levels of stop-signal cross-inhibition in the decision-making dynamics.

## 7.4 Separation of Timescales

The phase portraits in Figure 7.3 show a clear separation of timescales in the dynamics 7.7. In phase portrait (iii) for example, trajectories converge quickly onto the slow manifold corresponding to the heteroclinic connections between the central saddle and the boundary stable equilibria. The dynamics then evolve slowly on (near) this slow manifold. In Appendix F, we use singular perturbation theory [54] to compute a rigorous analytical approximation to the slow manifold of the dynamics; these results are summarized below.

Singular perturbation theory requires the identification of a small parameter in the model and a coordinate transformation that converts the dynamics into the singular perturbation 'standard form'. In Appendix F, we use  $\epsilon := 1/\bar{v}$  as the small parameter (thereby assuming large  $\bar{v}$ ) and convert the dynamics to the standard form using the

coordinate transformation  $(y_A, y_B) \mapsto (x, z)$  given by

$$z = (1 + y_A)(1 + y_B)$$

$$x = \frac{1 + y_A}{1 + y_B}.$$

We then go on to show that the slow manifold is given analytically by the implicit expression

$$\frac{\sigma}{2\bar{v}} y_A y_B = \frac{y_U(1 + y_A)(1 + y_B)}{3 - y_U} \quad (7.8)$$

in the  $(y_A, y_B)$  coordinates, and by the explicit expression

$$z = \left( \frac{d\hat{x}^2 + 6 + \sqrt{D}}{2(2+d)\hat{x}} \right)^2 =: h(x), \quad (7.9)$$

$$\text{where } d = \frac{\sigma}{\bar{v}}, \quad \hat{x} = \sqrt{x} + \frac{1}{\sqrt{x}} \text{ and } D = (d\hat{x}^2 + 6)^2 - 4d\hat{x}^2(2+d),$$

in the  $(x, z)$  coordinates.

In Figure 7.6, we plot a comparison of the analytically derived slow manifold (7.8) (or equivalently (7.9)) and trajectories of the dynamics (7.7) for various combinations of parameters  $\sigma$  and  $\Delta v$ , for large  $\bar{v}$  (taken to be  $\bar{v} = 10$  for this plot). The match between the approximation and the trajectories is excellent, except for the case when both  $\Delta v$  and  $\sigma$  are large. This case violates the limiting conditions of the singular perturbation calculation, as discussed in Appendix F.

In Appendix F we also compute the slow-timescale dynamics on the slow manifold and show that the equilibria of these dynamics match those of the two-dimensional system (7.7) in certain limits (symmetric  $v_A = v_B$ ,  $\sigma \rightarrow 0$  and  $\sigma = v$ ). A more general analysis of the slow dynamics and their equilibria is a topic of future work.

One of the main reasons to pursue the timescale separation results discussed in this section is to attempt to reduce the two-dimensional system (7.7) to a one-dimensional description. This reduction is particularly relevant when comparing the swarm dynamics described here with classical models of binary decision-making which are often in the form of one-dimensional stochastic differential equations (see the description of the drift diffusion model in §2.4 for example). We leverage the slow manifold calculation made here to explore this connection in more detail in a paper in preparation [95].

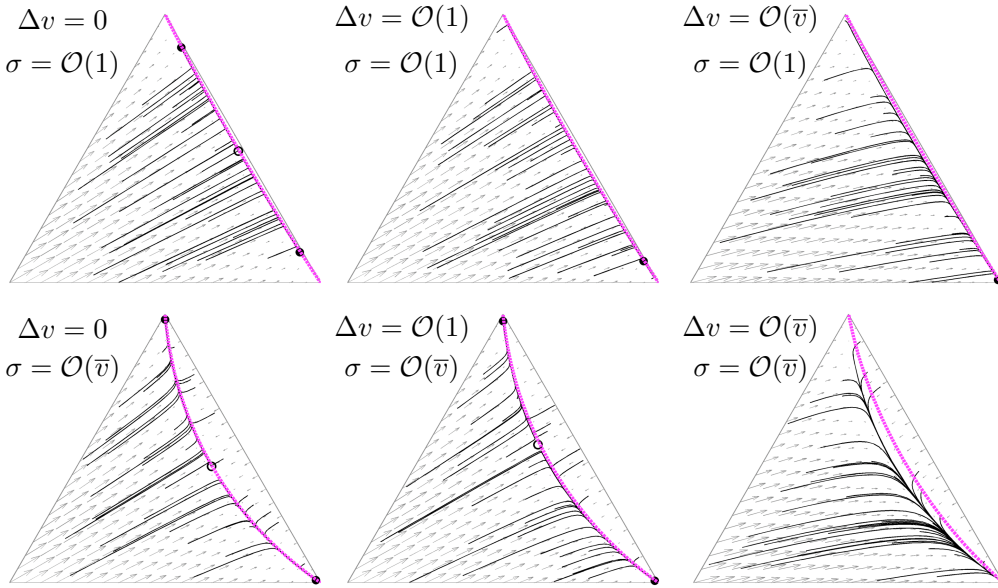


**Figure 7.6:** Comparison between the analytically computed slow manifold  $h(x)$  plotted in magenta and simulations of the stop-signaling dynamics (7.7). The match between the analytical slow manifold and the simulations is excellent, except for the case  $\Delta v = \mathcal{O}(\bar{v})$ ,  $\sigma = \mathcal{O}(\bar{v})$ . For this set of plots,  $\bar{v} = 10$ ,  $\mathcal{O}(\bar{v}) \equiv 10$  and  $\mathcal{O}(1) \equiv 1$ .

## 7.5 Stochastic Dynamics

Our analysis thus far has focused on bifurcations and timescale separation of the deterministic mean-field decision-making model (7.1). It is important to recognize, however, that the evaluations made by individual scout bees of nest site values  $v_i$  are inherently noisy. Experiments have shown that there is much overlap in distributions of dance strength (and correspondingly judgements of value) between scouts advertising a medium-quality and a high-quality nest site during the decision-making process [117]. Despite this noisy individual reporting of quality, there are clear differences in mean qualities reported, resulting in a sharp distinction at the swarm level.

In this section, we move beyond the deterministic model (7.1), and build a stochastic model to capture this inherent variability. The dynamics of this model can then be compared to other standard stochastic models of decision-making, such as the drift diffusion model (Figure 2.10(c)) which has been shown to optimally address the speed-accuracy tradeoff in two-alternative forced choice tasks [8]. We assume that the rates  $\gamma_i$ ,  $\rho_i$  and  $\alpha_i$  in (7.1) that depend on the stochastic measurement  $v_i$  are each subject to variability. Similar to the setup in [71], we add independent white noise terms of variance  $k^2$  to each of these rates (for example  $\alpha_i \mapsto \alpha_i + k\eta_{\alpha_i}$  where  $\eta_{\alpha_i}$

is a Gaussian random variable with mean 0 and variance 1) to obtain the stochastic decision-making dynamics

$$\begin{aligned} dy_A &= (\gamma_{AYU} + \rho_{AYAYU} - \alpha_{AYA} - \sigma_{BYAYB}) dt + k \sqrt{y_U^2 + y_A^2 + y_U^2 y_A^2} dW \\ dy_B &= (\gamma_{BYU} + \rho_{BYBYU} - \alpha_{BYB} - \sigma_{AYBYA}) dt + k \sqrt{y_U^2 + y_B^2 + y_U^2 y_B^2} dW. \end{aligned} \quad (7.10)$$

The parameter  $k$  in (7.10) sets the level of stochasticity or noisiness in the decision-making process; higher values of  $k$  correspond to noisier evaluations.

In Figure 7.7 we simulate the stochastic dynamics (7.10) using the parameterization used previously,  $\gamma_i = v_i$ ,  $\rho_i = v_i$ , and  $\alpha_i = \frac{1}{v_i}$ , for a finite time interval  $t \in [0, 30]$ . Parameters  $\bar{v}$ ,  $\Delta v$  and  $\sigma$  are chosen to correspond to the three cases shown in Figures 7.3 and 7.4. Each simplex in Figure 7.7 has 50 trajectories initialized at the origin. The dark dashed lines plotted are quorum decision thresholds ( $y_i = 0.7$ ,  $i = A, B$ ); a decision for a particular alternative  $A$  or  $B$  is assumed to be made when a trajectory first crosses the corresponding threshold. The simulations illustrate some key features of the stochastic decision-making dynamics:

- Deadlock and speed (Case 1): This case corresponds to equal alternatives  $\Delta v = 0$ . At low values of stop-signal  $\sigma$ , the population is in a state of deadlock with a majority of trajectories (75%) unable to reach a decision boundary (top row left). At intermediate levels of stop-signal, the bifurcation yields a much more successful decision-making outcome with most (82%) of the trajectories successfully breaking deadlock (top row middle). Speed increases (i.e. decision time shortens) at higher levels of stop-signal with all trajectories breaking deadlock (top row right).
- Intermediate stop-signal for accuracy (Case 2): This case corresponds to unequal alternatives  $\Delta v = 0.25$ . At low values of stop-signal, the population is in a state of near-deadlock with a single attractor slightly closer to corner  $A$  than  $B$ ; 60% of the trajectories do not reach a threshold (center row left). At intermediate levels of stop-signal, the bifurcation yields excellent decision-making performance with a vast majority (98%) of the trajectories reaching the correct threshold (center row middle). At higher levels of stop-signal, the increased speed of decision-making comes at the expense of poor accuracy; only 70% of trajectories reach the correct threshold (center row right). This performance degrades with increasing  $\sigma$ , illustrating a classical speed-accuracy trade-

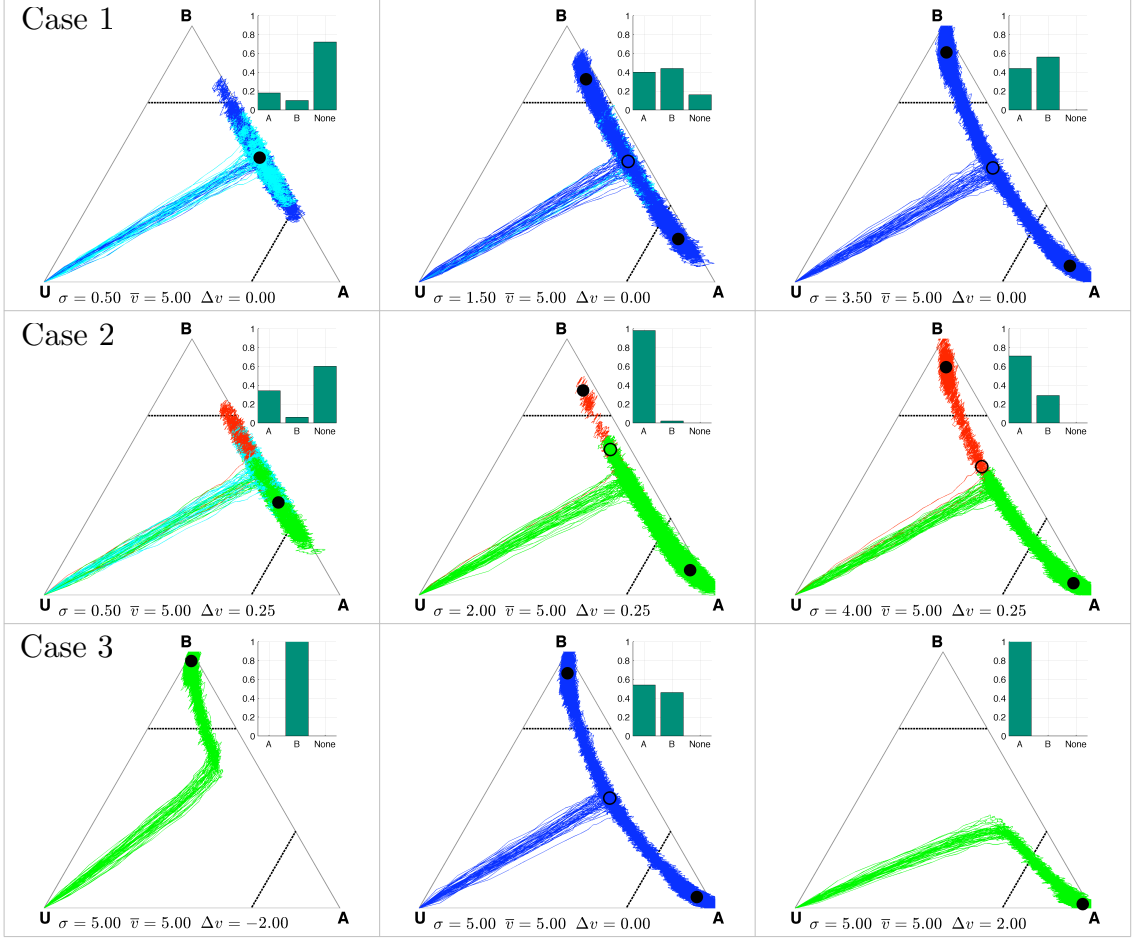


**Figure 7.7:** Simulations of the stochastic dynamics (7.10) with parameterization  $\gamma_i = v_i$ ,  $\rho_i = v_i$ ,  $\alpha_i = \frac{1}{v_i}$ ,  $k = 0.1$ , and for time  $t \in [0, 30]$ . Each simplex shows 50 trajectories initialized at the origin  $y_A = y_B = 0$  (correspondingly  $y_U = 1$ ). Circles are equilibria (filled stable, hollow unstable) of the deterministic dynamics (7.7), and the dashed lines are quorum thresholds  $y_A = 0.7$  and  $y_B = 0.7$ . The inset bar plots show the fraction of trajectories reaching each threshold; ‘none’ indicates trajectories reaching neither threshold in the given time (plotted in cyan). For  $\Delta v = 0$ , trajectories reaching either threshold are plotted in blue. For  $\Delta v \neq 0$  trajectories reaching the correct threshold (one with higher  $v_i$ ) are plotted in green, those reaching the incorrect threshold are in red. Parameter values appear below each plot.

off. However, unlike the speed-accuracy tradeoff for the linear DDM model [8] (also §2.4), here the tradeoff comes from nonlinear dynamics.

- **Hysteresis (Case 3):** The decision swings from  $B$ , to bistability, to  $A$ , as  $\Delta v$  varies from  $-2$  to  $2$ . Such continuous variations in quality difference  $\Delta v$  are unrealistic in a swarm decision dynamics, but may be more reasonable in other

decision systems (some examples are discussed in [95]). Experiments and analysis of neuronal decision-making models, for example, have shown that strong stimuli (similar to large  $\Delta v$  in this case) result in both faster and more accurate choices than weaker stimuli [38, 109, 99].

A detailed analysis of the speed-accuracy tradeoff described in Case 2 above is a topic on ongoing work. We are also in the process of investigating the role of parameter variations *during* the decision-making process for systems with two or more alternatives. Two such examples are shown in Figure 7.8:

- Breaking symmetric deadlock (Figure 7.8 left): The decision-making process is between two equal alternatives with value  $v_A = v_B = 3$ . The stop-signal  $\sigma$  ramps up linearly from an initial value of  $\sigma = 0$  to a final value of  $\sigma = 3$ . The increasing stop-signal enables the deadlock to be broken when  $\sigma > \sigma^* \approx 1.7$  with one option randomly winning out. This simulation is motivated in part by the fact that elapsed time might influence the computations that underlie decision processes since prolonged deliberation can be expensive [38]. In models of neuronal decision making [38, 11, 12], time-dependent ‘urgency’ signals (potentially analogous to the time-dependent stop-signal simulated here) have been suggested as a way to impose a soft deadline on deliberation.
- Deadlock enables better final outcome (Figure 7.8 right): For a system tuned to intermediate levels of stop-signal ( $\sigma = 1$  here), options of low quality result in deadlock. This enables the system to wait for other potentially better options to arrive into the mix and precipitate a decision. In this simulation, a third high-quality option ( $v_C = 4$ ) enters at  $t = 30$  and dominates.

## 7.6 Discussion

The decision-making process in honeybee swarms is rooted in the requirement that the swarm comes to a unanimous consensus decision about a suitable future home. The unanimity of the decision is critical because each swarm has only one queen, and because fragmentation of the swarm in the migration process to the new nest can be extremely costly, and potentially fatal. Experiments have shown that swarms are not only able to come to this consensus decision, but nearly always pick the *best* possible option of those available. This is remarkable given that the swarm decision-making process is completely decentralized and inherently stochastic.

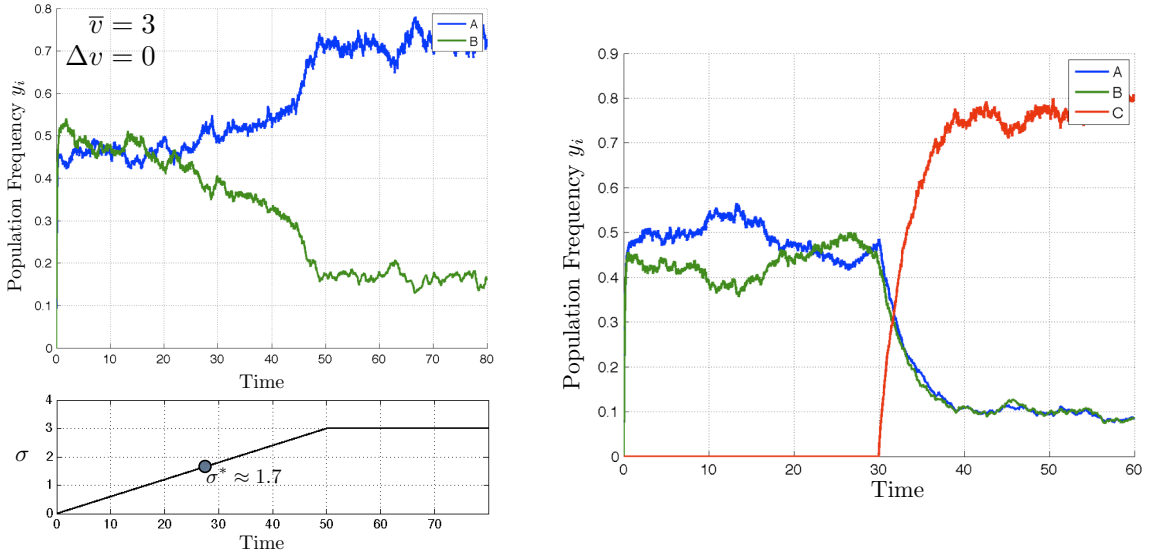


**Figure 7.8:** Simulations of the stochastic dynamics. (left) A deadlocked population is able to converge to a decision by picking one of two equal alternatives by slowly ramping up the stop-signal; the critical value of stop-signal for the pitchfork bifurcation is marked on the bottom plot. (right) For time  $t < 30$  the population is deadlocked while choosing between two low-value ( $v = 1$ ) equal alternatives; a third high-value alternative ( $v_C = 4$ ) enters the picture at  $t = 30$ , precipitating a decision in favor of this alternative.

As discussed in [116], there are two hypotheses for building consensus in a system. The first is known as the *compare and convert* hypothesis and corresponds to agents comparing their current state to neighbors and switching states to match those of neighbors with better outcomes. This is reminiscent of the imitation mechanism of the replicator-mutator dynamics in Chapters 3 and 4. The second is known as the *retire and rest* hypothesis in which agents have a decaying (leaking) interest in an option, thereby making each participant highly flexible in the decision-making process.

Experiments have shown that scouts in a honeybee swarm do not directly compare the options available, but instead rely on their decentralized interactions (recruitment, commitment, etc.) to produce a consensus outcome. It has also been shown that scouts decrease the number of dance circuits performed over time resulting in a decayed interest in the corresponding option. In addition to this decay, in this chapter we have shown the critical role played by the stop-signal cross-inhibitory mechanism in enabling effective swarm decision-making. Stop-signaling enables breaking deadlocks between equal alternatives and tunes the sensitivity of the dynamics to differences between alternatives. We prove a separation of timescales in the decision-

making model, thereby enabling a reduction of the dynamics to a one-dimensional system. Leveraging this reduction to make detailed comparisons between the stochastic swarm dynamics derived here, and other classical models of neuronal collective decision-making, is an important avenue of future work.

# Chapter 8

## Final Remarks

This thesis studies emergent collective behavior in selected biological systems from the perspective of evolution by natural selection. Our main aim has been to understand the mechanisms that endow biological collectives with extraordinary robustness and adaptability, and to leverage this understanding to inspire effective decision-making and collective motion protocols in artificial decentralized systems. We study four related topics: replicator-mutator dynamics, collective migration, pursuit and evasion, and swarm decision-making. The main conclusions from each of these topics are presented in §8.1. §8.2 comprises some of the common themes between the topics that have emerged through the analysis. We look ahead to future directions of investigation in §8.3.

### 8.1 Conclusions

*Replicator-mutator dynamics:* Much of the existing analysis of the replicator-mutator dynamics has focused on stable equilibria. The analysis in the literature has also primarily considered payoff and mutation matrices that are symmetric, which correspond to undirected payoff graph topologies. Here we prove conditions such that stable limit cycles in the replicator-mutator dynamics arise as a consequence of Hopf bifurcations for  $N \geq 3$  strategies and circulant payoff matrices. From a graph theoretic perspective, we show how breaking symmetry by considering directed graphs allows for oscillatory limiting behavior. We emphasize that the limit cycles are not restricted to circulant payoffs, but can exist for more general noncirculant cases as well. The simulations in Chapter 4 illustrate the structural stability in the dynamics to perturbations of circulant payoff, and show the tight connections between embed-

ded directed cycles in the payoff graph and the existence of stable limit cycles of the dynamics.

*Collective migration:* The study of leadership has received significant attention in both biology and multi-agent robotics. Agent-based simulations and experiments with fish schools have shown that a small group of leaders is capable of guiding the motion of a large group of followers. The ability of followers to leverage the investments made by leaders and essentially operate as free-riders in the system is an evolutionary paradox. In this work we focus on the role that the social graph connectivity plays in the evolutionary dynamics of a networked model of collective migration. We use tools from adaptive dynamics to study the all-to-all limit of the evolutionary model and derive bounds for branching of the population into leader and follower groups. For limited connectivity, we prove necessary and sufficient conditions for convergence of the noise-free migration model, and show that fitness of individuals in the stochastic model can be derived analytically using the Lyapunov equation. For random networks and lattices, we show a minimum connectivity bound that yields evolutionary population branching into leaders and followers. We also study a simple model of greedy adaptive nodes on small networks, inspired by collective robotic systems. We show that the network topology plays a critical role in determining the location of leaders in the adaptive system; we study bifurcations in node leadership as a function of investment costs.

*Pursuit and evasion:* Building on previous work that focuses on the evolutionary dynamics of three pursuit strategies playing against an environment of nonreactive evaders, we study an evolutionary game of three strategies of pursuit against three strategies of evasion, two of which are reactive. Monte-Carlo simulations of the evolutionary dynamics show convergence to a stable equilibrium of classical pursuit and classical evasion. Using the structure of the fitness matrices observed in these simulations, we analytically prove the convergence of replicator dynamics to the same classical pursuit and classical evasion equilibrium as in our Monte-Carlo simulations. We then go on to incorporate the winning pursuit and evasive strategies in a novel collective motion scheme and show conditions for the convergence of the dynamics to circular formations and more complex weaving patterns.

*Swarm decision-making:* We study bifurcations in a mean-field model of honeybee swarm decision-making and illustrate the critical role played by stop-signal cross-inhibition in enabling swarms to break deadlocks between equal alternatives and manage sensitivity to differences between unequal options. We carefully illustrate the cusp catastrophe bifurcation set of the dynamics and prove a timescale separation that

reduces the model to a one-dimensional system. We derive a stochastic version of the model and study its dynamics using simulations. These simulations illustrate the role of stop-signalling in managing the speed-accuracy tradeoff in the swarm decision dynamics.

## 8.2 Common Themes

In the introduction to the thesis, we made an effort to connect the various topics studied by looking at the systems from a robustness vs. adaptability perspective, as summarized in Figure 1.1. In this section, we identify some of the common themes that have emerged in our investigations of each topic. These themes are bifurcations, timescale separation, consensus and hysteresis.

*Bifurcations:* Bifurcations feature prominently in this thesis and include Hopf bifurcations studied in Chapters 3 and 4, cusp catastrophes studied in Chapter 7, bifurcations of collective dynamics in Chapter 6, and more complicated bifurcations of numerous equilibria as a function of graph topology in Chapter 5. These bifurcations correspond to macroscopic models of collective dynamics and represent significant changes in macroscopic emergent behavior as a consequence of relatively small changes in microscopic parameters governing inter-agent interactions. The nonlinear relationship between the microscopic and macroscopic descriptions that yields such bifurcations is an important hallmark of emergent systems.

*Timescale Separation:* Evolutionary models such as those studied in Chapters 3-6 inherently have two timescales. The fast timescale in these models corresponds to fitness computations as a function of ecological interactions. The slow timescale corresponds to the evolutionary process that modifies traits in the population as a result of fitness dependent replication and mutation. For example, for the migration problem in Chapter 5, the fast timescale corresponds to the stochastic migration dynamics and the slow timescale to the evolutionary change of agent strategies or investments. A very different kind of timescale separation is shown in Chapter 7. Here the fast timescale corresponds to individuals being attracted to an invariant decision manifold which corresponds roughly to the recruitment of uncommitted individuals to the decision making process. The slow timescale represents the dynamics along this manifold towards a collective decision.

*Consensus:* Consensus is critical to the functioning of most multi-agent cooperative systems and has inspired a vast literature in engineering, physics, mathematics and other fields. In fact, most systems (even those with complicated inter-agent

dynamics) that have emergent coordinated behavior can be approximated to first order by some form of simple linear consensus dynamics. In this thesis, consensus appears in the zero-mutation limit of the replicator-mutator model in Chapters 3 and 4, the stable OU process of the migration dynamics in Chapter 5, and the successful decisions of the swarm dynamics in Chapter 7.

*Hysteresis:* Hysteresis is a remarkable feature that has appeared several times in this thesis. In a basic sense, hysteresis corresponds to a delay associated with the restoration of a macroscopic state of a system with respect to variations in a bifurcation parameter. Specific parameters of the replicator-mutator Hopf bifurcations yield hysteretic curves (Figure 3.10(b) in Chapter 3 for example). Hysteresis was also observed for the adaptive evolutionary dynamics of migration in Chapter 5 and as part of the cusp catastrophe for the swarm dynamics in Chapter 7. In the context of animal behavior, hysteresis has been associated with *collective memory*. This refers to the phenomenon in which previous history of group structure influences collective behavior as individual interactions change, even though individuals have no knowledge of what that history is [15]. Figure 8.1 is a composite plot of the various hysteretic curves shown throughout the thesis.

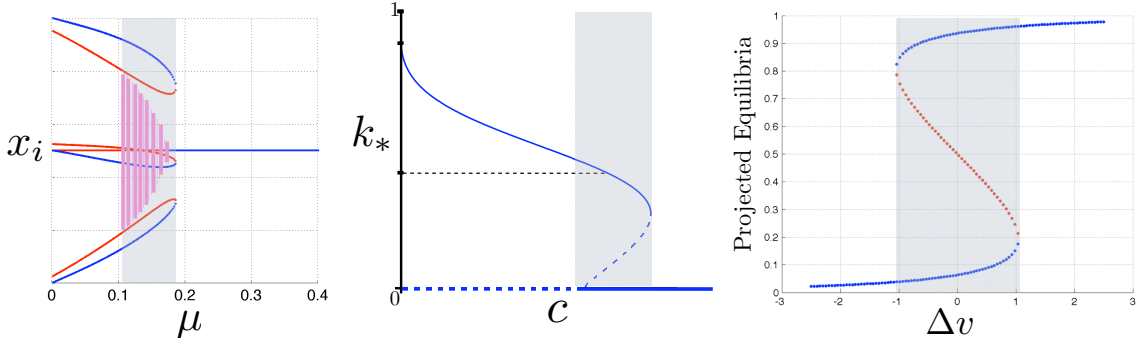


**Figure 8.1:** Three examples of hysteresis in the thesis. (left) from Figure 3.10(b) in Chapter 3, (center) from Figure 5.3 in Chapter 5, (right) from Figure 7.4 in Chapter 7. The shaded rectangles in each plot mark regions of bi(multi)-stability.

## 8.3 Looking Ahead

In a broad sense, the focus of robotic design and engineering over the past few decades has been on creating robust platforms that are configured to solve specific problems reliably, often with provable guarantees on performance. The rapid expansion of communication, distributed sensing, networking, learning algorithms, and advanced

software, however, have enabled a new generation of *intelligent* and interconnected multi-agent systems. These systems are often comprised of individual platforms or agents that are simple and robust, but can have collective emergent group behavior that is highly complex.

Two areas that are currently undergoing this transition from the focus on the individual agent, to the focus on both the individual as well as the collective, are autonomous driving for cars on the highway, and collective swarm robotics. In autonomous driving [138, 52], one of the main challenges involves the design of control protocols that leverage inter-agent interactions (sensing and communication between vehicles) to produce optimal group-level outcomes (efficient traffic flow and safe highway maneuvers). The alignment of individual interests (“I want to get there fast”) and group outcomes (overall traffic flow) poses an important challenge in such systems, and relates back to the evolutionary paradox of cooperation in natural swarms.

The developing area of swarm robotics focuses on using hundreds of relatively cheap and expendable robotic platforms that have limited sensing and communication capabilities, to perform collective tasks with a high degree of parallelism [79, 114]. These systems are designed to have significant flexibility and adaptability for applications such as foraging for information in dynamic and hazardous environments, distributed sensing, and distributed task allocation (the *Robobees* project at Harvard is a nice example [150, 79]). A key challenge in this area is the design of inter-agent control laws that yield provable collective solutions while still maintaining the adaptability and scalability of the system.

The impressive robust and adaptive behavior of biological collectives serves as an important source of inspiration in the design of *bio-inspired* algorithms for artificial multi-agent systems, including the two examples above. This is because natural collectives possess several attributes that are highly desirable for these artificial systems. The honeybee swarms studied in Chapter 7 are an excellent example: the decision-making in these swarms is completely decentralized, extensively accurate, highly adaptive, and robust to noise and disturbances. The analysis in Chapter 7 shows that cross-inhibition is a critical component of effective decision-making dynamics in honeybee swarms. We propose that cross-inhibition is a potentially important ingredient (along with recruitment, commitment and decay) for effective decision-making in robotic swarms as well. Hence, the study of cross-inhibition in the context of robotic swarms is a topic for future investigation.

Another important feature of natural collectives is the ability to rapidly transition between different regimes of behavior (collective foraging to prey evasion, for

example) without any centralized control. In macroscopic models, this feature manifests itself as bifurcations in the dynamics of the system as a function of usually one or two parameters. For the replicator-mutator model studied in Chapters 3 and 4, for example, bifurcations as a function of mutation strength  $\mu$  produce limit cycles. These bifurcations can be interpreted in the context of artificial multi-agent system as a transition from exploitation of a single option, to the cyclical examination of options, to the exploration of all options, as discussed in the Chapters 1 and 3, and illustrated in Figure 8.2. This ability to shape the macroscopic behavior of a collective system (comprising large numbers of agents) by tuning a single parameter is useful for applications. A detailed examination of the bifurcations studied in this thesis, applied to artificial collective systems, is an important future direction.

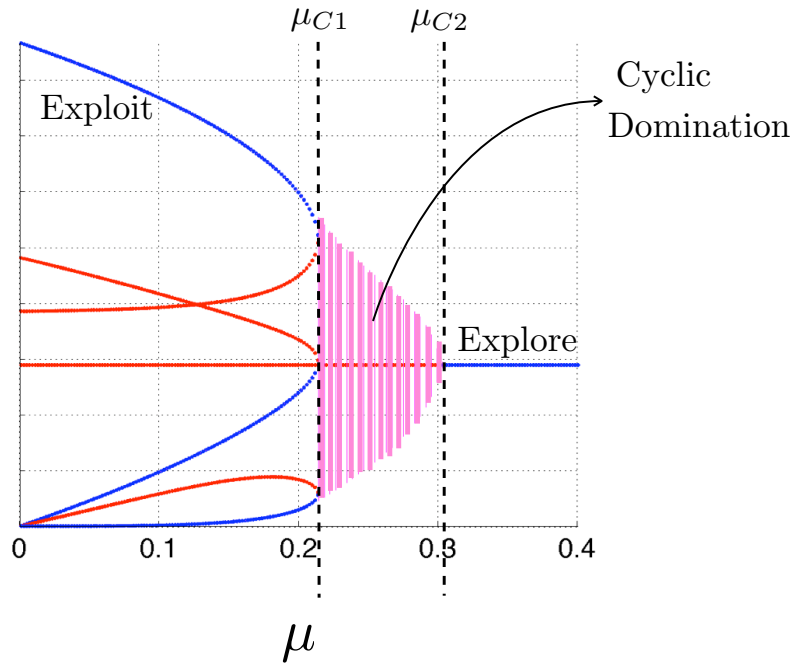


**Figure 8.2:** *Exploration vs. exploitation.* As bifurcation parameter  $\mu$  increases from  $\mu = 0$ , the dynamics transition from exploitation (only one dominant option  $\mu < \mu_{C1}$ ), to cyclical domination of options  $\mu \in (\mu_{C1}, \mu_{C2})$ , to exploration (all options have equal fractions of agents  $\mu > \mu_{C2}$ ). Adapted from Figure 3.5.

At the end of Chapter 5 we studied a simple model of greedy adaptation of nodes on a network and showed the emergence of leadership through bifurcations in the adaptive dynamics as a function of cost. We also showed the critical role played by interconnection topology in determining the locations of leaders in the network. We did not address, however, the connection between the equilibria of the adaptive process, and *optimal* group solutions. This is an area worth investigating to help elu-

cideate the connections between a local bottom-up process such as greedy adaptation and a global top-down optimal design approach. The fundamental tradeoff here is that local approaches, while being highly adaptive, reconfigurable to compensate for loss of agents, and computationally inexpensive, can come at the cost of suboptimal group performance. Understanding this tradeoff carefully, especially as a function of graph topology, is another potential future direction.

The rich variety of collective dynamics in swarms, flocks, schools and herds has inspired a generation of scientists and engineers. Recent advances in experimental and computational technology have enabled a careful examination of the mechanisms that produce the observed rich emergent behavior, including through the lens of evolution. The ongoing quest to better understand the interaction patterns in biological collectives, coupled with innovative bio-inspired ideas for artificial multi-agent systems, will continue to be an exciting area of research going forward.

# Appendix A

## Calculation of Lyapunov coefficient

As stated in Theorem 2.2, the sign of the first Lyapunov coefficient  $\ell_1|_{(\mathbf{x}_0, \mu_0)}$  evaluated at the fixed point  $\mathbf{x}_0$  and bifurcation point  $\mu_0$  determines the criticality of the Hopf bifurcation. What follows are the expressions for calculating  $\ell_1|_{(\mathbf{x}_0, \mu_0)}$  as presented in [59].

Consider the  $N$ -dimensional dynamical system  $\dot{\mathbf{x}} = \mathbf{f}(\mathbf{x}, \mu)$  where  $\mathbf{x} \in \mathbb{R}^N$  and  $\mu \in \mathbb{R}$ . Let  $A_0 = D_{\mathbf{x}}\mathbf{f}|_{(\mathbf{x}_0, \mu_0)}$ , where  $\mathbf{x}_0 \in \mathbb{R}^N, \mu_0 \in \mathbb{R}$ .  $A_0$  has two purely imaginary complex conjugate eigenvalues, given by  $\pm i\omega_0$ , where  $\omega_0 > 0$ . Define  $T_1, T_2$  and  $T_3$  as

$$\begin{aligned} T_1 &= \langle \mathbf{p}, \mathfrak{C}(\mathbf{q}, \mathbf{q}, \bar{\mathbf{q}}) \rangle \\ T_2 &= \langle \mathbf{p}, \mathfrak{B}(\bar{\mathbf{q}}, (2i\omega_0 - A_0)^{-1} \mathfrak{B}(\mathbf{q}, \mathbf{q})) \rangle \\ T_3 &= -2 \langle \mathbf{p}, \mathfrak{B}(\mathbf{q}, A_0^{-1} \mathfrak{B}(\mathbf{q}, \bar{\mathbf{q}})) \rangle. \end{aligned}$$

Here  $\langle \mathbf{r}, \mathbf{s} \rangle = \bar{\mathbf{r}} \cdot \mathbf{s}$  is the complex inner product between two complex vectors, and  $\mathbf{q}$  and  $\mathbf{p}$  are respectively the normalized eigenvector and adjoint-eigenvector of  $A_0$  satisfying  $A_0\mathbf{q} = i\omega_0\mathbf{q}$ ,  $A_0^T\mathbf{p} = -i\omega_0\mathbf{p}$ , and normalization  $\langle \mathbf{p}, \mathbf{q} \rangle = 1$ .  $\mathfrak{B}$  and  $\mathfrak{C}$  are high dimensional tensors given by

$$\begin{aligned} \mathfrak{B}(\mathbf{r}, \mathbf{s}) &= \begin{bmatrix} \mathfrak{B}_1(\mathbf{r}, \mathbf{s}) \\ \mathfrak{B}_2(\mathbf{r}, \mathbf{s}) \\ \vdots \\ \mathfrak{B}_N(\mathbf{r}, \mathbf{s}) \end{bmatrix}, \quad \mathfrak{B}_i(\mathbf{r}, \mathbf{s}) = \sum_{k,l} \frac{\partial^2 f_i}{\partial x_k \partial x_l} \Big|_{\mathbf{x}=\mathbf{x}_0} r_k s_l \\ \mathfrak{C}(\mathbf{r}, \mathbf{s}, \mathbf{t}) &= \begin{bmatrix} \mathfrak{C}_1(\mathbf{r}, \mathbf{s}, \mathbf{t}) \\ \mathfrak{C}_2(\mathbf{r}, \mathbf{s}, \mathbf{t}) \\ \vdots \\ \mathfrak{C}_N(\mathbf{r}, \mathbf{s}, \mathbf{t}) \end{bmatrix}, \quad \mathfrak{C}_i(\mathbf{r}, \mathbf{s}, \mathbf{t}) = \sum_{k,l,m} \frac{\partial^3 f_i}{\partial x_k \partial x_l \partial x_m} \Big|_{\mathbf{x}=\mathbf{x}_0} r_k s_l t_m \end{aligned}$$

The first Lyapunov coefficient  $\ell_1|_{(\mathbf{x}_0, \mu_0)}$  is given by

$$\ell_1|_{(\mathbf{x}_0, \mu_0)} = \frac{1}{2\omega_0} \operatorname{Re}(T_1 + T_2 + T_3).$$

## Appendix B

# Supporting material for Chapter 3

**Lemma B.1.** *The divergence of the vector field  $\mathbf{g}(\mathbf{x})$  restricted to the simplex  $\Delta_{N-1}$  is given by*

$$\begin{aligned} & \nabla \cdot \mathbf{g}(\mathbf{x}) \Big|_{\mathbf{x} \in \Delta_{N-1}} = \nabla \cdot \mathbf{h}(\tilde{\mathbf{x}}) \\ &= \mathbf{1}^T [(1 - \mu)B + S^T] \mathbf{x} - \mathbf{x}^T [NB + B^T] \mathbf{x}, \end{aligned}$$

where  $S = Q \circ B$ , the element-wise product of  $Q$  and  $B$ .

*Proof.* The divergence is given by

$$\nabla \cdot \mathbf{h}(\tilde{\mathbf{x}}) = \sum_{i=1}^{N-1} \frac{\partial h_i}{\partial x_i} = \sum_{i=1}^N \frac{\partial g_i}{\partial x_i} - \sum_{i=1}^N \frac{\partial g_i}{\partial x_N}. \quad (\text{B.1})$$

We substitute for  $g_i(\mathbf{x})$  from (3.2) in the first term of the difference in (B.1) and using (3.1) and (3.3) we have

$$\begin{aligned} & \sum_{i=1}^N \frac{\partial g_i}{\partial x_i} = \sum_i \frac{\partial}{\partial x_i} \left[ x_i(f_i q_{ii} - \phi) + \sum_{j \neq i} x_j f_j q_{ji} \right] \\ &= \sum_i \left[ f_i q_{ii} + x_i q_{ii} \frac{\partial f_i}{\partial x_i} - \phi - x_i \frac{\partial \phi}{\partial x_i} + \sum_{j \neq i} x_j q_{ji} b_{ji} \right] \\ &= (1 - \mu) \mathbf{1}^T B \mathbf{x} + (1 - \mu) - N\phi - \mathbf{x}^T \frac{\partial \phi}{\partial \mathbf{x}} + \sum_i \sum_{j \neq i} x_j q_{ji} b_{ji} \end{aligned}$$

$$\begin{aligned}
&= (1 - \mu)\mathbf{1}^T B\mathbf{x} + (1 - \mu) - N\phi - \mathbf{x}^T(B + B^T)\mathbf{x} + \sum_i \sum_{j \neq i} x_j s_{ji} \\
&= \mathbf{1}^T [(1 - \mu)B + S^T] \mathbf{x} - \mathbf{x}^T [(N + 1)B + B^T] \mathbf{x}. \tag{B.2}
\end{aligned}$$

where the last equality follows by  $\sum_i \sum_{j \neq i} x_j s_{ji} = \mathbf{1}^T S^T \mathbf{x} - (1 - \mu)$ . Computing the second term in the difference in (B.1) and using  $\sum_{i=1}^N q_{ji} = 1$  we have

$$\begin{aligned}
\sum_{i=1}^N \frac{\partial g_i}{\partial x_N} &= \frac{\partial}{\partial x_N} \left[ \sum_{i=1}^N \sum_{j=1}^N x_j f_j q_{ji} - x_i \phi \right] \\
&= \frac{\partial}{\partial x_N} \left[ (1 - \sum_{i=1}^N x_i) \phi \right] = -\phi = -\mathbf{x}^T B\mathbf{x}. \tag{B.3}
\end{aligned}$$

Substituting (B.2) and (B.3) in (B.1) we get the desired result.  $\square$

**Lemma B.2.** *Let  $B$  be circulant and invertible and define the row sums of  $B$  and  $B \circ B$  as  $r_B := \sum_{j=1}^N b_{ij}$  and  $r_{B \circ B} := \sum_{j=1}^N b_{ij}^2$  respectively, for any row  $i$ . Then the divergence  $\nabla \cdot \mathbf{h}(\tilde{\mathbf{x}}) \leq 0$  on the simplex  $\Delta_{N-1}$  if*

$$\begin{aligned}
\mu &\geq \frac{(N - r_B)(r_B - 1)}{N(r_B^2 - r_{B \circ B})} \text{ for mutation (Q1) ,} \\
\mu &\geq \frac{(N - 1)(N - r_B)}{N(N + Nr_B - 2r_B)} \text{ for mutation (Q2).}
\end{aligned}$$

*Proof.* From Lemma B.1, the divergence  $\nabla \cdot \mathbf{h}(\tilde{\mathbf{x}})$  is negative semi-definite on the simplex if

$$\max_{x \in \Delta_{N-1}} \mathbf{1}^T [(1 - \mu)B + S^T] \mathbf{x} \leq \min_{x \in \Delta_{N-1}} \mathbf{x}^T [NB + B^T] \mathbf{x}. \tag{B.4}$$

The term on the left hand side (LHS) of (B.4) is the maximum of a convex combination of non-negative scalars and hence evaluates to

$$\begin{aligned}
\text{LHS} &= \max_i \sum_{j=1}^N (1 - \mu)b_{ji} + s_{ij} \\
&= (1 - \mu) \max_i \sum_{j=1}^N b_{ji} + (1 - \mu) + \mu \max_i \sum_{j \neq i} b_{ij} q_{ij}
\end{aligned}$$

$$= \begin{cases} (1 - \mu)(1 + r_B) + \mu \left( \frac{r_{B \circ B} - 1}{r_B - 1} \right) & \text{for mutation (Q1)} \\ (1 - \mu)(1 + r_B) + \frac{\mu(r_B - 1)}{N-1} & \text{for mutation (Q2)} \end{cases} \quad (\text{B.5})$$

The term on the right hand side (RHS) of (B.4) is the minimum of a quadratic form that is positive on the simplex. Given that  $B$  is circulant and invertible (an  $N \times N$  circulant matrix  $B$  of the form (3.1) is always invertible for  $N$  prime [43]), this quadratic form has an isolated minimum at  $\mathbf{x}_{mix} = \frac{1}{N}\mathbf{1}$ . Thus,

$$\begin{aligned} \text{RHS} &= \min_{x \in \Delta_{N-1}} \mathbf{x}^T [NB + B^T] \mathbf{x} \\ &= \frac{N+1}{N^2} \mathbf{1}^T B \mathbf{1} = \frac{N+1}{N} r_B. \end{aligned} \quad (\text{B.6})$$

Substituting (B.6) and (B.5) in (B.4) and some rearranging gives the desired result.  $\square$

## Appendix C

# Supporting material for Chapter 4

## C.1 Proof of Lemma 4.2

*Proof.* To simplify notation in this proof, we denote the Jacobian  $D_{\mathbf{x}}\mathbf{g}|_{\mathbf{x}_{mix,N}}$  as matrix  $A$ . Since  $A$  is circulant, its eigenvalues are given by (4.3). From (4.3) we see that the eigenvalue  $\lambda_k(A)$  cannot be complex when  $\omega_N^k$  is real. To guarantee complex  $\omega_N^k$ , let  $k$  be given by

$$k \in \begin{cases} \{1, \dots, N-1\} & N \text{ odd} \\ \{1, \dots, N-1\} \setminus \{\frac{N}{2}\} & N \text{ even.} \end{cases}$$

One can then verify that  $\lambda_{N-k}(A) = \overline{\lambda_k(A)}$ . Hence, as long as the  $\lambda_k(A)$  are complex,  $A$  has  $\lfloor \frac{N-1}{2} \rfloor$  complex conjugate pairs of eigenvalues. Now we compute  $\text{Im}(\lambda_k(A))$

and hence obtain conditions for the existence of complex  $\lambda_k(A)$ . The calculations differ slightly between mutation matrices (Q1) and (Q2) as shown below. We obtain a simplified expression for the imaginary component of the eigenvalues by grouping identical terms of  $A$  and using the identity  $\sum_{j=1}^N \omega_N^{jk} = 0$ .

- Mutation (Q1):

$$\text{Im}(\lambda_k(A)) = \begin{cases} (a_{12} - a_{1N}) \sin\left(\frac{2\pi}{N}k\right) & N = 3, 4, 5 \\ (a_{12} - a_{1N}) \sin\left(\frac{2\pi}{N}k\right) + (a_{13} - a_{1,N-1}) \sin\left(\frac{2\pi}{N}2k\right) & N \geq 6 \end{cases}$$

- Mutation (Q2):

$$\text{Im}(\lambda_k(A)) = (a_{12} - a_{1N}) \sin\left(\frac{2\pi}{N}k\right) \quad N \geq 3$$

Substituting for the  $a_{ij}$  terms from (4.2),

$$\text{Im}(\lambda_k(A)) = 0 \iff \begin{cases} (\alpha - \beta) \left(1 - \mu - \mu^{\frac{(2+\alpha+\beta)}{\alpha+\beta}}\right) = 0 & \text{mutation (Q1)} \\ (\alpha - \beta) \left(1 - \mu - \frac{\mu}{N-1}\right) = 0 & \text{mutation (Q2).} \end{cases} \quad (\text{C.1})$$

The conditions of the Lemma follow from the expressions in (C.1).  $\square$

## C.2 Proof of Lemma 4.3

*Proof.* To simplify notation in this proof, we denote the Jacobian  $D_{\mathbf{x}}\mathbf{g}|_{\mathbf{x}_{mix,N}}$  as matrix  $A$ . From Lemma 4.2, for  $r = 1, \dots, \lfloor \frac{N-1}{2} \rfloor$ ,  $\lambda_r(A)$  is complex. Using the notation  $a_{1j} = \gamma_j + \mu\eta_j$  we obtain

$$\text{Re}(\lambda_r(A)) = \sum_{j=1}^N \gamma_j \cos\left(\frac{2\pi}{N}(j-1)r\right) + \mu \sum_{j=1}^N \eta_j \cos\left(\frac{2\pi}{N}(j-1)r\right)$$

which is zero if and only if

$$\mu = - \left[ \sum_{j=1}^N \gamma_j \cos\left(\frac{2\pi}{N}(j-1)r\right) \right] \left[ \sum_{j=1}^N \eta_j \cos\left(\frac{2\pi}{N}(j-1)r\right) \right]^{-1} =: \mu_{0,r}. \quad (\text{C.2})$$

Before we proceed, we need to establish that  $\mu_{0,r}$  is indeed well defined; that is, the denominator in (C.2) is non-zero. Let  $d_r$  denote the denominator of  $\mu_{0,r}$ . For

$N = 3$ ,  $d_r = 6(\alpha + \beta + \alpha\beta) \neq 0$  for mutation (Q1) and  $d_r = 3(4 + \alpha + \beta) \neq 0$  for mutation (Q2); for  $N = 4$ ,  $d_r = 2(\alpha + \beta + 2\alpha\beta) \neq 0$  for mutation (Q1) and  $d_r = 4(2 + \alpha + \beta) \neq 0$  for mutation (Q2). For  $N \geq 5$ , by grouping identical terms, using the identity  $\sum_{j=1}^N \omega_N^{jr} = 0$  and replacing the expressions for  $\eta_j$  in terms of  $\alpha$  and  $\beta$  we have,

$$d_r \neq 0 \iff \begin{cases} 2(\alpha + \beta)(\cos(\frac{2\pi}{N}r) - 1) + 2\alpha\beta(\cos(\frac{2\pi}{N}2r) - 1) \neq 0 & \text{mutation (Q1)} \\ \cos(\frac{2\pi}{N}r) \neq -\frac{2+\alpha+\beta}{\alpha+\beta} & \text{mutation (Q2)}. \end{cases}$$

The conditions above can be verified to always hold given that the cosine function is bounded between  $-1$  and  $1$  and  $\alpha$  and  $\beta$  satisfy the conditions in (4.1).

Finally, we establish that if  $r, s = 1, \dots, \lfloor \frac{N-1}{2} \rfloor$ ,  $r \neq s$  then  $\mu_{0,r} \neq \mu_{0,s}$ , i.e. the bifurcation points are distinct. If  $N = 3, 4$ , Lemma 4.2 establishes that there is only one bifurcation point. For  $N = 5$ , the two critical points can be shown to be distinct by a direct calculation. Here we show the distinctness of the critical points in the cases  $N \geq 6$ . Using (C.2),

$$\mu_{0,r} \neq \mu_{0,s} \iff \frac{\sum_{j=1}^N \gamma_j \cos(\frac{2\pi}{N}(j-1)r)}{\sum_{j=1}^N \eta_j \cos(\frac{2\pi}{N}(j-1)r)} \neq \frac{\sum_{j=1}^N \gamma_j \cos(\frac{2\pi}{N}(j-1)s)}{\sum_{j=1}^N \eta_j \cos(\frac{2\pi}{N}(j-1)s)}. \quad (\text{C.3})$$

By grouping identical terms, using the identity  $\sum_{j=1}^N \omega_N^{jr} = 0$ , and replacing the expressions for  $\gamma_j$  and  $\eta_j$  in terms of  $\alpha$  and  $\beta$ , we find that

$$(\text{C.3}) \iff \begin{cases} (1 + \alpha + \beta + 2\alpha\beta)(\alpha + \beta) \\ + 2\alpha\beta[\cos(\frac{2\pi}{N}r) + \cos(\frac{2\pi}{N}s)] \\ + 2(\alpha + \beta)\alpha\beta[\cos(\frac{2\pi}{N}r)\cos(\frac{2\pi}{N}s)] \neq 0 & \text{mutation (Q1)} \\ \cos(\frac{2\pi}{N}r) \neq \cos(\frac{2\pi}{N}s) & \text{mutation (Q2)}. \end{cases} \quad (\text{C.4})$$

For mutation (Q1), the left hand side of the inequality in (C.4) can be bounded below by  $(\alpha - \beta)^2 + (\alpha + \beta) > 0$ . For mutation (Q2), the condition in (C.4) is equivalent to the initial hypothesis of  $r \neq s$ . The distinctness result now follows.  $\square$

### C.3 Proof of Lemma 4.4

*Proof.* Here we compute the terms  $T_1$ ,  $T_2$  and  $T_3$  from Appendix A to obtain a simplified analytical expression for the first Lyapunov coefficient  $\ell_1|_{(\mathbf{x}_{mix,N}, \mu_{0,r})}$ . For a circulant matrix  $M \in \mathbb{R}^{N \times N}$ , let  $\{(\lambda_k, \mathbf{v}_k)\}$  be an eigenvalue–right eigenvector pair ( $M\mathbf{v}_k = \lambda_k \mathbf{v}_k$ ), where

$$\mathbf{v}_k = \begin{bmatrix} 1 & \omega_N^k & \omega_N^{2k} & \cdots & \omega_N^{(N-1)k} \end{bmatrix}^T \quad \text{and} \quad \lambda_k(M) = \sum_{j=1}^N m_{1j} \omega_N^{(j-1)k}. \quad (\text{C.5})$$

We compute  $\ell_1|_{(\mathbf{x}_{mix,N}, \mu_{0,r})}$  as a function of the parameters  $\alpha$  and  $\beta$ . From Appendix A, the Jacobian  $D_{\mathbf{x}}\mathbf{g}|_{(\mathbf{x}_{mix,N}, \mu_{0,r})}$  is denoted by  $A_0$  with eigenvalue  $\lambda_r(A_0) = \mathbf{i}\hat{\omega}$ . Let  $\omega_0 = |\hat{\omega}|$ ,  $t = r \operatorname{sign}(\hat{\omega})$ , and  $\mathbf{q} = \mathbf{v}_t$ . Note that  $A_0\mathbf{q} = \mathbf{i}\omega_0\mathbf{q}$ .

#### Computing $T_1$

Direct calculation and simplification gives

$$\mathfrak{C}_i(\mathbf{q}, \mathbf{q}, \bar{\mathbf{q}}) = -2N [2 + (\alpha + \beta) \omega_N^t + (\alpha + \beta) \omega_N^{-t}] \omega_N^{(i-1)t}.$$

Hence

$$\mathfrak{C}(\mathbf{q}, \mathbf{q}, \bar{\mathbf{q}}) = -2N [2 + (\alpha + \beta) \omega_N^t + (\alpha + \beta) \omega_N^{-t}] \mathbf{q},$$

which leads to

$$\begin{aligned} T_1 &= \langle \mathbf{p}, \mathfrak{C}(\mathbf{q}, \mathbf{q}, \bar{\mathbf{q}}) \rangle = -2N [2 + (\alpha + \beta) \omega_N^t + (\alpha + \beta) \omega_N^{-t}] \langle \mathbf{p}, \mathbf{q} \rangle \\ &= -2N [2 + (\alpha + \beta) (\omega_N^t + \omega_N^{-t})]. \end{aligned} \quad (\text{C.6})$$

#### Computing $T_2$

We compute

$$\mathfrak{B}(\mathbf{q}, \mathbf{q}) = 2 [1 + \alpha\omega_N^t + \beta\omega_N^{-t}] Q^T \mathbf{v}_{2t}.$$

Since  $Q$  is circulant, so is  $Q^T$  and  $\mathbf{v}_{2t}$  is a right eigenvector. Then

$$\mathfrak{B}(\mathbf{q}, \mathbf{q}) = 2 [1 + \alpha\omega_N^t + \beta\omega_N^{-t}] \lambda_{2t}(Q^T) \mathbf{v}_{2t}.$$

For each eigenvector-eigenvalue pair  $\mathbf{v}, \lambda$  of  $A_0$ , direct calculation shows that  $1/(2\mathbf{i}\omega_0 - \lambda)$  is the corresponding eigenvalue for the eigenvector  $\mathbf{v}$  of  $(2\mathbf{i}\omega_0 I - A_0)^{-1}$ ,

where  $I$  denotes the identity matrix. Then,

$$(2\mathbf{i}\omega_0 I - A_0)^{-1} \mathfrak{B}(\mathbf{q}, \mathbf{q}) = 2 \frac{[1 + \alpha\omega_N^t + \beta\omega_N^{-t}] \lambda_{2t}(Q^T)}{2\mathbf{i}\omega_0 - \lambda_{2t}(A_0)} \mathbf{v}_{2t}.$$

Since  $\mathfrak{B}(\mathbf{x}, \kappa\mathbf{y}) = \kappa\mathfrak{B}(\mathbf{x}, \mathbf{y})$  for any  $\kappa \in \mathbb{C}$ , then

$$\mathfrak{B}(\bar{\mathbf{q}}, (2\mathbf{i}\omega_0 - A_0)^{-1} \mathfrak{B}(\mathbf{q}, \mathbf{q})) = 2 \frac{[1 + \alpha\omega_N^t + \beta\omega_N^{-t}] \lambda_{2t}(Q^T)}{2\mathbf{i}\omega_0 - \lambda_{2t}(A_0)} \mathfrak{B}(\bar{\mathbf{q}}, \mathbf{v}_{2t}).$$

A calculation similar to that for  $\mathfrak{B}(\mathbf{q}, \mathbf{q})$  gives

$$\mathfrak{B}_i(\bar{\mathbf{q}}, \mathbf{v}_{2t}) = [\beta\omega_N^{-2t} + \alpha\omega_N^{-t} + 2 + \beta\omega_N^t + \alpha\omega_N^{2t}] \sum_{j=1}^N q_{ji} \omega_N^{(j-1)t}.$$

Hence

$$\mathfrak{B}(\bar{\mathbf{q}}, \mathbf{v}_{2t}) = (\beta\omega_N^{-2t} + \alpha\omega_N^{-t} + 2 + \beta\omega_N^t + \alpha\omega_N^{2t}) \lambda_t(Q^T) \mathbf{q}.$$

This implies that

$$\begin{aligned} & \mathfrak{B}(\bar{\mathbf{q}}, (2\mathbf{i}\omega_0 - A_0)^{-1} \mathfrak{B}(\mathbf{q}, \mathbf{q})) \\ &= \frac{2\lambda_t(Q^T) \lambda_{2t}(Q^T)}{2\mathbf{i}\omega_0 - \lambda_{2t}(A_0)} (1 + \alpha\omega_N^t + \beta\omega_N^{-t}) [\beta\omega_N^{-2t} + \alpha\omega_N^{-t} + 2 + \beta\omega_N^t + \alpha\omega_N^{2t}] \mathbf{q}, \end{aligned}$$

and

$$\begin{aligned} T_2 &= \langle \mathbf{p}, \mathfrak{B}(\bar{\mathbf{q}}, (2\mathbf{i}\omega_0 - A_0)^{-1} \mathfrak{B}(\mathbf{q}, \mathbf{q})) \rangle \\ &= \frac{2\lambda_t(Q^T) \lambda_{2t}(Q^T)}{2\mathbf{i}\omega_0 - \lambda_{2t}(A_0)} (1 + \alpha\omega_N^t + \beta\omega_N^{-t}) [\beta\omega_N^{-2t} + \alpha\omega_N^{-t} + 2 + \beta\omega_N^t + \alpha\omega_N^{2t}]. \quad (\text{C.7}) \end{aligned}$$

**Computing  $T_3$**

We show that  $\mathfrak{B}(\mathbf{q}, \bar{\mathbf{q}}) = \mathbf{0}$ .

$$\begin{aligned} \mathfrak{B}_i(\mathbf{q}, \bar{\mathbf{q}}) &= -2 - (\alpha + \beta)(\omega_N^t + \omega_N^{-t}) + [2 + (\alpha + \beta)(\omega_N^t + \omega_N^{-t})] \sum_{j=1}^N q_{ji} \\ &= [2 + (\alpha + \beta)(\omega_N^t + \omega_N^{-t})] \left[ -1 + \sum_{j=1}^N q_{ji} \right] = 0, \quad (\text{C.8}) \end{aligned}$$

where the last equality comes from the fact that  $Q$  is a doubly-stochastic matrix. This implies

$$T_3 = -2 \langle \mathbf{p}, \mathfrak{B}(\mathbf{q}, A_0^{-1} \mathfrak{B}(\mathbf{q}, \bar{\mathbf{q}})) \rangle = -2 \langle \mathbf{p}, \mathfrak{B}(\mathbf{q}, \mathbf{0}) \rangle = 0.$$

Combining the previous expressions for  $T_1$ ,  $T_2$  and  $T_3$ , the result follows.  $\square$

## C.4 Criticality analysis for Corollaries 4.1 and 4.2

In this section we establish that the Lyapunov coefficient at each of the  $d$  concurrent Hopf Bifurcations of the equilibria  $\mathbf{x}_{j,d,N}$  is identical to that at the equilibrium  $\mathbf{x}_{mix,N/d}$  for the simple cycle payoff  $B_{C,N/d}$  with  $\beta = 0$  (i.e.  $B_{N/d,1}$ ). The mutation matrix used is (Q1). Let  $N/d = N_1$  and  $N_2 = N - N_1$ .

In order to simplify the calculations, consider the payoff matrix  $\hat{B}_{N,d}$  given by

$$\hat{B}_{N,d} = \left[ \begin{array}{c|c|c|c} B_{N_1,1} & 0_{N_1 \times N_1} & \cdots & 0_{N_1 \times N_1} \\ \hline 0_{N_1 \times N_1} & B_{N_1,1} & \cdots & 0_{N_1 \times N_1} \\ \hline \vdots & \vdots & \ddots & \vdots \\ \hline 0_{N_1 \times N_1} & 0_{N_1 \times N_1} & \cdots & B_{N_1,1} \end{array} \right].$$

$\hat{B}_{N,d}$  is obtained by relabeling the graph nodes corresponding to  $B_{N,d}$  such that index labels for connected nodes are consecutive. The payoff graph topology induced by  $\hat{B}_{N,d}$  is isomorphic to that of  $B_{N,d}$ , see Figure 4.5. The dynamics (3.2), with payoff  $\hat{B}_{N,d}$  and mutation (Q1) have equilibria  $\hat{\mathbf{x}}_j = [\mathbf{0}_{N_1(j-1)}^T \quad \frac{1}{N_1} \mathbf{1}_{N_1}^T \quad \mathbf{0}_{N_1(d-j)}^T]^T$ , which correspond to the equilibria  $\mathbf{x}_{j,d,N}$ . The Jacobian of the system above evaluated at the equilibrium  $\hat{\mathbf{x}}_1$  is precisely  $M_{N,d}$  in (4.8). Using this definition of payoff, we compute the first Lyapunov coefficient as described in Appendix A. We focus on equilibrium  $\hat{\mathbf{x}}_1$ ; the analysis for the other  $\hat{\mathbf{x}}_j$  is equivalent.

The eigenvalues  $\lambda_k$  and eigenvectors  $\mathbf{v}_k$  of a circulant matrix are defined in (C.5). Let the Jacobian  $M_{N,d}$  evaluated at the critical point  $\mu_{0,r}$  (defined in Corollary 4.2) be denoted as

$$\hat{A}_0 = \left[ \begin{array}{c|c} A_0 & 0_{N_2 \times N_1} \\ \hline 0_{N_1 \times N_2} & -\frac{1+\alpha}{N_1} I_{N_2 \times N_2} \end{array} \right],$$

with eigenvalue  $\lambda_r(A_0) = \mathbf{i}\hat{\omega}$ . Let  $\omega_0 = |\hat{\omega}|$ ,  $t = r \operatorname{sign}(\hat{\omega})$ ,  $\mathbf{q} = \mathbf{v}_t(A_0)$ ,  $\hat{\mathbf{q}} = [\mathbf{q}^T \ \mathbf{0}_{d(N_1-1)}^T]^T$  and  $\langle \hat{\mathbf{p}}, \hat{\mathbf{q}} \rangle = 1$ . Note that  $A_0\mathbf{q} = \mathbf{i}\omega_0\mathbf{q}$  and hence  $\hat{A}_0\hat{\mathbf{q}} = \mathbf{i}\omega_0\hat{\mathbf{q}}$ . Let  $Q$  be the (Q1) mutation matrix corresponding to  $B_{N,d}$  and  $\hat{Q}$  be the (Q1) mutation matrix corresponding to  $\hat{B}_{N,d}$ .

With these definitions, we follow the calculations in Appendix A and compute each of the terms  $T_1$ ,  $T_2$  and  $T_3$  given below. A comparison of each of these terms, to the corresponding terms in Appendix C.3 shows that the Lyapunov coefficient is identical (when  $N \mapsto N_1$ ,  $\beta \mapsto 0$  in (C.6), (C.7) and (C.8)).

$$\begin{aligned} T_1 &= \langle \hat{\mathbf{p}}, \mathfrak{C}(\hat{\mathbf{q}}, \hat{\mathbf{q}}, \bar{\hat{\mathbf{q}}}) \rangle = -2N_1 [2 + \alpha\omega_{N_1}^t + \alpha\omega_{N_1}^{-t}], \\ T_2 &= \left\langle \hat{\mathbf{p}}, \mathfrak{B} \left( \bar{\hat{\mathbf{q}}}, \left( 2\mathbf{i}\omega_0 - \hat{A}_0 \right)^{-1} \mathfrak{B}(\hat{\mathbf{q}}, \hat{\mathbf{q}}) \right) \right\rangle \\ &= \frac{2\lambda_t(Q^T)\lambda_{2t}(Q^T)}{2\mathbf{i}\omega_0 - \lambda_{2t}(A_0)} (1 + \alpha\omega_{N_1}^t) [\alpha\omega_{N_1}^{-t} + \alpha\omega_{N_1}^{2t} + 2], \\ T_3 &= -2 \left\langle \hat{\mathbf{p}}, \mathfrak{B} \left( \hat{\mathbf{q}}, \hat{A}_0^{-1} \mathfrak{B}(\hat{\mathbf{q}}, \bar{\hat{\mathbf{q}}}) \right) \right\rangle = 0. \end{aligned}$$

## Appendix D

# Supporting material for Chapter 5

In this appendix we discuss the details of the adaptive dynamics analysis from Section 5.2. Define the function

$$G(k_R, k_M) = \frac{k_M^2 + (1 - k_M)^2\beta^2(1 - k_R)}{4(2k_M^2 - 2k_M + 1)} + ck_M^2.$$

Then the differential fitness from (2.3) is given by

$$S = \exp[-G(k_R, k_M)] - \exp[-G(k_R, k_R)].$$

The selection gradient  $g(k_R)$  is given by

$$g(k_R) = \frac{\partial S}{\partial k_M} \Big|_{k_M=k_R} = -\exp[-G(k_R, k_R)] \left( \frac{k_M(1-k_M)[1+\beta^2(k_R-1)]}{2(2k_M^2-2k_M+1)^2} + 2ck_M \right).$$

Solving for the singular strategy condition  $g(k_*) = 0$  gives the expression (5.19)

$$k_*(1-k_*)[1+\beta^2(k_*-1)] + 4ck_*(2k_*^2-2k_*+1)^2 = 0.$$

This expression has two sets of solutions that are plotted in Figure 5.3. One set corresponds to  $k_* = 0$  and the other is defined implicitly by the equation

$$c = \frac{(k_*-1)[1+\beta^2(k_*-1)]}{4(2k_*^2-2k_*+1)^2} =: \tilde{c}(k_*). \quad (\text{D.1})$$

To determine conditions for evolutionary branching we compute

$$\frac{\partial^2 S}{\partial k_M^2} \Big|_{k_M=k_R=k_*} = -\exp[-G(k_*, k_*)] \frac{(1-\beta^2+\beta^2k_*)(3k_*-10k_*^2+6k_*^3)}{2(1-2k_*+2k_*^2)^3}.$$

Hence the branching condition  $\frac{\partial^2 S}{\partial k_M^2} \Big|_{k_M=k_R=k_*} > 0$  corresponds to

$$\frac{(\beta^2(1-k_*)-1)k_*(3-10k_*+6k_*^2)}{2(1-2k_*+2k_*^2)^3} > 0. \quad (\text{D.2})$$

The zeros of function above in the range  $k_* \in [0, 1]$  are  $0, \frac{5-\sqrt{7}}{6}$ , and  $1 - \frac{1}{\beta^2}$ . A derivative test shows that the condition (D.2) is satisfied for  $k_* \in \left(0, \frac{5-\sqrt{7}}{6}\right)$ .

The critical cost parameter  $c_1$  in Figure 5.3, corresponds to the maximum singular value  $k_*$  for branching and is given from (D.1) by  $c_1 = \tilde{c}\left(\frac{5-\sqrt{7}}{6}\right)$ . The parameter  $c_2$  is determined by calculating the local maximum of the function  $\tilde{c}(k_*)$  as seen in Figure 5.3. We use the notation  $\tilde{c}(k_{crit}) = c_2$ .  $k_{crit}$  can be calculated analytically and is given by a particular root of a cubic equation. The analytical expression for  $k_{crit}$  (and correspondingly  $c_2$ ) is cumbersome and hence is left out of this text. Nonetheless, the sketch in Figure 5.3 clearly conveys the main ideas.

Finally we discuss the convergence stability of the singular strategies. The convergence stability condition is given by (2.5). For the  $k_* = 0$  singular strategy,

$$\frac{\partial g}{\partial k_R} \Big|_{k_R=0} = \exp\left[\frac{-\beta^2}{4}\right] \frac{\beta^2-1-4c}{2}, \text{ hence } \frac{\partial g}{\partial k_R} \Big|_{k_R=0} < 0 \iff c > \frac{\beta^2-1}{4}.$$

For the second singular strategy curve defined implicitly by (D.1), the derivative term in the convergence stability condition evaluates to

$$\frac{\partial g}{\partial k_R} \Big|_{k_R=k_*} = -\frac{k_* [3 - 10k_* + 6k_*^2 + 2\beta^2 (-1 + 5k_* - 6k_*^2 + 2k_*^3)] \exp [-G(k_*, k_*)]}{2(1 - 2k_* + 2k_*^2)^3}$$

The interior root of  $\frac{\partial g}{\partial k_R} \Big|_{k_R=k_*} = 0$  is precisely the value  $k_{crit}$  that maximizes  $\tilde{c}(k_*)$  (since  $c = \tilde{c}(k_*) \equiv g(k_*) = 0$ ); this root corresponds to  $c_2$  (see above). Hence one can verify that the singular strategies corresponding to the curve (D.1) are stable for  $k_* > k_{crit}$  and unstable for  $k_* < k_{crit}$  as shown in Figure 5.3.

## Appendix E

# Supporting material for Chapter 6

### E.1 Proof of Lemma 6.2

*Proof.*  $D$  is invariant with respect to the dynamics (6.6) since all boundaries of  $D$  are invariant ( $q_i \in \{0, 1\} \implies \dot{q}_i = 0$ ), and further  $q_3(0) > 0 \implies q_3(t) > 0$  for all  $t > 0$  since

$$\dot{q}_3 = \frac{q_3 f_3}{\mathbf{q}^T \mathbf{f}} - q_3 \geq -q_3 \implies q_3(t) \geq q_3(0)e^{-t} > 0.$$

Using the constraint  $\mathbf{q}^T \mathbf{1}_3 = 1$ , we restate the dynamics (6.6) as a two-dimensional system,

$$\begin{aligned} \dot{q}_1 &= \frac{q_1}{\hat{f}} (f_{31}(t)(q_1 - 1) + f_{32}(t)q_2) \\ \dot{q}_2 &= \frac{q_2}{\hat{f}} (f_{32}(t)(q_2 - 1) + f_{31}(t)q_1), \end{aligned} \tag{E.1}$$

where  $f_{32}(t) = f_3(t) - f_2(t) > 0$ ,  $f_{31}(t) = f_3(t) - f_1(t) > 0$ , and  $\hat{f} = \mathbf{q}^T \mathbf{f} = f_3 - q_1 f_{31} - q_2 f_{32}$ . One can check that the only three equilibria of the system (E.1) in

$\Delta_2$  (given properties (1)-(3)) are the vertices  $(q_{eq1}, q_{eq2}) = (0, 0), (0, 1), (1, 0)$ , of which  $(0, 0)$  is the only equilibrium in  $D$ .

Linearization about the  $(0, 0)$  equilibrium gives the dynamics,

$$\begin{bmatrix} \dot{q}_1 \\ \dot{q}_2 \end{bmatrix} = \begin{bmatrix} -f_{31}/f_3 & 0 \\ 0 & -f_{32}/f_3 \end{bmatrix} \begin{bmatrix} q_1 \\ q_2 \end{bmatrix}.$$

This non-autonomous linear system in diagonal form can be solved easily as

$$q_i(t) = q_i(0) \exp\left(-\int_0^t \frac{f_{3i}(t)}{f_3(t)} dt\right), \quad i = 1, 2.$$

For  $i = 1, 2$ ,  $\lim_{t \rightarrow \infty} q_i(t) = 0$  and hence the  $(0, 0)$  equilibrium point of the non-autonomous system (E.1) is locally asymptotically stable by Theorem 4.13 of [54]. To prove that the invariant domain  $D$  is the region of attraction for the asymptotically stable  $(0, 0)$  equilibrium point of (E.1), we use a Lyapunov function  $V = q_1 + q_2$ .  $V$  is positive definite on  $D$  with a unique minimum:  $V = 0 \iff q_1 = q_2 = 0$ . We compute

$$\dot{V} = \dot{q}_1 + \dot{q}_2 = \frac{1}{f}(q_1 f_{31} + q_2 f_{32})(q_1 + q_2 - 1) < 0.$$

Since  $\dot{V}$  is negative definite on the domain  $D$ , by Theorem 4.9 of [54] we have that  $D$  is the region of attraction for the equilibrium point  $q_{eq1} = 0, q_{eq2} = 0$  (and  $q_{eq3} = 1$ ). Hence the equilibrium point  $\mathbf{q}_{eq} = \begin{bmatrix} 0 & 0 & 1 \end{bmatrix}^T$  is the asymptotically stable limit for all  $\mathbf{q}(0) \in D$ .  $\square$

## E.2 Lemma E.1 used in Theorem 6.1

**Lemma E.1.** Let  $\mathbf{q} \in \Delta^2$ ,  $\mathbf{q}_{eq} = \begin{bmatrix} 1 & 0 & 0 \end{bmatrix}^T$  and  $\mathbf{f}_P = M\mathbf{q}$ , where  $M = T^\#$  and  $T$  satisfies Conjecture 6.1. Then  $\|\mathbf{q} - \mathbf{q}_{eq}\| < \epsilon \implies f_{P1} > f_{P2}$  and  $f_{P1} > f_{P3}$ , where  $\epsilon \leq \min \left\{ \frac{2(m_{11} - m_{21})}{(m_{11} - m_{21}) + \|M\|_1}, \frac{2(m_{11} - m_{31})}{(m_{11} - m_{31}) + \|M\|_1} \right\}$ .

*Proof.*  $\|\mathbf{q} - \mathbf{q}_{eq}\|_1 < \epsilon \implies q_1 > 1 - \frac{\epsilon}{2}, q_2 < \frac{\epsilon}{2}$  and  $q_3 < \frac{\epsilon}{2}$ . Suppose that

$$\begin{aligned} \epsilon &\leq \frac{2(m_{11} - m_{21})}{(m_{11} - m_{21}) + \|M\|_1} \\ \implies \epsilon &< \frac{2(m_{11} - m_{21})}{(m_{11} - m_{21}) + (m_{22} + m_{23})} \\ \implies (m_{11} - m_{21}) \left(1 - \frac{\epsilon}{2}\right) &> (m_{22} + m_{23}) \frac{\epsilon}{2} \end{aligned}$$

$$\begin{aligned}
&\implies (m_{11} - m_{21})q_1 > m_{22}q_2 + m_{23}q_3 \\
&\implies (m_{11} - m_{21})q_1 > m_{22}q_2 + m_{23}q_3 - m_{12}q_2 - m_{13}q_3 \\
&\implies \begin{bmatrix} m_{11} & m_{12} & m_{13} \end{bmatrix}^T \mathbf{q} > \begin{bmatrix} m_{21} & m_{22} & m_{23} \end{bmatrix}^T \mathbf{q}, \text{ or } f_{P1} > f_{P2}. \tag{E.2}
\end{aligned}$$

Similarly one can show that

$$\epsilon \leq \frac{2(m_{11} - m_{31})}{(m_{11} - m_{31}) + \|M\|_1} \implies f_{P1} > f_{P3}. \tag{E.3}$$

Combining (E.2) and (E.3) we get the desired result.  $\square$

## Appendix F

# Supporting material for Chapter 7

This appendix comprises the details of the timescale separation calculation for the stop-signalling dynamics (7.7),

$$\begin{aligned}
\frac{dy_A}{dt} &= \frac{-2y_A}{2\bar{v} + \Delta v} + \left(\bar{v} + \frac{\Delta v}{2}\right) y_U(1 + y_A) - \sigma y_A y_B \\
\frac{dy_B}{dt} &= \frac{-2y_B}{2\bar{v} - \Delta v} + \left(\bar{v} - \frac{\Delta v}{2}\right) y_U(1 + y_B) - \sigma y_A y_B.
\end{aligned}$$

We perform a nonlinear coordinate transformation of the dynamics (7.7) and apply singular perturbation theory to separate timescales and derive an analytic expression for the slow manifold (heteroclinic connections). Assuming large  $\bar{v}$ , define  $\epsilon := \frac{1}{\bar{v}}$  as the small parameter for the timescale separation calculations. We follow the notation used in Chapter 11 of [54] and apply Tikhonov's Theorem (Theorem 11.1 in [54]) to prove the timescale separation.

## Standard Singular Perturbation Model

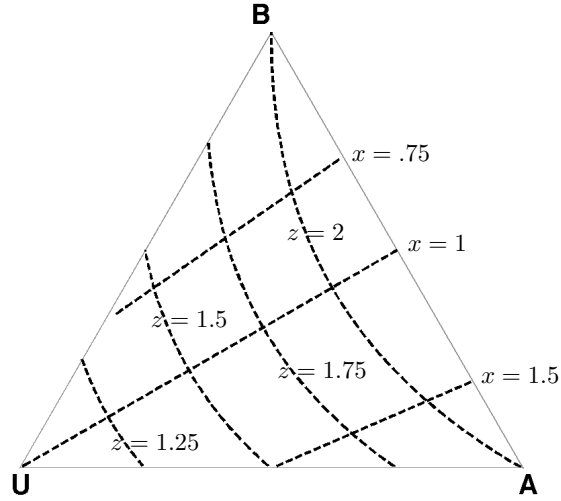
Consider the coordinate transformation  $(y_A, y_B) \mapsto (x, z)$  given by

$$\begin{aligned} z &= (1 + y_A)(1 + y_B) \\ x &= \frac{1 + y_A}{1 + y_B}. \end{aligned} \tag{F.1}$$

The transformation is well-defined on the domain  $(y_A, y_B) \in \Delta_2$  since the Jacobian of the linearization has non-zero determinant  $\frac{-2(1+y_A)}{1+y_B}$  on  $\Delta_2$ . The inverse transformation is given by

$$\begin{aligned} y_A &= \sqrt{zx} - 1 \\ y_B &= \sqrt{\frac{z}{x}} - 1. \end{aligned} \tag{F.2}$$

Note that  $(y_A, y_B) \in \Delta_2$  implies that  $z \in [1, \frac{9}{4}]$  and  $x \in [\frac{1}{2}, 2]$ . Level curves in  $x, z$  coordinates on the simplex are illustrated in the figure below.



*Level curves in  $x, z$  coordinates.*

Define the functions  $\alpha(x, z)$  and  $\beta(x, z)$  as

$$\alpha(x, z) = \sqrt{zx} + \sqrt{\frac{z}{x}} = 2 + y_A + y_B \tag{F.3}$$

$$\beta(x, z) = \sqrt{zx} - \sqrt{\frac{z}{x}} = y_A - y_B. \tag{F.4}$$

Then,

$$y_A y_B = z + 1 - \alpha, \quad y_A + y_B = \alpha - 2, \quad \text{and} \quad y_U = 3 - \alpha. \quad (\text{F.5})$$

Computing the time derivative of  $z$  and substituting from (7.7), (F.3), (F.4) and (F.5) we get

$$\begin{aligned} \dot{z} &= \dot{y}_B(1 + y_A) + \dot{y}_A(1 + y_B) \\ &= \frac{2}{4\bar{v}^2 - \Delta v^2} [\Delta v \beta(x, z) - 2\bar{v}(2z - \alpha(x, z))] \\ &\quad + 2\bar{v}z(3 - \alpha(x, z)) - \sigma\alpha(x, z)(z + 1 - \alpha(x, z)). \end{aligned} \quad (\text{F.6})$$

Computing the time derivative of  $x$  and substituting from (7.7), (F.3), (F.4) and (F.5) we get

$$\begin{aligned} \dot{x} &= \frac{\dot{y}_A(1 + y_B) - \dot{y}_B(1 + y_A)}{(1 + y_B)^2} \\ &= \frac{x\Delta v(4z - 2\alpha(x, z)) - 4x\bar{v}\beta(x, z)}{4\bar{v}^2 z - z(\Delta v)^2} + x\Delta v(3 - \alpha(x, z)) \\ &\quad + \frac{\sigma x\beta(x, z)}{z}(z + 1 - \alpha(x, z)). \end{aligned} \quad (\text{F.7})$$

With small parameter  $\epsilon = 1/\bar{v}$  and ratio  $d = \sigma/\bar{v}$ , the transformed dynamics (F.6), (F.7) can be written as a singular perturbation problem in standard form,

$$\begin{aligned} \epsilon \frac{dz}{dt} &= 2z(3 - \alpha) - d\alpha(z + 1 - \alpha) \\ &\quad + \frac{2\epsilon^3 \beta \Delta v}{4 - \epsilon^2(\Delta v)^2} - \frac{4(2z - \alpha)\epsilon^2}{4 - \epsilon^2(\Delta v)^2} \quad =: g(x, z, \epsilon) \end{aligned} \quad (\text{F.8})$$

$$\begin{aligned} \frac{dx}{dt} &= x(3 - \alpha)\Delta v + \frac{\sigma\beta x}{z}(z + 1 - \alpha) \\ &\quad - \frac{4\beta x\epsilon}{4z - z\epsilon^2(\Delta v)^2} + \frac{x(4z - 2\alpha)\epsilon^2\Delta v}{4z - z\epsilon^2(\Delta v)^2} \quad =: f(x, z, \epsilon). \end{aligned} \quad (\text{F.9})$$

To ensure that the  $\epsilon \rightarrow 0$  limit is well-defined we assume

$$\lim_{\bar{v} \rightarrow \infty} \frac{\Delta v}{\bar{v}} = \lim_{\epsilon \rightarrow 0} \epsilon \Delta v = 0. \quad (\text{F.10})$$

## Slow Manifold Calculation

The slow manifold is given by the root of  $g(x, z, 0) = 0$ .

$$g(x, z, 0) = 0 \implies 2z(3 - \alpha(x, z)) - d\alpha(x, z)(z + 1 - \alpha(x, z)) = 0$$

$$\begin{aligned}
&\implies 2zy_U - d\alpha(x, z)(z + 1 - \alpha) = 0 \\
&\implies 2(1 + y_A)(1 + y_B)y_U = d(3 - y_U)(y_A y_B) \\
&\implies \frac{d}{2} y_A y_B = \frac{y_U(1 + y_A)(1 + y_B)}{3 - y_U}.
\end{aligned} \tag{F.11}$$

(F.11) is an implicit expression for the slow manifold. Define the function  $\hat{x} = \sqrt{x} + \frac{1}{\sqrt{x}}$ . Then  $\alpha(x, z) = \sqrt{z}\hat{x}$ . In order to obtain an explicit expression we rewrite (F.11) in the  $(x, z)$  coordinates as follows,

$$\begin{aligned}
g(x, z, 0) = 0 &\implies 2z(3 - \alpha(x, z)) - d\alpha(x, z)(z + 1 - \alpha(x, z)) = 0 \\
&\implies 2z(3 - \sqrt{z}\hat{x}) - d\sqrt{z}\hat{x}(z + 1 - \sqrt{z}\hat{x}) = 0 \\
&\implies 6\sqrt{z} - 2z\hat{x} - d\hat{x}z - d\hat{x} + d\hat{x}^2\sqrt{z} = 0 \\
&\implies (2 + d)\hat{x}z - (d\hat{x}^2 + 6)\sqrt{z} + d\hat{x} = 0.
\end{aligned} \tag{F.12}$$

(F.12) is quadratic in  $\sqrt{z}$ . The solutions to the quadratic are given by

$$\sqrt{z} = \frac{d\hat{x}^2 + 6 \pm \sqrt{D}}{2(2 + d)\hat{x}}, \tag{F.13}$$

where the discriminant  $D = d^2\hat{x}^4 + 36 + 4d\hat{x}^2 - 4d^2\hat{x}^2$ . Hence we have two distinct solutions for the slow manifold given by

$$z = \left( \frac{d\hat{x}^2 + 6 + \sqrt{D}}{2(2 + d)\hat{x}} \right)^2, \left( \frac{d\hat{x}^2 + 6 - \sqrt{D}}{2(2 + d)\hat{x}} \right)^2. \tag{F.14}$$

The second solution in (F.14) lies outside the feasible domain  $z \in [1, \frac{9}{4}]$  (and correspondingly  $(y_A, y_B) \in \Delta_2$ ) and is hence rejected.

To summarize, the slow manifold is given by

$$z = \left( \frac{d\hat{x}^2 + 6 + \sqrt{D}}{2(2 + d)\hat{x}} \right)^2 =: h(x)$$

where  $\hat{x} = \sqrt{x} + \frac{1}{\sqrt{x}}$  and  $D = (d\hat{x}^2 + 6)^2 - 4d\hat{x}^2(2 + d)$ .

(F.15)

## Attractively of the Slow Manifold

The boundary layer dynamics are given by

$$\frac{dy}{d\tau} = g(x, y + h(x), 0), \quad (\text{F.16})$$

where  $x$  is treated as fixed parameter. Stability of the boundary layer dynamics requires the exponential stability of its origin, uniformly in the fixed parameter  $x$  [54]. To test for exponential stability of the origin, we compute the Jacobian of the dynamics (F.16) evaluated at the origin

$$\left. \frac{\partial}{\partial y} g(x, y + h(x), 0) \right|_{y=0} = -\frac{1}{12} \sqrt{1296 + \frac{(1+x)^2 \sigma (24x + (x-1)^2 \sigma)}{x^2}} \quad (\text{F.17})$$

and note that  $\left. \frac{\partial}{\partial y} g(x, y + h(x), 0) \right|_{y=0} < 0$  for all  $x \in [\frac{1}{2}, 2]$ .

## Reduced Dynamics of the Slow Model

The reduced dynamics on the slow manifold defined by (F.15) are given by

$$\begin{aligned} \dot{x} &= f(x, h(x), 0) \\ &= \frac{\sigma x}{h(x)} [h(x) + 1 - \alpha(x, h(x))] \beta(x, h(x)) + x(3 - \alpha(x, h(x))) \Delta v. \end{aligned} \quad (\text{F.18})$$

The general expression for the equilibria of (F.18) is complicated. Nonetheless, analytical solutions can be obtained for two special cases described below.

## Special Cases

- $d = \mathcal{O}(\epsilon)$ : The slow manifold is given by the  $d \rightarrow 0$  limit of the expression (F.15),

$$\lim_{d \rightarrow 0} h(x) = \frac{9x}{(x+1)^2}, \quad (\text{F.19})$$

which corresponds to  $y_U = 1 - y_A - y_B = 0$ . Another way of seeing this is computing  $g(x, z, 0)$  from (F.6) in the limit  $d \rightarrow 0$ , which gives  $2z(3 - \alpha) = 0 \iff 3 - \alpha = 0 \iff y_U = 0$ . The reduced dynamics on the slow manifold

are given by substituting (F.19) in (F.18)

$$\begin{aligned}
\dot{x} &= f(x, h(x), 0) \\
&= \sigma \frac{(x+1)^2}{9} \left[ \frac{9x}{(x+1)^2} + 1 - \alpha \left( x, \frac{9x}{(x+1)^2} \right) \right] \beta \left( x, \frac{9x}{(x+1)^2} \right) \\
&= \sigma \frac{(x+1)^2}{9} \left[ \frac{9x}{(x+1)^2} - 2 \right] \frac{3(x-1)}{(x+1)}. \tag{F.20}
\end{aligned}$$

Equilibria of (F.20) are  $x_{eq} = -1, \frac{1}{2}, 1, 2$ . These equilibria and their stability are summarized in Table F.1. The two stable equilibria,  $x_{eq} = \frac{1}{2}$  and  $x_{eq} = 2$ , correspond to  $y_B = 1$  and  $y_A = 1$ , respectively. The unstable equilibrium  $z_{eq} = 1$  corresponds to  $y_A = y_B = \frac{1}{2}$ . The  $x_{eq} = -1$  equilibrium is rejected since the dynamics are only defined for  $x \in [\frac{1}{2}, 2]$ .

**Table F.1:** Equilibria and stability for the reduced dynamics (F.20)

$x_{eq}$	$\frac{1}{2}$	1	2
$z_{eq}$	2	$\frac{9}{4}$	2
$y_{Aeq} = \frac{2x_{eq}-1}{x_{eq}+1}$	0	$\frac{1}{2}$	1
$y_{Beq} = 1 - y_{Aeq}$	1	$\frac{1}{2}$	0
$\frac{\partial f(x, h(x), 0)}{\partial x} \Big _{x=x_{eq}}$	$\frac{-\sigma}{3}$	$\frac{\sigma}{6}$	$\frac{-\sigma}{3}$
Stability	Stable	Unstable	Stable

- $d = 1, \Delta v = 0$ : A general expression for the equilibria of (F.18), even for the symmetric case  $\Delta v = 0$ , is challenging to determine. However, for  $d = 1$ , analytical expressions for the equilibria and their stability are summarized in Table F.2. In practice, the expressions from Table F.2 hold for a broad range of  $d$  as long as  $\bar{v}$  is sufficiently large.

Note that from Equation (7.4) (and assuming  $\sigma = \mathcal{O}(v)$ ),

$$\begin{aligned}
\lim_{v \rightarrow \infty} p_1 &= \lim_{v \rightarrow \infty} \left( \frac{2}{\frac{1}{v^2} + 1 + \sqrt{\frac{1}{v^4} + \frac{2}{v^2} + 9 + 4}}, \frac{2}{\frac{1}{v^2} + 1 + \sqrt{\frac{1}{v^4} + \frac{2}{v^2} + 9 + 4}} \right) \\
&= \left( \frac{2}{1 + \sqrt{13}}, \frac{2}{1 + \sqrt{13}} \right),
\end{aligned}$$

**Table F.2:** Equilibria and stability for the reduced dynamics (F.18) with  $d = 1$  and  $\Delta v = 0$

$x_{eq}$	2	1	$\frac{1}{2}$
$z_{eq}$	2	$\frac{1}{18}(19 + 5\sqrt{13})$	2
$y_{Aeq}$	1	$\frac{2}{1+\sqrt{13}}$	0
$y_{Beq}$	0	$\frac{2}{1+\sqrt{13}}$	1
$\frac{\partial f(x, h(x), 0)}{\partial x} \Big _{x=x_{eq}}$	$\frac{-4\sigma}{15}$	$\frac{4-\sqrt{13}}{3}\sigma$	$\frac{-4\sigma}{15}$
Stability	Stable	Unstable	Stable

which is precisely the unstable equilibrium point corresponding to  $x_{eq} = 1$  in Table F.2. Similarly, for  $\sigma = \mathcal{O}(v)$ ,  $\lim_{v \rightarrow \infty} p_2 = (1, 0)$  and  $\lim_{v \rightarrow \infty} p_3 = (0, 1)$ , which are precisely the two stable equilibria corresponding to  $x_{eq} = 2$  and  $x_{eq} = \frac{1}{2}$  in Table F.2, respectively. Hence, the equilibria of the reduced dynamics (F.18) and their stability match exactly those of the full dynamics computed in (7.4), in the limit as  $v \rightarrow \infty$  and  $\sigma = \mathcal{O}(v)$ .

## Appendix G

### Edge Detection

This section describes a simple algorithm to find the boundaries of an object in a specified region  $\mathcal{R}$  of parameter space. Though we use the planar case  $\mathbb{R}^2$  for illustration, the algorithm works generally in  $\mathbb{R}^N$ . The region  $\mathcal{R}$  is assumed to contain a domain  $\mathcal{D}$ , the boundary of which we intend to find.

#### Assumptions:

1. For each point  $\mathbf{p} \in \mathcal{R} \subset \mathbb{R}^N$ , there is a map  $f : \mathbb{R}^N \mapsto \{0, 1\}$  such that  $f(\mathbf{p}) = 1$  denotes a point inside the domain  $\mathcal{D}$  and  $f(\mathbf{p}) = 0$  denotes a point outside  $\mathcal{D}$ .

- Initial inside ( $f(\mathbf{p}_{in}) = 1$ ) and outside ( $f(\mathbf{p}_{out}) = 0$ ) points are easy to determine, such that the straight line from  $\mathbf{p}_{out}$  to  $\mathbf{p}_{in}$  has a single boundary in between.

## Algorithm:

- Initialize a point  $\mathbf{p}_{in}$  inside  $\mathcal{D}$  (i.e.  $f(\mathbf{p}_{in}) = 1$ ) and a point  $\mathbf{p}_{out}$  outside  $\mathcal{D}$  (i.e.  $f(\mathbf{p}_{out}) = 0$ ).
- Compute  $f(\mathbf{p}_{mid})$  where  $\mathbf{p}_{mid} = \frac{1}{2}(\mathbf{p}_{in} + \mathbf{p}_{out})$ .
- If  $f(\mathbf{p}_{mid}) = 1$  then set  $f(\mathbf{p}_{in}) = f(\mathbf{p}_{mid})$ . Else set  $f(\mathbf{p}_{out}) = f(\mathbf{p}_{mid})$ .
- Iterate steps 2 and 3 until  $\|f(\mathbf{p}_{in}) - f(\mathbf{p}_{out})\| < \epsilon$  for some chosen  $\epsilon$ .

One iteration of the algorithm above is illustrated in the figure below. A single run of the algorithm to convergence produce *one* point on the boundary. Successive points may be obtained by running the algorithm on several initializations of  $\mathbf{p}_{in}$  and  $\mathbf{p}_{out}$  (potentially randomly). The main computational barrier is the mapping  $f$ .

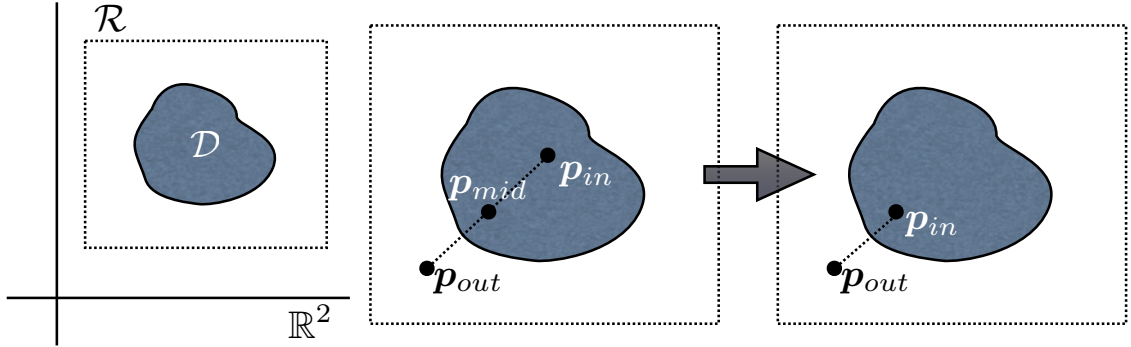


*Illustration of one iteration of the edge detection algorithm.*

# Bibliography

- [1] D. AANEN, P. EGGLERON, C. ROULAND-LEFÈVRE, T. GULDBERG-FRØSLEV, S. ROSENDALH, AND J. BOOMSMA, *The evolution of fungus-growing termites and their mutualistic fungal symbionts*, Proceedings of the National Academy of Sciences, 99 (2002), pp. 14887–14892.
- [2] R. ALBERT AND A. L. BARABÁSI, *Statistical mechanics of complex networks*, Rev. Mod. Phys., 74 (2002), pp. 47–97.
- [3] M. BALLERINI, N. CABIBBO, R. CANDELIER, A. CAVAGNA, E. CISBANI, I. GIARDINA, V. LECOMTE, A. ORLANDI, G. PARISI, A. PROCACCINI, ET AL., *Interaction ruling animal collective behavior depends on topological rather than metric distance: Evidence from a field study*, Proceedings of the National Academy of Sciences, 105 (2008), pp. 1232–1237.
- [4] A. BARABÁSI, H. JEONG, Z. NÉDA, E. RAVASZ, A. SCHUBERT, AND T. VICSEK, *Evolution of the social network of scientific collaborations*, Physica A: Statistical Mechanics and its Applications, 311 (2002), pp. 590–614.
- [5] S. BAZAZI, J. BUHL, J. HALE, M. ANSTEY, G. SWORD, S. SIMPSON, AND I. COUZIN, *Collective motion and cannibalism in locust migratory bands*, Current Biology, 18 (2008), pp. 735–739.
- [6] P. BERTHOLD, A. HELBIG, G. MOHR, AND U. QUERNER, *Rapid microevolution of migratory behaviour in a wild bird species*, Nature, 360 (1992), pp. 668–670.
- [7] A. BLADON, T. GALLA, AND A. MCKANE, *Evolutionary dynamics, intrinsic noise, and cycles of cooperation*, Physical Review E, 81 (2010), pp. 66122–66133.
- [8] R. BOGACZ, E. BROWN, J. MOEHLIS, P. HOLMES, AND J. COHEN, *The physics of optimal decision making: a formal analysis of models of performance in two-alternative forced-choice tasks*, Psychological Review, 113 (2006), pp. 700–765.
- [9] R. BÜRGER, *Mathematical properties of mutation-selection models*, Genetica, 102-103 (1998), pp. 279–298.
- [10] A. CAVAGNA, A. CIMARELLI, I. GIARDINA, G. PARISI, R. SANTAGATI, F. STEFANINI, AND M. VIALE, *Scale-free correlations in starling flocks*, Proceedings of the National Academy of Sciences, 107 (2010), pp. 11865–11870.
- [11] A. CHURCHLAND, R. KIANI, AND M. SHADLEN, *Decision-making with multiple alternatives*, Nature Neuroscience, 11 (2008), pp. 693–702.

- [12] P. CISEK, G. PUSKAS, AND S. EL-MURR, *Decisions in changing conditions: the urgency-gating model*, The Journal of Neuroscience, 29 (2009), pp. 11560–11571.
- [13] I. COUZIN AND N. FRANKS, *Self-organized lane formation and optimized traffic flow in army ants*, Proceedings of the Royal Society of London. Series B: Biological Sciences, 270 (2003), pp. 139–146.
- [14] I. COUZIN, J. KRAUSE, N. FRANKS, AND S. LEVIN, *Effective leadership and decision-making in animal groups on the move*, Nature, 433 (2005), pp. 513–516.
- [15] I. COUZIN, J. KRAUSE, R. JAMES, G. RUXTON, AND N. FRANKS, *Collective memory and spatial sorting in animal groups*, Journal of Theoretical Biology, 218 (2002), pp. 1–11.
- [16] C. DARWIN, *On the Origin of Species by Means of Natural Selection: or the Preservation of Favored Races in the Struggle for Life*, John Murray, Albemarle Street, 1st ed., 1859.
- [17] S. DEHAENE, *The neural basis of the Weber-Fechner law: A logarithmic mental number line*, Trends in Cognitive Sciences, 7 (2003), pp. 145–147.
- [18] O. DIEKMANN, *A beginner’s guide to adaptive dynamics*, Banach Center Publications, 63 (2004), pp. 47–86.
- [19] P. ERDŐS AND A. RÉNYI, *On the evolution of random graphs*, in Publication of the Mathematical Institute of the Hungarian Academy of Sciences, 1960.
- [20] S. EUBANK, H. GUCLU, V. KUMAR, M. MARATHE, A. SRINIVASAN, Z. TOROCZKAI, AND N. WANG, *Modelling disease outbreaks in realistic urban social networks*, Nature, 429 (2004), pp. 180–184.
- [21] P. FRIEDL AND D. GILMOUR, *Collective cell migration in morphogenesis, regeneration and cancer*, Nature Reviews Molecular Cell Biology, 10 (2009), pp. 445–457.
- [22] J. FRYXELL AND A. SINCLAIR, *Causes and consequences of migration by large herbivores*, Trends in Ecology & Evolution, 3 (1988), pp. 237–241.
- [23] K. GALLOWAY, E. JUSTH, AND P. KRISHNAPRASAD, *Portraits of cyclic pursuit*, in Proc. 50th IEEE Conference on Decision and Control, 2011, pp. 2724–2731.
- [24] C. GARDINER, *Handbook of Stochastic Methods: for Physics, Chemistry and the Natural Sciences*, Springer, 4th ed., 2009.
- [25] S. GERITZ, E. KISDI, G. MESZÉNA, AND J. METZ, *Evolutionarily singular strategies and the adaptive growth and branching of the evolutionary tree*, Evolutionary Ecology, 12 (1997), pp. 35–57.
- [26] S. GERITZ, J. METZ, É. KISDI, AND G. MESZÉNA, *Dynamics of adaptation and evolutionary branching*, Physical Review Letters, 78 (1997), pp. 2024–2027.
- [27] K. GHOSE, T. K. HORIUCHI, P. S. KRISHNAPRASAD, AND C. F. MOSS, *Echolocating bats use a nearly time-optimal strategy to intercept prey*, PLoS Biology, 4 (2006), pp. 0865–0873.

- [28] D. GILLEY, *The identity of nest-site scouts in honeybee swarms*, Apidologie, 29 (1998), pp. 229–240.
- [29] M. GIURFA, J. NUNEZ, L. CHITTKA, AND R. MENZEL, *Colour preferences of flower-naive honeybees*, Journal of Comparative Physiology A: Neuroethology, Sensory, Neural, and Behavioral Physiology, 177 (1995), pp. 247–259.
- [30] J. GOULD, *Animal navigation: the evolution of magnetic orientation*, Current Biology, 18 (2008), pp. R482–R484.
- [31] J. GOULD AND W. TOWNE, *Honey bee learning*, Advances in Insect Physiology, 20 (1988), pp. 55–86.
- [32] J. GUCKENHEIMER AND P. HOLMES, *Nonlinear Oscillations, Dynamical Systems, and Bifurcations of Vector Fields*, Springer, 2002.
- [33] V. GUTTAL AND I. COUZIN, *Social interactions, information use, and the evolution of collective migration*, Proceedings of the National Academy of Sciences, 107 (2010), pp. 16172–16177.
- [34] ——, *Leadership, collective motion and the evolution of migratory strategies*, Communicative & Integrative Biology, 4 (2011), pp. 294–298.
- [35] V. GUTTAL, P. ROMANCZUK, S. SIMPSON, G. SWORD, AND I. COUZIN, *Cannibalism can drive the evolution of behavioural phase polyphenism in locusts*, Ecology Letters, 15 (2012), pp. 1158–1166.
- [36] K. HADELER, *Stable polymorphisms in a selection model with mutation*, SIAM Journal on Applied Mathematics, 41 (1981), pp. 1–7.
- [37] N. HANDEGARD, K. BOSWELL, C. IOANNOU, S. LEBLANC, D. TJØSTHEIM, AND I. COUZIN, *The dynamics of coordinated group hunting and collective information transfer among schooling prey*, Current Biology, 22 (2012), pp. 1213 – 1217.
- [38] T. HANKS, M. MAZUREK, R. KIANI, E. HOPP, AND M. SHADLEN, *Elapsed decision time affects the weighting of prior probability in a perceptual decision task*, The Journal of Neuroscience, 31 (2011), pp. 6339–6352.
- [39] D. HIGHAM, *An algorithmic introduction to numerical simulation of stochastic differential equations*, SIAM Review, 43 (2001), pp. 525–546.
- [40] J. HOFBAUER AND K. SIGMUND, *Evolutionary Games and Replicator Dynamics*, Cambridge University Press, 1998.
- [41] ——, *Evolutionary game dynamics*, Bulletin of the American Mathematical Society, 40 (2003), pp. 479–520.
- [42] R. HOLLAND, M. WIKELSKI, AND D. WILCOVE, *How and why do insects migrate?*, Science, 313 (2006), pp. 794–796.
- [43] R. HORN AND C. JOHNSON, *Matrix Analysis*, Cambridge University Press, 1990.
- [44] I. HUSSEIN, *An individual-based evolutionary dynamics model for networked social behaviors*, in Proceedings of the American Control Conference, 2009, pp. 5789–5796.

- [45] C. C. IOANNOU, V. GUTTAL, AND I. D. COUZIN, *Predatory fish select for coordinated collective motion in virtual prey*, Science, 337 (2012), pp. 1212–1215.
- [46] R. ISAACS, *Differential Games: A Mathematical Theory with Applications to Warfare and Pursuit, Control and Optimization*, Dover Publications, 1999.
- [47] A. JADBABAIE, J. LIN, AND A. MORSE, *Coordination of groups of mobile autonomous agents using nearest neighbor rules*, IEEE Transactions on Automatic Control, 48 (2003), pp. 988–1001.
- [48] M. JANSSEN, *Use of complex adaptive systems for modeling global change*, Ecosystems, 1 (1998), pp. 457–463.
- [49] S. E. JORGENSEN, B. C. PATTEN, AND M. STRASKRABA, *Ecosystems emerging: toward an ecology of complex systems in a complex future*, Ecological Modelling, 62 (1992), pp. 1–27.
- [50] E. JUSTH AND P. KRISHNAPRASAD, *Steering laws for motion camouflage*, Proceedings of the Royal Society A, 462 (2006), pp. 3629–3643.
- [51] J. KARELAHTI, K. VIRTANEN, AND T. RAIVIO, *Near-optimal missile avoidance trajectories via receding horizon control*, Journal of Guidance Control and Dynamics, 30 (2007), pp. 1287–1298.
- [52] S. KATO, S. TSUGAWA, K. TOKUDA, T. MATSUI, AND H. FUJII, *Vehicle control algorithms for cooperative driving with automated vehicles and intervehicle communications*, IEEE Transactions on Intelligent Transportation Systems, 3 (2002), pp. 155–161.
- [53] B. KERR, M. RILEY, M. FELDMAN, B. BOHANNAN, ET AL., *Local dispersal promotes biodiversity in a real-life game of rock-paper-scissors*, Nature, 418 (2002), pp. 171–174.
- [54] H. KHALIL, *Nonlinear Systems*, Prentice Hall, 3rd ed., 2002.
- [55] N. KOMAROVA, *Replicator-mutator equation, universality property and population dynamics of learning*, Journal of Theoretical Biology, 230 (2004), pp. 227–239.
- [56] N. KOMAROVA AND S. LEVIN, *Eavesdropping and language dynamics*, Journal of Theoretical Biology, 264 (2010), pp. 104–118.
- [57] N. KOMAROVA, P. NIYOGI, AND M. NOWAK, *The evolutionary dynamics of grammar acquisition*, Journal of Theoretical Biology, 209 (2001), pp. 43–59.
- [58] S. KOTZ, N. JOHNSON, AND N. BALAKRISHNAN, *Continuous Multivariate Distributions: Models and Applications*, vol. 1, Wiley-Interscience, 2000.
- [59] Y. KUZNETSOV, *Elements of Applied Bifurcation Theory*, Springer, 1998.
- [60] Y. LEE, T. COLLIER, C. TAYLOR, AND R. OLFATI-SABER, *Simplicity from complexity: emergence of cohesion in the evolutionary dynamics of grammar networks*, Evolutionary Ecology, 11 (2009), pp. 433–445.
- [61] K. LERMAN, A. MARTINOLI, AND A. GALSTYAN, *A review of probabilistic macroscopic models for swarm robotic systems*, Swarm Robotics, (2005), pp. 143–152.

- [62] S. LEVIN, *Complex adaptive systems: exploring the known, the unknown and the unknowable*, Bulletin of the American Mathematical Society, 40 (2003), pp. 3–20.
- [63] S. LEVIN AND R. DURRETT, *From individuals to epidemics*, Philosophical Transactions of the Royal Society of London. Series B: Biological Sciences, 351 (1996), pp. 1615–1621.
- [64] Z. LIN, B. FRANCIS, AND M. MAGGIORE, *Necessary and sufficient graphical conditions for formation control of unicycles*, IEEE Transactions on Automatic Control, 50 (2005), pp. 121–127.
- [65] S. MANNOR AND J. SHAMMA, *Multi-agent learning for engineers*, Artificial Intelligence, 171 (2007), pp. 417–422.
- [66] S. MARRAS AND M. PORFIRI, *Fish and robots swimming together: attraction towards the robot demands biomimetic locomotion*, Journal of The Royal Society Interface, 9 (2012), pp. 1856–1868.
- [67] J. MARSHALL, *Coordinated autonomy: Pursuit formations of multivehicle systems*, PhD thesis, University of Toronto, Toronto, Ontario, Canada, 2005.
- [68] J. MARSHALL, M. BROUKE, AND B. FRANCIS, *Formations of vehicles in cyclic pursuit*, IEEE Transactions on Automatic Control, 49 (2004), pp. 1963–1974.
- [69] ———, *Pursuit formations of unicycles*, Automatica, 42 (2006), pp. 3–12.
- [70] J. A. R. MARSHALL, *Group selection and kin selection: formally equivalent approaches*, Trends in Ecology & Evolution, 26 (2011), pp. 325–332.
- [71] J. A. R. MARSHALL, R. BOGACZ, A. DORNHAUS, R. PLANQUÉ, T. KOVACS, AND N. FRANKS, *On optimal decision-making in brains and social insect colonies*, Journal of the Royal Society Interface, 6 (2009), pp. 1065–1074.
- [72] B. T. MILNE, *Motivation and benefits of complex systems approaches in ecology*, Ecosystems, 1 (1998), pp. 449–456.
- [73] M. MITCHELL, *An Introduction to Genetic Algorithms*, Bradford, 1998.
- [74] W. MITCHENER, *A Mathematical Model of Human Languages: The Interaction of Game Dynamics & Learning Processes*, Princeton University, 2003.
- [75] ———, *Bifurcation analysis of the fully symmetric language dynamical equation*, Journal of Mathematical Biology, 46 (2003), pp. 265–285.
- [76] W. MITCHENER AND M. NOWAK, *Chaos and language*, Proceedings of the Royal Society B: Biological Sciences, 271 (2004), pp. 701–704.
- [77] A. MIZUTANI, J. CHAHL, AND M. SRINIVASAN, *Motion camouflage in dragonflies*, Nature, 423 (2003), pp. 604–605.
- [78] B. NABET, *Dynamics and Control in Natural and Engineered Multi-Agent Systems*, PhD thesis, Princeton University, Princeton, NJ, 2009.

- [79] R. NAGPAL, S. BERMAN, AND Á. HALÁSZ, *Optimization of stochastic strategies for spatially inhomogeneous robot swarms: A case study in commercial pollination*, in Proceedings of the International Conference on Intelligent Robots and Systems, 2011, pp. 25–30.
- [80] P. NAHIN, *Chases and Escapes: The Mathematics of Pursuit and Evasion*, Princeton University Press, 2007.
- [81] F. NEUMAN, *On the approximate solution of complex combat games.*, Journal of Guidance, Control, and Dynamics, 13 (1990), pp. 128–136.
- [82] M. NEWMAN, *Models of the small world*, Journal of Statistical Physics, 101 (2000), pp. 819–841.
- [83] M. NEWMAN, S. STROGATZ, AND D. WATTS, *Random graphs with arbitrary degree distributions and their applications*, Physical Review E, 64 (2001), pp. 026118–026133.
- [84] M. NOWAK, *Five rules for the evolution of cooperation*, Science, 314 (2006), pp. 1560–1563.
- [85] M. NOWAK, N. KOMAROVA, AND P. NIYOGI, *Evolution of universal grammar*, Science, 291 (2001), pp. 114–118.
- [86] M. NOWAK AND K. SIGMUND, *Chaos and the evolution of cooperation*, Proceedings of the National Academy of Sciences, 90 (1993), pp. 5091–5094.
- [87] ———, *Evolutionary dynamics of biological games*, Science, 303 (2004), pp. 793–799.
- [88] M. NOWAK, C. TARNITA, AND E. WILSON, *The evolution of eusociality*, Nature, 466 (2010), pp. 1057–1062.
- [89] S. OKASHA, *Altruism researchers must cooperate*, Nature, 467 (2010), pp. 653–655.
- [90] R. OLFATI-SABER, *Evolutionary dynamics of behavior in social networks*, in 46th IEEE Conference on Decision & Control, 2007, pp. 4051–4056.
- [91] R. OLFATI-SABER, J. FAX, AND R. MURRAY, *Consensus and cooperation in networked multi-agent systems*, Proceedings of the IEEE, 95 (2007), pp. 215–233.
- [92] K. PAGE AND M. NOWAK, *Unifying evolutionary dynamics*, Journal of Theoretical Biology, 219 (2002), pp. 93–98.
- [93] D. PAIS, C. CAICEDO-NUNEZ, AND N. LEONARD, *Hopf bifurcations and limit cycles in evolutionary network dynamics*, SIAM Journal on Applied Dynamical Systems, (in press).
- [94] D. PAIS, M. CAO, AND N. LEONARD, *Formation shape and orientation control using projected collinear tensegrity structures*, in Proceedings of the American Control Conference, IEEE, 2009, pp. 610–615.
- [95] D. PAIS, P. HOGAN, T. SCHLEGEL, N. FRANKS, N. LEONARD, AND J. A. R. MARSHALL, *Value-sensitive decision-making in a model of collective choice*, (in prep).

- [96] D. PAIS AND N. LEONARD, *Pursuit and evasion: Evolutionary dynamics and collective motion*, in Proceedings of the AIAA Guidance, Navigation and Control conference, 2010, DOI: 10.2514/6.2010-7584.
- [97] ———, *Limit cycles in replicator-mutator network dynamics*, in Proceedings of the 50th IEEE Conference on Decision and Control, 2011, pp. 3922 –3927.
- [98] D. PALEY, N. LEONARD, R. SEPULCHRE, D. GRUNBAUM, AND J. PARRISH, *Oscillator models and collective motion*, Control Systems Magazine, IEEE, 27 (2007), pp. 89–105.
- [99] J. PALMER, A. HUK, AND M. SHADLEN, *The effect of stimulus strength on the speed and accuracy of a perceptual decision*, Journal of Vision, 5 (2005).
- [100] M. PEIXOTO, *Structural stability on two dimensional manifolds*, Topology, 1 (1962), pp. 101–120.
- [101] M. PONTANI AND B. CONWAY, *Optimal interception of evasive missile warheads: numerical solution of the differential game*, Journal of Guidance Control and Dynamics, 31 (2008), pp. 1111–1122.
- [102] T. POSTON AND I. STEWART, *Catastrophe Theory and its Applications*, vol. 2, Dover Publications, 1996.
- [103] I. POULAKAKIS, L. SCARDOVI, AND N. LEONARD, *Coupled stochastic differential equations and collective decision making in the two-alternative forced-choice task*, in Proceedings of the American Control Conference (ACC), 2010, pp. 69 –74.
- [104] ———, *Node certainty in collective decision making*, in Proceedings of the Conference on Decision and Control (CDC), IEEE, 2012 to appear.
- [105] G. PRICE, *Selection and covariance*, Nature, 227 (1970), pp. 520–21.
- [106] ———, *Extension of covariance selection mathematics*, Annals of Human Genetics, 35 (1972), pp. 485–490.
- [107] A. RAHMANI, M. JI, M. MESBAHI, AND M. EGERSTEDT, *Controllability of multi-agent systems from a graph-theoretic perspective*, SIAM Journal of Control and Optimization, 48 (2009), pp. 162–186.
- [108] T. RAIPIO AND H. EHTAMO, *Visual aircraft identification as a pursuit-evasion game*, Journal of Guidance, Control and Dynamics, 23 (2000), pp. 701–708.
- [109] R. RATCLIFF AND J. ROUDER, *Modeling response times for two-choice decisions*, Psychological Science, 9 (1998), pp. 347–356.
- [110] W. REN, *Multi-vehicle consensus with a time-varying reference state*, Systems & Control Letters, 56 (2007), pp. 474–483.
- [111] W. REN, R. BEARD, AND T. McLAIN, *Coordination variables and consensus building in multiple vehicle systems*, V. Kumar, N.E. Leonard, A.S. Morse (Eds.), Cooperative Control: Lecture Notes in Control and Information Sciences, (2005), pp. 439–442.

- [112] P. ROMANCZUK, I. COUZIN, AND L. SCHIMANSKY-GEIER, *Collective motion due to individual escape and pursuit response*, Physical Review Letters, 102 (2009), p. 10602.
- [113] W. RUGH, *Linear System Theory*, Prentice-Hall, Inc., 1996.
- [114] E. SAHIN, *Swarm robotics: From sources of inspiration to domains of application*, Swarm Robotics, (2005), pp. 10–20.
- [115] T. SEELEY, *Consensus building during nest-site selection in honey bee swarms: the expiration of dissent*, Behavioral Ecology and Sociobiology, 53 (2003), pp. 417–424.
- [116] ———, *Honeybee Democracy*, Princeton University Press, 2010.
- [117] T. SEELEY AND P. VISSCHER, *Sensory coding of nest-site value in honeybee swarms*, Journal of Experimental Biology, 211 (2008), pp. 3691–3697.
- [118] T. SEELEY, P. VISSCHER, T. SCHLEGEL, P. HOGAN, N. FRANKS, AND J. A. R. MARSHALL, *Stop signals provide cross inhibition in collective decision-making by honeybee swarms*, Science, 335 (2012), pp. 108–111.
- [119] A. SHAW AND S. LEVIN, *To breed or not to breed: a model of partial migration*, Oikos, 120 (2011), pp. 1871–1879.
- [120] S. J. SIMPSON AND G. A. SWORD, *Evolving migration*, Proceedings of the National Academy of Sciences, 107 (2010), pp. 16753–16754.
- [121] B. SINERVO AND C. LIVELY, *The rock-paper-scissors game and the evolution of alternative male strategies*, Nature, 380 (1996), pp. 240–243.
- [122] J. SMITH, *Evolution and the Theory of Games*, Cambridge University Press, 1982.
- [123] M. V. SRINIVASAN AND S. ZHANG, *Visual motor computations insects*, Annual Review of Neuroscience, 27 (2004), pp. 679–696.
- [124] P. STADLER AND P. SCHUSTER, *Mutation in autocatalytic reaction networks*, Journal of Mathematical Biology, 30 (1992), pp. 597–632.
- [125] S. STROGATZ, *Nonlinear Dynamics and Chaos: with Applications to Physics, Biology, Chemistry, and Engineering*, Westview Press, 1994.
- [126] D. SUMPTER, *Collective animal behavior*, Princeton University Press, 2010.
- [127] M. SURETTE, M. MILLER, AND B. BASSLER, *Quorum sensing in escherichia coli, salmonella typhimurium, and vibrio harveyi: a new family of genes responsible for autoinducer production*, Proceedings of the National Academy of Sciences, 96 (1999), pp. 1639–1644.
- [128] D. SWAIN, I. COUZIN, AND N. LEONARD, *Real-time feedback-controlled robotic fish for behavioral experiments with fish schools*, Proceedings of the IEEE, 100 (2012), pp. 150 –163.
- [129] P. TAYLOR AND L. JONKER, *Evolutionary stable strategies and game dynamics*, Mathematical Biosciences, 40 (1978), pp. 145–156.

- [130] H. TEMBINE, E. ALTMAN, R. EL-AZOUZI, AND Y. HAYEL, *Evolutionary games in wireless networks*, IEEE Transactions on Systems, Man, and Cybernetics, Part B, 40 (2010), pp. 634–646.
- [131] L. TESFATSION, *Economic agents and markets as emergent phenomena*, Proceedings of the National Academy of Sciences, 99 (2002), pp. 7191–7192.
- [132] C. TORNEY, S. LEVIN, AND I. COUZIN, *Specialization and evolutionary branching within migratory populations*, Proceedings of the National Academy of Sciences, 107 (2010), pp. 20394–20399.
- [133] C. TORNEY, Z. NEUFELD, AND I. COUZIN, *Context-dependent interaction leads to emergent search behavior in social aggregates*, Proceedings of the National Academy of Sciences, 106 (2009), pp. 22055–22060.
- [134] A. TRAULSEN, J. CLAUSSEN, AND C. HAUERT, *Coevolutionary dynamics: from finite to infinite populations*, Physical Review Letters, 95 (2005), pp. 238701–238704.
- [135] ———, *Coevolutionary dynamics in large, but finite populations*, Physical Review E, 74 (2006), pp. 11901–11908.
- [136] X. TREPAT, M. WASSERMAN, T. ANGELINI, E. MILLET, D. WEITZ, J. BUTLER, AND J. FREDBERG, *Physical forces during collective cell migration*, Nature Physics, 5 (2009), pp. 426–430.
- [137] G. UHLENBECK AND L. ORNSTEIN, *On the theory of the brownian motion*, Physical Review, 36 (1930), p. 823.
- [138] C. URMSON, J. ANHALT, D. BAGNELL, C. BAKER, R. BITTNER, M. CLARK, J. DOLAN, D. DUGGINS, T. GALATALI, C. GEYER, ET AL., *Autonomous driving in urban environments: Boss and the urban challenge*, Journal of Field Robotics, 25 (2008), pp. 425–466.
- [139] N. VAN KAMPEN, *Stochastic Processes in Physics and Chemistry*, vol. 1, North Holland, 1992.
- [140] N. VICKERS, *Mechanisms of animal navigation in odor plumes*, The Biological Bulletin, 198 (2000), pp. 203–212.
- [141] T. VINCENT AND J. BROWN, *Evolutionary Game Theory, Natural Selection, and Darwinian Dynamics*, Cambridge University Press, 2005.
- [142] T. VINCENT AND T. VINCENT, *Evolution and control system design: The evolutionary game*, Control Systems Magazine, IEEE, 20 (2000), pp. 20–35.
- [143] P. VISSCHER, *Group decision making in nest-site selection among social insects*, Annual Reviews Entomology, 52 (2007), pp. 255–275.
- [144] K. VON FRISCH, *The Dance Language and Orientation of Bees*, Harvard University Press, 1967.
- [145] Y. WANG AND I. HUSSEIN, *Evolutionary bandwidth allocation and routing in large-scale wireless sensor networks*, in Proceedings of the American Control Conference, 2010, pp. 1850–1855.

- [146] D. J. WATTS AND S. H. STROGATZ, *Collective dynamics of ‘small-world’ networks*, Nature, 393 (1998), pp. 440–442.
- [147] E. WEI, E. JUSTH, AND P. KRISHNAPRASAD, *Pursuit and an evolutionary game*, Proceedings of the Royal Society A, 465 (2009), pp. 1539–1559.
- [148] J. WEIBULL, *Evolutionary Game Theory*, The MIT press, 1997.
- [149] E. WILSON, *Caste and division of labor in leaf-cutter ants (hymenoptera: Formicidae: Atta)*, Behavioral Ecology and Sociobiology, 14 (1983), pp. 47–54.
- [150] R. WOOD, *The first takeoff of a biologically inspired at-scale robotic insect*, IEEE Transactions on Robotics, 24 (2008), pp. 341–347.
- [151] G. YOUNG, L. SCARDOVI, AND N. LEONARD, *Robustness of noisy consensus dynamics with directed communication*, in Proceedings of the American Control Conference, 2010, pp. 6312–6317.